Towards a Mapping Between Supernovae and Their Progenitors

by

K-Ryan C. M. Hinds

A thesis submitted in partial fulfillment for the
degree of Doctor of Philosophy

September 2025

Declaration

The work presented in this thesis was carried out at the Astrophysics Research Institute, Liverpool John Moores University. Unless otherwise stated, it is the original work of the author.

While registered as a candidate for the degree of Doctor of Philosophy, for which submission is now made, the author has not been registered as a candidate for any other award. This thesis has not been submitted in whole, or in part, for any other degree.

K-Ryan Hinds
Astrophysics Research Institute
Liverpool John Moores University
IC2, Liverpool Science Park
146 Brownlow Hill
Liverpool
L3 5RF
UK

September 2025

Abstract

Core-collapse supernovae, the explosive deaths of massive stars exceeding $\sim$8 $M_\odot$, exhibit remarkable diversity in their properties – spanning a wide range of luminosities, timescales, morphologies, and spectral evolution. This diversity reflects poorly understood heterogeneity in progenitor physical properties, with enhanced pre-explosion mass-loss emerging as a key driver of observed variations. While decades of detailed studies have characterised individual events, modern sky surveys like the Zwicky Transient Facility (ZTF) are now amassing large, homogeneous samples that are enabling novel statistical insights into the progenitor properties driving this diversity. The field stands at a transformative moment as upcoming surveys promise larger, more homogeneous supernova samples with enhanced temporal and wavelength coverage, enabling improved constraints on progenitor systematics and volumetric rates – insights long sought but limited by small samples and observational biases.

This thesis leverages Gaussian process regression to analyse forced photometry light curves from the magnitude-limited ZTF Bright Transient Survey, and thereby construct one of the largest catalogs of CCSN parameters to date. By correlating empirical features measured from these light curves (e.g. rise times, peak luminosities and colours) with physical parameters from an extensive grid of hydrodynamical models varying in progenitor properties (circumstellar material structure, mass-loss rate and progenitor mass), I quantify the proportion of Type II SNe with sufficient pre-explosion mass-loss to alter their light curves. Out of the 377 spectroscopically classified events with well-sampled light curves, I find that 67 $\pm$ 6% show evidence for substantial circumstellar material ($M_{\rm CSM} \geq 10^{-2.5}$ $M_\odot$) within 10^{15} cm of the progenitor at explosion. After applying volumetric corrections, I find that 36^{+5}_{-7}% of all Type II progenitors possessing dense circumstellar material at this radius. This high fraction of progenitors with dense circumstellar material, supported by both photometric and spectroscopic evidence of

previous supernovae, reveals mass-loss rates significantly exceeding those observed in local group red supergiants or predicted by current theoretical models.

Additionally, this thesis investigates late-time radioactive ^{56}Ni tails using an automated image-subtraction pipeline I developed for the Liverpool Telescope and expanded to multiple facilities. This analysis constrains synthesised ^{56}Ni masses for 136 Type II SNe, which probes explosion energies and mechanisms through enhanced late-time photometric coverage spanning multiple wavelengths. The weighted median ^{56}Ni mass from the sample is $M_{\rm Ni} = 3.08^{+1.66}_{-1.08} \times 10^{-2}$ M$_\odot$ and $3.82^{+2.04}_{-1.33} \times 10^{-2}$ M$_\odot$ (across two methodologies), aligning with literature values of $2 - 30{\times}10^{-2}$ M$_\odot$.

These findings establish a framework for interpreting upcoming survey data from next-generation facilities that will probe fainter events and earlier explosion phases. This thesis advances our understanding of massive stars' final moments, linking pre-explosion activity to explosive outcomes and establishing a foundation for comprehensive models of CCSN diversity.

K-Ryan Hinds September 2025

Publications

In the course of completing the work presented in this thesis, its contents have been submitted and/or accepted for publication in a refereed journal:

1. Inferring CSM Properties of Type II SNe Using a Magnitude Limited ZTF Sample. **Hinds et al. (2025)**, MNRAS *accepted*.

Whilst writing this thesis, Hinds, K. R. has also contributed to the following publications, which are focused on topics related to this thesis work:

1. The case of AT2022wtn: a Tidal Disruption Event in an interacting galaxy.
Onori, F. et al. (**incl. Hinds, K. R.**) 2025. MNRAS *accepted*.

2. The nebular spectra of SN 2023ixf: A lower mass, partially stripped progenitor may be the result of binary interaction.
Michel, P. D, Mazzali, P. A., Perley, D. A., **Hinds, K. R.** and Wise, J. L. MNRAS, 539, 2.

3. A Massive Black Hole 0.8 kpc from the Host Nucleus Revealed by the Offset Tidal Disruption Event AT2024tvd.
Yao, Y et al. (**incl. Hinds, K. R.**) 2025. ApJ *accepted*.

4. Low-Luminosity Type IIP Supernovae from the Zwicky Transient Facility Census of the Local Universe I: Luminosity Function, Volumetric Rate.
Das, K. K et al. (**incl. Hinds, K. R.**) 2025. PASP, 137, 4.

5. A Luminous Red Optical Flare and Hard X-ray Emission in the Tidal Disruption Event AT2024kmq.

Ho, A. Y. Q. et al. (**incl. Hinds, K. R.**) 2025. arXiv e-prints. ApJ *accepted*.

6. The BTSbot-nearby discovery of SN 2024jlf: rapid, autonomous follow-up probes interaction in an 18.5 Mpc Type IIP supernova.

Rehemtulla, N. et al. (**incl. Hinds, K. R.**) 2025. arXiv e-prints. ApJ *accepted*.

7. Searching for Gravitational Wave Optical Counterparts with the Zwicky Transient Facility: Summary of O4a.

Ahumada, T. et al. (**incl. Hinds, K. R.**) 2024. PASP, 136, 11, 114201.

8. Eruptive mass loss less than a year before the explosion of superluminous supernovae: I. The cases of SN 2020xga and SN 2022xgc.

Gkini, A. et al. (**incl. Hinds, K. R.**) 2025. A&A, 694, 292.

9. A cosmic formation site of silicon and sulphur revealed by a new type of supernova explosion.

Schulze, S. et al. (**incl. Hinds, K. R.**) 2024. arXiv e-prints. Nature *accepted*.

10. Probing Presupernova Mass Loss in Double-peaked Type Ibc Supernovae from the Zwicky Transient Facility.

Das, K K. et al. (**incl. Hinds, K. R.**) 2024. ApJ, 972, 1, 91.

11. Sample of hydrogen-rich superluminous supernovae from the Zwicky Transient Facility.

Pessi, P J. et al. (**incl. Hinds, K. R.**) 2025. A&A, 695, A142.

12. The Early Ultraviolet Light Curves of Type II Supernovae and the Radii of Their Progenitor Stars.

Irani, I. et al. (**incl. Hinds, K. R.**) 2024. ApJ, 970, 1, 96.

13. SN 2023zaw: An Ultrastripped, Nickel-poor Supernova from a Low-mass Progenitor.
Das, K K. et al. (**incl. Hinds, K. R.**) 2024. ApJ, 969, 1, L11.

14. Dramatic Rebrightening of the Type-changing Stripped-envelope Supernova SN 2023aew.
Sharma, Y. et al. (**incl. Hinds, K. R.**) 2024. ApJ, 966, 2, 199.

15. Spectroscopic observations of progenitor activity 100 days before a Type Ibn supernova.
Brennan, S J. et al. (**incl. Hinds, K. R.**) 2024. A&A, 684, L18.

16. The complex circumstellar environment of supernova 2023ixf.
Zimmerman, E A. et al. (**incl. Hinds, K. R.**) 2024. Nature, 627, 8005, 759.

17. Characterizing the Ordinary Broad-line Type Ic SN 2023pel from the Energetic GRB 230812B.
Srinivasaragavan, G P. et al. (**incl. Hinds, K. R.**) 2024. ApJ, 960, 2, L18.

18. SN 2022joj: A Peculiar Type Ia Supernova Possibly Driven by an Asymmetric Helium-shell Double Detonation.
Liu, C. et al. (**incl. Hinds, K. R.**) 2023. ApJ, 958, 2, 178.

19. Minutes-duration optical flares with supernova luminosities.
Ho, A. Y. Q. et al. (**incl. Hinds, K. R.**) 2023. Nature, 623, 7989, 927.

20. The broad-lined Type-Ic supernova SN 2022xxf and its extraordinary two-humped light curves. I. Signatures of H/He-free interaction in the first four months.
Kuncarayakti, H. et al. (**incl. Hinds, K. R.**) 2023. A&A, 678, A209.

21. Uncovering a population of gravitational lens galaxies with magnified standard candle SN Zwicky.
Goobar, A. et al. (**incl. Hinds, K. R.**) 2023. Nature Astronomy, 7, 1098.

22. The Hydrogen-poor Superluminous Supernovae from the Zwicky Transient Facility Phase I Survey. II. Light-curve Modeling and Characterization of Undulations.
Chen, Z H. et al. (**incl. Hinds, K. R.**) 2023. ApJ, 943, 1, 42.

23. The Hydrogen-poor Superluminous Supernovae from the Zwicky Transient Facility Phase I Survey. I. Light Curves and Measurements.
Chen, Z H. et al. (**incl. Hinds, K. R.**) 2023. ApJ, 943, 1, 41.

Dedicated to Tanya,

Thank you.

Acknowledgements

In a series of fortunate events, I came to be where I am. Perseverance and commitment through extremely difficult periods of my life, combined with a burning curiosity, have propelled me thus far, and (I hope) will continue to drive me even further. The series of fortunate events relates to the strangers this young student/adult/man met along the way that have shaped him into the Doctor he will be. So, whilst I do believe I have ability, it would not be without the guidance, imparted knowledge, wisdom and, most importantly, belief from those I've met on the way that has greatly helped me in ways I cannot hope to repay back to them, but I will endlessly endeavour to pay this forward. Chief among these is my amazing supervisor, Dan. I cannot say thank you enough for your patience and guidance during this adventure! I also want to thank my master's supervisors, Matt and Sam, for setting me on this path, for which I have no regrets. Thank you Chris, and especially Marie, for the numerous chats and help securing my future.

I'd also like to thank my mum, dad, Rheanna and Ny for their endless support. I dedicate this to my late sister Tanya because, since the beginning, she was always my number one supporter. It also goes without saying that I owe a lot to the patience, humour and kindness my partner has shown me over the years. Bella, I cannot thank you enough for the support and stability you have provided for me. Thank you also for agreeing to continue to put up with me for many long years to come. Huge thanks to Simon, Sam and Teddy for the various amounts of support and prep that enabled me to secure a wonderful future that I will soon begin.

I thank everyone I have met during my undergrad at Birmingham and PhD in Liverpool, particularly the amazing Callum, Jason, Jonah, Siân, Greg, David, Sam, Becky, Liv, Zish, many others I do not have space to name and, of course, Arlo.

Contents

List of Figures

List of Tables

Abbreviations

AIC	**Akaike Information Criterion**
BTS	**Bright Transient Survey**
BSG	**Blue supergiant**
BIC	**Bayesian Information Criterion**
CSM	**Circumstellar Material**
CCSNe	**Core-collapse Supernovae**
ECDF	**Empirical Cumulative Distribution Function**
FP	**Forced Photometry**
GRB	**Gamma-ray Burst**
GP	**Gaussian process**
GPR	**Gaussian process regression**
GW	**Gravitational Wave**
KDE	**Kernel Density Estimate**
KNe	**Kilonovae**
LT	**Liverpool Telescope**
LBV	**Luminous Blue Variable**
Mpc	**Megaparsec**
MOGP	**Multi-output Gaussian Process**
PSF	**Point Source Function**
RSG	**Red supergiant**
SBO	**Shock breakout**
SC	**Shock Cooling**
SEDM	**Spectral Energy Density Machine**
SESNe	**Stripped Envelope Supernovae**
SLSNe	**Superluminous Supernovae**

SN	**Supernova**
SNe	**Supernovae**
SNR	**Signal to Noise Ratio**
YSG	**Yellow supergiant**
ZTF	**Zwicky Transient Facility**

Chapter 1

Introduction

1.1 Preface

The landscape of observational astronomy has transformed over the past three decades, ushering in what could be considered the golden age of time-domain astrophysics, with projects such as the Zwicky Transient Facility (ZTF; Bellm et al., 2019b; Graham et al., 2019), the All-Sky Automated Survey for Supernovae (ASAS-SN; Shappee et al., 2014), and the Vera C. Rubin Observatory's Legacy Survey of Space and Time (LSST; LSST Science Collaboration et al., 2009; Ivezić et al., 2019) enabling systematic monitoring of vast regions of the sky at much higher and regular cadences than previously available. This technological renaissance – powered by increasingly sensitive wide-field imaging arrays, sophisticated real-time processing pipelines (Masci et al., 2019), and collaborative funding models – has produced an explosion in supernova (SN) discovery rates from approximately 20 SNe annually in the early 1990s (Filippenko, 1997) to over 1,000 SNe per year today (e.g., Sullivan, 2013; Perley et al., 2020). The $\sim$2 order-of-magnitude-increase transitioned the field from an era of painstaking individual object studies to one where statistical analyses of thousands of events create both unprecedented opportunities and novel challenges for our theoretical understanding of stellar evolution and cosmic transients.

In the current era of astronomy, where the number of known supernovae (SNe) reaches into the tens of thousands, questions naturally arise about the scientific value of observing thousands or tens of thousands of additional SNe. Naturally, this also calls into

question the rationale for extending multi-million pound facilities beyond their planned operational lifetimes as newer observatories come online and operating costs do not decrease. This dialogue within the scientific community reflects a healthy tension between resource allocation and knowledge acquisition. Despite our century-long understanding that 'super-novae' (Baade & Zwicky, 1934) represent the terminal phase of stellar evolution and our detailed theoretical grasp of their core-collapse mechanism following iron core formation (e.g., Arnett, 1972; Woosley & Weaver, 1986; Bethe, 1990; Woosley et al., 2002; Heger et al., 2003; Smartt, 2009), profound gaps persist in our fundamental knowledge that can only be addressed through continued and expanded observational efforts.

While the sheer number of discovered SNe might suggest diminishing returns, this view underestimates the scientific power of systematic and well-characterised samples. The value of large samples does not lie merely in their size, but in their uniformity, completeness, and the precision with which selection effects are understood. The Bright Transient Survey (BTS; Fremling et al., 2020; Perley et al., 2020), for example, is not just a numerical expansion of previous efforts but a fundamentally different dataset: its design prioritises systematic discovery and follow-up, offering an unbiased view of the local transient sky. This systematic approach enables robust population studies and statistical comparisons that are often limited by archival or heterogeneous samples. In this context, the BTS sample is foundational, providing a controlled reference against which to compare more distant or less complete samples – allowing unrivalled exploration and the ability to uncover subtle populations that may have been obscured in less homogeneous datasets.

The statistical power gained from larger sample sizes remains crucial as we have yet to *conclusively* constrain the mapping between zero-age main sequence (ZAMS) progenitor parameters – mass ($M_{\rm ZAMS}$), radius ($R_\star$), metallicity (Z), rotation – and the resulting explosion energetics ($E_{\rm exp}$), a challenge only exacerbated by inherent degeneracies in observational diagnostics (e.g., Goldberg et al., 2019; Hillier & Dessart, 2019; Irani et al., 2024) and complications involved in predicting how binary companions will impact the ensuing SNe. (e.g., Eldridge et al., 2008; Sana et al., 2012; Sana et al., 2013; Eldridge et al., 2018).

Put eloquently by Smartt (2009), the goal 10 years ago was to theoretically predict what

type of stars can produce Fe or OMgNe cores and collapse to give these explosions (for example, a non-exhaustive list of recent work is: Quimby et al., 2007a; Smartt, 2009; Jerkstrand et al., 2025). And whilst progress has been made testing theories and ruling out specific scenarios, more questions have been raised. As ever, more questions require more data, and with the emergence of new classes of SNe and new transients altogether, the need for all-sky coverage has grown exponentially in demand. Consequently, our central challenge persists: determining how specific progenitor properties – the unique combination of mass, radius, density, chemical structure, and explosion energy – manifest in observable signatures.

Major uncertainties still surround the evolutionary pathways that lead to specific SN subtypes. For instance, the ongoing debate between single- and double-degenerate scenarios for Type Ia progenitors (e.g., Whelan & Iben, 1973; Iben & Tutukov, 1984; Nomoto et al., 1984; Webbink, 1984; Li & van den Heuvel, 1997; Nelemans et al., 2001; Han & Podsiadlowski, 2004) and the challenge in confirming theoretically possible SNe from common transients, such as electron capture SNe (ECSNe; Miyaji et al., 1980; Wanajo et al., 2009; Doherty et al., 2017; Hiramatsu et al., 2021) and pair-instability SNe (PISNe; Rakavy & Shaviv, 1967; Barkat et al., 1967; Smith et al., 2007; Gal-Yam et al., 2009).

The intriguing "red supergiant problem" (Smartt, 2009, 2015) – the apparent dearth of higher-mass (>17 $M_{\odot}$) red supergiant (RSG) progenitors for Type IIP SNe, despite theoretical predictions – suggests either significant gaps in our understanding of late-stage stellar evolution, observational biases, or a failure mode where some massive stars collapse directly to black holes without luminous explosions (e.g., Kochanek, 2015, 2020; Beasor et al., 2020; Strotjohann et al., 2024b; Beasor et al., 2025).

Perhaps most interesting is the boundary between 'classical' SNe and recently discovered exotic fast transients that remains poorly defined, with events exhibiting a continuum of properties that challenge our existing taxonomic frameworks (e.g., Gal-Yam, 2019a; Ofek et al., 2021; Perley et al., 2021a,b; Ho et al., 2023a,b). Such challenges make it clear that expanding and refining our observational datasets remains not only valuable but essential. Each new observation – whether it confirms, contradicts, or expands upon existing models – enhances our ability to detect rare phenomena, identify outliers, and ultimately, construct a more complete physical understanding of how stars die.

In retrospect, the remarkable diversity and complexity now evident from modern all-sky surveys should not have surprised us. SNe are notorious for their heterogeneity, a fact reflected in our classification schemes, which continue to expand with each passing year (e.g., Filippenko, 1997; Gal-Yam, 2019a; Schulze et al., 2024). This diversity is largely attributed to mass, binarity, metallicity, rotation rate, mass-loss rate and probably magnetic fields which play critical roles in forming evolved objects of various radii, density profiles and surrounding circumstellar medium (e.g., Schlegel, 1990; Podsiadlowski et al., 1992; Chugai & Danziger, 1994a; Heger et al., 2000; Eldridge & Tout, 2004; Hirschi et al., 2004; Gilkis et al., 2025).

Despite the thousands of documented SNe, continued observational campaigns remain indispensable. Volumetric rates – the frequency of different SN subtypes per unit volume – provide the crucial bridge between stellar evolution theory and explosion mechanisms. Only through broad and unbiased population-level studies can we account for all evolutionary pathways and address the critical gaps in our theoretical understanding. Furthermore, rare events often reveal previously unrecognised physical processes that challenge existing paradigms and ultimately lead to transformative insights into fundamental astrophysical mechanisms. Whether through detections (e.g., Li et al., 2011; Shivvers et al., 2017; Perley et al., 2020) or limits (e.g., Kasliwal et al., 2020; Andreoni et al., 2021; Ho et al., 2023b; Van Bemmel et al., 2025), both outcomes provide invaluable information. Positive detections establish baseline occurrence rates for known phenomena, while non-detections and statistical upper limits constrain the parameter space of theoretical models and help eliminate unrealistic scenarios. This symbiotic relationship between observations and theory directly informs stellar evolutionary models, improves our understanding of potential progenitor pathways, and refines population synthesis predictions. Moreover, the systematic analysis of detection efficiencies and selection functions across different survey strategies yields crucial insights for optimising future observational campaigns.

Current estimates of volumetric rates are often limited by pervasive observational biases. Faint events, rapidly evolving transients, and heavily dust-obscured explosions remain systematically underrepresented in existing samples, creating a partially distorted view of cosmic explosion demographics. Without addressing these biases through continued and increasingly sensitive observations, we risk constructing theoretical frameworks on

fundamentally incomplete data. The comprehensive characterisation of every extragalactic transient subpopulation – from common Type Ia and Type II SNe to exotic calcium-rich transients, superluminous SNe (SLSNe), gamma-ray bursts (GRBs), and fast blue optical transients (FBOTs) – is essential for developing a holistic understanding of stellar endpoints. The recent discoveries of unusual transients sitting at the boundaries between traditional categories – FBOTs like AT 2018cow (e.g., Prentice et al., 2018; Perley et al., 2019; Ho et al., 2023b), AT 2022tsd (e.g., Ho et al., 2023a; Matthews et al., 2023), and their ilk – demonstrate that our understanding remains far from complete. Such enigmatic objects exist in their own region of the luminosity-duration phase space, given their GRB-like luminosities and faster-than-SNe timescales, potentially representing critical or extreme transition zones in the mass-metallicity-binary stellar configurations. These events challenge our conventional boundaries between distinct explosion mechanisms, residing at interfaces between SNe and tidal disruption events (TDEs), magnetar-powered transients and relativistic jets, and CCSNe (Prentice et al., 2018; Coppejans et al., 2020; Perley et al., 2021a). Their intermediate properties suggest a continuum rather than discrete categories in stellar death, and understanding their physical drivers may provide crucial insights into the extremes of stellar evolution (Pursiainen et al., 2018; Ho et al., 2020; Perley et al., 2021b; Yao et al., 2022; Ho et al., 2023a).

In the emerging era of multi-messenger astronomy, comprehensive SN monitoring has implications that extend well beyond the field itself. Confirming counterparts to gravitational wave (GW) detections requires precise transients identification, which necessitates a thorough understanding of the transient sky at any given moment. When LIGO, Virgo, and KAGRA detect a binary neutron star (BNS) merger, we must be able to *confidently* distinguish the resulting kilonova (KN) from the multitude of more common transients that may mimic its appearance. This discrimination is only possible with detailed knowledge of transient demographics across all subtypes and luminosity ranges, underscoring the far-reaching impact of continued transient observations.

Beyond addressing demographic biases in our volumetric rate estimates, perhaps the most glaring observational gap persists in the earliest moments of SN evolution. These initial seconds to hours post-explosion – critically undersampled phase – contain unique physical information, soon to be explored by the ULtraviolet Transient Astronomy SATellite (ULTRASAT; Shvartzvald et al., 2024). During this ephemeral window, the

explosion physics, progenitor structure, and circumstellar environment all leave distinctive spectroscopic and photometric signatures that are rapidly overwritten as the ejecta expands. Capturing this fleeting phase requires not merely the occasional fortunate detection but systematic, high-cadence monitoring with unprecedented temporal resolution – precisely the capability that next-generation surveys promise to deliver. Just as increased sample sizes mitigate selection effects across the transient population, enhanced temporal coverage addresses our historical bias toward later evolutionary phases, completing our observational picture of stellar death from first light to final fade.

1.2 Brief Stellar Evolution Background

The fundamental questions surrounding SNe diversity and their observable characteristics demand a deeper understanding of the massive stars that produce these terminal explosions. In the previous sections, various gaps were highlighted between progenitor properties and explosion phenomenology. The theoretical foundation of sequential nuclear burning stages, layer formation, and core evolution provides the essential framework for interpreting the diverse transient population revealed by modern time-domain surveys. Examining how massive stars with $M_{\rm init} \gtrsim 7$–8 $\mathrm{M}_{\odot}$ (e.g., Heger et al., 2003; Eldridge & Tout, 2004; Ekström et al., 2012) progress from main sequence through advanced burning phases helps clarify how variations in initial mass, metallicity, rotation, and binary interactions manifest in the stunning variety of explosion energetics and spectroscopic signatures observed in the SN population.

Massive stars possess sufficient mass to exhaust all nuclear fuel stages and evolve beyond the point where electron degeneracy pressure can resist gravitational collapse. Such stars evolve from birth to core-collapse through well-defined nuclear burning stages, governed by the balance between fusion pressure and gravity. Their cores sequentially fuse heavier elements (hydrogen to silicon), with each transition requiring higher temperatures and densities (e.g., Woosley & Weaver, 1995; Janka et al., 2007; Jerkstrand et al., 2025). Convective mixing continuously replenishes the core with fresh fuel while distributing newly-synthesised material through the central region (e.g., Burbidge et al., 1957; Woosley et al., 2002; Heger et al., 2005). This process creates concentric layers of increasingly heavy elements, forming distinct core structures (e.g., helium core after hydrogen exhaustion) that determine the star's subsequent evolution.

Following central hydrogen exhaustion, the core contracts and heats until temperatures become sufficient for helium ignition. Simultaneously, hydrogen shell burning activates immediately outside the helium core, driving envelope expansion and cooling as the star evolves off the main sequence. A steep pressure gradient develops at the helium core boundary, creating a distinct separation between the core and the hydrogen-rich extended envelope. The star's subsequent evolution diverges based on its initial mass: stars with zero-age main sequence masses ($M_{\rm ZAMS}$) between 8 – 25 $M_\odot$ typically expand to become RSGs, while more massive stars ($M_{\rm ZAMS} \gtrsim 30$ – 40 $M_\odot$) may evolve into Wolf-Rayet stars (WR; Wolf & Rayet, 1867; Crowther, 2007) through intense mass-loss.

During the expansion phase, the outermost envelope regions become only weakly gravitationally bound, facilitating significant mass-loss. This process is particularly pronounced in WR stars, luminous blue variables (LBVs; Pickering, 1897; Hubble & Sandage, 1953; Humphreys, 1975; Conti, 1984), and very massive stars (VMS; $M_{\rm ZAMS} \gtrsim 10^2$ $M_\odot$; Vink et al., 2011; Bestenlehner et al., 2014; Vink, 2018), which undergo (potentially regular) periods of extreme mass-loss ($\dot{M} \sim 10^{-5}$ $M_\odot$ yr^{-1}; Underhill, 1969; Abbott et al., 1986; Nugis & Lamers, 2000; Smith, 2014).

The pace of stellar evolution dramatically accelerates following core helium depletion. The star proceeds through carbon, neon, oxygen, and silicon burning phases with progressively shorter timescales – the compression from hydrogen to silicon burning spans ten orders of magnitude in duration. This acceleration reflects both decreasing energy yields as the core composition approaches iron and increasing temperature sensitivity of the nuclear reactions (e.g., Woosley & Weaver, 1986; Woosley et al., 2002; Heger et al., 2003). As this evolution proceeds, the star develops a complex onion-like structure of concentric burning shells surrounding an increasingly heavy central core (see Fig. 1.1).

During the advanced burning stages, the dominant energy loss mechanism transitions from photon radiation to neutrino (ν) emission, which occurs through both thermal processes and weak nuclear interactions (Woosley & Weaver, 1986; Bethe & Wilson, 1985; Bethe, 1990; Janka, 2012). This neutrino cooling accelerates core contraction, further raising temperatures and densities, and ultimately driving the star toward its inevitable collapse.

The final significant burning episode involves silicon fusion, producing an inert iron (^{56}Fe) core that cannot undergo further exothermic nuclear reactions since iron-group

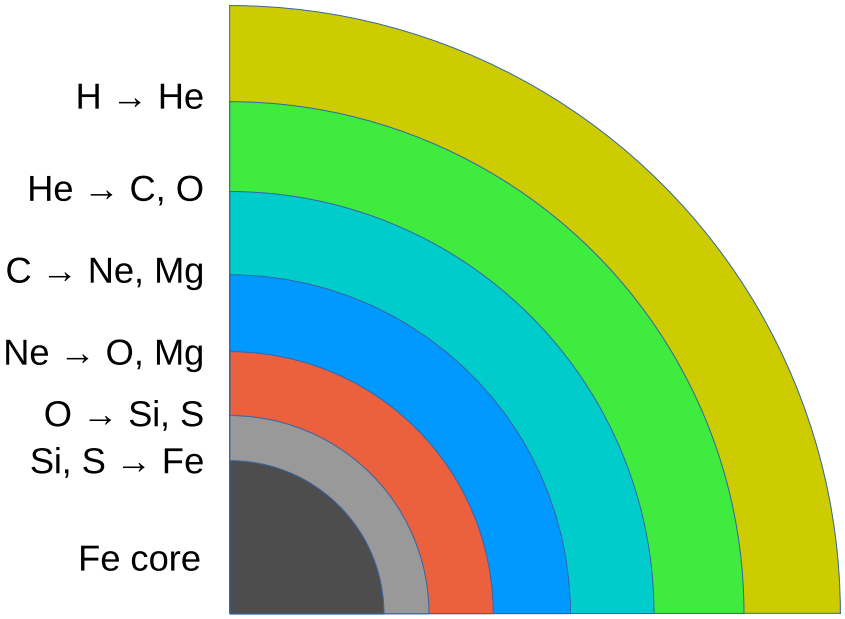

FIGURE 1.1: Schematic of the onion-shell structure of a massive RSG prior to iron core-collapse. This layered composition results from sequential nuclear burning stages, with each fusion cycle leaving behind shells of processed material. From the outermost to innermost regions: the hydrogen envelope, helium shell, carbon/oxygen shell, neon/-magnesium shell, silicon/sulfur shell, and finally the iron core. Figure from Jerkstrand et al. (2025).

nuclei possess the highest binding energy per nucleon (e.g., Bowers & Wilson, 1982; Heger et al., 2003). The iron core, supported primarily by electron degeneracy pressure, continues growing until it approaches the Chandrasekhar limit of $\sim 1.4\ M_\odot$ (e.g., Woosley & Weaver, 1986; Woosley et al., 2002; Janka et al., 2007), with the central density and temperature reaching approximately 10^9 g cm^{-3} and 10^{10} K, respectively (Woosley et al., 2002; Janka, 2012; Jerkstrand et al., 2025).

1.3 Mass-Loss

Mass-loss fundamentally reshapes massive stars in their final evolutionary stages, with the mass-loss rate ($\dot{M}$) and mechanism (e.g., line-driven winds, eruptive mass-loss, or binary interactions) dictating their ultimate fate. The stripping of outer layers directly alters three critical pre-SN properties: (1) core mass, which determines compactness and collapse dynamics; (2) envelope composition, governing early SN light curves; and (3) stellar radius, influencing shock breakout (SBO) signatures. Recent observational studies and theoretical advancements have demonstrated that mass-loss not only governs

the progenitor's evolutionary trajectory but also profoundly impacts both the early- and late-time photometric and spectroscopic evolution of the SNe.

Mass-loss mechanisms remove material from the stellar envelope and deposit the material in the circumstellar environment as circumstellar material (CSM) or an extended wind, typically within 10 – 1000 AU of the progenitor that is not bound. The density profile of the CSM/wind, $\rho_{\rm CSM}$, is typically described by a power-law distribution (Eq. 1.1), where $\rho_{\rm CSM} \propto r^{-2}$ and $v_{\rm wind}$ (Eq. 1.2) – which is parameterised by the stellar structure parameter, β, describing the wind acceleration (see Moriya et al., 2017; Moriya et al., 2016).

$$\rho_{\rm CSM}(r) = \frac{\dot{M}}{4\pi v_{\rm wind}} r^{-2} \tag{1.1}$$

$$v_{\rm wind}(r) = v_0 + (v_\infty - v_0)\left(1 - \frac{R_0}{r}\right)^{\beta} \tag{1.2}$$

Depending on the strength of the wind, a RSG can travel blueward on the Hertzsprung-Russel (HR) diagram, driven to be a LBV or generally out of the RSG phase (e.g., Vanbeveren et al., 1998; Salasnich et al., 1999; Georgy et al., 2012; Groh et al., 2013) for a short time before further transitioning. For supergiants with $M_{\rm ZAMS}$ between 10 – 30 $M_\odot$ and effective surface temperatures $\sim 30{,}000 \leq T_{\rm eff} \leq 50{,}000$K, $\dot{M}$ are thought to be between 10^{-7} – 10^{-5} $M_\odot$ yr^{-1} (see Figs. 7 and 8 in Vink et al., 2000).

While stellar evolution models typically assume smooth, time-averaged $\dot{M}$, observations reveal that mass-loss in late-stage massive stars is often episodic or eruptive (e.g., Gal-Yam et al., 2014; Groh, 2014b; Yaron et al., 2017) – especially during LBV phases, pre-SN outbursts, or binary-driven ejections. This mismatch between theory and observation highlights a key uncertainty in predicting final progenitor structures, as impulsive mass-loss can drastically alter envelope stripping, core-envelope coupling, and CSM density, ultimately determining the SN type. Dominant mass-loss mechanisms in the final evolutionary stages include: radiation/line-driven mass-loss, wave-driven energy heating into the stellar envelope, pulsation-driven 'superwinds' and common envelope interactions as a result of binary interactions.

Radiation/line-driven mass-loss occurs when photons impart momentum ($h\nu/c$) onto metal ions, which subsequently share this momentum with the more abundant hydrogen and helium, creating steady stellar outflows ($\sim 10^{-6}$ $M_\odot$ yr^{-1}; Milne, 1926; Lucy & Solomon, 1970; Castor et al., 1975; Puls et al., 2008). This mechanism operates primarily through interactions with numerous UV metal spectral lines, as hydrogen and helium possess relatively few lines in the relevant wavelength range (Vink et al., 2001). The process exhibits strong metallicity dependence ($\dot{M} \propto Z^{0.7-0.8}$) and becomes particularly efficient near the Eddington limit ($\log(L/L_\odot) \approx 5.3$ – 5.8; Davies & Beasor, 2017; Vink, 2022).

Convectively driven hydrodynamic waves provide a compelling mechanism for late-stage mass-loss in massive stars. First proposed by Quataert & Shiode (2012) and subsequently developed in detail (e.g., Shiode & Quataert, 2014; Quataert et al., 2016; Fuller, 2017; Leung & Fuller, 2020; Wu & Fuller, 2021), this process becomes significant during late nuclear burning phases when core luminosities approach the Eddington limit. As neutrino cooling dominates during carbon burning and beyond, the core loses thermal equilibrium, leading to super-Eddington burning luminosities that drive vigorous convection. The resulting internal gravity waves propagate outward, partially converting to acoustic waves in the stellar interior. When these waves dissipate at the base of the hydrogen envelope (through radiative diffusion and boundary reflections), they deposit sufficient energy ($\sim 10^{40}$ – 10^{41} erg) to drive convection in the outer layers. This generates a super-Eddington outflow capable of ejecting $\lesssim 0.1$ $M_\odot$ of material, typically confined within 10^{14} – 10^{15} cm of the photosphere. Crucially, this mechanism does not fully unbind the envelope but can significantly alter the progenitor's circumstellar environment in the final years before core-collapse.

Pulsation-driven 'superwinds' emerge when partial ionisation of hydrogen in the stellar envelope creates a runaway instability. This occurs as the luminosity-to-mass ratio ($L/M_{\rm ZAMS}$) increases with mass-loss, establishing a positive feedback cycle. Li & Gong (1994) first demonstrated that RSGs become unstable to radial pulsations due to hydrogen partial ionisation in their outer layers. Subsequent work by Heger et al. (1997) showed these pulsations can reach amplitudes comparable to asymptotic giant branch (AGB) stars when the pulsation period approaches the envelope's thermal timescale. This creates a steady-state outflow with very high $\dot{M}$ operating within the last $\sim 10^2$ –

10^3 yrs, enough to remove $\sim 10^{-2}$ $M_\odot$ yr^{-1} (e.g., Yoon & Cantiello, 2010; Förster et al., 2018; Davies et al., 2022)

Common envelope interactions become increasingly significant during post-main sequence evolution of multiple star systems as stars expand dramatically. This expansion may cause a star to fill its Roche lobe – the equipotential surface beyond which material is no longer gravitationally bound to the star (Paczyński, 1971; Eggleton, 1983). When the stellar photosphere reaches the first Lagrangian point (L1), mass transfer initiates as gas flows toward the companion through Roche lobe overflow (RLOF), operating with high efficiency at rates of $\sim 10^{-3}$ – 10^{-1} $M_\odot$ yr^{-1} (Iben & Tutukov, 1984; Hurley et al., 2002; Langer, 2012) – potentially stripping the entire hydrogen envelope within $\sim 10^4$ years. Under specific conditions, particularly when the mass-donating star possesses a convective envelope or substantially exceeds its companion's mass, transferred material may accumulate faster than it can be accreted, leading to the formation of a common envelope (CE) that engulfs both stars. The subsequent orbital evolution through this shared envelope dramatically reduces the binary separation through hydrodynamic drag forces, culminating in either stellar mergers or the formation of compact binaries with significantly reduced orbital periods (e.g., Paczyński, 1971; Hurley et al., 2002; Ivanova et al., 2013) – outcomes that profoundly influence the final evolutionary pathway and potential SN characteristics.

The mass-loss mechanisms described above create distinctive progenitor structures immediately before core-collapse, forming a direct bridge between stellar evolution and explosion physics. These processes determine not only the final mass and composition of the core that will collapse but also establish the crucial outer envelope structure and circumstellar environment that shape the resulting SN. While traditional models employ simplified, time-averaged mass-loss prescriptions, the observed diversity of SNe demands more nuanced scenarios incorporating episodic, eruptive, clumpy and binary-induced mass-loss (Sundqvist & Owocki, 2013; Smith, 2014; Beasor et al., 2020). The degree and timing of envelope stripping directly maps onto SN spectroscopic classifications, from hydrogen-rich Type II to stripped-envelope Type Ib/c events (Smartt, 2009; Yoon & Cantiello, 2010; Groh et al., 2013; Smartt, 2015).

1.4 The Collapse

When fusion reactions in the core cease to generate sufficient outward pressure, hydrostatic equilibrium fails and gravitational collapse proceeds dynamically, releasing energy on the order of the core's gravitational binding energy ($\sim 10^{53}$ erg; Woosley & Weaver, 1986; Janka et al., 2007). Early theoretical models proposed that the SN explosion was driven entirely by a "prompt" hydrodynamical mechanism, triggered when the iron core becomes effectively incompressible upon reaching nuclear densities of $\sim 10^{14}$ g cm^{-3}. During this catastrophic collapse, the core exhibits differential infall dynamics: approximately 1/3 of its mass collapses homologously (with velocity proportional to radius), while the remainder falls more rapidly, creating a characteristic velocity profile (e.g., Bowers & Wilson, 1982; Bethe, 1990). As the inner homologous core reaches nuclear densities, it attempts to rebound elastically, but this bounce is initially suppressed by the substantial momentum of the still infalling outer core material, creating a complex hydrodynamic interaction at the interface (e.g., Janka, 2012).

A "core-bounce" occurs when the newly formed nuclear fluid generates a strong repulsive force arising from the nuclear strong interaction and the Pauli exclusion principle. This resistance to further compression produces a hydrodynamic shock wave at the interface between the homologous inner core and the supersonically infalling outer layers (e.g., Bethe, 1990). The shock forms at approximately 20 – 30 km from the centre and propagates outward with initial velocities approaching $\sim 10^4$ km s^{-1} (e.g., Woosley & Weaver, 1986; Bethe, 1990; Janka, 2012). In idealised early models, this shock was theorised to propagate outward through the stellar envelope until reaching the surface, ultimately expelling the star's mass to infinity (e.g., Colgate & Johnson, 1960; Arnett, 1966; Bethe & Wilson, 1985).

However, it was quickly shown that the shock wave slows as it encounters progressively more material with increasing enclosed mass, whilst simultaneously suffering rapid energy depletion through two critical processes: first, the dissociation (Eqs. 1.3 and 1.4) of in-falling iron-group materials by high energy photons (γ) into free protons (p), neutrons (n), or alpha (α) particles, each consuming approximately 9 MeV per nucleon; and second, neutronisation (Eq. 1.5) within the core producing electron neutrinos (ν_e) in a

burst that carries away substantial energy (Bethe, 1990; Burrows et al., 1995; Janka et al., 2007).

$$^{56}_{26}\mathrm{Fe} + \gamma \rightarrow 13\,^{4}_{2}\mathrm{He} + 4\,n \tag{1.3}$$

$$^{4}_{2}\mathrm{He} + \gamma \rightarrow 2\,p^{+} + 2\,n \tag{1.4}$$

$$p + e^{-} \rightarrow n + \nu_e \tag{1.5}$$

This ultimately causes the shock to stall at ~ 100 – 200 km and turn into an accretion shock (Bethe, 1990; Janka et al., 2007). This necessitates additional energy input to revive the stalled shock and power the observed SN explosion.

Colgate & White (1966) and Wilson (1971) first proposed a neutrino-driven heating mechanism for shock revival. Neutrinos – generated predominantly through neutronisation at extreme densities of $\sim 10^{15}$ g cm^{-3} where matter becomes neutrino-opaque – diffuse outward from the proto-neutron star core, depositing energy in the "gain region" just outside the core (Janka et al., 2007; Matsumoto et al., 2020; Müller, 2020). The energy deposition occurs primarily through charged-current interactions of electron neutrinos (ν_e) and anti-electron neutrinos ($\overline{\nu_e}$) with free nucleons (Eq. 1.6; Bethe & Wilson, 1985).

$$\begin{aligned} \nu_e + n &\rightarrow e^{-} + p \\ \overline{\nu_e} + p &\rightarrow e^{+} + n \end{aligned} \tag{1.6}$$

While computational models have demonstrated varying degrees of success over the past decades (e.g., Bethe & Wilson, 1985; Burrows, 1987; Myra et al., 1987; Müller, 1987; Wongwathanarat et al., 2015; Utrobin et al., 2017), the increasing sophistication of multi-dimensional simulations incorporating detailed neutrino transport has consistently reinforced the neutrino-driven paradigm as the most physically plausible explosion mechanism for the majority of core-collapse SNe (CCSNe) (e.g., O'Connor & Couch,

2018; Müller et al., 2019; Mezzacappa et al., 2020; Boccioli & Roberti, 2024; Janka, 2025).

Here, convection occurs as the neutrino-heating results in a turbulent and unstable pressure gradient and re-energises the shock. The highly-compressed iron core (proto-neutron star) radiates $\sim 10^{53}$ erg in neutrinos, which, given the efficiency of neutrino-heating, provides $\sim 10^{52}$ erg within hundreds of milliseconds (e.g., Jerkstrand et al., 2025). Much of this energy is used to unbind the heated material in the vicinity of the neutron star (NS), leaving 10^{50} – 10^{51} erg for the CCSN (e.g., Müller, 2020; Bollig et al., 2021).

During collapse, a dense compact object forms, with its nature primarily determined by the $M_{\rm ZAMS}$, metallicity, and rotation of the progenitor. For stars with $M_{\rm ZAMS} \lesssim 20$ – 25 $M_\odot$, neutron degeneracy pressure and strong nuclear forces halt further gravitational collapse, creating a NS – a dense sphere of neutron-rich material $\sim$ 10 – 15 km in radius (e.g., Bethe, 1990; Fryer, 1999; Janka et al., 2007; Ott, 2009). For more massive progenitors, the proto-NS masses typically exceed $\sim$ 2 – 3 $M_\odot$, breaching the Tolman-Oppenheimer-Volkoff (TOV; Oppenheimer & Volkoff, 1939) limit beyond which neutron degeneracy pressure cannot prevent further collapse, resulting in a black hole (BH; Thielemann et al., 1996; Fryer, 1999; Heger et al., 2003; O'Connor & Ott, 2011).

However, the true picture is considerably more complex than this simple mass threshold suggests. Recent work reveals "islands of explodability" where non-monotonic relationships between progenitor and remnant masses create regions where similar initial masses can produce different remnant types (O'Connor & Ott, 2011; Ugliano et al., 2012; Pejcha & Thompson, 2015; Sukhbold et al., 2016). Additionally, the emerging understanding of failed SNe – where massive cores collapse directly to a BH with minimal or no external explosion – and collapsars that potentially power GRBs (e.g., Woosley & Bloom, 2006) has further complicated this mapping (MacFadyen & Woosley, 1999; Dessart et al., 2008). Rotation plays a particularly critical role in collapsar formation, as centrifugal support can temporarily stabilise a proto-NS above the TOV limit, creating a metastable configuration that powers a relativistic jet before complete collapse occurs (MacFadyen & Woosley, 1999; Dessart et al., 2008).

As the shock propagates outward from the core, it compresses and heats the overlying shells of previously synthesised material. When post-shock temperatures exceed

$\sim 10^9$ K, explosive nucleosynthesis is triggered in the layers, operating on timescales orders of magnitude shorter than the preceding hydrostatic burning phases (e.g., Woosley et al., 2002; Janka et al., 2007). Explosive burning converts intermediate mass elements (oxygen, silicon, neon, magnesium) into a rich diversity of iron-peak nuclei – including ^{47}Ca, ^{56}Fe, ^{56}Co, and ^{56}Ni – which subsequently power different phases of the SN light curves. The extreme conditions near the shock front also enable the synthesis of elements beyond the iron peak through distinct neutron-capture pathways: the s-process (slow neutron capture relative to beta decay), p-process (proton capture or photodisintegration), and r-process (rapid neutron capture) – see, e.g., Clayton et al. (1961); Clayton & Craddock (1965); Seeger et al. (1965); Woosley & Weaver (1986); Meyer (1994).

The shock continues to propagate through the progressively less dense outer layers of the progenitor star (e.g., Bethe, 1990), eventually emerging at the stellar surface. In cases where the star experienced significant mass-loss prior to core-collapse, the shock may instead emerge as it reaches the optically thin regions of the surrounding CSM. Behind the shock front, nuclei are dissociated into free nucleons, and the previously trapped neutrinos – confined by the high densities of the stellar interior – begin to escape once the density at the shock front falls below the neutrino trapping threshold (e.g., Bethe & Wilson, 1985; Bethe, 1990). These neutrinos then diffuse outward, producing an intense, ultra-luminous burst that marks one of the earliest observable signatures of the explosion (Thompson et al., 2003).

1.5 The Emission

Colgate (1975) and Falk & Arnett (1977) first demonstrated that the initial electromagnetic signature of a SN occurs when the shock wave reaches the stellar surface (SBO). This is a brief, luminous flash heralding the first photons to escape the exploding star. The spectral and temporal characteristics of SBO depend sensitively on the envelope mass and, critically, on the density structure of the outermost stellar layers (Quimby et al., 2007a; Waxman & Katz, 2017). Throughout its propagation through the stellar interior, the shock exists in a radiation-dominated regime where photons carry the majority of the post-shock energy density. This radiative character arises because the fundamental mechanism converting kinetic energy to thermal energy at the shock transition is mediated predominantly by Compton scattering rather than particle collisions

(e.g., Klein & Chevalier, 1978; Bethe, 1990; Waxman et al., 2007; Waxman & Katz, 2017). As the shock approaches the stellar surface and the optical depth decreases, these trapped photons begin to diffuse ahead of the shock front, ultimately breaking free in a spectacular UV/X-ray flash once the radiation can effectively outrun the matter.

Within the shock transition layer itself, the optical depth satisfies the condition $\tau_s = c/v_s$, where v_s is the shock velocity (Nakar & Sari, 2010). As the shock approaches the stellar surface, it encounters progressively decreasing Thompson optical depths in the overlying material. When these optical depths approach τ_s, a critical threshold is reached where Compton scattering can no longer maintain the hydrodynamic shock structure. At this juncture, the photon diffusion timescale becomes comparable to or shorter than the hydrodynamic timescale, enabling radiation to effectively decouple from the matter and propagate ahead of the shock front (e.g., Colgate, 1975; Klein & Chevalier, 1978; Ensman & Burrows, 1992; Matzner & McKee, 1999; Waxman et al., 2007; Soderberg et al., 2008; Nakar & Sari, 2010; Chevalier & Irwin, 2011; Waxman & Katz, 2017). This radiative precursor manifests as the observable SBO flash.

Klein & Chevalier (1978) showed that hydrogen-rich, Type II, SNe are likely to produce strong X-ray, far and near UV and optical signatures of SBO, with X-ray luminosities exceeding 10^{44} erg s^{-1} within $\sim 10^3$ s post SBO (e.g., Falk & Arnett, 1977; Ensman & Burrows, 1992; Nakar & Sari, 2010; Chevalier & Irwin, 2011). This is supported by serendipitous observations (X-ray, UV and optical detections) of SNe at the moment of SBO (e.g., Schmidt et al., 1993; Richmond et al., 1994; Stritzinger et al., 2002; Schawinski et al., 2008; Gezari et al., 2008; Modjaz et al., 2009; Tominaga et al., 2009; Gezari et al., 2010; Maeda, 2013; Gezari et al., 2015; Garnavich et al., 2016; Rubin & Gal-Yam, 2017; Huang et al., 2018; Vallely et al., 2021; Li et al., 2024)

As mentioned, the opacity and density profiles of the outermost layers critically govern SBO dynamics, with progenitor radius, $R_\star$, emerging as a comparably influential parameter, along with the effective temperature of the emitting region, $T_{\rm eff}$ and chemical composition, Z, of the local media (Gal-Yam et al., 2014; Dessart et al., 2017). Matzner & McKee (1999) and Nakar & Sari (2010) explore the dependence of the SBO luminosity and 'pulse' duration on $R_\star$, finding that the energy released during the SBO increases with $R_\star$, reaching $\sim$0.1% of the SN explosion energy in a RSG.

The presence of dense CSM surrounding the progenitor can substantially modify the SBO signal, delaying its emergence by $\sim$ hours to $\sim$ days. This occurs because dense, optically thick CSM efficiently absorbs and thermalises the ionising continuum radiation from the shock-heated stellar surface, significantly increasing the photon diffusion time (e.g., Chevalier & Irwin, 2011; Moriya et al., 2011; Svirski et al., 2012; Gal-Yam et al., 2014; Dessart et al., 2017; Dessart & Jacobson-Galán, 2023). In such scenarios, the effective location of SBO shifts outward from the stellar photosphere to a radius within the CSM where the optical depth drops to approximately τ_s (e.g., Waxman et al., 2007; Waxman & Katz, 2017; Goldberg, 2022). This reconfiguration of the breakout physics fundamentally alters both the spectral energy distribution (SED) and the temporal evolution of the early emission, providing critical diagnostic information about the progenitor's mass-loss history immediately preceding core-collapse (see Fig. 1.2).

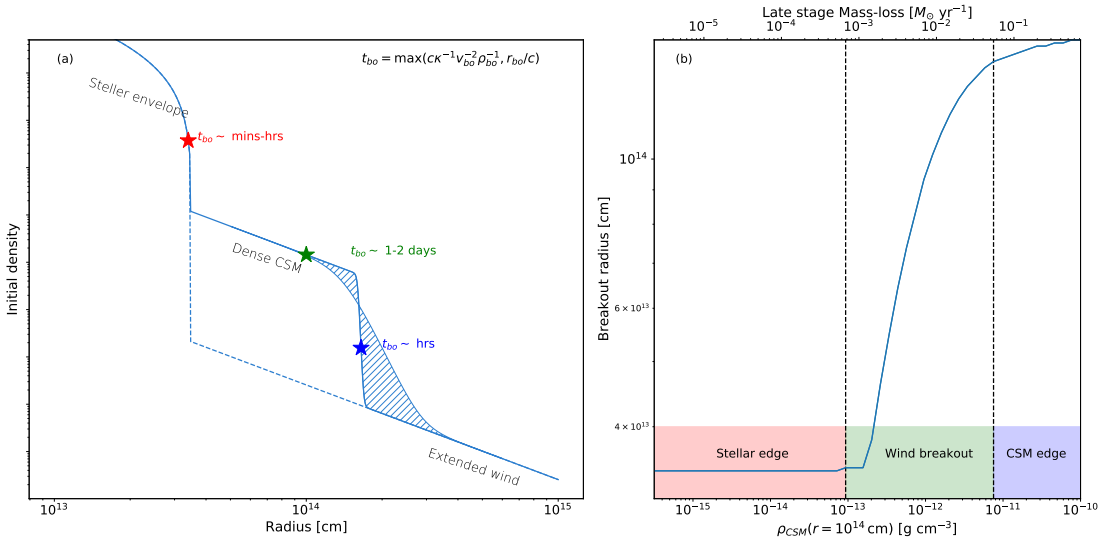

FIGURE 1.2: (a) Schematic of possible SN SBO scenarios depending on the CSM density profile ($\rho(r)$). Red star: breakout at stellar surface with short, light-travel-time limited emission. Blue star: breakout at dense CSM shell edge with hour-long emission. Green star: breakout in shallow density profile resulting in day-long emission. The density structure at different radii determines early light curves, spectra, and subsequent X-ray emission. (b) Breakout radius calculations for a 500 $R_\odot$ progenitor with 1 $M_\odot$ envelope surrounded by varying amounts of confined CSM (assuming $v_{\rm wind} = 50$ km s^{-1}). Figure from Irani et al. (2024).

The ejecta-CSM interaction generates a classical double-shock structure: a forward shock propagates outward, sweeping up, compressing, and heating the surrounding CSM while accelerating it; concurrently, a reverse shock propagates inward relative to the expanding material, decelerating and heating the oncoming SN ejecta (e.g., Chevalier & Irwin, 2011; Smith, 2014). This configuration efficiently converts kinetic energy to thermal energy,

which is subsequently radiated across a range of wavelengths – predominantly X-rays for high shock velocities or optical/UV wavelengths for denser, slower interactions (e.g., Moriya et al., 2011; Svirski et al., 2012; Fransson et al., 2014).

The presence of dense, confined ($\leq 10^{15}$ cm) CSM allows the shock-heated material to cool more effectively before radiation emerges, shortening the timescale for spectral evolution toward optical bands and producing a steeper rise to maximum light in optical light curves (e.g., Moriya et al., 2017; Morozova et al., 2018; Davies et al., 2022).

The intense UV/X-ray radiation from SBO creates a flash ionisation front that propagates through the CSM at light speed – outpacing the shock itself. As described by Gal-Yam et al. (2014), this UV radiation instantaneously ionises the CSM, creating a highly ionised plasma extending from 10^{13} cm. The incoming X-rays become thermalised in the dense CSM, converting into optical and UV continuum radiation, resulting in spectra that closely resemble a blackbody (e.g., Fransson et al., 2014). Any outgoing X-rays will be absorbed by the pre-shock CSM, giving rise to UV and optical emission lines (e.g., Nayana et al., 2024). The ionisation state of the CSM depends primarily on the radiation temperature and the distance from the source, with inner regions reaching extreme ionisation states (e.g., O VI, N V, C IV) while outer regions maintain lower ionisation potentials.

The recombination time of the CSM scales inversely with electron density ($t_{rec} \propto 1/n_e$; Quimby et al., 2007a; Fransson et al., 2014; Gal-Yam et al., 2014; Groh, 2014b; Khazov et al., 2016; Garnavich et al., 2016), resulting in a time-dependent ionisation structure that evolves over hours to days. Given the high densities expected in the CSM ($n_e \sim 10^{10}$ cm^{-3}; Moriya et al., 2011; Gal-Yam et al., 2014; Smith et al., 2015; Yaron et al., 2017), the recombination time is expected to be of order minutes. High-ionisation species (O VI, N V, He II) disappear first, followed by progressively lower ionisation states (O III, N III, He I), creating a time-series of spectra that maps the changing ionisation structure (e.g., Smith et al., 2015; Yaron et al., 2017). The majority of the interaction power emerges at early times in the NUV from the forest of metal ions (e.g., Kulkarni et al., 2023) and transforms to large contributions from Lyα and Mg II doublet at $\lambda\lambda$ 2795, 2802 (e.g., Luo et al., 2024) – see Fig. A.1 for a representation of the relative contribution from NUV – NIR to broadband filters from theoretical CSM interaction in Type II SNe over time.

Following ionisation, the CSM undergoes recombination through a cascade process, with electrons transitioning sequentially through decreasing energy states, generating distinctive narrow emission lines. These sharp spectral features reveal characteristic velocities of ~ 10 – 100 km s $^{-1}$ (Schlegel, 1990; Kiewe et al., 2012; Ofek et al., 2013), consistent with pre-explosion stellar winds and eruptive mass-loss events, and markedly slower than SN ejecta. The emission lines develop characteristic electron scattering wings through a mechanism where line-emitted photons undergo multiple Thomson scatterings with free electrons in the ionised, optically thick CSM, creating symmetric broadened profiles while preserving the narrow core (e.g., Chugai, 2001; Dessart et al., 2009; Gräfener & Vink, 2015).

The recombination-driven emission signature is ultimately terminated as the high-velocity SN ejecta ($v_{\rm ejecta} \gtrsim 10{,}000$ km s^{-1}) overtakes and sweeps up the relatively stationary CSM ($v_{\rm CSM} \sim 10$ km s^{-1}). Thus, given that $v_{\rm ejecta} \gg v_{\rm CSM}$ and assuming a maximum radial extent of CSM of 10^{15} cm, the CSM is expected to be swept up on a timescale proportional to $R_{\rm CSM}/v_{\rm ejecta}$, which is approximately 10 days. The spectroscopic signatures of this interaction are even more fleeting, with narrow emission features typically lasting $\lesssim$1 week as the strengthening broad ejecta emission rapidly dominates and outshines the narrow CSM components.

Several observational features – including the modest CSM velocities, the relatively rapid disappearance of narrow emission lines within days post-breakout, and the absence of narrow features from lower ionisation states (e.g., He I) – collectively provide strong evidence that these emission lines originate from a compact, confined region. This emitting zone typically extends $\lesssim 10^{14}$ – 10^{15} cm from the progenitor (corresponding to an optical depth ~ 1), with characteristic densities of $\sim 10^{-12}$ – 10^{-14} g cm^{-3}. The fully ionised state of this material, combined with typical wind velocities (10 km s^{-1}), constrains the ejection timescale to within $\lesssim$ 1000 years prior to core-collapse (e.g., Woosley & Weaver, 1986; Quimby et al., 2007a; Moriya et al., 2011; Groh, 2014b; Gal-Yam et al., 2014; Fransson et al., 2014; Smith et al., 2015; Khazov et al., 2016; Garnavich et al., 2016; Yaron et al., 2017; Smith, 2017b; Moriya et al., 2017; Morozova et al., 2018; Förster et al., 2018).

As this interaction stops, the narrow emission lines from unshocked CSM diminish while broader components from the accelerated, shocked material become more prominent

(e.g., Chugai & Danziger, 1994a). Meanwhile, the bulk of the SN ejecta continues expanding nearly homologously ($v \propto r$) behind the reverse shock, cooling adiabatically in free expansion (e.g., Woosley & Weaver, 1986; Quimby et al., 2007a; Jerkstrand et al., 2025). This expansion drives the photosphere inward in mass coordinate while its radius increases in physical space, progressively revealing deeper layers of the explosion. At late times, radio detections or rebrightenings have been seen, which also give insights into the local CSM environment (see Nayana et al., 2024; Sfaradi et al., 2025).

The SN now enters the regime governed by diffusion, releasing internal energy on a timescale of weeks to months, dependent on the outer envelope, ejecta composition and circumstellar environment (e.g., Woosley & Weaver, 1986; Young, 2004; Kasen & Woosley, 2009). The radiation efficiency depends largely on the $R_\star$ with most of the energy deposited by the shock being converted to kinetic bulk expansion energy of the stellar debris rather than being radiated away. In the most common case, a RSG, close to 99% of the deposited energy ($\sim 10^{51}$ erg) is converted to kinetic energy, leaving $\sim 10^{49}$ erg to be radiated away when the star becomes optically thin (e.g., Woosley & Weaver, 1986; Bethe, 1990; Quimby et al., 2007a; Jerkstrand et al., 2025).

Following SBO, the dominant emission mechanism transitions to the cooling of the shock-heated stellar envelope, initiating the characteristic shock cooling (SC) phase of the light curve. This critical early phase is powered primarily by the release of thermal energy deposited by the shock as it traversed the star. During this period, the heated material undergoes rapid adiabatic expansion while radiation gradually diffuses outward through the progressively more transparent ejecta (e.g., Woosley & Weaver, 1986; Bethe, 1990; Chevalier, 1992; Matzner & McKee, 1999; Woosley et al., 2002; Nakar & Sari, 2010; Rabinak & Waxman, 2011).

The extreme post-shock compression initially drives the material to temperatures exceeding 10^5 K, but adiabatic expansion and radiative diffusion rapidly reduce this temperature as the ejecta expands homologously (e.g., Woosley & Weaver, 1986; Chevalier, 1992). In scenarios where minimal CSM exists above the photosphere, this phase produces smooth but rapidly evolving light curves and spectra characterised by blue continua and progressively developing absorption features, providing direct diagnostic insight into the structure, composition, and extent of the progenitor's outermost layers

– properties otherwise inaccessible through later observations (e.g Bersten et al., 2013; Dessart et al., 2013; Piro, 2015; Piro et al., 2021; Morag et al., 2023).

SN from progenitors that retain substantial hydrogen envelopes (predominantly RSGs) evolve as Type II events with distinct characteristic phases. Following SBO, their initial spectra appear nearly featureless and remarkably blue, exhibiting high colour temperatures exceeding 10,000 K, with Balmer lines gradually developing characteristic P-Cygni profiles indicative of expanding atmospheres. This temperature decreases rapidly to approximately 6000 K within weeks post-explosion due to adiabatic expansion (e.g., Kirshner et al., 1973; Kirshner & Kwan, 1974; Filippenko, 1997; Dessart & Hillier, 2011).

During these early phases, the photosphere resides within the outermost layers of the completely ionised hydrogen envelope. This region initially maintains extreme opacity with photon diffusion timescales measured in thousands of years. As this envelope expands homologously, its rapidly increasing surface area facilitates more efficient radiative cooling while the receding photosphere maintains a relatively constant temperature through a self-regulating mechanism (e.g., Falk & Arnett, 1977; Woosley & Weaver, 1986; Arnett, 1996). The critical transition occurs when the photospheric temperature drops to approximately 6000 K, triggering hydrogen recombination – the characteristic plateau phase of Type II-"P" SNe.

During the plateau phase, the recombination front propagates inward through the hydrogen-rich envelope ($H_{\rm env}$, typically $\sim$10 $M_\odot$), converting ionised hydrogen to neutral hydrogen and reducing the local opacity by several orders of magnitude (e.g., Grassberg et al., 1971; Popov, 1993; Filippenko, 1997; Smartt, 2009). This recombination process establishes a self-regulatory mechanism: as the ejecta expands and would otherwise cool below the recombination temperature, the photosphere instead recedes to deeper, hotter layers where hydrogen remains ionised, effectively maintaining a nearly constant temperature and luminosity.

This process allows the hydrogen envelope to gradually release the energy initially deposited by the shock wave over an extended period (e.g., Kasen & Woosley, 2009; Dessart et al., 2013). This balance between expansion, cooling, recombination, and photospheric recession directly encodes the progenitor's envelope mass and $R_\star$ in the observed light

curve, making plateau durations ($t_{\rm plat}$) and luminosities powerful diagnostics of the exploding star's structure (e.g., Hamuy, 2003; Young, 2004; Anderson et al., 2014; Goldberg et al., 2019).

The plateau luminosity correlates strongly with explosion energy and progenitor radius, while its duration primarily reflects the mass of the hydrogen envelope (e.g., Hamuy, 2003; Kasen & Woosley, 2009; Martinez et al., 2022a). ^{56}Ni synthesised during explosive nucleosynthesis can significantly modify plateau characteristics by providing an additional energy source. This radioactive component can flatten and extend the plateau duration by approximately 20% through two complementary mechanisms: maintaining higher temperatures (thus preserving ionisation), and increasing the average opacity, which extends photon diffusion timescales (e.g., Young, 2004; Kasen & Woosley, 2009; Bersten et al., 2011; Kozyreva et al., 2019; Jerkstrand et al., 2025; Matsumoto et al., 2025). The magnitude of this effect depends sensitively on both the total nickel mass produced and its spatial distribution throughout the envelope, with more extensive mixing producing more pronounced effects on the plateau morphology.

The relative recession rates of the recombination front and photospheric expansion ultimately determine the light curve shape – creating either the distinctive plateau in Type IIP SNe or the more rapid, near-linear decline in Type IIL events – depending primarily on the hydrogen envelope mass and density structure (e.g., Popov, 1993; Bersten et al., 2013; Valenti et al., 2016; Goldberg et al., 2019).

For hydrogen-rich and hydrogen-poor CCSNe alike, the late-time light curve is driven by the radioactive decay of ^{56}Ni, synthesised in the outer envelopes during the explosion, and its subsequent products:

$$^{56}_{28}\mathrm{Ni} \rightarrow ^{56}_{27}\mathrm{Co} + e^{+} + \nu_e + \gamma \qquad (\tau_{\frac{1}{2}} \approx 6 \text{ days}) \tag{1.7}$$

$$^{56}_{27}\mathrm{Co} \rightarrow ^{56}_{26}\mathrm{Fe} + e^{+} + \nu_e + \gamma \qquad (\tau_{\frac{1}{2}} \approx 77 \text{ days}) \tag{1.8}$$

In the radioactive decay chain, high-energy gamma-ray photons emitted from ^{56}Ni decay are initially trapped within the expanding ejecta, where they undergo Compton scattering and photoelectric absorption (e.g., Hamuy, 2003; Valenti et al., 2016; Martinez et al., 2022b). These interactions generate energetic electrons that subsequently

thermalise, depositing energy that heats, ionises, and excites the surrounding gas (e.g., Nakar et al., 2016; Kozyreva et al., 2019). For explosions of progenitors that have shed most or all of their hydrogen envelope prior to core-collapse – such as blue supergiants (BSGs) or stripped helium cores – this radioactive powering mechanism dominates the light curve evolution within days of explosion, as minimal envelope mass exists to sustain an extended shock cooling phase or plateau (e.g., Nakar et al., 2016; Kozyreva et al., 2019).

For Type II SNe with substantial hydrogen envelopes, radioactive heating becomes the primary energy source only during the nebular "tail" phase, which commences after hydrogen recombination has progressed through the entire envelope, typically 100 – 120 days post-explosion. During this nebular phase, the light curve transitions to an exponential decline that closely tracks the 77.3 day half-life of the $^{56}\mathrm{Ni} \rightarrow {}^{56}\mathrm{Co}$ decay chain (see Eqs. 1.7 and 1.8) , with a characteristic decline rate of 0.01 mag day^{-1} (e.g., Anderson et al., 2014; Valenti et al., 2016; Anderson, 2019). In scenarios involving extensive CSM ($\geq 10^{15}$ – 10^{16} cm and $\gtrapprox 0.1$ – 1 $\mathrm{M}_{\odot}$), additional energy contributions may supplement or even dominate the radioactive component at late times, manifesting as sustained luminosity plateaus or distinctive rebrightening episodes that signal ongoing interaction between the expanding ejecta and surrounding CSM shells or filaments (e.g., Morozova et al., 2018; Moriya et al., 2018; Moriya et al., 2023).

1.6 Supernovae and their Progenitors

As demonstrated in the preceding sections, the complex physics of core-collapse and the subsequent SN emission mechanisms create observable signatures directly linked to their progenitor systems. Type II SNe serve as particularly valuable probes of stellar evolution, galactic chemistry, and cosmic structure formation (Smartt, 2009; Arcavi, 2017; Anderson, 2019).

These hydrogen-rich explosions contribute fundamentally to cosmic evolution through their energetic feedback, heavy element nucleosynthesis, and dust production (Hoyle & Fowler, 1960; Woosley & Weaver, 1995; Heger & Woosley, 2002; Kotak et al., 2009; Nomoto et al., 2013; Paxton et al., 2015; Maoz & Graur, 2017). The mechanical energy from these SNe regulates star formation by disrupting molecular clouds, while their

nucleosynthetic yields directly influence subsequent stellar generations via galactic enrichment (Gibson et al., 1997; Schaye et al., 2015; Kobayashi et al., 2020). Observations confirm they are significant dust producers, contributing essential materials for planet formation and interstellar chemistry (Matsuura et al., 2011; Weil et al., 2020).

The volumetric rates and properties of Type II SNe provide crucial constraints on massive stellar evolution pathways (Li et al., 2011; Strolger et al., 2015; Shivvers et al., 2017; Graur et al., 2017a,b; Perley et al., 2020), primarily linking to RSG progenitors with initial masses between 8 – 25 $M_{\odot}$ (Smartt, 2015; Davies & Beasor, 2017). This direct connection between observable SN characteristics and progenitor properties provides the foundation for the detailed analyses presented in the following chapters.

Up to now, I have discussed the general mechanism by which most SNe (hydrogen-rich and hydrogen-poor) between 8 and $\sim$ 50 $M_{\odot}$ explode via core-collapse and I will focus on hydrogen-rich SNe from hereon. For simplicity, I group Type II, IIn, and IIb SNe – along with other, rarer subtypes that exhibit hydrogen features in their spectra – as "hydrogen-rich CCSNe". This categorisation reflects their origin from massive star progenitors that retained at least some portion of their hydrogen envelopes at the time of explosion. Within this classification, Type II refers specifically to events that show broad hydrogen lines with P-Cygni profiles, excluding Type IIn (characterised by persistent narrow hydrogen emission lines from strong circumstellar interaction) and Type IIb (which exhibit weak hydrogen features early on, transitioning to helium-dominated spectra at later times).

Moreover, the growing availability of large, homogeneous spectroscopically classified SN catalogues has revealed an increasing number of peculiar hydrogen-rich CCSNe that do not exhibit the "standard photometric" classes of Type II, IIn, IIb, or superluminous SNe – even when their spectra appear nominally "normal." Events such as iPTF14hls (Wang et al., 2018; Sollerman et al., 2019; Wang et al., 2022), SN 2023ufx (Ravi et al., 2025), and SN 1987A-like SNe (e.g., SN 1987A – Arnett et al. 1989; Suntzeff et al. 1992; SN 2018hna – Singh et al. 2019; SN 2020faa – Salmaso et al. 2023; SN 2021aatd – Szalai et al. 2024), as well as objects like DES16C3cje (Gutiérrez et al., 2020a), often require non-standard progenitors (e.g., BSGs), invoke still-unconfirmed mechanisms (e.g., pair-instability), or demand additional power sources (e.g., fallback accretion or magnetar energy injection)

to account for their highly irregular behaviour. With each new detection, the boundaries between these subclasses grow increasingly blurred.

1.6.1 Type II

The most commonly occurring subtype of CCSNe, Type IIP SNe, are photometrically identified by their ∼100 day plateau powered by hydrogen recombination, being given the suffix "P" for plateau, with the other common subtype recognised for a linear post-peak decline, given the suffix "L" for linear (e.g., Barbon et al., 1979; Filippenko, 1997; Chieffi et al., 2003; Young, 2004; Anderson et al., 2014; Gal-Yam, 2017b). Photometrically, both variants show sharp rises ($\lesssim$ 5 d; Langer, 2012; Anderson et al., 2014; Gall et al., 2015; González-Gaitán et al., 2015; Rubin et al., 2016; Valenti et al., 2016) and bright peaks (mean $M_V \approx -16.7$ mag; Anderson et al., 2014; Richardson et al., 2014; Galbany et al., 2016a; de Jaeger et al., 2019) with a range $M_V \sim -14$ to -19 mag (e.g., Li et al., 2011; de Jaeger et al., 2018; Martinez et al., 2022a).

Type II SNe show a recognisable linear decay phase from the radioactive decay chain of ^{56}Ni $\rightarrow$ ^{56}Co $\rightarrow$ ^{56}Fe, typically 10^{-3} – 10^{-2} M$_\odot$ (inferred from light curves, e.g., Müller et al., 2017; Anderson, 2019; Goldberg et al., 2020; Rodríguez et al., 2021; Rodríguez, 2022; Martinez et al., 2022b). However, the main distinction in post-peak behaviour (whether a plateau is seen or not) is likely driven by the mass of the hydrogen envelope. Type IIP SNe possess more massive envelopes (typically 5 – 10 M$_\odot$) which sustain the recombination period for an extended duration, whereas linearly decaying Type IIL and shorter-plateau Type II events likely have less massive hydrogen envelopes (0.1 – 3 M$_\odot$, e.g., Grassberg et al., 1971; Blinnikov & Bartunov, 1993; Anderson et al., 2014; Gall et al., 2015; Valenti et al., 2016; Hillier & Dessart, 2019; Dessart & Hillier, 2019; Reynolds et al., 2020; Hiramatsu et al., 2021), resulting from stripping via binary interactions or large $\dot{M}$.

In both instances, the ejecta mass is thought to be large enough to efficiently absorb and thermalise the decay energy[1], leading to a luminosity decline rate close to the nuclear decay rate at late times (e.g., Arnett, 1980; Kasen & Woosley, 2009; Sukhbold et al., 2016; Bose et al., 2018; Anderson, 2019). Various studies (e.g., Arcavi et al., 2012;

[1]The process by which gamma-rays and positrons produced in the decay chain are absorbed by the ejecta and converted to thermal (heat) energy. In high mass ejecta, gamma-rays undergo multiple Compton scatterings before depositing their energy, resulting in efficient thermalisation.

Anderson et al., 2014; Valenti et al., 2016) have examined hydrogen-rich SN light curves to determine whether Type IIP and IIL represent distinct classes or endpoints of a continuous distribution. The debate remains active, with some researchers identifying bi-modality, suggesting separate physical mechanisms (e.g., Patat et al., 1993, 1994; Arcavi et al., 2012; Faran et al., 2014), while others find a smooth continuum indicating a single population with varying envelope masses (Anderson et al., 2014; Sanders et al., 2015; Valenti et al., 2016; Rubin et al., 2016).

Spectroscopically, the early spectra of Type IIP/IIL SNe are dominated by prominent P-Cygni profiles of Balmer hydrogen features. These distinctive P-Cygni profiles arise when photons emitted from the hot photosphere encounter the expanding ejecta, where cooler outflowing material creates a velocity-dependent opacity structure. The resulting spectral profile combines blueshifted absorption (from material moving toward us along our line of sight to the photosphere) with a redshifted emission component (from material scattering photons from the sides of the expanding shell into our line of sight), directly encoding both expansion velocities and density structure of the SN atmosphere (Filippenko, 1997; Dessart & Hillier, 2011; Gräfener & Vink, 2015; Gutiérrez et al., 2017). As the SN evolves into the nebular phase, the photosphere recedes toward the inner ejecta, revealing strong emission lines of oxygen, calcium, and other metals synthesised both during the progenitor's lifetime and during the explosion itself (Filippenko, 1997; Jerkstrand et al., 2015; Anderson, 2019).

Type II SNe are the most common cosmic explosions per unit volume ($\sim 53 - 60\%$ in volume-limited surveys; Smartt, 2009; Li et al., 2011; Eldridge et al., 2013; Shivvers et al., 2017) and, as the progenitors are massive stars, trace star formation across the universe given their short lifecycles (8 – 50 Myr; Smartt, 2015; Strolger et al., 2015; Anderson et al., 2016). Type II SNe are often associated with bright H II regions, illuminated by UV radiation from clusters of hot and bright young massive stars (e.g., Anderson et al., 2010; Kuncarayakti et al., 2013). Spatially resolved studies have demonstrated that these SNe preferentially occur in spiral arms and other regions of active star formation, with environmental metallicities generally ranging from slightly sub-solar to solar values (Anderson et al., 2016; Galbany et al., 2016b; Kuncarayakti et al., 2018; Pessi et al., 2023b,c). Their host galaxy demographics span from dwarf irregulars to massive spirals, consistently following the distribution of cosmic star formation (Kelly & Kirshner, 2012; Graur et al., 2017a,b).

1.6.1.1 Type II Progenitors

The association between Type IIP SNe and RSGs represents the most robustly established relationship connecting SNe to their specific stellar progenitors. This connection was initially proposed based on theoretical constraints: Type II progenitors must have extensive radii of order 10^{13} – 10^{14} cm (300 – 1500 $R_{\odot}$) and substantial hydrogen envelopes to explain the dominant hydrogen features in their spectra (e.g., Chevalier, 1976; Arnett, 1980; Filippenko, 1997). Additionally, stellar evolution models demonstrate that stars within the 8 – 30 $M_{\odot}$ range naturally expand and cool once they initiate core helium burning, evolving into the RSG phase prior to core-collapse (e.g., Eldridge & Tout, 2004; Smartt, 2009).

This theoretical association has been definitively confirmed through direct progenitor detections over the past several decades (see Smartt, 2009; Van Dyk, 2017, for comprehensive reviews). This powerful but challenging technique involves identifying the progenitor star in archival images, typically from the Hubble Space Telescope (HST), obtained years before explosion, followed by subsequent imaging to confirm the candidate's disappearance. The method demands exceptional precision in astrometric alignment (sub-pixel scale accuracy) and, ideally, multiple epochs of high-resolution imaging. For RSG/Type II SNe, this approach has proven remarkably successful, with numerous confirmed progenitor identifications establishing RSGs as the direct ancestors of Type IIP explosions (e.g., Smartt et al., 2001; Van Dyk et al., 2003; Smartt et al., 2004; Li et al., 2005; Maund et al., 2005; Hendry et al., 2006; Mattila et al., 2008; Leonard et al., 2008; Elias-Rosa et al., 2009; Crockett et al., 2011; Kochanek et al., 2012; Fraser et al., 2012; Van Dyk et al., 2012; Tomasella et al., 2013; Maund et al., 2013, 2015; Smartt, 2015; Takáts et al., 2015; Kochanek et al., 2017; O'Neill et al., 2019; Rui et al., 2019; Van Dyk et al., 2019; O'Neill et al., 2021; Kilpatrick et al., 2023; Van Dyk et al., 2023; Soraisam et al., 2023; Pledger & Shara, 2023; Qin et al., 2024; Van Dyk et al., 2024; Luo et al., 2025; Jencson et al., 2023; Neustadt et al., 2024; Niu et al., 2023). Complementary evidence has emerged from the detection of UV flashes associated with SBO through the extended hydrogen envelopes characteristic of RSG progenitors (e.g., Schawinski et al., 2008; Gezari et al., 2008; Garnavich et al., 2016), further solidifying this critical connection between progenitor type and SN classification.

Determining $M_{\rm ZAMS}$ from direct progenitor detections relies on a conversion of pre-SN luminosity to initial stellar mass through theoretical stellar evolution models. The bolometric luminosity is often calculated by computing the observed SED and using precise distance measurements to the host galaxy to anchor the bolometric luminosity, establishing direct constraints on the progenitor's mass through systematic comparison with end-of-life evolutionary models (e.g. Smartt, 2009; Smartt et al., 2009; Davies & Beasor, 2017). This rigorous approach identified an apparent upper mass limit for Type II progenitors at approximately 16 – 17 $M_\odot$. This limit is substantially below the theoretical expectation that stars up to 25 – 30 $M_\odot$ should complete their evolution as RSGs, based on the Salpeter initial mass function (IMF; Salpeter, 1955). This significant discrepancy, termed the "red supergiant problem", represents one of the most intriguing and highly debated challenges in modern stellar astrophysics (e.g., Smartt, 2009, 2015; Kochanek, 2020; Beasor et al., 2025; Fang et al., 2025a). Further evidence for the discrepancy is provided by an apparent mismatch between the SN rate and rate of massive star formation (e.g., Horiuchi et al., 2011).

The estimated bolometric luminosity, $L_{\rm bol}(t)$, must be numerically transformed into $M_{\rm init}$ by assuming a stellar evolutionary model via $\log(L_{\rm bol}(t)/{\rm L}_\odot) = C + \alpha \log(M_{\rm init}/M_\odot)$, where α depends on the stellar evolutionary model (e.g., Smartt, 2009; Davies & Beasor, 2017; Eldridge et al., 2018). In this conversion, extinction corrections represent perhaps the most critical source of systematic error in this analysis. RSGs are frequently associated with dusty star-forming regions and often produce their own circumstellar dust shells through pre-explosion mass-loss. This circumstellar extinction can be highly variable and tends to increase with progenitor mass as more massive RSGs experience stronger mass-loss (Beasor & Davies, 2016, 2018). When inadequately accounted for, this extinction may preferentially obscure the most massive progenitors, blocking more optical light than IR, shifting the peak of the SED from the optical to the IR, potentially leading to significant underestimation of $L_{\rm bol}(t)$.

The systematics involved in measuring the progenitor mass using the photometry have led to extensive debates surrounding the significance of the RSG problem (e.g., Yoon & Cantiello, 2010; Groh et al., 2013; Gerke et al., 2015; Adams et al., 2017b; Davies & Beasor, 2017; Kochanek, 2020; Sukhbold & Adams, 2020; Beasor & Smith, 2022; Strotjohann et al., 2024b; Beasor et al., 2025; Fang et al., 2025a). Possible explanations for a

physically motivated dearth include enhanced pre-SN mass-loss resulting in a hydrogen-poor SESN instead of a hydrogen-rich SN or direct collapse to a BH without a luminous electromagnetic counterpart. The former is interesting as it implies a continuum between Type IIP and SESNe governed primarily by the strength and timing of mass-loss (e.g., Gutiérrez et al., 2020b; Reguitti et al., 2024). The latter has prompted targeted observational campaigns (e.g., Gerke et al., 2015; Adams et al., 2017a,b), though no definitive detections have yet been made. Both Davies & Beasor (2017) and Beasor et al. (2025) show that, while accounting for systematics, the observed Type II progenitor distribution becomes consistent with expectations from the IMF, $M_{\rm low}^{\rm RSG} = 6 - 8$ M$_\odot$ and M$_{\rm up}^{\rm RSG} \approx 25$ –27 M$_\odot$, quoting a less than 3 σ significance.

While alternative methods exist for estimating progenitor masses, such as hydrodynamical modelling of light curves (e.g., Blinnikov et al., 2000, 2006; Bersten & Hamuy, 2009; Utrobin & Chugai, 2009; Pumo & Zampieri, 2011; Bersten et al., 2011; Wongwathanarat et al., 2015; Pumo et al., 2017; Das & Ray, 2017; Morozova et al., 2018; Moriya et al., 2023; Martinez et al., 2022a; Moriya & Singh, 2024), these approaches suffer from their own degeneracies (see Hillier & Dessart, 2019; Dessart & Hillier, 2019). Various combinations of progenitor properties ($E_{\rm exp}$, $M_{\rm ZAMS}$, $M_{\rm H}^{\rm env}$, $M_{\rm He}^{\rm env}$, $R_\star$, $M_{\rm Ni}$, and $\dot{M}$) can yield remarkably similar photometric evolution, complicating unique progenitor determinations from light curves alone. A promising and comprehensive route for an independent measure of $M_{\rm ZAMS}$ was recently presented in Fang et al. (2025a) using nebular phase [O I] emission. Various caveats are explored and statistical tests are carried out to validate the robustness of the tests, though they find an upper luminosity cutoff $\log(L_{\rm up}) = 5.31^{+0.09}_{-0.07}$ dex which equates to $M_{\rm up}^{\rm RSG} = 20.63^{+2.63}_{-1.64}$ M$_\odot$, again below the maximum mass of $M_{\rm ZAMS} \sim 29.4$ M$_\odot$ (converted from $\log(L) = 5.5$ dex; Fang et al., 2025a), quoting a significance at a 1 – 3 σ level.

Inextricably linked to determining $M_{\rm ZAMS}$ is the impact of mass-loss. Historic estimates for typical RSG mass-loss rates ranged from $\dot{M} \sim 10^{-7} - 10^{-4}$ M$_\odot$ yr^{-1} (e.g., Reimers, 1975; de Jager et al., 1988; Nieuwenhuijzen & de Jager, 1990), derived primarily from Galactic RSGs using diverse observational techniques including infrared excesses, maser emission, and radio continuum measurements. More recent systematic studies of Local Group RSGs have refined these values, with particular focus on Magellanic Cloud populations where distance uncertainties are minimised. van Loon et al. (2005) derived mass-loss rates of $\dot{M} \sim 10^{-6}$ to 10^{-5} $M_\odot$ yr^{-1} for luminous RSGs in the LMC based on

dust emission, while Mauron & Josselin (2011), Taddia et al. (2013) and Fransson et al. (2014) found similar ranges for Galactic RSGs.

Evidence for CSM interacting with SBO at early times (Gal-Yam et al., 2014; Kochanek, 2019) was possibly first seen by Niemela et al. (1985) and Fassia et al. (2000). Since then, numerous reports of flash ionisation have since been gathered, with the prevalence of such features being indicative of a period of intense mass-loss across large samples of RSG progenitors immediately before core-collapse, rather than being a rare phenomenon (e.g., Bruch et al., 2021, 2023; Irani et al., 2024; Jacobson-Galán et al., 2024a). These recent studies generally agree that $\dot{M}$ increase from the typical $\lesssim 10^{-5}$ $M_{\odot}$ yr^{-1} seen in local group RSGs to enhanced rates of 10^{-3} – 10^{-1} $M_{\odot}$ yr^{-1} (assuming v_{CSM} =10 km s^{-1}) in a large proportion of SNe ($\sim$ 60%; Bruch et al., 2023), specifically in the last $<$ 1000 years before core-collapse (e.g., Kochanek, 2011; Groh, 2014b; Gal-Yam et al., 2014; Yaron et al., 2017; Morozova et al., 2018; Bruch et al., 2021; Tinyanont et al., 2022; Pearson et al., 2023; Moriya et al., 2023; Irani et al., 2024; Jacobson-Galán et al., 2024a) owing to the late stage instabilities or binary induced mass transfer discussed previously.

1.6.2 Type IIn

Type IIn SNe constitute a distinctive spectroscopic class characterised by prominent, narrow hydrogen emission lines ($\lesssim$ 1000 km s^{-1}) superimposed on broader emission components, definitively indicating sustained, strong interaction between the high-velocity SN ejecta and dense CSM (e.g., Schlegel, 1990; Stathakis & Sadler, 1991; Turatto et al., 1993; Filippenko, 1997; Smith et al., 2011; Smith, 2017b). Unlike the transient flash ionisation signatures seen in some normal Type II events, these spectroscopic interaction features persist throughout the duration of the light curve evolution, often for hundreds of days.

The "n" designation in the classification specifically refers to these narrow spectral features, which originate from relatively slow-moving ($\sim$ 10 – 1000 km s^{-1}) pre-existing CSM ($\gtrsim 10^{16}$ cm) that has been photo-ionised by the SN's initial UV radiation burst and subsequently maintained in an ionised state by ongoing shock interaction. The simultaneous presence of intermediate-width ($\sim$1000 – 5000 km s^{-1}) and broad ($\sim$10,000 km s^{-1}) components in the emission line profiles reveals the complex velocity

structure of the interaction region, with material spanning from the unshocked CSM to the post-shock cooling layers and the decelerated outer ejecta.

When the high-velocity ejecta collides with the slow-moving, dense CSM, a forward shock propagates outward through the CSM while a reverse shock travels back into the ejecta. At the interface between these shocks, a cold dense shell (CDS) forms as the shocked material rapidly cools through efficient radiative processes (e.g., Chugai & Danziger, 1994a,b; Smith et al., 2010, 2011; Taddia et al., 2013). This cooling occurs primarily through collisional de-excitation as electrons recombine with ions in the dense post-shock region, where densities can exceed 10^{12} cm^{-3} and temperatures drop from $\sim 10^9$ K to $\sim 10^4$ K over timescales of hours to days.

High-energy radiation produced near the shock front propagates ahead, ionising the unshocked CSM. As this gas recombines, it produces the characteristic narrow emission lines with widths reflecting the pre-explosion CSM velocity structure. These lines span a wide range of ionisation states, with higher ionisation features typically appearing earlier and then fading as the shock propagates outward and the ionisation front recedes. This mechanism closely parallels the flash ionisation process observed in the earliest spectra of Type IIP SNe, where SBO radiation briefly illuminates a compact, dense CSM shell ejected shortly before core-collapse, though the more extensive and persistent CSM in Type IIn events sustains these narrow features for significantly longer timescales. The conversion of kinetic energy to radiation during this interaction process can power exceptionally luminous light curves, with some Type IIn SNe reaching peak absolute magnitudes of $M_V < -20$ mag and maintaining high luminosities for months or even years (e.g., Smith et al., 2007; Rest et al., 2011; Kiewe et al., 2012; Pessi et al., 2025; Hiramatsu et al., 2024).

In these interactions, whether from CDS formation in high-density CSM or more simple SBO through extended CSM, high temperatures are achieved that initially cause emission to peak in the extreme-UV to X-ray bands. The post-shock gas cools via free-free emission (e.g., Chevalier, 2012; Kochanek, 2019), thermal line emission, and Compton scattering. At later times, as the shock continues to propagate and accelerate particles, these SNe can become radio and X-ray bright through synchrotron and bremsstrahlung radiation, with peak emission occurring months to years post-explosion (e.g., Margutti et al., 2017; Chandra, 2018; Stroh et al., 2021).

Photometrically, Type IIn SNe display extraordinary diversity, with light curves ranging from rapidly declining events lasting weeks to extremely long-lived transients continuing for years or even decades (e.g., Kiewe et al., 2012; Taddia et al., 2013; Nyholm et al., 2020). The spread in absolute magnitudes is remarkable, spanning from $M_V \approx -16$ to ≥ -22 mag (Nyholm et al., 2020; Hiramatsu et al., 2024; Pessi et al., 2025), and reflects the wide range of CSM masses, densities, and geometries surrounding the progenitors. The luminosity is primarily powered by the conversion of kinetic energy to radiation as the ejecta decelerates against the dense CSM, allowing these events to achieve extreme peak luminosities exceeding 10^{44} erg s^{-1} in some cases (e.g., Smith et al., 2007; Rest et al., 2011; Ofek et al., 2014). The formation of extensive ($\geq 10^{16}$ cm) and massive ($\gtrsim 1$ – 10 M$_\odot$) CSM requires multiple mass-loss mechanisms, which can allow for different progenitor types and scenarios. For Type IIn SNe, not all progenitors necessitate enhanced mass-loss immediately before explosion, but can also be explained via large or periodic eruptions occurring millennia before core-collapse.

The most luminous Type IIn events led to the recognition of SLSNe as a distinct class of cosmic explosions. The pioneering discoveries of extraordinarily bright transients like SN 2006gy (Quimby et al., 2007b; Ofek et al., 2007) revealed objects reaching absolute magnitudes of $M_V < -22$ mag, making them 10 – 100 times more luminous than typical SNe. These events defied explanation by traditional SNe mechanisms, requiring either extreme CSM interaction, pair-instability physics, or exotic energy sources like magnetars (e.g., Quimby et al., 2013). In a review, Gal-Yam (2012) established the formal classification of SLSNe, dividing them into hydrogen-rich (SLSN-II, most showing narrow Type IIn features) and hydrogen-poor (SLSN-I) subtypes, both characterised by peak luminosities exceeding $M_{AB} \lesssim -21$ mag in any band – revised in Gal-Yam (2019b). This classification has been roughly followed, though the distinction between normal Type II, Type IIn, luminous SNe (LSNe) and SLSN II has been called into question (e.g., Kangas et al., 2022; Hiramatsu et al., 2024; Pessi et al., 2025), indicating these events may represent a continuum of interaction-powered phenomena rather than physically distinct explosions.

1.6.2.1 Type IIn Progenitors

Progenitor identifications for Type IIn SNe suggest a heterogeneous population rather than a single progenitor channel. Direct detections have linked some Type IIn events to LBVs undergoing eruptive mass-loss shortly before explosion (e.g., Gal-Yam et al., 2007; Gal-Yam & Leonard, 2009; Smith, 2011; Smith et al., 2011; Ofek et al., 2014). LBVs, with their episodic mass ejections of several solar masses at velocities of 100 – 1000 km s^{-1}, provide the necessary dense circumstellar environment to power the prolonged interaction-dominated emission characteristic of Type IIn SNe (Smith, 2014; Smith, 2017b).

Evidence also exists linking Type IIn SNe with more extreme progenitors, including VMS ($M_{\rm ZAMS} > 50\ M_{\odot}$) that undergo significant pre-explosion mass-loss (Gal-Yam et al., 2007; Gal-Yam & Leonard, 2009; Smith, 2011). These connections challenge traditional stellar evolution models, which typically place LBVs as transitional objects rather than terminal evolutionary states, suggesting alternative evolutionary pathways possibly involving binary interactions or modified mass-loss prescriptions (Smith et al., 2015; Inserra et al., 2016).

The extreme mass-loss rates required to produce the dense CSM observed in Type IIn SNe ($\dot{M} \sim 10^{-2}$ – 1 $M_{\odot}$ yr^{-1}) exceed those achievable through steady stellar winds, suggesting that progenitors must undergo eruptive or explosive mass-loss episodes in the final years to decades before core-collapse (e.g., Smith, 2014; Smith, 2017b). Similarly, as most massive stars are thought to be in at least binary systems (e.g., Sana et al., 2012; Sana et al., 2013; Groh, 2014a,b), common envelope ejections likely play a critical role in stripping significant amounts of material.

Along with the mass-loss mechanisms mentioned previously, for the more massive progenitors ($M_{\rm ZAMS} \gtrsim 40\ M_{\odot}$), and VMS, pulsational pair instability is predicted to play a significant role. Pulsational pair instability occurs when oxygen/carbon cores reach temperatures exceeding $\sim 10^9$ K, causing gamma ray photons to convert into electron-positron pairs ($\gamma \rightarrow e^+ + e^-$), temporarily reducing radiation pressure support (Barkat et al., 1967; Rakavy et al., 1967; Fraley, 1968; El Eid & Langer, 1986; Heger et al., 2005). This triggers partial collapse followed by explosive oxygen burning, ejecting several solar masses of material at velocities of ~ 1000 – 3000 km s^{-1} while leaving the core

intact (Woosley & Weaver, 1986; Woosley et al., 2007; Yoshida et al., 2016). Unlike full PISNe, these eruptions can repeat at intervals ranging from days to millennia as the star re-stabilises, contracts, and heats again (Woosley, 2017; Leung et al., 2019).

1.6.3 Type IIb

Type IIb SNe exhibit a distinctive dual-peaked light curve evolution. The initial peak, lasting $\lesssim 1$ d, is only explainable by SC as the low-mass shock-heated ejecta undergoes rapid adiabatic expansion following SBO (e.g., Chevalier, 1992; Nomoto et al., 1993; Podsiadlowski et al., 1993; Woosley et al., 1994; Chevalier & Fransson, 2008; Bersten et al., 2018). This extremely short-lived feature is frequently missed in observational campaigns due to its ephemeral nature. This is followed by a more prominent secondary maximum universally observed in Type IIb events 2 – 3 weeks after SBO (e.g., Woosley et al., 1994; Lyman et al., 2016), attributed to the radioactive decay of ^{56}Ni synthesised during the explosion (e.g., Nomoto et al., 1993; Shigeyama et al., 1994; Nakar & Piro, 2014). The peak magnitude varies based on the SC and ^{56}Ni peaks (which ultimately depend on the hydrogen envelope and CSM) but vary between $M_V = -14$ and -18 mag (e.g., Claeys et al., 2011; Pessi et al., 2019), making up $\sim 12\%$ of Type II SNe in the LOSS volume-limited survey (Li et al., 2011; Shivvers et al., 2017) – see Ayala et al. (2025) for a review.

Following the second maximum, the light curve transitions to a radioactive decay-powered phase governed by the ^{56}Ni$\rightarrow^{56}$Co$\rightarrow^{56}$Fe decay chain, with the light curve width sensitive to both the progenitor structure and the amount of ^{56}Ni synthesised (e.g., Nakar & Sari, 2010; Nakar & Piro, 2014). Rayleigh-Taylor instabilities during shock propagation through the helium envelope promote ^{56}Ni mixing into the outer ejecta (e.g., Hachisu et al., 1991; Nomoto et al., 1993), critical for powering the secondary maximum.

Spectroscopically, Type IIb SNe transform from hydrogen-dominated to helium-dominated features over days to weeks (e.g., Filippenko, 1997; Ben-Ami et al., 2015). This evolution traces the photosphere's progression from the thin hydrogen envelope to the more substantial helium layer beneath. Spectra exhibit P-Cygni profiles of Balmer hydrogen lines at early times before evolving to resemble Type Ib SESNe at later times (e.g., Filippenko, 1997; Smartt, 2009). The relatively low temperatures and low-ionisation

species in early spectra support the compact progenitor scenario (e.g., Arcavi et al., 2011; Nakar & Piro, 2014).

1.6.3.1 Type IIb Progenitors

Direct progenitor detections have linked Type IIb SNe to yellow supergiants (YSGs) with effective temperatures of $3.6 \lesssim \log(T_{\rm eff}/K) \lesssim 3.8$ (Maund et al., 2011; Georgy, 2012; Van Dyk et al., 2014). The rapid initial rise and brief first peak provide evidence for progenitors with small radii ($\sim 50 - 650$ $R_\odot$) compared to typical RSGs, and minimal but non-negligible hydrogen-rich envelopes ($\lesssim 1$ $M_\odot$, see also Woosley et al., 1994; Pastorello et al., 2008; Georgy, 2012; Morales-Garoffolo et al., 2014, 2015; Waxman & Katz, 2017; Arcavi, 2017; Bersten et al., 2018; Sravan et al., 2019; Medler et al., 2022; Yamanaka et al., 2025).

The binary nature of these systems has been confirmed in several cases, most notably SN 1993J, where the companion was identified years after the explosion (Aldering et al., 1994; Cohen et al., 1995; Maund et al., 2004; Fox et al., 2014). These observations provide evidence that envelope stripping through binary interaction is the dominant mechanism producing Type IIb progenitors (Eldridge et al., 2008; Claeys et al., 2011; Yoon et al., 2017). However, if the progenitors are indeed WR stars, strong stellar winds could eject the outer layers if the metallicity is high enough (e.g., Gal-Yam et al., 2014; Gräfener & Vink, 2015).

1.6.4 SN 1987A-like and peculiarities

Perhaps the most famous example illustrating the complexity of progenitor-SN mapping is SN 1987A, which unexpectedly originated from a BSG rather than the predicted RSG (e.g., Gilmozzi et al., 1987; Sonneborn et al., 1987). Its distinctive light curve exhibited an unusually rapid rise, reminiscent of SC, followed by a broad, delayed peak (reaching $M_V \sim -16.1$ mag), powered primarily by ^{56}Ni decay rather than the typical cooling envelope recombination (Arnett et al., 1989; Suntzeff et al., 1992). This was driven by elevated ^{56}Ni production ($M_{\rm Ni} \gtrsim 0.1$ $M_\odot$) compared to the 10^{-3} – 10^{-2} $M_\odot$ typically inferred for Type II SNe (e.g., Anderson, 2019; Rodríguez et al., 2021). This unique morphology directly reflected the BSG's compact radius (~ 50 $R_\odot$), which yielded

minimal initial cooling emission but enabled efficient thermalisation of radioactive decay energy (Woosley, 1988; Nomoto & Hashimoto, 1988).

This SN will be remembered for its field-defining nature, due to: (1) the coincident detection of neutrinos, providing concrete evidence for neutrino heating restarting the stalled shock (e.g., Hirata et al., 1987; Bionta et al., 1987; Schaeffer et al., 1987; Burrows & Lattimer, 1987; Kolb & Turner, 1987; Janka, 2017); (2) the discovery of a BSG progenitor (e.g., Arnett et al., 1989; Suntzeff et al., 1992; Chevalier, 1992; Pastorello et al., 2005; Kleiser et al., 2011); and (3) discovery of extensive CSM in the immediate vicinity of the progenitor, most notably a triple-ring nebular structure (e.g., Burrows et al., 1995; Fransson et al., 2007, 2015).

1.6.4.1 SN 1987A-like Progenitors

The peculiar BSG progenitor and surrounding CSM could not be explained through single-star evolution, leading to a binary merger scenario where two stars ($\sim$15 – 20 $M_\odot$+ 5 $M_\odot$) coalesced approximately 20,000 years before explosion (Podsiadlowski et al., 1992; Morris & Podsiadlowski, 2007). This merger hypothesis simultaneously explains the equatorial and polar ring structure, unusual chemical abundances, and the BSG's unexpected properties, including its rotation and mixed composition (Podsiadlowski et al., 2007; Pastorello et al., 2012; Xiang et al., 2023).

Several subsequent events have shown similarities to SN 1987A, including SN 1998A (e.g., Pastorello et al., 2005), SN 2009E (e.g., Pastorello et al., 2012) and SN 2018hna (e.g., Singh et al., 2019; Xiang et al., 2023), collectively termed "87A-like" SNe (Kleiser et al., 2011; Taddia et al., 2016). These diverse progenitor scenarios highlight the critical role of binary interactions in producing the observed diversity of CCSNe. Modern surveys indicate that approximately 70 – 75% of massive stars exist in binary systems with orbital periods sufficiently close for interaction (Sana et al., 2012; Sana et al., 2013), with roughly one-third expected to undergo significant envelope stripping before death (Langer, 2012; Smith, 2014). This high binary fraction, combined with the variety of interaction scenarios (stable mass transfer, common envelope evolution, mergers), creates numerous evolutionary pathways beyond traditional single-star channels.

1.7 On the hunt for Supernovae

The landscape of SN discovery has undergone a remarkable transformation since Fritz Zwicky's pioneering work in the mid-1900s (e.g., Zwicky, 1938b, 1942). Zwicky's first systematic searches using photographic plates at Palomar with the Palomar Supernova Search, yielding discoveries at the modest rate of approximately 1 – 5 SNe per year (Zwicky, 1938a, 1964; Sargent et al., 1974). The era of photographic plate astronomy continued through the 1980s with programs like the Asiago Supernova Search and Crimean Supernova Search contributing dozens of discoveries over decades of operation (Rosino, 1964; Cappellaro et al., 1993, 1997).

The 1980s witnessed a fundamental paradigm shift in SN science driven by two transformative developments: the transition from photographic plates to digital Charge Coupled Device detectors (CCD; Boyle & Smith, 1970) and the evolution from galaxy-targeted surveys to untargeted, wide-field observational strategies. Prior to this revolution, SN searches had focused exclusively on monitoring known galaxies, introducing severe selection effects that biased discoveries toward luminous, face-on spiral galaxies while systematically overlooking events in low-surface-brightness hosts, galaxy nuclei, and highly inclined systems.

The introduction of CCD technology catalysed multiple breakthroughs simultaneously – delivering orders of magnitude greater sensitivity compared to conventional photographic plates, enabling reliable digital photometry and facilitating the automation of detection processes. This combination of attributes dramatically increased the efficiency and completeness of SN searches, an advantage further amplified by the increasingly widespread availability and decreasing cost of CCD systems. The Berkeley Automated Supernova Search emerged as a pioneering implementation of this new approach (e.g., Kare et al., 1981, 1982; Perlmutter et al., 1989, 1992; Richmond et al., 1993), demonstrating capabilities that had been previously unattainable: systematic observations of faint targets, improved resolution of crowded fields, and digital image subtraction to isolate transient sources from their host galaxy backgrounds (e.g., Filippenko, 1992).

As Paczyński (2000) emphasised, digital image subtraction fundamentally transformed transient astronomy by enabling the detection of variable sources regardless of their location within complex backgrounds, greatly reducing biases against SNe in galaxy nuclei or

edge-on disk galaxies. The Katzman Automatic Imaging Telescope (KAIT; Filippenko et al., 2001) at Lick Observatory marked the beginning of truly systematic, fully automated monitoring with digital detectors. Complemented by the deployment of robotic follow-up telescopes, this technological ecosystem enabled rapid spectroscopic classification of unprecedented numbers of candidates. Though still primarily galaxy-targeted, the resulting Lick Observatory Supernova Search (LOSS) dramatically demonstrated the power of dedicated robotic facilities with real-time processing capabilities, increasing the annual SN discovery rate from approximately 1 to over 10 between 1998 and 2012.

The true revolution came with untargeted, all-sky surveys that systematically and homologously scanned large areas of sky at regular cadences. This approach further reduced selection biases and revealed SNe in previously undersampled environments, including dwarf galaxies, galaxy outskirts, and the intergalactic medium (Arcavi et al., 2010; Perets et al., 2010). The Sloan Digital Sky Survey (SDSS; York et al., 2000) Supernova Search and the Texas Supernova Search (Quimby, 2006) represented an early transition to this model (Frieman et al., 2007), followed by the pioneering ASAS-SN (Shappee et al., 2014). ASAS-SN kickstarted the era of all-sky surveys by observing the entire visible sky in V-band on a regular cadence (5 d) using a network of small telescopes, finding mostly bright transients, which enabled a plethora of follow-up from similar class and much bigger telescopes to gather an unprecedented amount of follow-up.

This success has sparked a new wave of all-sky dedicated transient surveys across multiple wavelengths and timescales. The PANoramic Survey Telescope and Rapid Response System (Pan-STARRS; Kaiser et al., 2002; Chambers et al., 2016) in Hawaii provided comprehensive mapping of the northern sky. The Asteroid Terrestrial-impact Last Alert System (ATLAS; Tonry et al., 2018) currently scans the entire visible sky every two nights to a depth of $\sim$19.5 mag, discovering hundreds of bright SNe annually. The Young Supernova Experiment (YSE; Jones et al., 2021) and Distance Less Than 40 Mpc (DLT40, see; Yang et al., 2017; Tartaglia et al., 2018, for details) leverages Pan-STARRS for high-cadence transient discovery while integrating with the Las Cumbres Observatory Global Telescope (LCOGT; Brown et al., 2013) network for automated follow-up. The CHilean Automatic Supernova sEarch (CHASE; Pignata et al., 2009; Hamuy et al., 2012), similar to the DLT40, targeted the southern hemisphere at high cadences.

Chief among these were the dedicated transient surveys, the Palomar Transient Factory (PTF; Law et al., 2009; Rau et al., 2009) and its successor, the Zwicky Transient Facility (ZTF; Bellm et al., 2019a,b; Graham et al., 2019; Masci et al., 2019; Dekany et al., 2020). Since 2018, ZTF has been observing the entire accessible northern night sky from Palomar on a $\sim$ 2 d cadence in g and r to a depth of $\sim$ 20.5 mag – both PTF and ZTF use the Palomar 48-inch (P48) Schmidt telescope, with ZTF utilising a 47 deg^2 field of view camera.

ZTF has fundamentally transformed the time-domain landscape by systematically discovering and monitoring over 10,000 transient events annually, increasing SN detection rates by several orders of magnitude compared to the $\lesssim$ 100 SNe discovered per year in years prior. Most importantly, the statistical power has facilitated considerable breakthroughs including: rigorous volumetric rate measurements across SN subtypes (e.g., Perley et al., 2020); identification of exotic transients like AT2018cow and AT2022tsd (prototypical FBOTs; Perley et al., 2019; Ofek et al., 2021; Ho et al., 2023a), new Type Icn SNe (e.g., Perley et al., 2022; Pellegrino et al., 2022), lensed SNe (e.g., Goobar et al., 2023) and Type Ien SNe (e.g., Schulze et al., 2024); systematic early-time observations capturing flash spectroscopy signatures in Type II SNe (e.g., Bruch et al., 2021, 2023; Irani et al., 2024; Zimmerman et al., 2024), and the largest systematic studies of Type Ia SNe (e.g., Ginolin et al., 2025; Rigault et al., 2025) and SLSNe (hydrogen-rich and -poor Kangas et al., 2022; Chen et al., 2023; Pessi et al., 2025).

Where ZTF excels is the dedicated follow-up surveys and resources to classify extragalactic transients, namely the BTS and the Spectral Energy Distribution Machine (SEDM; Blagorodnova et al., 2018; Rigault et al., 2019; Kim et al., 2022) on the Palomar 60-inch (P60) telescope. The BTS is a magnitude-limited survey aiming to spectroscopically classify all extragalactic transients detected by ZTF in the northern hemisphere, satisfying a few basic conditions: a peak apparent magnitude, m_{peak}, $\leq$18.5 mag, visibility from Palomar, and a location outside of the Galactic Plane. Combined with the SEDM, which automatically takes spectra and classifies SNe rapidly, the BTS has classified over 10,000 events in $\sim$ 7 years with a spectroscopic completeness of $\sim$ 93% down to 18.5 mag.

The modern transient discovery infrastructure functions as a sophisticated ecosystem with several integrated components. Survey facilities generate real-time alert packages – standardised data structures containing coordinates, magnitudes, historical light curves,

and host galaxy associations for detected transients (Masci et al., 2019; Bellm et al., 2019b). ZTF alone produces over 100,000 alerts nightly (Masci et al., 2019), while Rubin-LSST is projected to increase this output to approximately 10 million (Ivezić et al., 2019; Kessler et al., 2019; Hložek et al., 2023). These massive data streams are processed and distributed globally through specialised event brokers including ANTARES, Lasair, and ALeRCE (Narayan et al., 2018; Smith et al., 2019; Carrasco-Davis et al., 2021; Matheson et al., 2021; Möller et al., 2021). These brokers serve as intelligent middleware, implementing sophisticated machine learning algorithms to classify events, perform cross-matching with existing catalogues, and filter the enormous data volume into targeted subsets optimised for specific science objectives – effectively transforming an otherwise overwhelming flood of information into actionable discovery opportunities for both automated and human-guided follow-up campaigns.

Importantly, the previously unexplored or inaccessible regimes are beginning to be probed with all-sky surveys, which will again enlighten us by probing new transients and regimes of transients. The WIde-field Infrared Transient ExploreR (WINTER; Lourie et al., 2020) targets optically-faint, IR-bright transients, while the Argus Array ($<$ day cadence with depths $\sim$ 24 mag in g and r Law et al., 2022b; Law et al., 2022a) aims to provide unprecedented high-cadence observations at deep limiting magnitudes. New specialised facilities include BlackGEM (Bloemen et al., 2016; Groot et al., 2024), an array of wide-field optical telescopes in La Silla, Chile, originally designed for optical counterpart searches of gravitational wave sources but with significant capabilities for general transient science. Also focusing on the southern hemisphere, the La Silla Schmidt Southern Survey (LS4; Miller et al., 2025) employs the 0.5m ESO Schmidt telescope with a wide-field CCD camera to conduct deep, high-cadence observations optimised for transient detection.

Since LOSS, these robotic facilities have enabled robust measurements of volumetric SN rates across cosmic history. Estimates from LOSS, SDSS, ZTF (up to 2020) on the local measurements of CCSNe to approximately 1×10^{-4} yr^{-1} Mpc^{-3} in the nearby universe, with Type II SNe making up 53 – 60% of the CCSNe rate ($z \lesssim 1$; Li et al., 2011; Shivvers et al., 2017; Graur et al., 2017a,b; Perley et al., 2020).

The transition to untargeted surveys has been particularly crucial for these rate measurements, eliminating the systematic uncertainties associated with galaxy-targeted approaches. Galaxy-targeted surveys like LOSS required complex corrections for the galaxy luminosity function, inclination biases, and survey completeness, potentially introducing systematic errors of up to 40% (Leaman et al., 2011; Li et al., 2011). In contrast, untargeted wide-field surveys like ZTF sample the universe more uniformly, with selection functions that depend primarily on apparent magnitude and sky position rather than host galaxy properties (Perley et al., 2020).

1.8 Thesis Outline

Despite the tremendous strides we have taken in the last ∼century of observing the night sky, our understanding of massive stellar evolution remains surprisingly incomplete, e.g., how do progenitor mass, progenitor radius, mass-loss, binarity, metallicity and rotation map to the SN light curves? This motivates our continued vigilance of the cosmos through new observational windows and at previously inaccessible timescales, as we seek to quantitatively address several outstanding questions: How does SBO occur, and how does the circumstellar environment impact the subsequent explosion dynamics? What is the true mass distribution of Type II SN progenitors, and is the apparent dearth of high-mass progenitors observationally induced or physically motivated? Do "failed" SNe exist, or do all massive stars explode in ways that might be extraordinarily different from expectations (e.g., with sub-day timescales or off-axis jets)? What are the progenitors of more exotic CCSNe like Types Ibn/Icn/Ien?

These fundamental questions motivated this thesis, which specifically addresses how common "enhanced" mass-loss is in Type II SN progenitors. The primary contribution of my work is a new investigation into the circumstellar environments of Type II SN progenitors using the early light curves from the ZTF BTS – the highly complete, magnitude-limited survey that has provided the largest and, critically, most unbiased sample for demographic analysis. Chapter 2 describes my methodology for interpolating SN light curves to maximise the information retrieved from them, along with measuring a comprehensive set of empirical parameters that characterise their evolution. In Chapter 3, I present the largest and one of the most constraining studies to date of Type II SN light curves used to infer circumstellar properties and recent histories of mass-loss.

Chapter 4 extends my analysis to the late-time radioactive nickel tail of Type II SNe, deriving ^{56}Ni mass estimates from the BTS sample and examining their correlations with other SN properties. In Chapter 5, I detail the image subtraction photometry pipeline I have extensively developed, which has been used for numerous publications based on Liverpool Telescope data and the P60 telescope at Palomar Observatory. Finally, in Chapter 6, I present concluding remarks and outline future research directions that naturally progress from this work, particularly in the context of forthcoming all-sky surveys that will further revolutionise our understanding of stellar death.

Throughout the thesis, I correct for Galactic extinction using the NASA Extragalactic Database (NED) extinction tool (using the dust map from Schlafly & Finkbeiner 2011). I assume a cosmological model with $\Omega_M = 0.3$, $\Omega_\Lambda = 0.7$ and $h = 0.7$.

Chapter 2

Gaussian Process Regression in Astronomy

2.1 Setting the Stage

A fundamental aim of science is to construct models grounded in rigorously tested physical theories, capable of describing observed phenomena and predicting future observations with quantifiable uncertainty. In time-domain astronomy, this pursuit often begins with parametric or phenomenological models – mathematically simple, computationally efficient tools that approximate observations but lack direct physical interpretation. While these models are invaluable for rapid analysis, their empirical nature limits their ability to uncover the underlying physics governing transient events or to generalise beyond the data they are fit to.

Hydrodynamic simulations offer a powerful alternative. By integrating complex physics – such as radiative transfer, neutrino interactions, and multidimensional progenitor structures – these simulations can predict the photometric and spectroscopic evolution of astrophysical transients like CCSNe. However, their computational cost is staggering: simulations often require days to months of runtime and demand expertise to fine-tune parameters for individual objects. Even state-of-the-art suites of analytical (e.g., Bazin et al., 2009; Pejcha & Prieto, 2015a; Villar et al., 2019) and hydrodynamical models (e.g., Hillier & Miller, 1998; Hillier & Lanz, 2001; Morozova et al., 2015; Das & Ray, 2017; Morozova et al., 2018; Vogl et al., 2020; Moriya et al., 2023) struggle to balance

physical fidelity with scalability, particularly given the extreme diversity of CCSN light curves. These observations arise from nonlinear interactions between powering mechanisms (e.g., radioactive decay, CSM interaction) and progenitor properties (e.g., $M_{\rm ZAMS}$, Z), making them resistant to simplistic parameterisations.

In the context of this thesis, Gaussian Process regression (GPR; Press, 1997; Seeger, 2004; Rasmussen, 2004) provides a crucial methodological bridge between these approaches. By extracting consistent, empirical properties from both observational data and simulated light curves, GPR creates a common parameterisation framework that enables direct mapping between them, without the staggering computational cost involved in detailed modelling. This approach offers three key advantages: 1) it provides a computationally efficient method for characterising light curve morphology without imposing rigid functional forms, 2) it creates a standardised feature space where both observations and simulations can be directly compared with minimal assumptions, and 3) it enables the creation of surrogate models that link observed properties to physical parameters with robust uncertainty quantification. Rather than attempting to directly fit hydrodynamic simulations to each individual transient – a computationally prohibitive task – GPR allows one to establish a statistical mapping between the empirical properties of observed light curves and the underlying physical parameters that produce them in simulations, effectively translating between observational and theoretical domains while maintaining physical interpretability.

Thus, I utilise GPR – a flexible, non-parametric framework that combines the scalability of empirical models with the statistical rigour needed to infer physical properties. Unlike parametric models, GPR does not assume a predefined functional form, instead allowing the data itself to guide the structure of the model through probabilistic correlations. This makes it uniquely suited to capture the complexity of astrophysical transients while quantifying predictive uncertainties – a critical advantage over both ad hoc fitting and computationally expensive hydrodynamic codes.

Originally developed in geostatistics, GPR gained prominence in astronomy in the 1990s (Press et al., 1992) and has since revolutionised tasks ranging from time-series analysis (see for a review Aigrain & Foreman-Mackey, 2023) to interstellar dust mapping (e.g., Miller et al., 2022), stellar surface reconstruction (e.g., Luger et al., 2021) in addition to machine-learning (ML) photometric classification of transients (e.g., Lochner et al.,

2016; Boone, 2019; Villar et al., 2020; Qu et al., 2021). This chapter positions GPR as a transformative tool for the field, demonstrating its capacity to model CCSN light curves, infer progenitor characteristics, and guide targeted hydrodynamic simulations.

2.2 Gaussian Processes

Rooted in ML and Bayesian statistics, GPR is a versatile, data-driven method for interpolating, modelling, and predicting datasets of varying complexity (e.g., Rasmussen, 2004; Aigrain & Foreman-Mackey, 2023). A Gaussian process (GP) is a stochastic process defined by a prior over functions, generating a probability distribution over all possible functions that fit a given dataset. This non-parametric approach excels at handling heteroscedastic (non-uniform) uncertainties and is particularly advantageous when the underlying function is unknown or data are sparse and noisy (e.g., McLaughlin et al., 2024). In astronomy, these challenges are ubiquitous: time-series data often exhibit correlated noise, faint signals embedded in stochastic variability, and highly non-uniform and irregular sampling functions (caused by weather, visibility constraints etc.) necessitating methods that rigorously account for observational uncertainties (e.g., Foreman-Mackey et al., 2017; Angus et al., 2019; Gordon et al., 2020). GPR provides consistent interpolation without imposing rigid functional forms that could bias physical interpretation, providing meaningful uncertainty propagation.

By extending probability distributions to infinite-dimensional function spaces, GPR provides a natural framework for modelling such systems (e.g., Bailer-Jones, 2012; van der Wilk et al., 2020). Its key strengths include: statistically principled error estimates for predictions; adaptability to complex, nonlinear relationships without predefined functional forms; efficient handling of large datasets via optimised kernel implementations; seamless application to unevenly spaced time-domain data; and a logical basis for comparing models or inferring parameters. They offer quantifiable answers to questions like: Which model best describes the data? What values of the parameters of this model best explain the data?

GPs quantify similarities between data points through a covariance kernel, which encodes assumptions about the system's behaviour. For an unknown function, $f(\mathbf{x})$, observed with noise, ϵ_i, at inputs $\mathbf{x} = \{x_i\}$, the GP is defined as:

$$p(\mathbf{y} \mid \mathbf{x}) = \mathcal{N}\left(\mu(\mathbf{x}),\, \mathbf{K} + \sigma_n^2\right) \tag{2.1}$$

where $\mu(\mathbf{x})$ is the mean function (often assumed zero for simplicity), $\mathbf{K}$ is the covariance matrix constructed from a kernel function $k(x, x')$, and σ_n^2 represents observational noise variance (e.g., Rasmussen, 2004; Seeger, 2004).

The kernel dictates the structure of the GP and is the implementation of our physical understanding of the complex system, encoding specific behaviours such as periodicity or controlling how smooth or the variability one expects the unknown function is expected to be. Common kernels, such as,

- Constant Kernel:

$$k(x, x') = \alpha^2 \tag{2.2}$$

- Exponential Kernel:

$$k(x, x') = \alpha^2 \exp\left(-\frac{\tau}{\ell}\right) \tag{2.3}$$

- Squared Exponential Kernel:

$$k(x, x') = \alpha^2 \exp\left(-\frac{\tau^2}{2\ell^2}\right) \tag{2.4}$$

- Matérn-3/2 Kernel:

$$k(x, x') = \alpha^2 \left(1 + \sqrt{3}\frac{\tau}{\ell}\right) \exp\left(-\sqrt{3}\frac{\tau}{\ell}\right) \tag{2.5}$$

- Matérn-5/2 Kernel:

$$k(x, x') = \alpha^2 \left(1 + \sqrt{5}\frac{\tau}{\ell} + \frac{5}{3}\left(\frac{\tau}{\ell}\right)^2\right) \exp\left(-\sqrt{5}\frac{\tau}{\ell}\right) \tag{2.6}$$

- Rational Quadratic Kernel:

$$k(x, x') = \left(1 + \frac{\tau^2}{2\gamma\ell^2}\right)^{-\gamma} \tag{2.7}$$

Kernels introduce hyper-parameters α (signal amplitude), ℓ (characteristic length scale), which control the variability and smoothness of functions drawn from the GP (e.g., Seikel et al., 2012) and τ, the Euclidean distance between x_i and x_j such that $\tau = |x_i - x_j|$. In time-series applications, ℓ corresponds to the timescale of variations, while α scales the amplitude of fluctuations. Crucially, hyper-parameters are inferred from data via marginal likelihood optimisation or Bayesian sampling, distinguishing them from fixed model parameters – they do not specify the form of a function, instead characterising the "bumpiness" of the function and reproducing any repeated behaviour (e.g., Seikel et al., 2012). Moreover, while the kernel choice is critical for capturing the data's underlying structure, GPs are inherently probabilistic: the same kernel can generate diverse functions that fit the data, reflecting uncertainty in regions with sparse observations (e.g., Angus et al., 2019; McLaughlin et al., 2024).

For astronomical time series, GPR's ability to disentangle signal from correlated noise – while quantifying uncertainties – makes it indispensable for tasks like light-curve interpolation, periodicity detection, and progenitor property inference.

2.3 GP Regression and Optimisation

As the GP treats each reconstructed value $f(x_i)$ as a Gaussian random variable, correlations between neighbouring points are governed by a covariance function. This probabilistic framework inherently marginalises over systematic noise sources, embedding observational uncertainties directly into the posterior distribution (e.g., Rasmussen, 2004; Seeger, 2004). Thus, the starting point of regression is to define a prior GP that closely expresses our beliefs about the unknown $f(\mathbf{x})$ (e.g., Braun et al., 2024). Training GPs involves optimising the kernel and mean function hyper-parameters by maximising the log-marginal likelihood of the observed data, balancing fit quality against model complexity (e.g., Foreman-Mackey et al., 2017; Braun et al., 2024). Once optimised, the

joint Gaussian distribution is conditioned on the training data to compute the predictive posterior, enabling robust inference at unobserved input points while quantifying uncertainties.

The general procedure for GPR is as follows:

1. **Kernel Selection**: Choose a covariance function to model correlations in the data.
2. **Mean Function Specification**: Define a baseline trend.
3. **Parameter Optimisation**: Use gradient-based methods (e.g., L-BFGS-B) to maximise the log-likelihood, providing initial estimates for Bayesian sampling.
4. **Uncertainty Quantification**: Employ Markov chain Monte Carlo (MCMC) to sample the posterior distribution of hyper-parameters, enabling robust error estimation and hypothesis testing.

This methodology, specifically #4, allows hypothesis testing by creating distributions over parameters and allowing one to analyse how likely a given model is. Training GPs with MCMC is optimal but comes at the cost of computational time and resources. For the purposes of this thesis, I use the GP package `george` (Foreman-Mackey, 2015) with the `scipy.optimize minimize` function which optimises an objective function. Often, this is the marginalised log-likelihood which is readily implemented in most GP modules, along with a function to calculate the gradient with respect to mean function model parameters and hyper-parameters (e.g., Rasmussen, 2004).

2.4 More Kernels

Kernels parameterised by the Euclidean distance $\tau = |x_i - x_j|$ between two points are termed 'stationary kernels', where a single length scale governs the entire GP. These are effective when the variability scale is uniform across the dataset. However, astronomical phenomena often exhibit non-stationary behaviour – rapid fluctuations (e.g., SBO) followed by prolonged quiescence (e.g., radioactive decay phases). Stationary kernels therefore struggle to fully encapsulate such order of magnitude variations, as they enforce identical covariance for point pairs with matching τ, regardless of location in input

space (e.g., Noack & Sethian, 2021). Thus, two points in one corner of the input space will have the same covariance as two other points in the other corner so long as the distances (τ) are the same (e.g., Noack & Sethian, 2021; Noack et al., 2024). This rigidity can oversmooth rapidly varying regions or overfit smoother regions. While mixtures like the Rational Quadratic kernel approximate multiple length scales (e.g., Aigrain & Foreman-Mackey, 2023), 'non-stationary kernels' explicitly accommodate spatially varying correlations.

Non-stationary kernels (e.g., Paciorek & Schervish, 2003; Rasmussen, 2004; Heinonen et al., 2015), specified by $\mathbf{K} = k(x, x') \neq k(|x - x'|)$, capture varying length scale through either additive kernels (Eq. 2.8), multiplicative kernels (Eq. 2.9) or allowing the length scale to vary in their function form (Eq. 2.10; Gibbs, 1998).

- Additive Kernels:

$$k(x, x') = k_1 + k_2 + ... \tag{2.8}$$

- Multiplicative Kernels:

$$k(x, x') = k_1 \times k_2 \times .... \tag{2.9}$$

- Gibbs Kernel:

$$k(x, x'; l) = \sqrt{\left(\frac{2\ell(x)\ell(x')}{\ell(x)^2 + \ell(x')^2}\right)} \quad \exp\left(-\frac{(x - x')^2}{\ell(x)^2 + \ell(x')^2}\right) \tag{2.10}$$

  where $\ell(x)$ is a function that Dynamically adapts across the domain (see Gibbs, 1998).

- Changepoint Kernel:

$$k(x, x'; c, \sigma) = k_1(x, x') \cdot \sigma(x, c) \cdot \sigma(x', c) + k_2(x, x') \cdot (1 - \sigma(x, c)) \cdot (1 - \sigma(x', c)) \tag{2.11}$$

  where c is the Changepoint location, $\sigma(x, c)$ is a sigmoid function; $\sigma(x, c) = \frac{1}{1+\exp(-(x-c)/\omega)}$ transitioning smoothly from 0 – 1; ω controls the smoothness of

the transition; and k_1 and k_2 are the kernels that apply before and after the Changepoint with length scales ℓ_1 and ℓ_2, respectively.

A more general form for multiple Changepoints at locations $\{c_1, c_2, ..., c_n\}$ can be written as:

$$k(x, x') = \sum_{i=0}^{n} k_i(x, x') \cdot p_i(x) \cdot p_i(x') \tag{2.12}$$

where $p_i(x)$ are weight functions that determine the contribution of each kernel at point x.

Non-stationary kernels are more complex both functionally and to implement in software typically used, so the application of these in astronomy is limited. Aside from this, non-stationary GPs have been shown to provide significant advantages over their stationary counterparts (see for a review Noack et al., 2024).

As shown in Fig. 2.1 (see Noack & Sethian, 2021), non-stationary kernels outperform stationary counterparts by adapting ℓ to these regimes, avoiding under/overfitting. While implementation complexity has limited their use in astronomy, recent advances in scalable GP libraries (e.g., Noack et al., 2024) are bridging this gap.

In astronomy, one can naturally connect the changing length scale to different regimes in SN light curves, for example: small length scales around explosion and SBO as microphysics dominates, with rapid changes on sub-second to hour time scales sees orders of magnitude change in flux; compared to a more moderate length scale around-immediately post peak and along the plateau where there is very little (comparatively no variation) on the scale of minutes, hours or days; and finally another, a much longer length scale during the radioactive decay which is set by the half life of the radioactive nuclei. In this, there are certainly advantages provided in using the additional flexibility provided by changing length scales, given that the kernel is a function not only of the Euclidean distance but also the location.

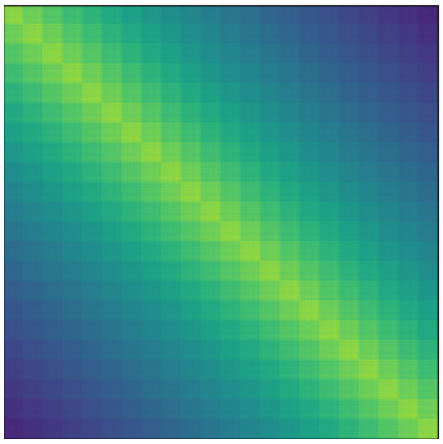

Figure 2.1.1

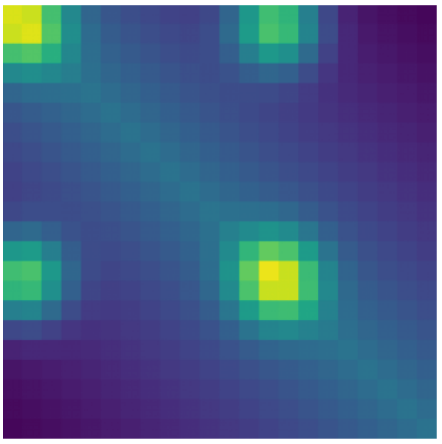

Figure 2.1.2

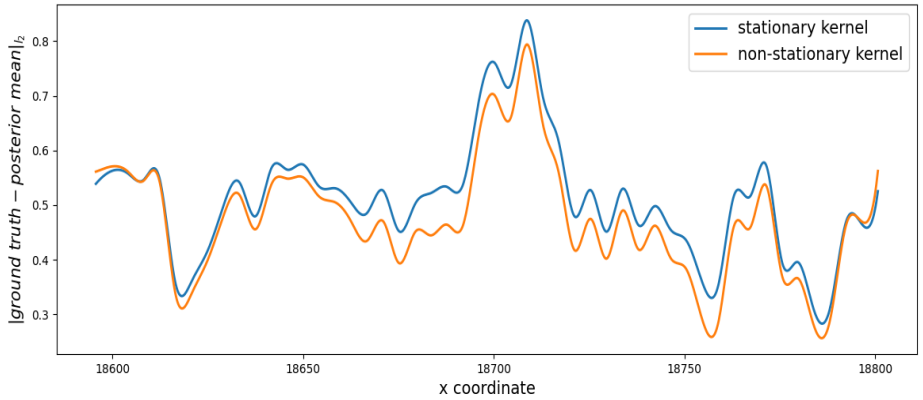

Figure 2.1.3

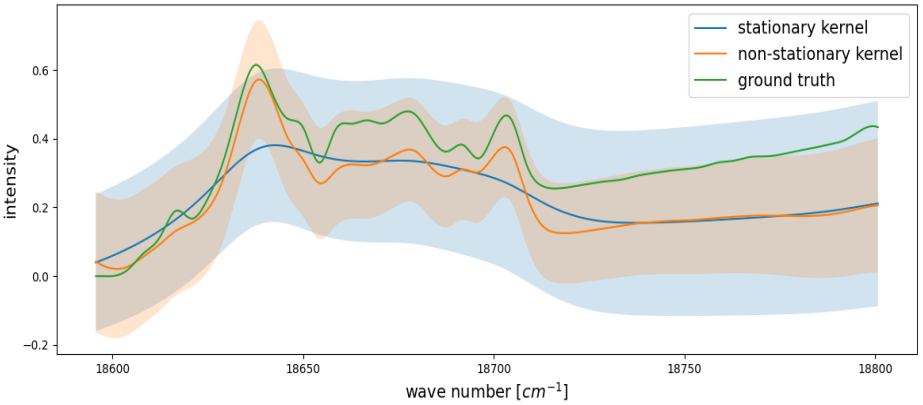

Figure 2.1.4

FIGURE 2.1: GPR applied to IR spectroscopy data using stationary and non-stationary kernels. *Top:* Covariance matrices for stationary (*left*) and non-stationary (*right*) kernels. The stationary kernel produces a diagonal pattern, reflecting its inability to distinguish similarities between spectral features (tasks) at constant distances. The non-stationary kernel adapts to local variations, capturing complex correlations. Non-stationary GP outperforms its stationary counterpart, with lower mean Euclidean distance to the ground truth (*middle*) and posterior predictions aligning closely with the true spectrum (green), exhibiting smaller uncertainties and finer detail (*lower*). Adapted from Noack & Sethian (2021).

2.5 Multioutput Gaussian Process

Multioutput Gaussian processes (MOGPs) extend traditional GPs to model correlated outputs across multiple dimensions, enabling shared information between related tasks (e.g., Álvarez et al., 2012; Roberts et al., 2012). In astronomy, this is particularly powerful for analysing time-domain multi-band observations, where fluxes (F_i) and uncertainties (σ_i) across filters are inherently correlated due to their wavelength-dependent transmission curves and SEDs. By incorporating both time (t) and wavelength (λ) as input dimensions, MOGPs leverage these correlations to interpolate and predict fluxes across bands, even in sparsely sampled datasets. The GP framework becomes:

$$p(y \mid t, \lambda) = \mathcal{N}\left(\mu(t, \lambda), \mathbf{K}\right) \tag{2.13}$$

where $\mathbf{K}$ encodes covariances across time and wavelength (Appendix F, Ni et al., 2025).

With this, I am leveraging the difference in spectral dependences of the source emission compared to the correlated variability. This method has increased in popularity (e.g., Gibson et al., 2012; Lochner et al., 2016; Boone, 2019; Villar et al., 2019, 2020, 2021; Gordon et al., 2020; Kornilov et al., 2023). In essence, this is the GP producing a model of the spectrum convolved with a broad filter rather than modelling the spectrum as I assume a constant colour evolution with time (e.g., Boone, 2019) – if the kernel is stationary. During the regression, the kernels are optimised and can be used to predict at any wavelength, including the rest-frame, producing a SED (e.g., Boone, 2019; Hiramatsu et al., 2024; Thornton et al., 2024).

In this work, I use this methodology to take cross-band information into account, modelling both in time and wavelength across all bands simultaneously. Data is modelled in the observer frame using effective wavelengths (λ_{eff}) from filter transmission profiles (e.g., Tokunaga & Vacca, 2005; Rodrigo & Solano, 2020). While λ_{eff} simplifies computation by collapsing each filter's response to a single value, it assumes a smooth SED, potentially overlooking narrow spectral features. Rest-frame parameters (e.g., luminosities) are derived by predicting at $\lambda_{\text{eff}} \times (1 + z)$, balancing fidelity with computational

feasibility. This also establishes a baseline with which to compare physical parameters across a heterogeneous sample while preserving the original photometric information.

The use of λ_{eff} represents a practical simplification whereby each filter's complex transmission function is reduced to a single value, characterising the overall response of the filter when convolved with a source spectrum (e.g., Tokunaga & Vacca, 2005). λ_{eff} is defined as a weighted average of the wavelength across the filter's transmission profile, where the weighting factor is the energy distribution of the source over the band – a product of the filter transmission function and the source spectrum (see Tokunaga & Vacca, 2005). This reduces computational cost and model dimensionality at the tradeoff of colour corrections if this was not corrected for in the photometry processing. In this, the shape of the SED is assumed to be smooth, thus, I am ignorant of any sharp emission features that are present (e.g., Boone, 2019). The smoothness assumption becomes particularly important in multi-wavelength studies of transients, where one attempts to reconstruct the full SED from discrete filter measurements. This allows the GP model to reasonably interpolate between the observed filter bands. In the regime where the emission is dominated by narrow features instead of the smoothly varying continuum, a consequence is that valuable information about the emission features is lost as well as colour terms arising from interactions between filter transmission functions and the shape of the source spectra, which may change and move λ_{eff}.

Fits are conducted in flux space rather than magnitude space to preserve statistical rigour, maintain symmetric error distributions, and accommodate negative or near-zero flux values. The standard transformation from flux (f) to magnitude (m), defined as $m = m_0 - 2.5 \log_{10}(f)$, inherently distorts the noise properties of the data. If the flux measurements are initially governed by Gaussian noise, this logarithmic transformation skews the resulting magnitude uncertainties into a non-Gaussian, asymmetric distribution. This skewness disproportionately affects faint sources, where low signal-to-noise ratios (SNR) amplify the asymmetry, biasing uncertainties toward fainter magnitudes. GPs assume Gaussian noise in their likelihood models, making flux space a natural choice to align with this foundational assumption.

Furthermore, flux space avoids numerical instabilities arising near zero or negative flux values. The logarithmic transformation diverges to infinity as $f \to 0$ and is undefined for $f \leq 0$, complicating optimisation and uncertainty quantification. By contrast, flux space

retains numerical stability across all physically plausible values, including non-detections or negative fluxes caused by background subtraction. While magnitudes remain a useful observational convention, they can be derived post-hoc from the GP's flux-space predictions without compromising the model's statistical integrity or computational robustness.

On the other hand, it is impossible for a flux to be negative in reality, so logarithmic transforms or equivalent approaches still offer certain advantages – they naturally constrain the model to physically possible values, avoiding unphysical negative predictions that can occasionally arise in flux-space models, particularly in regions with sparse data, high uncertainty or measurements at the noise limit.

2.6 Mean Functions

The mean function in GRP serves as a critical prior assumption, encoding domain-specific knowledge about the expected behaviour of the underlying system, similar to the kernel. While the kernel governs the covariance structure (e.g., smoothness, periodicity), the mean function establishes a baseline trend around which the GP infers deviations. By default, the mean is often set to zero – a choice for problems lacking strong prior expectations. However, this is not a strict requirement; the mean function can (and should) be tailored to reflect physical intuition, empirical patterns, or known system dynamics.

Including a well-justified mean function helps mitigate "ballooning" uncertainties in sparsely sampled regions. Without such guidance, the GP's posterior predictions diverge freely in data gaps, as the infinite set of possible functions consistent with the data leads to rapidly inflating variances. A physically motivated mean function anchors predictions, reducing this divergence by steering the GP toward plausible solutions.

However, overly rigid mean functions risk introducing bias. A constant mean, for instance, forces the GP to oscillate back to this value between data points, creating artificial undulations. Similarly, a linear mean imposed on nonlinear phenomena (e.g., stellar rotation cycles) may distort inferred correlations. To balance flexibility and constraint,

mean function parameters are typically marginalised over during hyper-parameter optimisation, allowing the data to refine their values while preserving physical interpretability.

In this work, I have experimented with the mean functions seen below:

- Zero/Constant Mean:

$$m\left(\mathbf{t}, \lambda_{\text{eff}}\right) = c \tag{2.14}$$

- Polynomial Mean[1]:

$$m\left(\mathbf{t}, \lambda_{\text{eff}}\right) = mt + b + \alpha \exp\left(\frac{(t-l)^2}{2\sigma^2}\right) \tag{2.15}$$

  where m controls a linear slope, b is the intercept, α controls the height of the Gaussian centred on l with width σ – this is a highly flexible and prominently peaked model used mainly for unconstrained behaviour.

- Bazin Model (Bazin et al., 2009, 2011):

$$m\left(\mathbf{t}, \lambda_{\text{eff}}\right) = A\frac{\exp\left(-(t-t_0)/\tau_{\text{fall}}\right)}{1+\exp\left(-(t-t_0)/\tau_{\text{rise}}\right)} + c \tag{2.16}$$

  where A is the amplitude (in flux space), t_0 is interpreted as the peak (inflection point) of the light curve, τ_{rise} and τ_{fall} control how quickly the light curves rises and falls, respectively, and c corresponds to the baseline which accounts for background contributions.

- Supernova Parametric Model (SPM; Villar et al., 2019; Sánchez-Sáez et al., 2021)

$$\begin{aligned} m\left(\mathbf{t}, \lambda_{\text{eff}}\right) = \frac{A\left(1-\beta\frac{t-t_0}{t_1-t_0}\right)}{1+\exp\left(-\frac{t-t_0}{\tau_{\text{rise}}}\right)} \cdot \left[1-\sigma\left(\frac{t-t_1}{\omega}\right)\right] \\ + \frac{A\left(1-\beta\right)\exp\left(-\frac{t-t_1}{\tau_{\text{fall}}}\right)}{1+\exp\left(-\frac{t-t_0}{\tau_{\text{rise}}}\right)}\left[\sigma\left(\frac{t-t_1}{\omega}\right)\right] \end{aligned} \tag{2.17}$$

  where A is the amplitude, t_0 is interpreted as the "start time" (thought not necessarily the explosion time), τ_{rise}, t_1, and τ_{fall} control the rise, plateau onset, and fade

[1] See https://george.readthedocs.io/en/latest/tutorials/model/

time of the light curve, respectively, and β controls the plateau slope. Like Villar et al. (2019) and Sánchez-Sáez et al. (2021), I re-parameterise t_1 to be $\gamma = t_1 - t_0$ to represent the plateau duration. The original SPM from Villar et al. (2019) employed a piecewise formulation with abrupt transitions at t_1, leading to sharp discontinuities. Similar to Sánchez-Sáez et al. (2021), I replace sharp boundaries with a sigmoid-weighted transition. The sigmoid function, $\sigma(t) = \frac{1}{1+\exp^{-t/\omega}}$, allows a smooth transition between 1 and 0 based on a window size ω.

Each choice carries trade-offs. While physical models enhance interpretability, misspecification can degrade performance. Conversely, data-driven means improve fit quality but may obscure underlying mechanisms.

2.7 GPR Performance

For model comparison and selection, I compute the Akaike Information Criterion (AIC; Akaike, 1974) and Bayesian Information Criterion (BIC; Schwarz, 1978) to assess the trade-off between model complexity and goodness of fit, penalising additional parameters to avoid overfitting (see Ni et al., 2025, for GP examples in astrophysics). The AIC emphasises predictive accuracy by penalising complexity (k) while rewarding better likelihood ($\mathcal{L}$), whereas the BIC strongly favours simpler models in large datasets (n) by scaling its penalty with $\ln(n)$. While both metrics aim to balance explanatory power and simplicity, the AIC prioritises minimising information loss relative to an idealised "true" model, while the BIC asymptotically selects the model closest to the data-generating process if it exists among candidates (Burnham & Anderson, 2004).

In astronomy, where datasets are often vast and physically motivated models are preferred, the BIC's emphasis on simplicity and asymptotic consistency – its tendency to converge to the "true" model as $n \to \infty$ – makes it particularly suited for identifying models that align with theoretical expectations while avoiding unnecessary complexity (Liddle, 2007).

$$\text{AIC} = 2k - 2\ln(\mathcal{L}) \tag{2.18}$$

$$\text{BIC} = k\ln(n) - 2\ln(\mathcal{L}) \tag{2.19}$$

The likelihood, $\mathcal{L}$, is readily computed in GP modules, offering a straightforward avenue for this type of model comparison.

As emphasised by Stevance & Lee (2023), systematic kernel comparison is critical in GP applications. Stochastic variations in optimisation (e.g., local likelihood maxima) and differences in software implementations (e.g., gradient calculations, hyper-parameter initialisation) can significantly alter performance. This analysis underscores the need to test multiple kernels to identify optimal choices – a practice essential for ensuring reproducibility and physical interpretability in transient light curve modelling.

Fig. 2.2 shows the relative performance of each kernel to a Type II SN, using no mean function. The Squared Exponential, Matérn 5/2 and Rational Quadratic kernels provide some of the best fits (lowest BIC and AIC values), which can be attributed to flexible functional forms.

The inclusion of a mean function (e.g., not 0 or <Flux>) significantly constrains GP fits by providing an informed baseline for the model to revert to in data-sparse regions. As demonstrated in Fig. 2.2, models leveraging domain-specific mean functions (e.g., Eqs. 2.16 and 2.17) – outperform simpler alternatives (e.g., constant or polynomial means). These models particularly excel in coverage gaps because their functional forms encode prior knowledge about astrophysical processes, such as radioactive decay or SC. By anchoring predictions to physically plausible trajectories, they partially mitigate the "ballooning" uncertainties typical of purely data-driven GPs while retaining flexibility to model deviations from the mean.

The performance of stationary GPs in modelling multi-phase astronomical transients is inherently limited by their assumption of a single characteristic ℓ across the entire dataset. As demonstrated in Fig. 2.2, stationary kernels struggle to do an adequate job at representing the dataset but struggle to adapt to the distinct regimes of Type II SNe (e.g., rapid rise, plateau, radioactive decay), particularly in sparsely sampled phases. While mean functions (e.g., Eq. 2.17) partially mitigate over-smoothing by anchoring

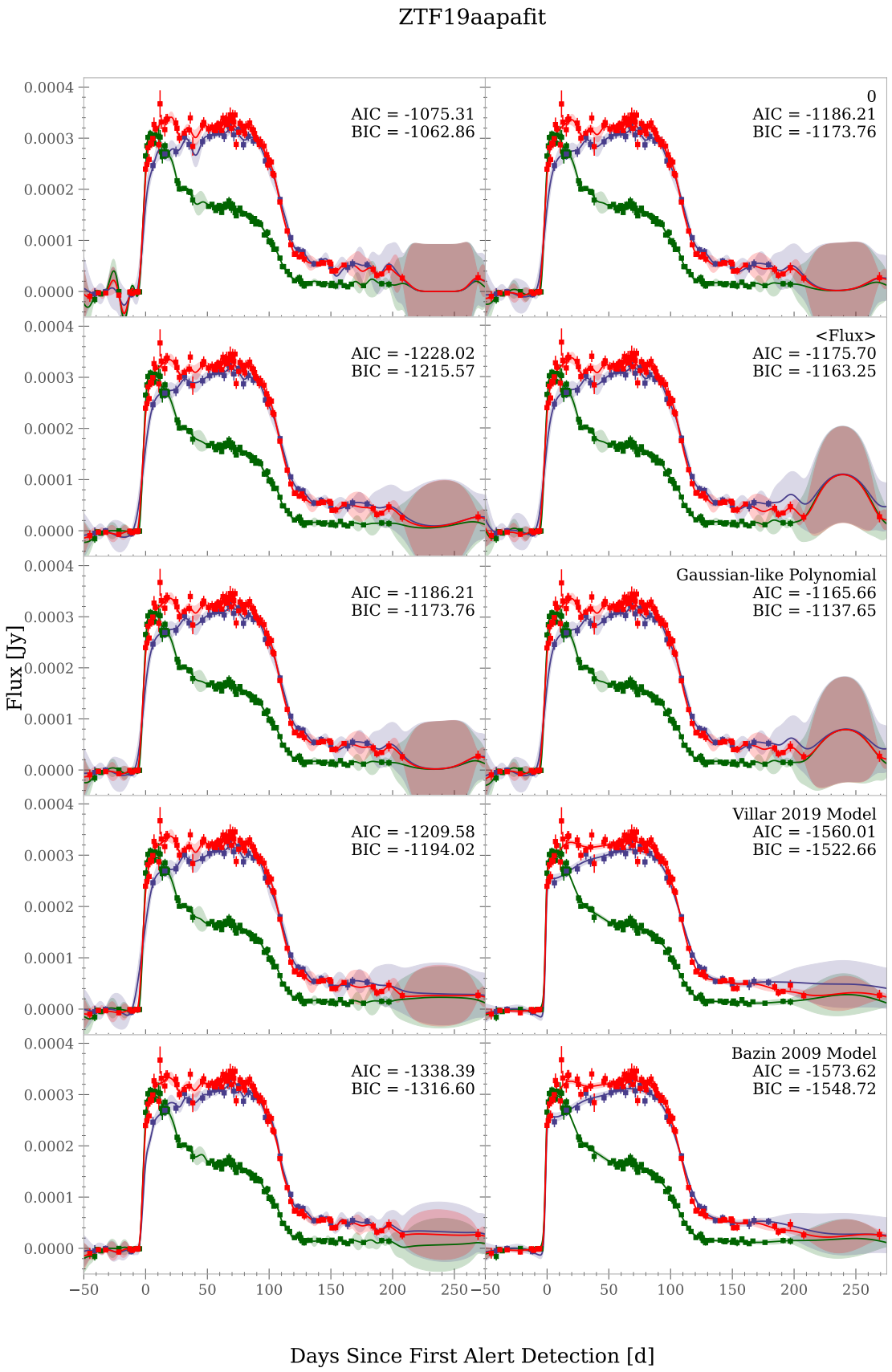

FIGURE 2.2: Performance of MOGP regression models with different kernels for the Type II SN ZTF19aapafit ZTF g (*green*), r (*red*) and i (*blue*) forced photometry light curves. From *top left* to *bottom left*: Squared Exponential, Matérn 3/2, Matérn 5/2, Rational Quadratic, and Rational Quadratic × Squared Exponential. From *top right* to *bottom right*: 0, mean flux (<Flux>), Gaussian-like polynomial (Eq. 2.15), SPM (Eq. 2.17; Villar et al., 2019), and Bazin et al. (2009) model (Eq. 2.16) – using a Matérn 5/2 kernel. Performances are based on AIC/BIC scores, with the best representing kernels/models achieving the lowest AIC and BIC scores.

predictions to physically motivated trends, they fail to resolve unphysical oscillations in data gaps (e.g., late-time undulations), where the GP reverts to its prior due to insufficient constraints.

To address these limitations, I use a non-stationary Changepoint kernel (Fig. 2.3) using `gpflow`, partitioning the light curve into four regimes, each governed by physics-informed covariance functions:

1. Pre-explosion phase: A constant kernel models quiescent progenitor behaviour, enforcing $\sim$zero flux variability prior to the explosion epoch (t_0).
2. Rise to peak: A Matérn 3/2 kernel ($\ell_{\rm rise}$) captures short-time SC emission, accommodating rapid, small-scale fluctuations.
3. Post-peak decline: A second Matérn 3/2 kernel ($\ell_{\rm peak-decline}$) tracks the smooth hydrogen-recombination-driven plateau phase.
4. Radioactive tail: A linear kernel ($\ell_{\rm tail}$) encodes the predictable ^{56}Ni $\rightarrow$ ^{56}Co$\rightarrow$ ^{56}Fe decay slope, with $\ell_{\rm tail}$.

This architecture attempts to eliminate artificial undulations while preserving phase-dependent stochasticity. Visually, the model from the Changepoint kernel (Fig. 2.3) is much smoother from the peak-on compared to the models shown with stationary kernels (Fig. 2.2). Quantitatively, the AIC and BIC from this are more positive, indicating less well-fitting models compared to the stationary counterparts. Though this is penalised by the increased complexity (e.g., more hyper-parameters).

In addition to more complicated kernels or forms of kernels, data transformations are possible to try and become more numerically stable. Linear transformations along the time dimension, such as normalisation (subtracting the mean and dividing by the standard deviation such that $t' = [t - \mu]/\sigma$), help standardise the input domain, allowing the GP kernel to operate on a more uniform scale. Logarithmic transformations, on the other hand, compress the dynamic range of the data, making the GP more sensitive to relative rather than absolute changes in the input space. This is particularly useful for astronomical transients, where key features (e.g., rise and fall times) may span orders of magnitude in time. By transforming the data appropriately, the GP's length scales remain physically meaningful across the entire parameter space. These transformations

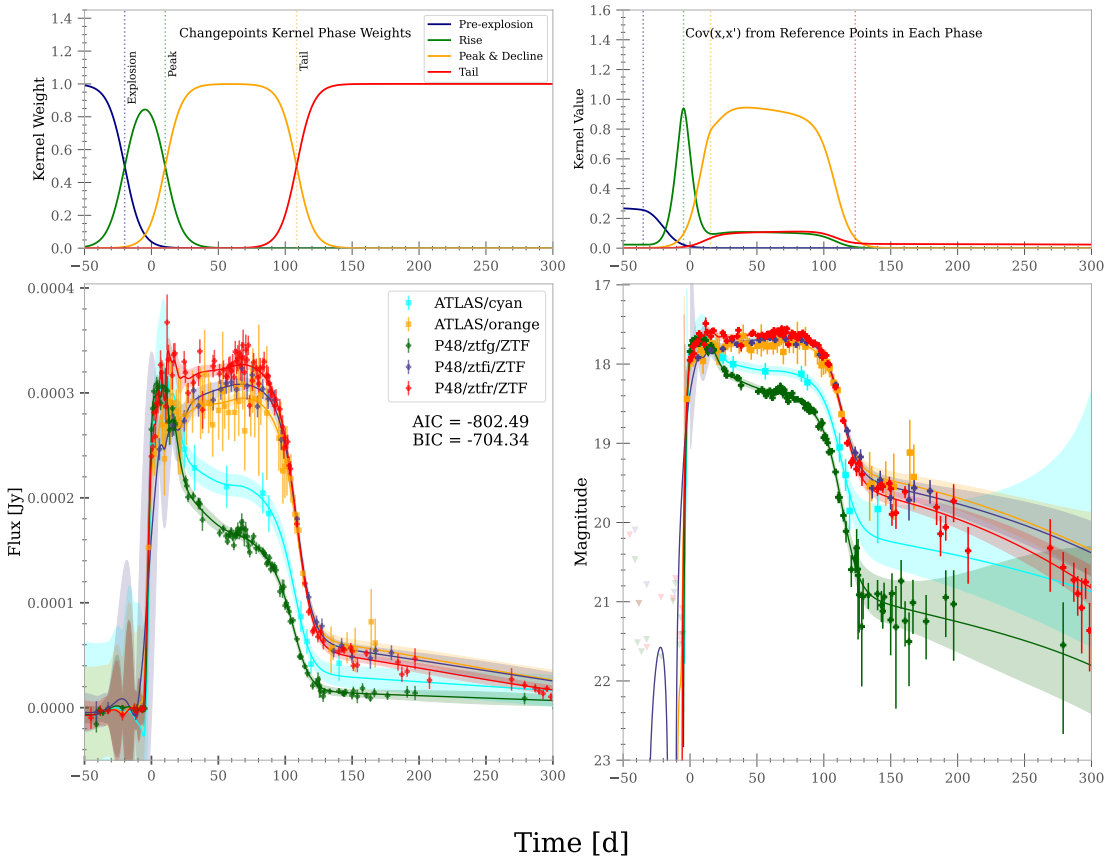

FIGURE 2.3: MOGP modelling of the Type II SNe ZTF19aapafit using a non-stationary Changepoint kernel. *Top left*: Weighting functions for each sub-kernel, illustrating the transition between distinct physical regimes (pre-explosion, rise, post-peak and radioactive tail). *Top right*: Evolving covariance contributions of individual kernels (Linear, Matérn 3/2 for rise/decline and linear for tail phase) as a function of time. *Bottom left*: Light curve fit in flux space, with shaded 1 σ uncertainties. *Bottom right*: Light curve in magnitude space. ZTF *gri* data is forced photometry from the BTS and ATLAS *co* are from the ATLAS forced photometry service, included to demonstrate ease of handling various data streams.

effectively decouple the intrinsic variability of the astrophysical source from the functional form of the kernel, allowing the GP to capture the underlying physical processes more accurately – see Fig. 2.4. The logarithmic x-axis transformations appear to produce the lowest BIC and AIC values, suggesting that this transformation is optimal compared to no transformations or normalisation.

Beyond optimising kernel selection and complexity, data transformations offer powerful approaches for enhancing GP model stability and interpretability. Linear transformations along the input domain, such as normalisation (subtracting the mean and dividing by the standard deviation), standardise the scale of independent variables, enabling GP

kernels to operate on a uniform numerical range. This standardisation prevents length-scale parameters from being dominated by the inherent scaling of input dimensions and improves numerical stability during hyper-parameter optimisation. Logarithmic transformations, conversely, fundamentally alter the representation of the data by compressing the dynamic range, making the GP more sensitive to proportional rather than absolute changes across the input space. This property can prove particularly valuable for modelling astronomical transients, where critical temporal features – such as rise times, decay rates, and transition points – frequently span multiple orders of magnitude. By implementing logarithmic transformations on the time domain, the GP's length-scale hyper-parameters maintain consistent physical significance throughout the entire evolution of the transient, from the rapid early phases to the extended late-time decline.

These transformations effectively decouple the intrinsic variability patterns of astrophysical sources from the specific functional form of the selected kernel, allowing the GP to capture underlying physical processes with greater fidelity (see Fig. 2.4). AIC and BIC for these transformations, particularly the transformation to log-space along the time dimension, substantiate this advantage, demonstrating significant improvement over both untransformed data and linear normalisation approaches.

2.8 Summary of GPs for Multi-band Light Curves

This chapter has established GPR as a transformative framework for modelling transients, bridging the gap between rigid parametric models and computationally prohibitive hydrodynamic simulations. By leveraging non-parametric flexibility, GPR accommodates the stochastic, multi-phase nature of phenomena like CCSNe, while rigorously quantifying uncertainties – a critical advancement for time-domain astronomy.

Key advancements demonstrated include:

- Non-stationary kernels, particularly Changepoint and multiplicative formulations, generally outperform stationary counterparts by adapting to distinct physical regimes (e.g., SBO, plateau, radioactive decay of ^{56}Ni). These kernels encode astrophysical priors, such as phase-specific timescales, while avoiding unphysical oscillations in data-sparse regions.

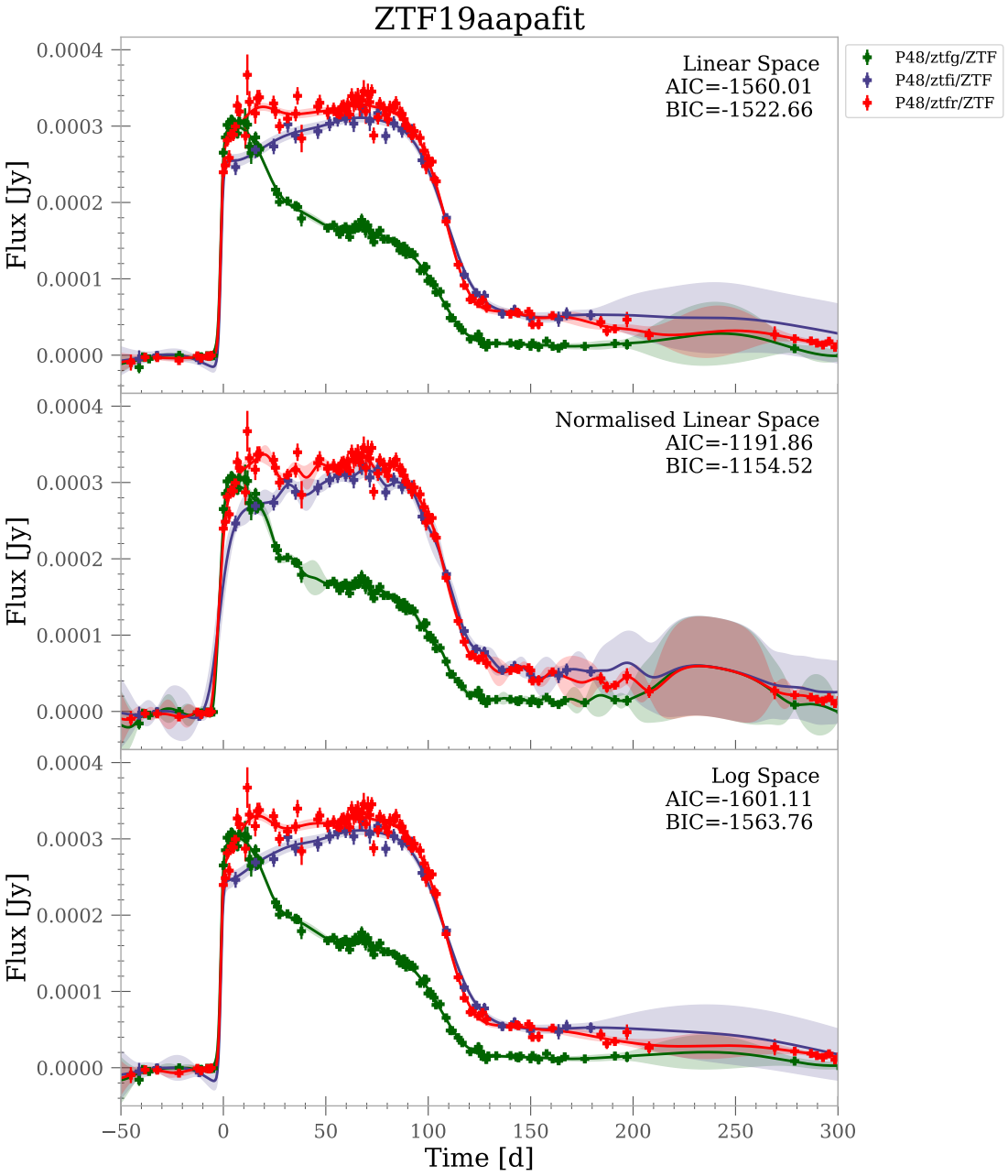

FIGURE 2.4: Comparison of linear versus logarithmic time domain transformations in MOGP modelling of the Type II SN ZTF19aapafit. *Top* to *bottom*: linear time domain, normalised time domain ($t' = [t - \mu]/\sigma$) and log space time domain, with shaded regions indicating 1 σ prediction uncertainties. Note the improved capture of early-time features in the logarithmic transformation.

- Logarithmic or normalised scaling of the time axis dynamically adjusts the effective length scale across phases, enabling stationary kernels to adapt to multi-timescale evolution. By compressing the dynamic range, $\log(t)$, or standardising inputs, $t' = (t - \mu)/\sigma$, these transformations preserve kernel simplicity while aligning covariance structures with astrophysical timescales.

This chapter primarily serves as an in-depth exploration of GPR and its astrophysical applications. While it lays the foundational framework for subsequent chapters, it also extends beyond this purpose by investigating advanced methodological adaptations, particularly the use of non-stationary kernels (e.g., the Gibbs and changepoint kernels; Eqs. 2.10 and 2.11).

Although these approaches show substantial potential for capturing complex temporal variability and are of broad relevance to time-domain astrophysics, in Chapters 3 and 4, I adopt more standard GPR frameworks for reasons of consistency and comparability. Specifically, in Chapter 3, I employ a single Matérn-5/2 kernel (Eq. 2.6) alongside the SPM mean function (Eq. 2.17) to align with prior work and ensure robust population-wide comparisons. Chapter 4 builds on this by adopting a multiplicative kernel structure (e.g., Matérn-5/2 $\times$ Squared-Exponential), selected via model comparison metrics (BIC), to better accommodate the broader temporal scale and complexity of full light curves, particularly during radioactive decay phases. Thus, while this chapter offers a glimpse at the potential and enhanced flexibility of GPR methods, the subsequent analysis chapters implement a more targeted subset of these techniques tailored to their specific scientific goals.

Chapter 3

Inferring CSM Properties of Type II SNe Using a Magnitude-Limited ZTF Sample

This chapter was previously accepted by MNRAS as Hinds et al. (2025).

3.1 Abstract

Although all Type II supernovae (SNe) originate from massive stars in possession of a hydrogen-rich envelope, the light curve morphology of these events is diverse, reflecting poorly characterised heterogeneity in the physical properties of their progenitor systems. Here, we present a detailed light curve analysis of a magnitude-limited sample of 639 Type II SNe from the Zwicky Transient Facility Bright Transient Survey. Using Gaussian processes, we systematically measure various empirical light curve features (e.g., rise times, peak colours and luminosities) in a robust sampling-independent manner. We focus on rise times as they are highly sensitive to pre-explosion progenitor properties, especially the presence of a dense circumstellar medium (CSM) shed by the progenitor in the years immediately pre-explosion. By correlating our feature measurements with physical parameters from an extensive grid of STELLA hydrodynamical models with varying progenitor properties (CSM structure, mass-loss rate, $R_{\rm CSM}$ and progenitor masses), we quantify the proportion of events with sufficient pre-explosion mass-loss

to significantly alter the initial light curve (roughly $M_{\rm CSM} \geq 10^{-2.5}$ $M_\odot$) in a highly complete sample of 377 spectroscopically classified Type II SNe. We find that 67 $\pm$6% of observed SNe in our magnitude-limited sample show evidence for substantial CSM ($M_{\rm CSM} \geq 10^{-2.5}$ $M_\odot$) close to the progenitor ($R_{\rm CSM} < 10^{15}$ cm) at the time of explosion. After applying a volumetric-correction, we find 36^{+5}_{-7}% of all Type II SN progenitors possess substantial CSM within 10^{15} cm at the time of explosion. This high fraction of progenitors with dense CSM, supported by both photometric and spectroscopic evidence of previous SNe, reveals mass-loss rates significantly exceeding those observed in local group red supergiants or predicted by current theoretical models.

3.2 Introduction

Light curves of core-collapse supernovae (CCSNe), Type II SNe in particular, exhibit a large amount of diversity, varying across orders of magnitude in rise times, luminosities, and durations. The simple progenitor scenario, in which the initial mass is the only factor affecting the SN type or its light curve, cannot adequately explain the extensive observational diversity we see in photometry and spectroscopy – particularly with the acknowledgement of the role binarity plays in stellar evolution (e.g., Eldridge et al., 2008; Sana et al., 2012; Eldridge et al., 2018; Zapartas et al., 2019, 2021) via binary induced mass transfer and mergers.

An area being explored in greater detail is the degree to which diversity arises from stars with similar initial masses and evolutionary histories that, nonetheless, produce distinct observational signatures at the time of explosion; e.g., varying mass of H envelopes, progenitor radii and H-richness of the outer envelope (e.g., Popov, 1993; Chieffi et al., 2003; Young, 2004; Reynolds et al., 2020; Humphreys et al., 2020; Hiramatsu et al., 2021; Moriya et al., 2023; Dessart & Jacobson-Galán, 2023). Type II SNe result from the core-collapse of stars with initial masses between 8–20 $M_\odot$ (e.g., Eldridge & Tout, 2004; Smartt, 2009, 2015; Van Dyk, 2017; Beasor et al., 2020). The most common subtype, Type IIP, originate from red supergiants (RSGs) – a connection confirmed through pre-explosion HST imaging (see Smartt, 2009, 2015). Their light curves exhibit H-recombination powered $\sim$100 d plateaus following steep rises to peak brightness, typically occurring within days to a week (e.g., Langer, 2012; Anderson et al., 2014; González-Gaitán et al., 2015; Rubin et al., 2016; Valenti et al., 2016).

Less common hydrogen-rich subtypes include: Type IIb SNe showing H-to-He spectral evolution from thin H envelopes (Podsiadlowski et al., 1993; Benson et al., 1994; Woosley et al., 1994; Jerkstrand et al., 2015); Type IIn SNe with slower rises and narrow emission lines from circumstellar material (CSM) interactions (Schlegel, 1990; Mauron & Josselin, 2011; Smith, 2014; Arcavi, 2017); and SN 1987A-like events from blue supergiants with extended >30 d nickel-powered rises (Schaeffer et al., 1988; Suntzeff & Bouchet, 1990; Arnett et al., 1989; Woosley, 1988; Schlegel, 1990; Arcavi, 2017; Singh et al., 2019; Sit et al., 2023).

From the emergence of narrow emission lines in early spectra of young SNe (flash ionisation; Gal-Yam et al., 2014; Groh, 2014b; Yaron et al., 2017; Gal-Yam, 2017a; Bruch et al., 2023), strong evidence has been presented for the presence of a substantial mass of dense material close to the progenitor at the time of core-collapse. Narrow lines are likely the result of shock breakout (SBO) shock-heating and ionising a slow-moving, dense material (e.g., Yaron et al., 2017; Irani et al., 2024; Jacobson-Galán et al., 2024a). As the narrow lines typically persist for only a $\sim$ few days post-explosion, it is assumed that the CSM required is the result of mass-loss from the star in the years immediately preceding core-collapse (e.g., Das & Ray, 2017; Davies et al., 2022; Tinyanont et al., 2022; Pearson et al., 2023).

Measurements of the CSM properties from the flash ionisation allow for constraints on the mass-loss rate, $\dot{M}$, and late-stage RSG instabilities experienced in the centuries-decades-years immediately before core-collapse (e.g., Mauron & Josselin, 2011; Yaron et al., 2017; Morozova et al., 2018; Stroh et al., 2021; Pearson et al., 2023; Tinyanont et al., 2022; Bruch et al., 2021, 2023; Moriya et al., 2023). These analyses typically assume that the CSM is an unbound, spherically symmetric material escaping with velocities of order $\sim$10 – 100 km s^{-1} (Smith, 2014; Morozova et al., 2017), following a density profile that decreases with radius ($\rho \propto r^{-2}$ for steady-state mass loss Morozova et al., 2018; Moriya et al., 2018; Davies et al., 2022; Moriya et al., 2023). Bruch et al. (2021, 2023) find that $\sim$ 60% of Type II SNe show evidence for significant amounts of dense CSM confined to a region around the progenitor at the time of explosion – although, this figure is not corrected for observational biases and not volume-limited. Potential precursor events (e.g., Fraser et al., 2013; Jacobson-Galán et al., 2022; Dong et al., 2024; Warwick et al., 2025) provide further evidence of eruptions close to the 'classical' core-collapse event.

The notion that many Type IIP SNe progenitors are surrounded by dense CSM at the time of explosion is further supported by detailed studies of nearby events: SN 2021yja (≈23 Mpc; Kozyreva et al., 2022; Hosseinzadeh et al., 2022), SN 2023ixf (≈7 Mpc; Bostroem et al., 2023; Hosseinzadeh et al., 2023; Hiramatsu et al., 2023; Jencson et al., 2023; Jacobson-Galán et al., 2023; Li et al., 2024; Singh et al., 2024; Zimmerman et al., 2024) and SN 2024ggi (≈7 Mpc; Chen et al., 2024, 2025; Xiang et al., 2024; Pessi et al., 2024; Jacobson-Galán et al., 2024b; Shrestha et al., 2024), which, combined with early photometric and spectroscopic data, confirm CSM around their RSG progenitors. In these cases, dense, optically thick CSM causes the SBO to occur within the CSM rather than at the stellar surface (Förster et al., 2018; Tinyanont et al., 2022; Pearson et al., 2023), producing rapid rises and enhanced peak luminosities (e.g., Moriya et al., 2011; Das & Ray, 2017; Morozova et al., 2017, 2018; Bruch et al., 2021, 2023; Tinyanont et al., 2022; Pearson et al., 2023; Moriya et al., 2023; Li et al., 2024).

$\dot{M}$ for RSGs have been measured through multiple techniques: mid-IR observations of circumstellar dust in clusters show $\dot{M}$ $\sim 10^{-6}$ – 10^{-5} $M_\odot$ yr^{-1} (e.g., Beasor & Davies, 2018; Beasor et al., 2020), consistent with rates derived from molecular line and radio measurements (e.g., Mauron & Josselin, 2011) and comparing pre-explosion progenitor properties to theoretical stellar evolution models (e.g., Smartt, 2009). Type IIn progenitors exhibit much higher rates of 10^{-3} – 1 $M_\odot$ yr^{-1}, derived from multi-wavelength observations (e.g., Kiewe et al., 2012; Taddia et al., 2013; Fransson et al., 2014), and combined X-ray, radio, and spectroscopic signatures (e.g., Smith, 2017a,b).

However, $\dot{M}$ inferred from RSG observations alone are insufficient to produce the measured $M_{\rm CSM}$ and $R_{\rm CSM}$ on the timescale of decades to months pre-explosion (e.g., Bruch et al., 2021, 2023). Popular mechanisms for end-of-life mass-loss include: wave-driven energy heating into the stellar envelope (e.g., Fuller, 2017; Morozova et al., 2020; Wu & Fuller, 2021), radiation-driven mass-loss (e.g., Vink, 2008; Vink, Jorick S. & Sabhahit, Gautham N., 2023), instabilities caused by explosive shell burning (e.g., Arnett & Meakin, 2011; Smith & Arnett, 2014), common envelope interactions caused by binary interactions (e.g., Chevalier, 2012; Sana et al., 2012) and RSG 'superwinds' (e.g., Davies et al., 2022).

Previous studies have been successful in characterising smaller subsets of Type II SN properties such as luminosities and rise times (e.g., Taddia et al., 2013; Anderson et al.,

2014; Sanders et al., 2015; Gall et al., 2015; Rubin et al., 2016; Valenti et al., 2016; Graur et al., 2017b; Davis et al., 2019) but are limited to small numbers or incomplete samples, made up of well-observed SNe detected in heterogeneous galaxy-targeted surveys. Infrequent and inconsistent survey cadence lead to inadequate coverage on the rise, limiting the amount of information one can infer from the rising light curve. The wide area, high cadences and untargeted nature of modern surveys allow for larger, more complete samples to be curated – lending to more detailed statistical analysis of population characteristics and their frequencies. This work builds upon previous studies by making use of robust statistical methods and large, highly complete surveys.

To address these questions, we present detailed light curve analysis of spectroscopically classified Type II SNe from the Zwicky Transient Facility (ZTF; Bellm et al., 2019a,b; Graham et al., 2019; Masci et al., 2019; Dekany et al., 2020). In Section §3.3 we introduce our sample, present the forced photometry light curves and the Gaussian process methodology and data analysis processes used in this work. We present the sample in Section §3.4 and explore the diversity of Type II SNe. In Section §3.5, we empirically infer progenitor properties using a correlation-based analysis based on previous studies. In Section §3.6, we present the volume corrected ($V_{\rm max}$ method; Schmidt, 1968) distributions for $M_{\rm CSM}$, $R_{\rm CSM}$ and $\dot{M}$. We then analyse and discuss the implications in Section §3.7.

Throughout the paper, we correct for Galactic extinction using the NASA Extragalactic Database (NED) extinction tool (using the dust map from Schlafly & Finkbeiner 2011). We assume a cosmological model with $\Omega_M = 0.3$, $\Omega_\Lambda = 0.7$ and $h = 0.7$.

3.3 Methods I – Sample, Forced Photometry and Light Curve Modelling

3.3.1 The Zwicky Transient Facility and The Bright Transient Survey

Of the total observing time available to ZTF, a major fraction has been devoted to public surveys – 40% in the initial 2.5 years, and 50% in subsequent phases. Most of this public observing time is used for a Northern Sky Survey (NSS) of fields above declination $-30°$ in ZTF g and r-bands (Bellm et al., 2019b). The NSS began as a 3 d cadence survey

and now runs at 2 d cadence. The public surveys generate alerts which are distributed to various community alert brokers (Patterson et al., 2019). ZTF *i*-band observations are available for some fields which overlap partnership surveys.

The Bright Transient Survey (BTS), described in Fremling et al. (2020), Perley et al. (2020) and Qin et al. 2025 (in prep.), is a magnitude-limited survey aiming to spectroscopically classify all extragalactic transients in the northern hemisphere, satisfying a few basic conditions: a peak apparent magnitude, m_{peak}, $\leq$ 18.5 mag, visibility from Palomar, and a location out outside of the Galactic Plane. As of December 31st 2024, the BTS catalogue includes >10,000 classified SNe brighter than 19 mag; spectroscopic classification is 95.5% complete down to 18.5 mag for events passing visibility and cadence criteria (see Perley et al., 2020, for a review)[1]. The 2 – 3 d or less cadence and sensitive nature of the survey are required to adequately sample enough of the rise to constrain it with some certainty, and secure detections during the early phase of the light curve, close to the explosion time.

Final classifications (used here), volumetric rates and luminosity functions from the BTS sample will be presented in the upcoming paper Qin et al. 2025 (in prep.) which covers the period starting 2018 to the end of 2024. Both Qin et al. 2025 (in prep.) and this work have made use of ZTF observing time, instruments and software: Spectral Energy Distribution Machine (SEDM; Blagorodnova et al., 2018; Rigault et al., 2019; Kim et al., 2022), the DouBle Spectrograph (DBSP; Oke & Gunn, 1982), Global Relay of Observatories Watching Transients Happen Marshal (GROWTH; Kasliwal et al., 2019) and the Fritz SkyPortal Marshal (Duev et al., 2019; van der Walt et al., 2019; Duev & van der Walt, 2021; Coughlin et al., 2023).

This study analyses the spectroscopically classified SNe from the BTS database[2], incorporating both BTS classifications and TNS reports archived in the BTS from May 1st 2018 to December 31st 2023, retrieved via the BTS internal Sample Explorer[3]. Beyond the apparent magnitude threshold, Palomar visibility constraints, and Galactic plane exclusion previously discussed, the BTS requires: sufficient temporal coverage spanning 7.5 – 16.5 d pre-peak to 16.5 – 28.5 d post-peak, with multiple observations near peak brightness; spectroscopic accessibility up to 30 d post-peak; the transient must be absent

[1]These statistics are available on the ZTF Bright Transient Survey homepage: https://sites.astro.caltech.edu/ztf/bts/bts.php.
[2]Finalised in Qin et al. 2025 (in prep.)
[3]A public version is available at: https://sites.astro.caltech.edu/ztf/bts/explorer.php

in the reference image; and alerts to pass the BTS alert stream filtering criteria detailed in Perley et al. (2020).

The quality cuts ensure light curves are sampled during the rise to peak and well after peak, and are generally independent of light curve properties. Key values drawn from the sample that are used to comment on demographics have the additional criterion of light curves peaking brighter than 18.5 mag. From hereon, Type II SNe refer to SNe spectroscopically classified as Type II or Type IIP and do not include Type IIn or Type IIb, which are referred to as such.

3.3.2 Forced Photometry Light Curve Analysis

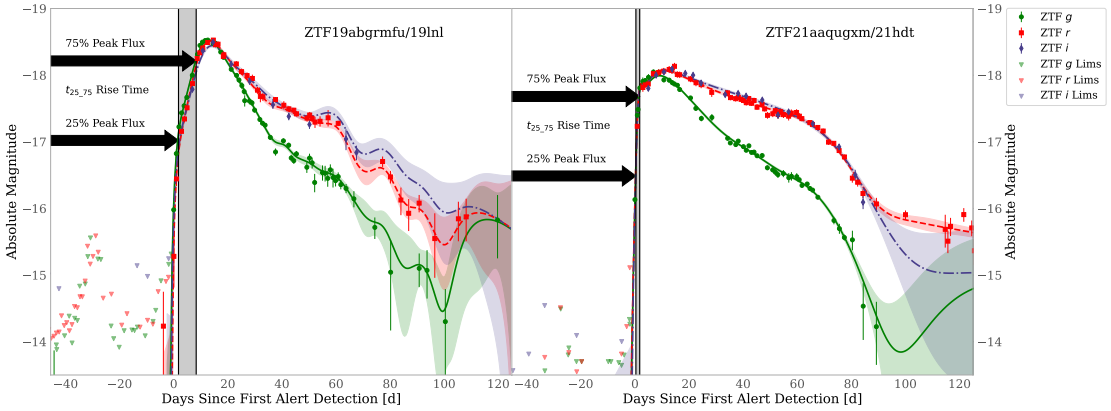

FIGURE 3.1: Type II SNe ZTF19abgrmfu/SN 2019lnl at z = 0.035 (*left*) and ZTF21aaqugxm/ SN 2021hdt at z = 0.019 (*right*). ZTF *gri* forced photometry light curve modelled with 2D Gaussian process regression. We have annotated how a rise time metric (time to rise from 25 – 75% of the peak flux t_{25_75}) is measured. The inverted triangles represent the upper limits generated by the fps pipeline – where the limit is determined to be the maximum of [flux + $2\times\sigma_{\rm flux}$,$3\times\sigma_{\rm flux}$]. Green circles and solid lines represent ZTF *g*, red squares and dotted lines represent ZTF *r* and dark blue diamonds and dark blue dash-dotted lines represent ZTF *i*. The shaded regions represent the 68% CI.

The ZTF real-time data stream operates by producing alert packets, where an alert is generated based on real-time and historical contextual information (Masci et al., 2019). Point source function (PSF) photometry and difference imaging using ZTF archives generate upwards of 100,000 alerts nightly. Photometric measurements are performed based on image-subtracted photometry (`ZOGY`; Zackay et al. 2016a). The distributed alert packets do not allow for measurements below the detection threshold and do not fix the position, creating room to miss detections if the software does not recover an alert.

Photometry for this study is produced using the ZTF forced photometry (FP) service (fps; Masci et al., 2023), with post-processing conducted following the procedures in Miller et al. (2025, in prep.). Briefly, the fps estimates the PSF flux at a user-specified location in all ZTF difference images with coverage of the specified position. The flux measurement uses the same PSF model defined by the `ZOGY` algorithm that is used to perform image subtraction in the production of ZTF real-time alerts. Observations in which the fps pipeline processing produces a flag, typically because the photometric calibration is excessively noisy or the initial image subtraction failed, are excluded from the analysis. The fps flux measurements require a systematic baseline correction, i.e., there is a small constant offset that needs to be removed to make the pre-SN flux measurements consistent with zero flux (see Masci et al., 2023). The baseline is estimated using observations that were obtained > 100 d before maximum and several hundred days after maximum, where the duration after the peak is determined by conservatively assuming the transient is purely powered by radioactive ^{56}Co decay. Following the baseline correction, the uncertainties for the individual flux measurements are adjusted to account for a systematic trend whereby brighter sources have underestimated uncertainties (see Miller et al., 2025, in prep. for further details). As a final output, this post-processing produces a measurement of the transient flux and its uncertainty in units of μJy, including in images where there is no flux detected from the transient. For this study, Public + Partnership + Caltech ZTF data was used.

3.3.3 Gaussian Process Regression

CCSN light curves are difficult to model due to the extensive variety in their photometric behaviour. There exist analytical attempts to address the problem using parametric fitting functions (e.g., Villar et al., 2017, 2019) and there are advancements in theoretical models to produce synthetic light curves with more likeness to observed light curves (Morozova et al., 2017; Das & Ray, 2017; Moriya et al., 2023, and references therein). Whilst certain parameterisation and generalised empirical models have proven to be adequate in some scenarios, few of these models can fully characterise the diversity of parameters and properties present in transients being uncovered by large surveys. Thus, we are motivated to use a non-parametric technique such as Gaussian process regression (GPR; Rasmussen 2004).

GPR is a non-parametric, Bayesian machine learning method for modelling data with functions of an unknown form (see Aigrain & Foreman-Mackey, 2023, for a review). For single-band SN light curve interpolation, the unknown function a 1-dimensional Gaussian process (GP) approximates is flux as a function of time. We include the effective wavelength, $\lambda_{\rm eff}$, of each filter band, and train in 2-dimensions – e.g., flux as a function of time and effective wavelength – which is often expressed as probability by Eq. 3.3.3, similar to methodology used in Thornton et al. (2024).

$$P(f|t, \lambda_{\rm eff}) = \mathcal{N}(\mu(t,\, \lambda_{\rm eff}), \mathbf{K})$$

where f is flux and $\lambda_{\rm eff}$ for ZTF g, r and i is 4753.15 Å, 6369.99 Å and 7915.49 Å respectively (Rodrigo & Solano, 2020; Rodrigo et al., 2024). The data is input in the observer frame and for plotting purposes, we plot in the observer frame. For parameter measurements (luminosities, timescales and colours), we standardise to rest frame ZTF g by predicting at $\lambda_{\rm eff,g} \times (1 + z)$. This approach allows us to consistently compare physical parameters across our sample while preserving the original photometric information.

For modelling diverse SN light curves, we use a Matèrn-5/2 covariance function ($\mathbf{K}$) that captures both smooth evolution in addition to the sharp transitions characteristic of SNe – the kernel includes an additive white noise term to account for photometric uncertainties. We implement the GPR using the `python` package `george` (Ambikasaran et al., 2015), combining the Matèrn-5/2 kernel with the piecewise mean function from Villar et al. (2019) to constrain the behaviour in coverage gaps.

GPR allows robust parameter extraction despite heterogeneous sampling and measurement uncertainties, facilitating empirical correlation analysis without detailed individual modelling. By fitting in flux space, we incorporate non-detections to better constrain early light curve evolution.

Fig. 3.1 demonstrates our 2D GPR modelling of ZTF *gri* light curves for ZTF19abgrmfu/SN 2019lnl and ZTF21aaqugxm/SN 2021hdt. This approach leverages cross-filter correlations to simultaneously predict temporal and spectral evolution – particularly valuable when sampling is irregular across bands. While ZTF g and r observations maintain a regular 2 – 3 d cadence, ZTF i-band data is often sparse due to partnership-specific scheduling. Our multi-band GPR uses well-sampled bands to constrain the less frequently observed

ones, enabling more consistent and precise measurements of colour, rise times, and peak magnitudes across all bands.

Our 2D GPR approach uses a single length scale parameter to handle heterogeneous sampling by controlling correlation strength between observations. While this flexibility accommodates diverse light curve shapes, it presents challenges: the kernel must balance modelling rapid early evolution with slower late-time decline, potentially overfitting lower signal-to-noise data during the radioactive decay phase. Even with the Villar et al. (2019) function providing a smooth mean function, the GP's flexibility can introduce unphysical variations at late times. The method also assumes consistent colour evolution, potentially misrepresenting rapid colour changes.

However, these limitations primarily affect the faint and late phases, having minimal impact on our scientific conclusions since we focus on bright events ($m_{peak} \leq 18.5$ mag) and measure parameters during well-sampled phases near peak brightness.

3.3.3.1 Feature Extraction

Combining the fps pipeline and GPR developed for this work, we have used 2D GPR to interpolate across all available filters for each SN in the BTS sample, including Type Ia SNe. Using the interpolated light curves and $\lambda_{\rm eff}$ information, we have empirically measured >20 metrics (see Table 3.1) for each band where the coverage allowed for measurements to be reliably taken – for example, coverage constraints are placed on the rise to ensure reliability, we explore this in more detail in a proceeding section. Metrics relevant for this paper rely first on the peak flux (flux at maximum light) and include: rise times from 10%, 25%, 50% of the peak flux to the peak flux or 50%, 60%, 75%, 80%, 90% of the peak flux; the peak flux; magnitude; luminosity; time of the peak relative to the first alert detection; colour at several times before, at and after the peak; plateau length and plateau magnitude; and other metrics for analysis in future works. As mentioned, we standardise these measurements by predicting the GP model for each filter in the rest-frame ZTF band.

Parameter	Symbol	Unit	Definition
P1 - Parameters measured empirically from the GPR model used here			
Peak Apparent Magnitude	m_{peak}	mag	Apparent magnitude at peak [1]
Time of Peak	t_{peak}	d	Time at which the peak occurs [2]
X – Y% Rise Time	$t_{\mathtt{X\_Y}}$	d	Time between X% and Y% of the peak (e.g., 25 – 75%) [3]
Fade Time	t_{Peak_50}	d	e.g., time between peak and 50% peak flux
Duration Time	t_{50}	d	e.g., time spent above 50% peak flux
Apparent Magnitude at X d	$m_{g,Xd}$	mag	Apparent ZTF g magnitude at 5, 10 & 50 d post ZTF g peak
Plateau Duration	$t_{\rm plat}$	d	Measured using the gradient of the GP interpolated light curve
Colour	$(g-r)_{r,-Xd}$	mag	e.g., ZTF $g-r$ calculated X d before r-band peak
P2 - Additional parameters measured empirically from the GPR model not used here			
Plateau Colour	$(g-r)_{plat}$	mag	Colour at the end of the plateau
MJD Explosion Time	T_{exp}	d	Explosion time [2]
Colour Evolution	$g-r$	mag	ZTF $g-r$ colour relative to ZTF r-band peak
Peak Luminosity	L_{peak}	erg s^{-1}	Luminosity at peak
Plateau Slope	∇_{plat}	mag d^{-1}	Gradient of the plateau
No. Bumps	N_{bumps}	-	The number of peaks in the light curves
Decline Rates	Δm_{Xd}	mag d^{-1}	Difference in magnitude between peak and peak + X d
Optical Energy	E_{opt}	erg	Total integrated optical energy in each band ($\int \nu f_\nu d\nu$)
P3 - Parameters indirectly measured from relationships involving P1 parameters			
CSM Mass	$M_{\rm CSM}$	M$_\odot$	Mass of circumstellar material
Mass-Loss Rate	$\dot{M}$	M$_\odot$ yr^{-1}	Rate of mass-loss of the progenitor
CSM Radial Extent	$R_{\rm CSM}$	cm	Radial extent of circumstellar material
Iron Core Mass	$M_{\rm Fe,Core}$	M$_\odot$	Iron core mass of progenitor prior to explosion

[1] Defined as being the peak with the highest flux and it must have previous detections or non-detections on the rise to confirm it is the peak. In the case of multiple peaks, all peaks are identified and the peaks are ranked in order of strength and time (earliest first). All relative time intervals are reported in the rest frame; [2] Relative to first alert detection; [3] We also measure 20 – 60%, 60 – 90%, 20 – 50% & 50 – 80% rise times.

TABLE 3.1: Description of parameters empirically measured directly using GPR interpolations (P1), or calculated using measured parameters and established relationships – see Section §3.6.2 for $M_{\rm CSM}$, $\dot{M}$ and $R_{\rm CSM}$. We standardise all measurements by predicting the GP model at $\lambda_{eff} \times (1+z)$ such that all measurements are in the rest-frame ZTF band or relative to the rest-frame measurements. Most parameters are filter-dependent and have been measured for each filter. The table is split into sections: P1 are the empirical GP measured parameters used specifically in this work, P2 are parameters also empirically measured using the GP interpolation but not used in this work and P3, which shows parameters estimated from relationships or methods involving parameters in P1.

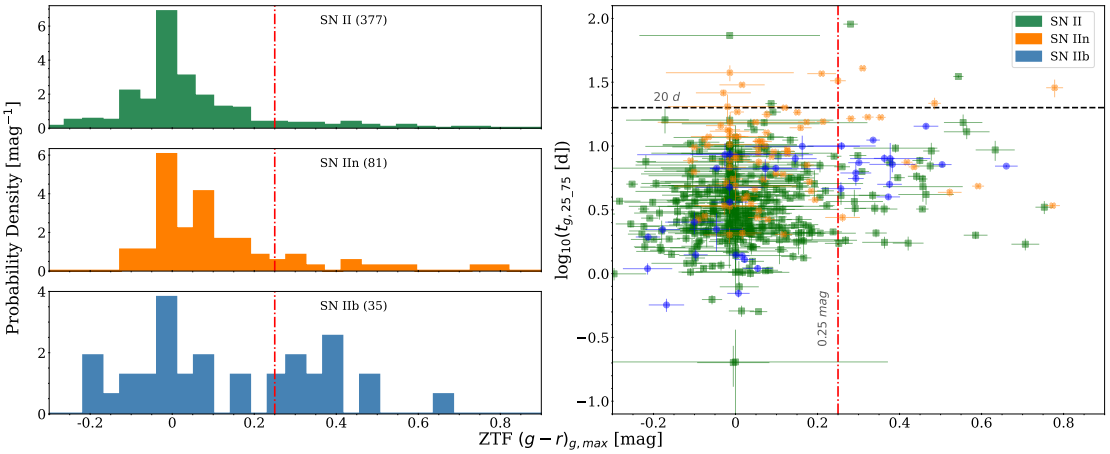

FIGURE 3.2: $(g-r)_{g,\max}$ histograms (*left*) and ZTF g time to rise from 25 – 75% peak flux vs $(g-r)_{g,\max}$ (*right*) for Type II, Type IIn and Type IIb SNe (*top left* to *bottom left*) for those with a m_{peak} in any filter ≤ 18.5 mag. The histograms for Type II and Type IIn are sharply peaked and have a tail in the red direction, indicating a standard colour distribution and the presence of some 'dusty', $(g-r)_{g,\max} \geq 0.25$ mag, SNe. The horizontal line shows 20 d and the vertical line at 0.25 mag is the limit we define, beyond which we identify objects as 'dusty'. This plot is used to distinguish the likely heavily host dust-extinguished SNe (rise < 20 d, and red, $g-r > 0.25$ mag) from those likely intrinsically red (rise ≥ 20 d and red, $g-r > 0.25$ mag).

We estimate parameter uncertainties by drawing 1,000 samples from the GPR posterior distribution, leveraging the probabilistic nature of the GP. The 1 σ uncertainties are derived from the resulting distribution of measured values, capturing both photometric uncertainties and the range of light curve behaviours consistent with our data.

3.3.4 Galactic and Host Extinction Corrections

We correct for line of sight Galactic extinction using NED extinction tools (based on the dust map from Schlafly & Finkbeiner 2011). For $M_{g,\text{peak}}$ used in this work, we calculate the peak of the GP model, correct for Galactic extinction at the interpolated central wavelength and apply a uniform K-correction of $2.5\log_{10}(1+z)$, which is typically small.

As ZTF is a survey in gri, a comprehensive host extinction correction is not feasible with the survey photometry alone. One can approximately find the host extinction using the ZTF $g-r$ colour at the ZTF g peak, $(g-r)_{g,\max}$, and apply a correction based on this colour. For Type II and Type IIn SNe, we find the unweighted histogram of the peak colour $(g-r)_{g,\max}$, Fig. 3.2, is sharply peaked around 0 mag, which is characteristic of a well-defined intrinsic population and suggests standard colour distribution, consistent with the findings of de Jaeger et al. (2018).

The Type II SN colour distribution, shown in Fig. 3.2, has an asymmetric tail toward redder colours. This asymmetry is particularly informative – if there existed a significant population of intrinsically red SNe, we would expect a more symmetric distribution or a secondary peak, rather than the observed sharp core with a red tail. Based on the distribution in Fig. 3.2, we find the 90th and 95th percentiles for Type II SN $(g-r)_{g,\mathrm{max}}$ to be $\approx$ 0.2 mag and $\approx$ 0.39 mag, respectively. We establish $(g-r)_{g,\mathrm{max}} \geq$0.25 mag as the threshold for identifying 'dusty' events that necessitate host-extinction correction. Using an Empirical Cumulative Distribution Function (ECDF), we find that 9^{+12}_{-6}% of the observed Type II population have $(g-r)_{g,\mathrm{max}} \geq 0.25$ mag, confirming that heavily dust-extinguished events constitute a minority of the sample. For Type IIn and Type IIb SNe, we find 14^{+14}_{-8}% and 40 $\pm$ 20%, respectively, have $(g-r)_{g,\mathrm{max}} \geq 0.25$ mag – uncertainties reported here are the binomial CI.

Using a rise time definition we present in Section §3.3.5.1, we investigate the rise time vs colour parameter space to understand how this correction is applied to SNe across a variety of rise times – see Fig. 3.2. The majority of SNe with rise times $<$ 20 d exhibit peak $g-r$ colours blueward of 0.25 mag. Objects redward of this threshold likely suffer significant dust-extinction, forming a skewed tail extending from an otherwise approximately normal colour distribution. Those with $(g-r)_{g,\mathrm{max}} > 0.25$ and rise $>$ 20 d are likely intrinsically red, owing to photons emitted from the core being trapped for longer, which increases diffusion time and rise time to maximum light. We perform this exercise to avoid applying an incorrect host-correction to those SNe that are likely intrinsically red, therefore artificially boosting their luminosity. As we have identified this population in the top right quadrant (rise $>$ 20 d and $(g-r)_{g,\mathrm{max}} > 0.25$ mag) as intrinsically red, we correct the subset in the bottom right quadrant (rise $<$ 20 d and $(g-r)_{g,\mathrm{max}} > 0.25$ mag).

To ensure that our method is accurately identifying events affected by dust extinction (requiring host-extinction corrections) we inspected the host galaxy environments of the 'dusty' SNe (22 Type II, 8 Type IIn and 11 Type IIb after 18.5 mag cut for completeness, see Table B.1 for a summary of properties). We examined these environments for indicators that could explain the reddening, such as substantial dust content, location within dense spiral arms, the galactic bulge or edge-on or highly inclined host galaxy orientations. We see that these events are predominantly located in regions associated with significant dust content – specifically within their host galactic plane or

star-forming regions. These SNe also show a persistent red colour throughout their rise phase, consistent with dust extinction rather than intrinsic colour variation. This environmental association, combined with their photometric evolution, suggests that their red appearance stems from host galaxy extinction rather than intrinsic properties. We perform our later analysis both with and without host extinction corrections, finding no significant differences in our primary results.

One event in particular, ZTF18acbwaxk/SN 2018hna (Singh et al., 2019; Thévenot, 2020; Tinyanont et al., 2021; Maund et al., 2021; Sit et al., 2023; Xiang et al., 2023), is both red and rises slowly with similar light curve morphology and timescales to SN 1987A. This SN appears in a face-on dwarf galaxy, the minimal expected host extinction suggests its red colour is intrinsic – for comparison, SN 1987A was $g - r \gtrsim 0.4$ mag at peak. We interpret this as an intrinsically red event and do not apply a host-correction.

We perform a correction for host extinction with the colour at peak, $(g - r)_{g,\mathrm{max}}$, for this subset of SNe described above. Relative to V-band ($A_V = 1$ mag) and based on the assumption of a standard Milky Way $R_V = 3.1$ mag (e.g., Cardelli et al., 1989) reddening law (as implemented in `python extinction` package). We assume an extinction of $A_g/A_V = 1.19$ mag, $A_r/A_V = 0.84$ mag and $A_i/A_V = 0.61$ mag – we ignore the effect of redshift here. For a ZTF g extinction relative to $(g - r)_{g,\mathrm{max}}$ reddening of 1 mag, we find an extinction of $A_g = 3.37\ (g - r)_{g,\mathrm{max}}$ mag. For our correction to ZTF g luminosities, we multiply the $(g - r)_{g,\mathrm{max}}$ by 3.37 and apply this to ZTF g magnitudes of all Types. From this point on, we carry through this extinction correction for light curves where $(g - r)_{g,\mathrm{max}} > 0.25$ and $t_{25\text{-}75} \leq 20$ d. However, the volumetric-correction weighting applied in Section §3.4.2 is based on the uncorrected peak magnitude.

To minimise over-weighting low-luminosity, nearby events in our magnitude-limited analysis, we adopt more precise luminosity distances from recent literature for events within $d_{l,\mathrm{max}} \leq 50$ Mpc (Table 3.2).

3.3.5 Rise Time

We focus on the rise time and how it relates to the CSM as recent studies (e.g., Morozova et al., 2016; Yaron et al., 2017; Morozova et al., 2018; Pearson et al., 2023; Tinyanont et al., 2022; Bruch et al., 2021, 2023; Jacobson-Galán et al., 2023; Hosseinzadeh et al.,

ZTF	TNS ID	d_l [Mpc]	Reference
ZTF18acbwaxk	2018hna	12.82 ± 2.02	[1]
ZTF18abwkrbl	2018gjx	35.00 ± 5.00	[2]
ZTF19abwztsb	2019pjs	40.10	[3,4]
ZTF19acfejbj	2019sox	48.78	[5]
ZTF20acrzwvx	2020aatb	40.50 ± 5.11	[4,6]
ZTF20acwqqjs	2020acat	35.30 ± 4.40	[7]
ZTF20aapchqy	2020cxd	22.00 ± 3.00	[8]
ZTF20aatzhhl	2020fqv	17.30 ± 3.60	[9,10]
ZTF20abeohfn	2020mjm	28.30 ± 2.00	[3,4]
ZTF21aadoizf	2021aai	20.90 ± 1.90	[11]
ZTF21aaqgmjt	2021gmj	13.10 ± 2.00	[12]
ZTF21abvcxel	2021wvw	44.12	[5]
ZTF22abtjefa	2022aaad	11.10	[5]
ZTF22abtspsw	2022aagp	21.83 ± 3.00	[4]
ZTF22aaotgrc	2022ngb	43.07	[4]
ZTF22aauurbv	2022pgf	36.63 ± 2.60	[4]
ZTF22abfzdkz	2022uop	44.65	[5]
ZTF22abnejmu	2022ycs	44.65	[5]

[1] Singh et al. (2019); [2] Prentice et al. (2020); [3] Strotjohann et al. (2021); [4] Helou et al. (1991); [5] NASA/IPAC Extragalactic Database Helou et al. (1991); [6] Theureau et al. (2005); [7] Medler et al. (2022); [8] Yang et al. (2021); [9] Tinyanont et al. (2022); [10] Theureau et al. (2007); [11] Valerin et al. (2022); [12] Zimmerman et al. (2021)

TABLE 3.2: Sources of improved luminosity distance for events closer than 50 Mpc to improve the luminosity weighted volumetric-corrections of close events, particularly those at the extremes – close and faint.

2018, 2023; Irani et al., 2024) have shown substantial evidence of the sensitive nature of the rise time to the progenitor properties and pre-explosion conditions (e.g., $M_{\rm CSM}$, $R_{\rm CSM}$, CSM density and progenitor radius).

Traditional rise time measurements – from explosion to peak – require well-constrained explosion epochs through deep non-detections immediately before explosion and good sampling of the early rise. These observational constraints significantly limit the number of events for which explosion epochs can be reliably determined, though this is partially alleviated by fitting the early light curve with power-law or polynomial functions to approximate the explosion time (Gall et al., 2015; González-Gaitán et al., 2015; Bruch et al., 2021, 2023). To analyse our heterogeneously sampled dataset, we instead adopt a mathematically defined rise time that does not depend on explosion epoch constraints.

3.3.5.1 Rise Distribution

We define rise time (t_{25_75}) as the interval from 25% to 75% of peak flux in ZTF g-band. This definition offers several advantages: it's robust against sampling errors and low S/N measurements; captures the epoch where CSM signatures are strongest; and avoids plateau phases where other physical processes dominate. We select ZTF g-band for its sensitivity to CSM interaction signatures in the blue optical (e.g., Groh, 2014b; Gal-Yam et al., 2014; Yaron et al., 2017; Kulkarni et al., 2023) – a choice validated by recent modelling of SN 2023ixf, where g-band provided optimal fits (minimum χ^2 per progenitor model) across all bands (Moriya & Singh, 2024).

Events peaking at 18.5 mag have 25% peak flux at 20th mag (i.e., + 1.5 mag), which does not typically exceed the ZTF detection limit under favourable conditions but may fall below the threshold during sub-optimal conditions (e.g., bright time). Thus, this ensures we capture a substantial portion of the rise whilst remaining sensitive to fainter objects. Fig. 3.1 shows our measurement methodology.

For consistent measurements on the rise, we place additional constraints on the rising light curve coverage to minimise the impact large gaps in coverage have on the GP modelling. For the measurement, we required at least one observation (detection or non-detection) in each of the following regions:

$$\text{A. } T_{g,75} - 4 \leq T \leq T_{g,75} + 4 \text{ [d]}$$

$$\text{B. } T_{g,75} - 12 \leq T \leq T_{g,75} - 4 \text{ [d]}$$

$$\text{C. } T_{g,75} - 20 \leq T \leq T_{g,75} - 12 \text{ [d]}$$

Here, $T_{g,75}$ marks when the flux reaches 75% of its peak during the rising phase in ZTF g. To measure rise times in the ZTF g-band, we begin by examining only the g-band data. When ZTF g-band coverage is incomplete (missing regions B and/or C), we expand our analysis to include ZTF r and i-band data, evaluating them relative to $T_{g,75}$. In cases where ZTF g-band data only covers region A, we classify the measurement as an upper limit if the ZTF r and i-bands cover either regions A and B together or regions A and C together. For early rise measurements ($T_{b,25}$, time at 25% peak flux relative to ZTF g), we require coverage of only region A. This requirement is typically met

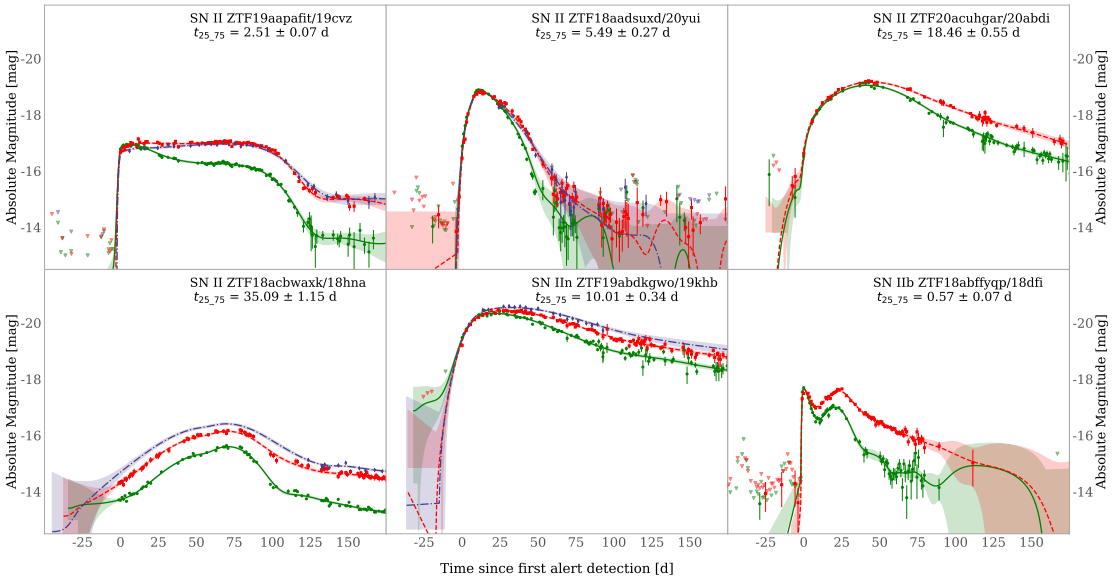

FIGURE 3.3: ZTF *gri* forced photometry GPR light curve panel showing the diversity of Type II SNe and the ZTF g t_{25_75} rise times.

automatically through our $T_{g,75}$ criteria since most objects complete their rise within 20 d. The diversity of light curve morphologies is shown in Fig. 3.3.

From our sample of SNe with forced photometry (as of December 31st 2023), we identified 1323 CCSNe that meet the quality criteria established by Perley et al. (2020). Of these, 981 are hydrogen-rich CCSNe (including regular Type II/IIP, IIn, IIb, and H-rich superluminous SNe; SLSNe), while the remaining 342 are classified as stripped-envelope SNe (SESNe). The other SNe in the quality sample, 4009, are Type Ia SNe (see Table 3.3). Our Type IIb sample is relatively small due to classification challenges inherent to this subtype. The limited spectral resolution of the SEDM makes it difficult to identify the characteristic evolution – specifically, the disappearance of H features and the emergence of often weak He lines in later spectra. Comprehensive classification typically requires multiple spectra obtained at different epochs, which is not always feasible. While this likely results in some incompleteness in our Type IIb sample, the impact on our overall study conclusions is minimal, as these events represent a small fraction of the H-rich SN population. We discuss and quantify this systematic impact of in appendix B.11.

Given the coverage constraints and the availability of forced photometry at the time of writing, 639 H-rich SNe make it through our quality cuts, allowing for constraining measurements of the t_{25_75} metric to be made – see Table 3.3 for a breakdown. For this

Type	Total	BTS Cut	Rise Cut	$m_{peak} \leq 18.5$ mag
		H-rich CCSNe		
II/IIP	1387	716	479	377
IIn	241	145	94	71
IIb	136	97	50	35
SL II	38	23	16	10
Tot.	1802	981	639	493
		H-poor CCSNe		
Ib/c	363	223	-	-
Ic-BL	63	45	-	-
Ibn	36	27	-	-
Icn	1	1	-	-
SL I	75	46	-	-
Tot.	538	342	-	-
		Type Ia SNe		
SN Ia	6329	4009	-	-

TABLE 3.3: Figures showing the number of SNe in the Bright Transient Survey quality sample (see Perley et al., 2020) as of the 31st of December 2023, in addition to the number of SNe that make up the final sample of this work after applying rise time constraints to ensure an adequate sampling of the rise and a m_{peak} cut for volumetric weighting – m_{peak} can be in any ZTF band.

paper, we consider SLSNe II as Type IIn based on the ambiguous boundary between the classes. Additionally, for the 23 SLSNe passing the quality cuts from the BTS and outlined here, we checked their spectra and found obvious narrow lines indicative of Type IIn SNe in all except ZTF19ackzvdp/SN 2019uba which showed slightly broader emission lines (see also Nyholm et al., 2020; Kangas et al., 2022; Pessi et al., 2023a), prompting us to exclude this from the sample completely. Fig. 3.4 is the rise time distribution using t_{25_75} rise, including comparison events from the literature.

In Fig. 3.4, we have included the well-studied Type II SNe SN 2023ixf, SN 2024ggi and SN 1987A to determine where amongst the larger population these events lie. For SN 2023ixf[4] and SN 2024ggi[5], we use publicly available data and model the multi-band light curve using the same process as described in Section §3.3.3, and for SN 1987A we use figures from Schaeffer et al. (1988); Catchpole (1989); Suntzeff et al. (1992); Suntzeff (1997); Fransson et al. (2007) to extract the data using a data extractor[6]. As shown in

[4]Data gathered from https://www.wiserep.org/object/23278
[5]Data gathered from Shrestha et al. (2024)
[6]WebPlotDigitizer: https://apps.automeris.io/wpd/

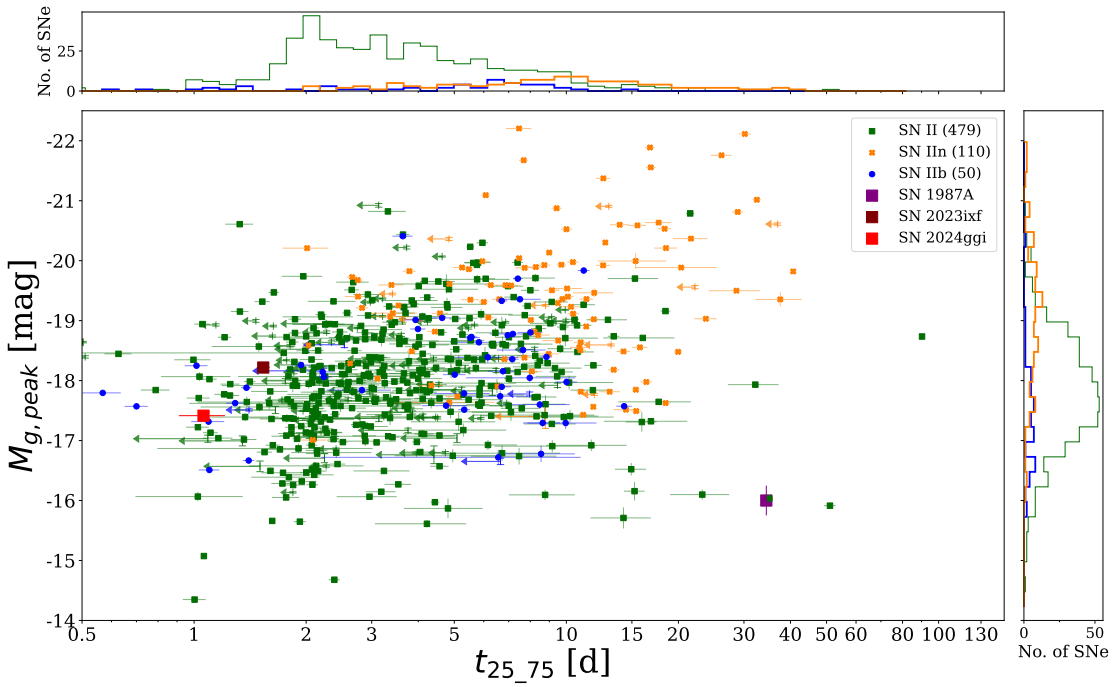

FIGURE 3.4: Rise time distribution in ZTF g-band for spectroscopically classified SNe II, SNe IIn and SNe IIb. The purple square is SN 1987A, the brown square is SN 2023ixf and the red square is SN 2024ggi. Arrows represent upper limits on the rise times as they meet only two of the criteria from Section §3.3.5.1. These peak magnitudes are corrected for Galactic and host extinction, as described in Section §3.3.4.

Fig. 3.4, Type II SNe occupy a large range in this parameter space, highlighting the large diversity present in H-rich CCSNe. The Type IIn SNe are preferentially more luminous and generally longer rising, attributed to their larger and more diffuse CSM components driving a prolonged CSM interaction.

3.3.5.2 Rise Time Limitations

A possible bias emerges when measuring rise times similar to or less than the survey cadence of 2 – 3 d. The discrete sampling of the light curve means rise times on these timescales are typically less well-constrained than longer-rising events, where multiple observations sample the rising phase. With this in mind, we tested the predictive power of the GPR method by taking well-sampled light curves (with cadences $\sim$ 2 d or less between peak $-$ 50 and peak + 200 d where the origin is the first alert detection) and resampled the light curves based on the sampling function of 20 events with much worse and more irregular cadences[7]. Using the actual light curve of the well-observed SN as

[7]Chosen by finding events with an average cadence from peak -50 – peak + 200 d $\geq$ 5 d.

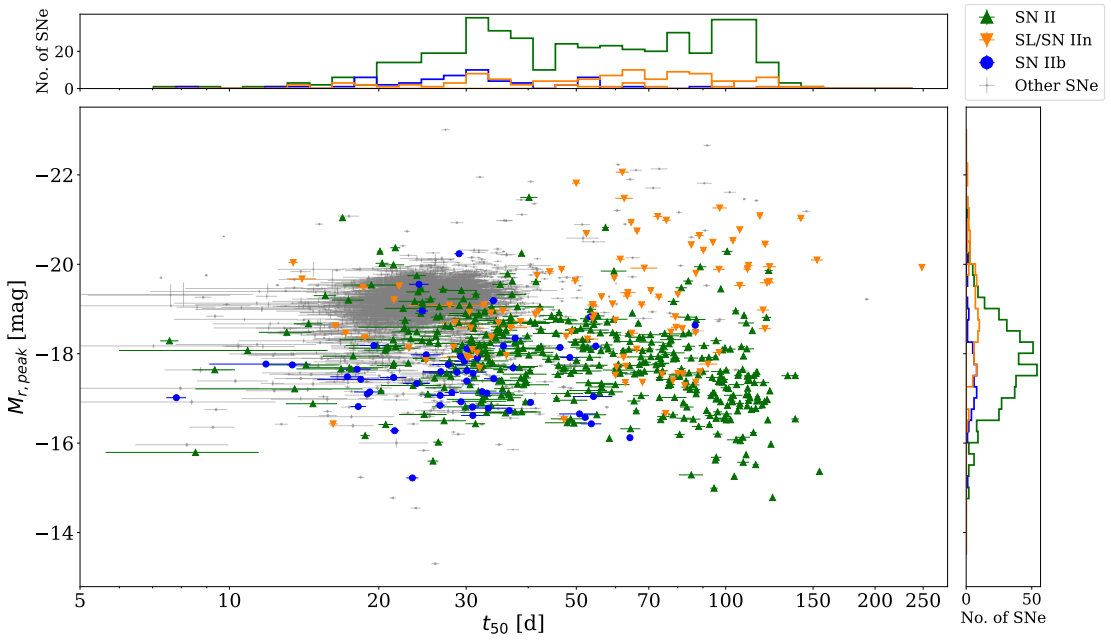

FIGURE 3.5: Phase-space diagram showing peak absolute magnitude in ZTF r ($M_{r,\mathrm{peak}}$) vs. rest-frame duration above half-maximum brightness (t_{50}) for all SNe with $m_{peak} \leq 19$ mag classified in the BTS through December 31, 2023. Type II SNe are colour-coded by subtype, with other SN classes (e.g., Ia, Ib/c, SLSNe-I) shown in grey for comparison. $M_{r,\mathrm{peak}}$ corrected for Galactic extinction only.

the 'ground truth', we shift it according to the sampling function of another light curve to emulate the 'ground truth' light curve being sampled differently.

Applying our standard rise time definition and constraints to these resampled light curves, we confirm that events maintain their classification as fast ($t_{25\_75} \leq 5$ d) or slow ($t_{25\_75} > 5$ d) risers regardless of sampling pattern. This was done to explore the range of a measured rise time based on the sampling function applied to a light curve. We find the range in rise times is increased for shorter rise times compared to longer risers, particularly at $t_{25\_75} \leq 5$ d – see Fig. B.1. For t_{25_75} between 1 – 2 d we see a range of ≈ 0.7 dex, for t_{25_75} between 3 – 5 d we see a range of ≈ 0.4 dex and for $t_{25\_75} > 5$ d there is a range ≈ 0.2 dex.

Our t_{25_75} metric requires consideration for Type IIb SNe, which often show double-peaked light curves due to the SC peak lasting hours to days, followed by a radioactively-powered peak (Chevalier, 1992; Richmond et al., 1994; Chevalier & Fransson, 2008). As we are only concerned with measuring the rise time and peak magnitude for Type IIb and Type IIn and not progenitor properties, this remains an adequate descriptive measurement to characterise these SNe.

3.4 Population Properties

In Fig. 3.5 we show the luminosity-duration phase-space distribution of all classified SNe (Type I and Type II) in the BTS sample (as of December 31st 2023). Fig. 3.5 is included to both show the increased number of events as compared to Perley et al. (2020) (Fig. 7a from 1D interpolation of data points)[8] and to demonstrate the reliability of GPR when measuring light curve parameters due to the likeness between the two figures. Classifications and redshifts used in this work are part of the upcoming BTS classification paper (Qin et al., in prep.) for events with a $m_{peak} \leq 18.5$ mag. For events with a $m_{peak} > 18.5$ mag, we used the current TNS classifications stored on an internal BTS catalogue[8]. We do not expect the provisional nature of these classifications to significantly impact the study.

3.4.1 Overall Distribution

Studies of the relationship between rise time and peak luminosity in Type II SNe have yielded conflicting results. Significant correlations have been reported for Type II, IIb, and IIn SNe (e.g., González-Gaitán et al., 2015; Pessi et al., 2019; Hiramatsu et al., 2024), suggesting the rise and peak may be intrinsically coupled by their power source. However, other analyses find no significant correlation (e.g., Gall et al., 2015; Rubin et al., 2016; Valenti et al., 2016; Nyholm et al., 2020). These discrepant findings likely stem from small sample numbers, limiting their statistical power to comment on population characteristics.

Motivated by the possibility of an enhanced population with fast rises and luminous peaks, either from SBO occurring in the CSM or at the surface of the star, we tested the strength of any existing correlation between t_{25_75} and $M_{g,\mathrm{peak}}$. For Type II SNe, a Spearman rank test between t_{25_75} in ZTF g and $M_{g,\mathrm{peak}}$ finds a correlation, with a correlation coefficient $\rho = -0.21$ and p-value $p < 10^{-5}$. The scatter present in the correlation is likely caused by the large diversity of Type II SNe and lack of clear division within Type II SNe (e.g., IIP vs IIL vs 87A-like) as from Fig. 3.4, it can be seen that Type II SNe occupy both bright and faint, fast and slow regions, see Fig. 3.3.

[8] Also available to see on the BTS Homepage: https://sites.astro.caltech.edu/ztf/bts/bts.php

In our sample of 110 Type IIn SNe (which includes 16 SNe classified as super-luminous), we find $\rho = -0.18$ and p-value $p \sim 0.05$, a correlation both weaker and less significant than the recent findings of Hiramatsu et al. (2024). We see great diversity in our Type IIn light curve morphology, which seems to suggest a range of progenitor pathways are possible, with a large range in t_{25_75} of $\sim$ 2 d to 40 d and $M_{g,\mathrm{peak}}$ of -22.20 to -17.01 mag. As Type IIn SNe are well-understood to be CSM-driven (e.g., Smartt, 2009; Taddia et al., 2013; Ransome et al., 2021), and under this scenario, it is expected that both the rise time and luminosity increase with the amount of CSM present (continuing the interaction), this possible correlation is not surprising (Section §3.7). For Type IIb SNe, we find no significant correlation as $p > 0.1$.

3.4.2 Volume Corrected Distributions

With a highly complete magnitude-limited survey, we can perform a volume correction such that we can offer a more accurate representation of the true distribution of properties for a given population of SNe. The corrections account for intrinsic observational biases that favour the detection of more luminous events since they can be observed to greater distances in a magnitude-limited survey (Malquist bias; Malmquist, 1920).

The volumetric correction we apply is according to a $1/V_{\mathrm{max}}$ weighting (Schmidt, 1968). Initially, we perform a magnitude at $m_{peak} < 18.5$ mag in any filter (based on the GP model peak) given that the BTS is $\gtrsim$95% complete at this level. The peak magnitude cut reduces the sample to 377 Type II SNe, 81 Type IIn SNe, and 35 Type IIb SNe.

For the maximum luminosity distance, $d_{l,\mathrm{max}}$, this is set determined by $\max[d_{l,g,\mathrm{max}}, d_{l,r,\mathrm{max}}]$, where both $d_{l,g,\mathrm{max}}$ and $d_{l,r,\mathrm{max}}$ are calculated assuming a limiting magnitude of 18.5 mag, an average Galactic extinction, A_{Gal}, of 0.19 mag (g) or 0.12 mag (r), calculated using the A_{Gal} of the SNe in the sample, and the peak absolute magnitude of the GP model in the corresponding filter – which are standardised to the rest frame ZTF bands, corrected only for Milky Way extinction and not host extinction. We calculate V_{max} to be $d^3_{l,\mathrm{max}}/(1+z)^3$ (based on the comoving distance), and use its reciprocal for weighting after normalising the weights to unity.

To represent the intrinsic distribution of parameters, we use Kernel Density Estimation (KDE). For each observed value, we generate a normalised Gaussian kernel centred

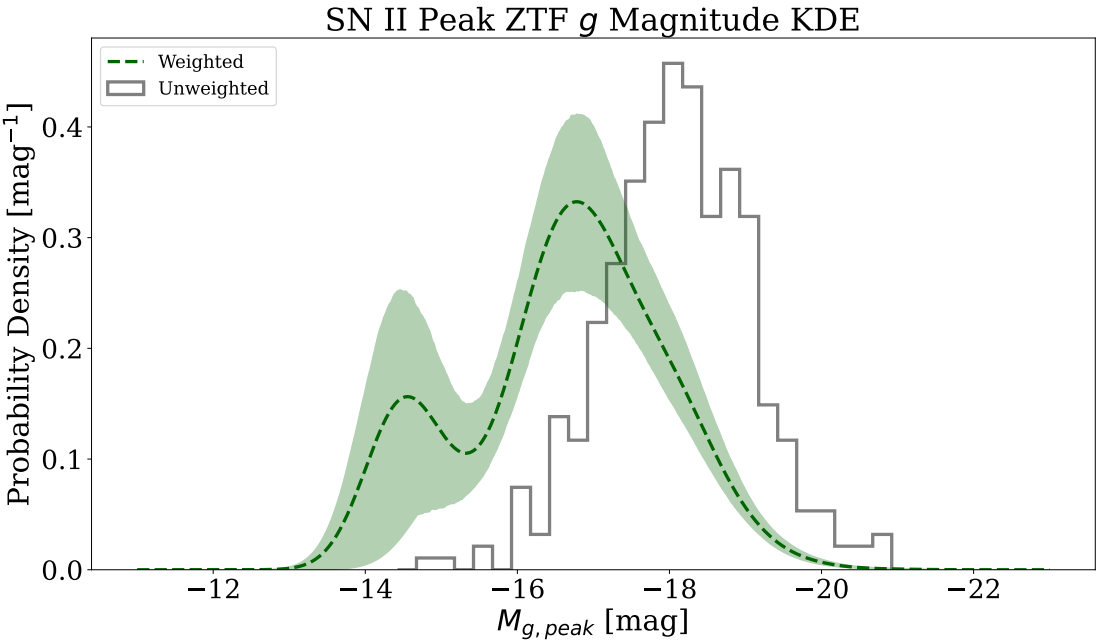

FIGURE 3.6: Type II $M_{g,\mathrm{peak}}$ KDE distribution. We plot the weighted KDE distributions in the darker colours (*dashed* line) and the unweighted histogram in *solid black*.

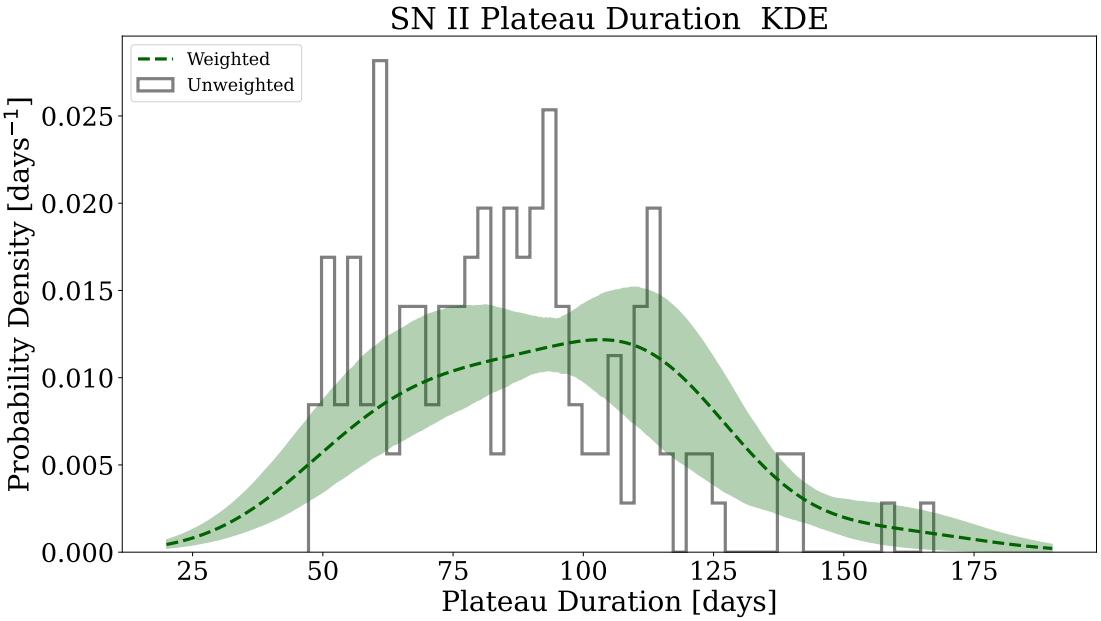

FIGURE 3.7: Type II t_{plat} KDE distribution. Plotted are the weighted KDE and unweighted histogram as described in Fig. 3.6.

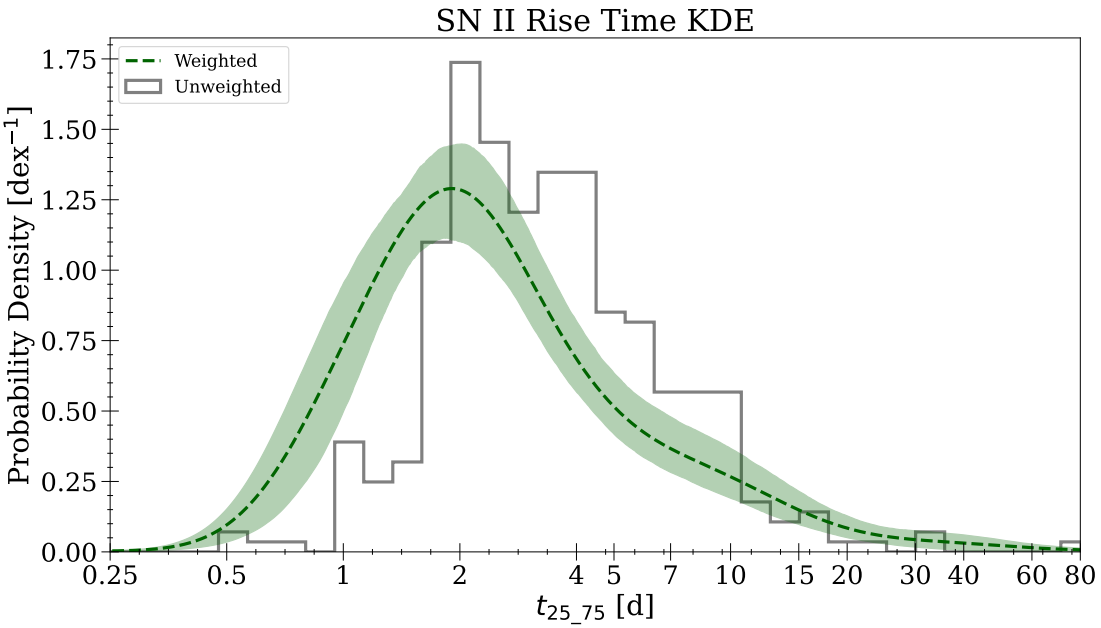

FIGURE 3.8: Type II t_{25_75} KDE distribution and the associated 80% CIs. We plot the weighted KDE distributions in the darker colours (dashed line) and the unweighted histogram in solid black.

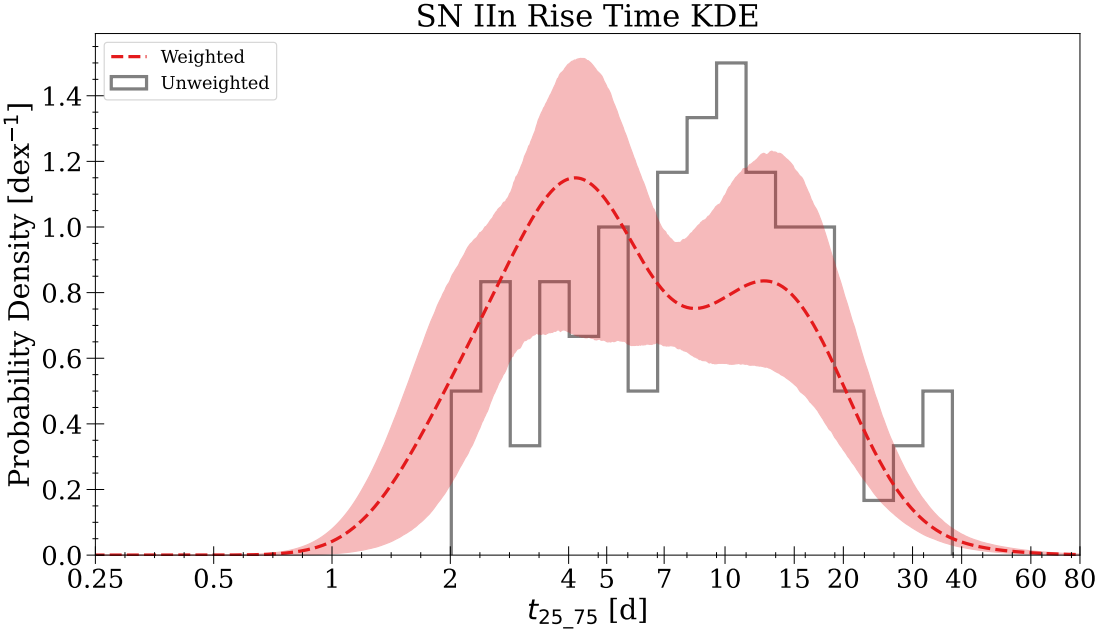

FIGURE 3.9: Type IIn t_{25_75} KDE distribution. The KDE (*dashed*), histogram (*solid*) and CI (*shaded*) are described in Fig. 3.8.

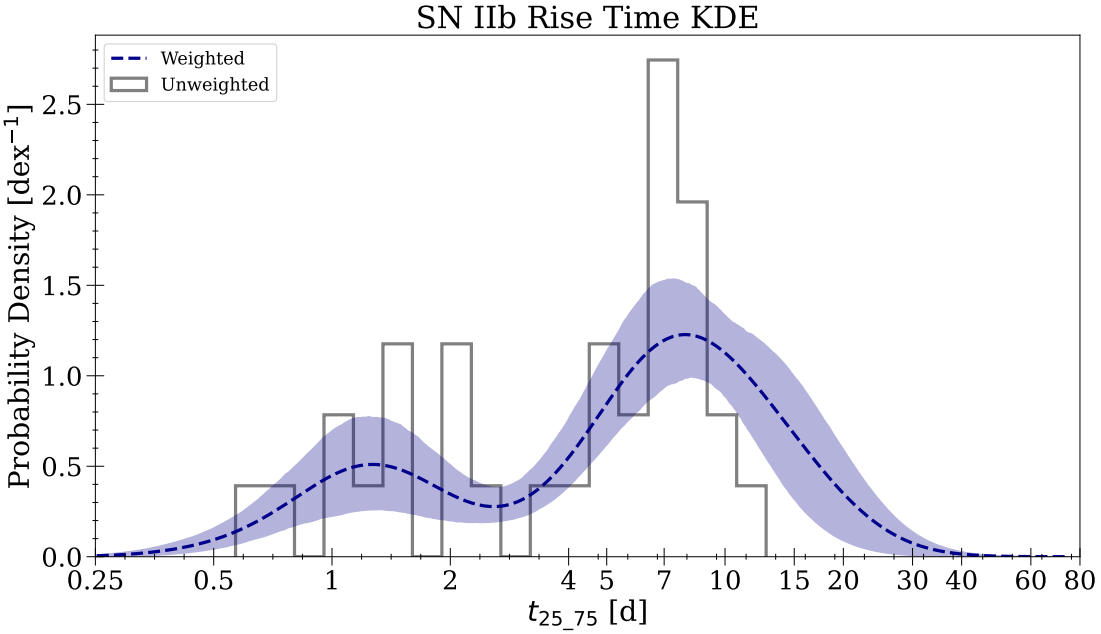

FIGURE 3.10: Type IIb t_{25_75} KDE distribution. The KDE (*dashed*), histogram (*solid*) and CI (*shaded*) are described in Fig. 3.8.

on that real value and weight each Gaussian as $1/V_{\max}$. The width (sigma) of each kernel is optimised using cross-validation (e.g., Wu, 1997). This approach estimates the underlying probability density function of the parameter distribution. We also normalise the KDE by the sum of weights, allowing us to account for Malmquist bias. We also verify this correction and find it performs as expected, see Appendix B.5.

We quantify uncertainty in the weighted KDE as a 80% CI, calculated by bootstrapping our sample with replacement. Similarly, we compute the ECDF with 95% CI for unweighted distributions and bootstrapped 80% confidence intervals for weighted distributions.

3.4.3 Data Exploration

Type	Weighted				Unweighted			
	Mean	25th%ile	50th%ile	75th%ile	Mean	25th%ile	50th%ile	75th%ile
				t_{25_75} [d]				
II (377)	$2.48^{+0.30}_{-0.27}$	$1.65^{+0.57}_{-0.11}$	$2.18^{+0.25}_{-0.23}$	$3.38^{+0.31}_{-0.74}$	$3.39^{+0.12}_{-0.12}$	$2.13^{+0.07}_{-0.08}$	$3.21^{+0.11}_{-0.11}$	$5.09^{+0.47}_{-0.64}$
IIn (81)	$6.01^{+1.09}_{-0.92}$	$3.41^{+0.66}_{-0.94}$	$5.59^{+1.44}_{-1.14}$	$11.83^{+2.10}_{-1.71}$	$8.54^{+0.73}_{-0.67}$	$4.85^{+1.35}_{-1.48}$	$8.73^{+0.86}_{-0.78}$	$14.32^{+3.06}_{-2.22}$
IIb (35)	$4.97^{+1.27}_{-1.01}$	$2.00^{+0.61}_{-2.68}$	$6.32^{+1.72}_{-1.35}$	$8.59^{+0.67}_{-1.69}$	$3.99^{+0.61}_{-0.53}$	$1.79^{+0.69}_{-1.53}$	$4.87^{+0.93}_{-0.78}$	$7.54^{+0.89}_{-1.03}$
				$M_{g,\mathrm{peak}}$ [mag]				
II (377)	-16.59 ± 0.29	$-16.03^{+0.28}_{-0.39}$	-16.71 ± 0.25	$-17.44^{+0.22}_{-0.09}$	-18.10 ± 0.05	$-17.54^{+0.10}_{-0.15}$	-18.11 ± 0.05	$-18.74^{+0.16}_{-0.08}$
IIn (81)	-18.19 ± 0.19	$-17.68^{+0.14}_{-0.12}$	-18.02 ± 0.21	$-18.82^{+0.56}_{-0.43}$	-19.35 ± 0.13	$-18.49^{+0.56}_{-0.43}$	-19.32 ± 0.13	$-19.98^{+0.55}_{-0.27}$
IIb (35)	-17.79 ± 0.17	$-17.45^{+0.12}_{-0.16}$	-17.79 ± 0.19	$-18.37^{+0.35}_{-0.24}$	-18.15 ± 0.14	$-17.58^{+0.31}_{-0.27}$	-18.09 ± 0.14	$-18.76^{+0.46}_{-0.40}$
				$(g-r)_{g,\mathrm{max}}$ [mag]				
II (377)	0.17 ± 0.05	$0.01^{+0.01}_{-0.02}$	0.09 ± 0.03	$0.25^{+0.09}_{-0.14}$	0.04 ± 0.01	$-0.04^{+0.02}_{-0.02}$	0.02 ± 0.01	$0.08^{+0.02}_{-0.03}$
IIn (81)	0.21 ± 0.08	$0.00^{+0.01}_{-0.02}$	0.10 ± 0.07	$0.49^{+0.32}_{-0.02}$	0.11 ± 0.02	$-0.01^{+0.01}_{-0.02}$	0.08 ± 0.01	$0.16^{+0.06}_{-0.05}$
IIb (35)	0.25 ± 0.06	$0.00^{+0.02}_{-0.04}$	0.26 ± 0.06	$0.41^{+0.04}_{-0.04}$	0.13 ± 0.04	$-0.03^{+0.11}_{-0.04}$	0.12 ± 0.04	$0.31^{+0.16}_{-0.07}$
				t_{plat} [d]				
II (151)	93.86 ± 6.39	$71.89^{+10.63}_{-6.87}$	93.88 ± 7.96	$112.50^{+14.85}_{-1.25}$	83.98 ± 2.11	$61.25^{+2.51}_{-5.47}$	82.29 ± 2.19	$96.45^{+4.75}_{-9.81}$

TABLE 3.4: Mean and median of the volume corrected KDE for t_{25_75}, ZTF $M_{g,\mathrm{peak}}$, $(g-r)_{g,\mathrm{max}}$ and t_{plat} in the final sample, measured directly using the GPR described in Sections §3.3.3 and §3.3.3.1. Uncertainties reported here are the 1 σ standard deviation on the bootstrapped values.

After weighting the distributions, we create weighted KDEs for direct light curve properties of Type II SNe $M_{g,\mathrm{peak}}$, t_{plat}, Figs. 3.6 for all classes and Figs. 3.8. We extract various statistical properties relating to t_{25_75}, $M_{g,\mathrm{peak}}$, $(g-r)_{g,\mathrm{max}}$ and t_{plat} of each subclass from the KDE distributions and show these in Table 3.4, with uncertainties based on the 1 σ standard deviations for each quantity.

Our demographic analysis of Type II SNe reveals a median absolute magnitude of $M_{g,\mathrm{peak}} = -16.71 \pm 0.25$ mag and a median rise time of $t_{25\_75} = 2.18^{+0.25}_{-0.23}$ d. From the volume-weighted ECDF, we find that 82^{+11}_{-12}% of the population has $M_{g,\mathrm{peak}} \leq -15$ mag, with the first and third quartiles at -16.03 and -17.44 mag, respectively. Most notably, 84 ± 3% of the weighted population exhibits remarkably brief rise times (≤ 5 d), with first and third quartiles at 1.65 d and 3.38 d. These distributions highlight the significant heterogeneity within the Type II SN population.

3.5 Methods II – Comparison to Simulated Light Curves

Light curve models are increasingly incorporating CSM or extended stellar envelopes (e.g., Hillier & Dessart, 2012; Dessart et al., 2015; Dessart et al., 2017; Das & Ray, 2017; Morozova et al., 2018; Pearson et al., 2023; Tinyanont et al., 2022; Moriya et al., 2023; Morag et al., 2023). Morozova et al. (2018) demonstrated that including CSM in `SNEC` [9] (Morozova et al., 2015) models significantly improved fits for 20 well-observed, multi-band light curves to estimate progenitor parameters, such as R_{CSM}, CSM density, and M_{CSM} – see Figs. 2 and 3 and Table 2 in Morozova et al. 2018. Similar conclusions emerge from studies by Das & Ray (2017), Bruch et al. (2023), Moriya et al. (2023), Irani et al. (2024), and Jacobson-Galán et al. (2024a), which collectively find that substantial CSM masses near Type II SN progenitors are common and deposited shortly before core-collapse.

While fitting detailed physical models to the entire BTS Type II sample is possible, the computational demands and data heterogeneity make empirically derived relationships more practical for large-scale analysis. Our GP parameter catalogue enables efficient estimation of CSM properties through the use of empirical relations. Additionally, we

[9] Supernova ExplosioN Code.

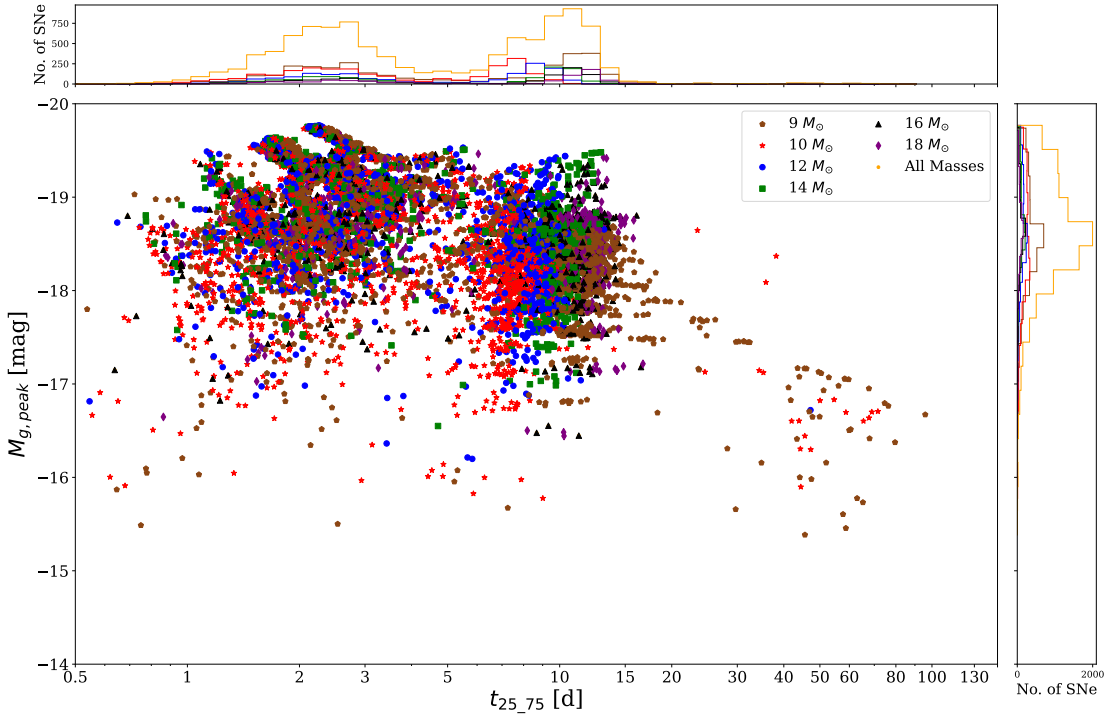

FIGURE 3.11: t_{25_75} vs $M_{g,\mathrm{peak}}$ distribution for the theoretical light curve grid from M23, with points drawn from a sample of 10,000 models colour-coded by progenitor mass. Models are weighted by $V_{\mathrm{max}} \times M_{\mathrm{ZAMS}}^{-2.35}$, combining volume-limited sampling (calculated using a magnitude limit of 18.5 mag) with the Salpeter initial mass function. This weighting scheme reproduces both the observational bias against fainter events and the natural frequency of different progenitor masses.

leverage this catalogue to investigate progenitor iron core masses ($M_{\mathrm{Fe,Core}}$), which significantly influence neutron star formation and properties (Barker et al., 2022; Barker et al., 2023). By applying simulation-based empirical relations to our light curve parameters, we provide constraints on $M_{\mathrm{Fe,Core}}$ distributions (see appendix B.7).

3.5.1 Measuring Theoretical Light Curve Metrics

To probe the physical origin of the rise time distribution shown in Fig. 3.4, we leverage our highly complete observational sample and the extensive grid of theoretical light curves from Moriya et al. (2023) (hereafter M23) using `STELLA` (Blinnikov et al., 1998, 2000, 2006). This comparison between observations and models enables us to systematically explore how progenitor and CSM properties shape the observed diversity. The models from M23 are some of the most comprehensive performed to date, as they sample several progenitor zero-age main sequence masses, (M_{ZAMS}; 9 – 18 $\mathrm{M}_\odot$), $\dot{M}$

(10^{-5} – 10^{-1} $M_\odot$ yr^{-1}), RSG wind structure parameter, (β[10]; 0.5 – 5) and R_{CSM} (10^{14} – 10^{15} cm) among other progenitor properties (see Table 2 in M23 for more details). The published grid contains over 200,000 models sampled from these parameters and is a base for comparing observed light curves.

To derive M_{CSM}, we first calculate the wind velocity, v_{wind}, at R_{CSM} using the velocity profile from Eq. 2 in Moriya et al. (2023), which depends on β and the progenitor radius $R_\odot$. M_{CSM} is calculated using $M_{CSM} = \dot{M} \times R_{CSM} / v_{wind}$.

We measure various rise times – including the same t_{25_75} described in Section §3.3.5 – directly from the M23 ZTF bandpass light curves, in addition to absolute magnitudes (at peak and various N days after peak), magnitude decline rates and colours, e.g., $(g - r)_{g,max}$ – Fig. 3.1 shows example measurements using ZTF SN light curves.

With the empirically measured light curve parameters from M23, we create a similar luminosity-rise distribution plot[11] of t_{25_75} vs $M_{g,peak}$ in ZTF g – see Fig. 3.4. We apply a probabilistic weighting of $V_{max} \times M_{ZAMS}^{-2.35}$ to the M23 models to mimic the combined effects of the initial mass function (IMF; Salpeter, 1955) and Malmquist bias on an observed sample, and draw 10,000 events to show in Fig. 3.11

In Fig. 3.11, we see a clear bi-modality, suggesting the dichotomy seen in observations is reflecting the transition between purely shock cooling (SC) dominated rises and rises dominated by the interaction heating from SBO shocking the CSM (e.g., Irani et al., 2024; Jacobson-Galán et al., 2024a). Correlation tests between progenitor-SN parameters confirm this dichotomy stems from significant relationships between CSM properties and light curve observables, as well as between different CSM parameters[12]. This is further evidenced by the colour gradient seen when we apply a colour map based on $\dot{M}$ or R_{CSM} – see appendix B.6 for further details.

Two distinct populations emerge in the theoretical models: fast risers ($t_{25\_75} \leq 5$ d) with moderately more luminous peaks, possessing higher M_{CSM} and smaller R_{CSM} (e.g., confined and dense); and slower risers ($t_{25\_75} > 5$ d) with overall less luminous peaks, less massive M_{CSM} and larger R_{CSM} (e.g., less confined and less dense). Within the slower population, the most luminous events still require substantial M_{CSM}, suggesting CSM

[10]Determined by the efficiency of wind acceleration, for RSGs $\beta > 1$ (Moriya et al., 2023).

[11]We also included unpublished 9 and 10 $M_\odot$ mass progenitor models with lower and higher explosion energies than in M23.

[12]Correlations between CSM parameters likely reflect physics pre-defined in the simulations.

mass remains a key driver of peak luminosity. This bi-modality emerges naturally from the underlying physics rather than parameter choices, hinting at fundamental differences in mass-loss mechanisms.

For slower-rising events, the correlation between t_{25_75} and CSM parameters lessens, giving way to a stronger dependence on progenitor mass ($M_{\rm ZAMS}$), which serves as a proxy for progenitor radius. This transition reflects both the increasing dominance of light travel time and diffusion processes in more massive, extended progenitors, as well as the slower cooling of the shocked envelope (e.g., Nakar & Sari, 2010; Ofek et al., 2010; Tominaga et al., 2011; Morozova et al., 2016; Irani et al., 2024). Notably, for events with longer rise times (≥ 5 d), the progenitor radius influences rise time by affecting the SBO time and location (Chevalier & Irwin, 2011; Moriya et al., 2011; Svirski et al., 2012; González-Gaitán et al., 2015; Morozova et al., 2016), though the light curve evolution is still predominantly shaped by CSM interaction rather than envelope cooling, depending critically on the CSM density profile (Moriya et al., 2023; Irani et al., 2024).

Notably, the contrast between the smooth distribution in our observational data (Fig. 3.4) and the distinct bi-modality in theoretical models (Fig. 3.11) implies that there are physical process that lead to restrictive prior distributions on progenitor properties, deviating notably from the exploratory, uniform parameter sampling employed in M23 for physical progenitor parameters.

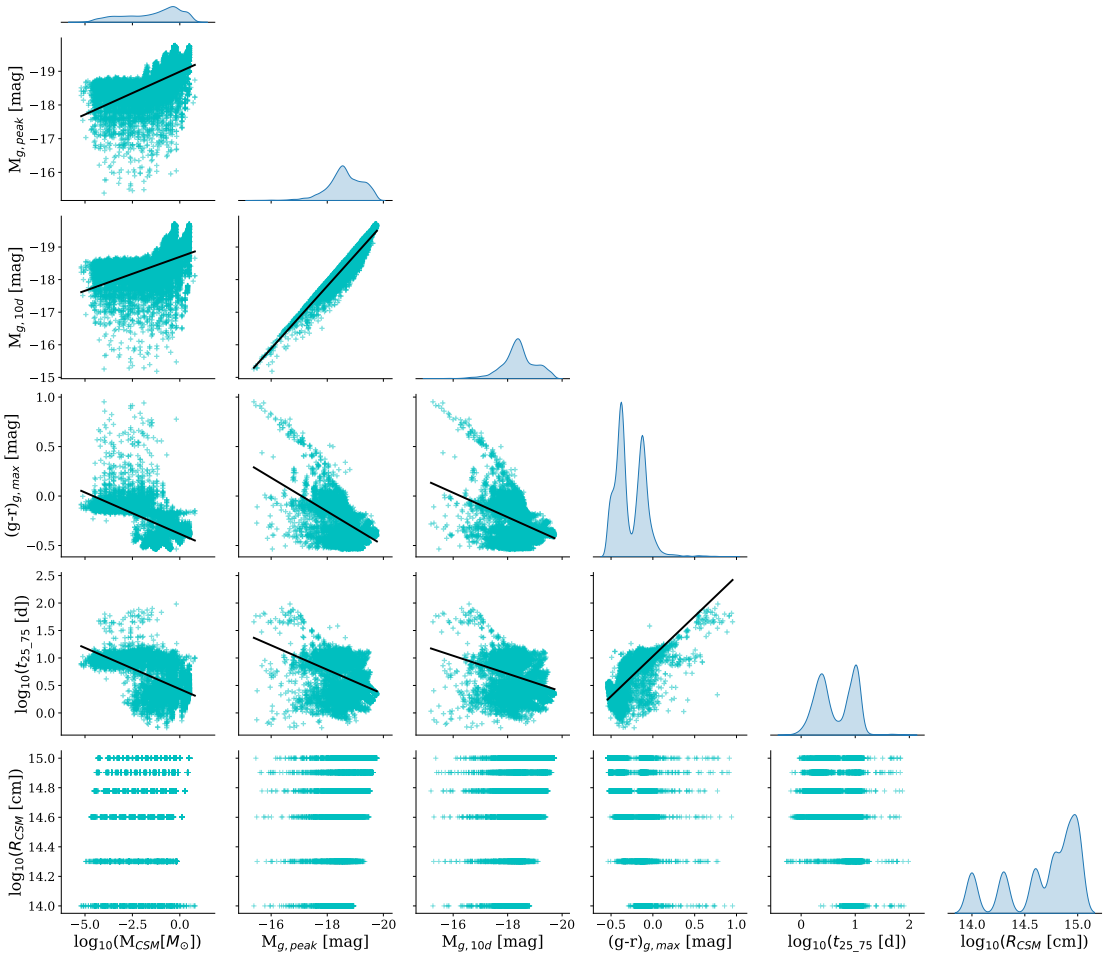

FIGURE 3.12: Corner plot showing the relationship between M23 theoretical light curve parameters measured in this work, t_{25_75}, $M_{g,\mathrm{peak}}$, $(g-r)_{g,\mathrm{max}}$ and $M_{g,10\mathrm{d}}$ to the M_{CSM} and R_{CSM} values returned in the modelling. The solid black line is a first-order polynomial fit to the data.

Data Regime	Formula	Order	D.o.F	$M_{\rm CSM}$			$R_{\rm CSM}$		
				R^2	BIC	RMS [dex]	R^2	BIC	RMS [dex]
All	Eq. 2	1	298980	0.47	839466	0.30	0.14	175163	0.12
All	Eq. 3	2	298970	0.57	777999	0.28	0.23	141781	0.12
All	Eq. 4	3	298950	0.62	736557	0.26	0.28	121588	0.11
≤ 5 d	Eq. 2	1	112263	0.45	210328	0.21	0.47	-89654	0.07
≤ 5 d	Eq. 3	2	112253	0.52	193260	0.20	0.53	-103416	0.06
≤ 5 d	Eq. 4	3	112233	0.58	180362	0.19	0.55	-109371	0.06
> 5 d	Eq. 2	1	186711	0.29	536827	0.31	0.04	146335	0.13
> 5 d	Eq. 3	2	186701	0.41	502875	0.29	0.07	138972	0.13
> 5 d	Eq. 4	3	186681	0.48	480037	0.27	0.12	129340	0.13

TABLE 3.5: Comparing the performance over different orders of polynomials used in the multiple regression to determine the relations between observed features and CSM properties, $M_{\rm CSM}$ and $R_{\rm CSM}$, using models from M23.

3.6 Physical Progenitor Property Inference Analysis

To quantify the percentage of RSGs that are surrounded by significant components of CSM at the time of core-collapse, we use the early light curve to infer the presence and properties of CSM. As the rise of Type II SNe is highly sensitive to the CSM parameters and progenitor radius (e.g., Morozova et al., 2016, 2018; Pearson et al., 2023; Tinyanont et al., 2022; Moriya et al., 2023; Irani et al., 2024), we can estimate and place constraints on these properties from photometry alone. The high cadence and good coverage on the rise specifically, combined with the high completeness of the BTS lends itself well to such a detailed study.

3.6.1 Defining Light Curve - CSM Relations

We examined relationships between observational and progenitor parameters by performing systematic correlation tests across the M23 model grid. Fig. 3.12 reveals significant pairwise correlations between progenitor properties (e.g., $M_{\rm CSM}$ and $R_{\rm CSM}$) and the observational parameters measured in this work ($M_{g,\rm peak}$ and t_{25_75}), providing a statistical foundation for our subsequent parameter estimation.

When we analyse simple two-variable analysis, e.g., $M_{\rm CSM} = f\,(M_{g,\rm peak},\ t_{25\_75})$, the relations show substantial scatter, indicating that these parameters alone cannot capture the complex CSM-ejecta interaction physics. To better characterise the evolution, we decompose the rise time into: 20 – 60%, t_{20_60}, and 60 – 90%, t_{60_90}, or 20 – 50%, t_{20_50}, and 50 – 80%, t_{50_80}. This approach provides additional diagnostics through the shape of the rise. Additionally, we include ZTF $g-r$ colour at ZTF g peak flux, $(g-r)_{g,\rm max}$, and the ZTF g absolute magnitude at 10 d post ZTF g peak, $M_{g,\rm 10d}$, to account for any contribution to the early plateau or post-peak behaviour by the CSM (or lack of). We perform multiple regression analysis, attempting to express $M_{\rm CSM}$ empirically as $M_{\rm CSM} = f\,(M_{g,\rm peak},\ t_{20\_60},\ t_{60\_90},\ (g-r)_{g,\rm max},\ M_{g,\rm 10d})$ and a similar expression for $R_{\rm CSM}$.

We analyse the relationship between CSM parameters and observables using multivariate polynomial regression, implemented via the `statsmodels ols` package in `python`.

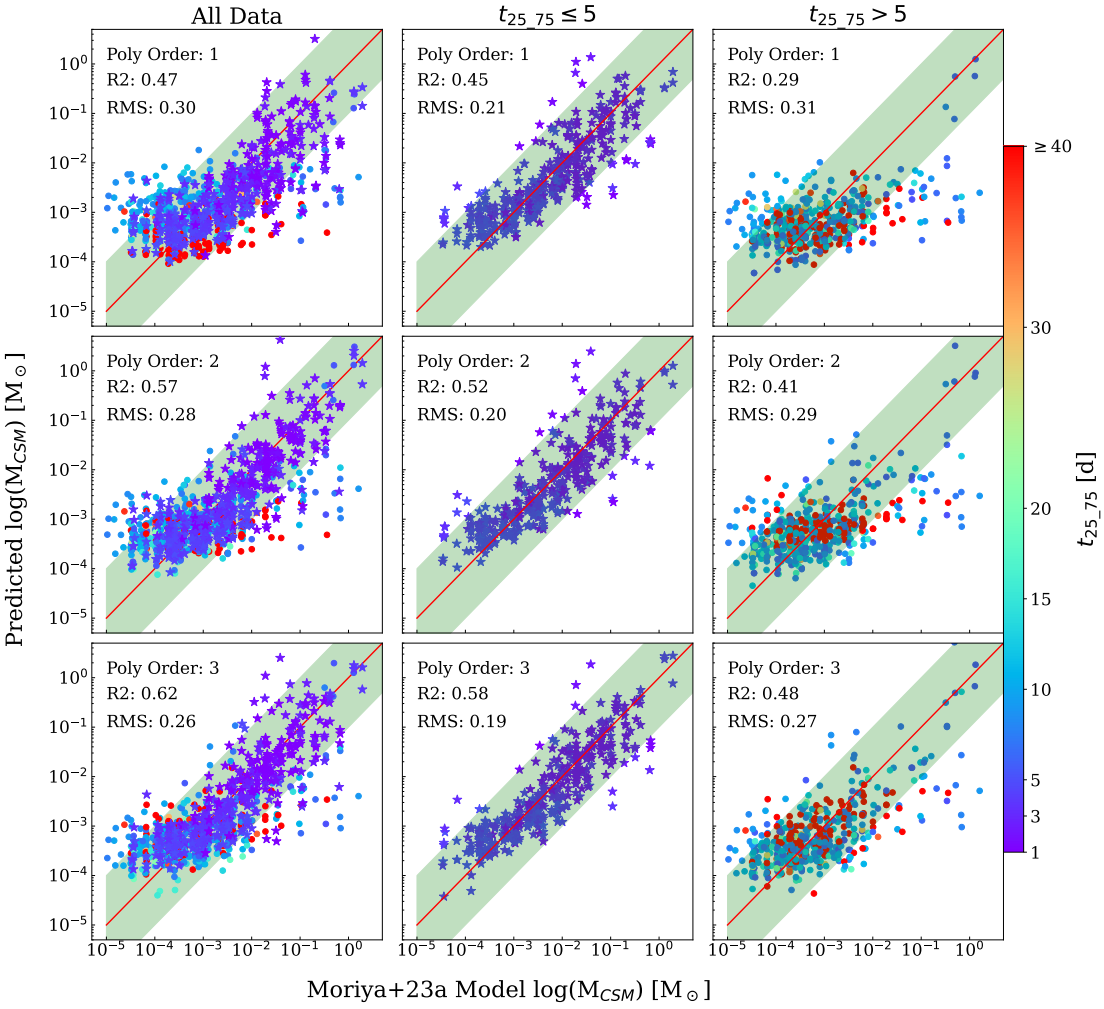

FIGURE 3.13: Multivariate analysis results of the predicted $M_{\rm CSM}$ mass (y-axis) vs. the M23 $M_{\rm CSM}$ mass (x-axis). The top, middle and bottom rows are polynomial orders 1, 2 and 3, respectively. The first column contains all the data, and stars are those with $t_{25\_75} \leq 5$ d with the 2nd and 3rd rows containing only data with $t_{25\_75} \leq 5$ d and $t_{25\_75} > 5$ d to show how the correlations predictive power decreases significantly with $t_{25\_75} \geq 5$ d. The diagonal red line is the 1:1 line, with the green shaded region showing 1 order of magnitude above and below. 1,000 models were used in the plot to avoid overcrowding.

For $M_{\rm CSM}$, we achieve $R^2 > 0.5$ across most polynomial orders, indicating robust correlations. The relationships with $R_{\rm CSM}$ exhibit somewhat weaker but still significant correlations, as detailed in Table 3.5. Our goal is to develop reliable predictive relationships that enable rapid estimation of physical parameters ($M_{\rm CSM}$ and $R_{\rm CSM}$) from observable quantities such as t_{25_75} and $M_{g,\rm peak}$.

The performance of each polynomial order is analysed using the Bayesian Information Criterion (BIC; Table 3.5). We split the correlation testing into $t_{25\_75} \leq 5$ d and > 5 d

as the correlation appears strongest for the fast-rising models $t_{25\_75} \leq 5$ d and under-predicts $M_{\rm CSM}$ for several long-rising $t_{25\_75} > 5$ d models by up to 1 – 2 orders of magnitude – see Fig. 3.13. This likely reflects the physics of CSM interaction: confined, dense CSM shells enable rapid conversion of kinetic energy to radiation, producing brief, bright emission with fast rise times (e.g., Moriya et al., 2011; Chevalier, 2012; Tinyanont et al., 2022; Pearson et al., 2023; Li et al., 2024). In contrast, longer rise times can result from either more extended CSM configurations where energy is released more gradually, or from different physical processes entirely, weakening the direct correlation between $M_{\rm CSM}$ and light curve properties (e.g., Moriya, 2023; Jacobson-Galán et al., 2024a).

The systematic under-prediction of $M_{\rm CSM}$ for models with higher masses and longer rise times motivated our inclusion of post-peak magnitude as an additional predictor variable. For $R_{\rm CSM}$, the strongest correlations are consistently found in the subset of models with $t_{25\_75} \leq 5$ d.

We restrict polynomial orders to 3 or less to avoid introducing unphysical complexity into the model. For $M_{\rm CSM}$, the reduction in residuals and increasing R^2 from first to third order indicates improved model performance, with third-order polynomials providing the best balance between model complexity and fit quality across both data regimes ($t_{25\_75} \leq 5$ d and > 5 d), highlighting the importance of curvature terms in the relation. To better visualise the scatter in these correlations, we add 10% random scatter to the plotted $R_{\rm CSM}$ values in Fig. B.15.

$R_{\rm CSM}$ measurements become most reliable in regimes where $M_{\rm CSM}$ is large enough to influence observables such as $M_{g,\rm peak}$ and t_{25_75} significantly (e.g., make $M_{g,\rm peak}$ brighter or t_{25_75} shorter). We determine the critical value – below which the CSM does not notably influence the early light curve – of $M_{\rm CSM}$ by varying the physical parameters $\dot{M}$, $R_{\rm CSM}$, and β independently (noting that $M_{\rm CSM}$ is a function of these three variables within the model). Below this minimum $M_{\rm CSM}$, the CSM will become too diffuse to meaningfully influence the early light curve evolution, effectively transitioning to a regime where CSM interaction is negligible. This physical expectation is reinforced by the distinct bi-modality observed in M23's theoretical models,

Fig. 3.11, which reveals these two distinct populations: one where CSM properties strongly correlate with observables ($M_{g,\rm peak}$ and t_{25_75}); and another showing no clear correlation, indicating negligible CSM influence. Our analysis reveals an observational

transition at $M_{\rm CSM} \approx 10^{-2.5}$ $M_\odot$, below which we cannot detect significant changes in observed parameters ($M_{g,\rm peak}$ and t_{25_75}) – see appendix B.10 for more details. Given this limitation, we restrict our subsequent analysis of $R_{\rm CSM}$ and $\dot{M}$ to events where the predicted $M_{\rm CSM}$ exceeds this threshold.

When we reanalysed the $R_{\rm CSM}$ correlations with this $M_{\rm CSM}$ threshold ($\geq 10^{-2.5}$ $M_\odot$), we find substantially stronger correlations, especially for rapid-rise events ($t_{25\_75} \leq 5$ d). For these rapid-rise events, our third-order polynomial fit achieves $R^2 = 0.59$ with an RMS scatter of 0.06 dex. Slower-rising events ($t_{25\_75} > 5$ d) still show a weaker correlation with $R^2 = 0.38$ and larger scatter (RMS = 0.10 dex). Based on these results, we adopt the third-order polynomial fits for $R_{\rm CSM}$ in both time regimes.

3.6.2 Mass-Loss Rate

The conversion of $M_{\rm CSM}$ estimates to $\dot{M}$, Eq. 3.6.2, requires the stellar wind velocity (v_{wind}). Although M23's models are parameterised using $\dot{M}$ (which implicitly assumes a wind velocity), the resulting light curves depend solely on the CSM density profile at the time of explosion. Consequently, our $M_{\rm CSM}$ measurements can be directly compared to their models, with the assumed wind velocity affecting only the conversion between $M_{\rm CSM}$ and $\dot{M}$, not the underlying physics.

$$\frac{\dot{M}}{\mathrm{M_\odot\ yr^{-1}}} = \left(\frac{M_{CSM}}{\mathrm{M_\odot}}\right)\left(\frac{v_{wind}}{\mathrm{10\ km\ s^{-1}}}\right)\left(\frac{R_{CSM}}{\mathrm{10^{14}\ cm}}\right)^{-1}$$

For Type II SNe, we assume a stellar wind velocity of 10 km s^{-1}, consistent with previous literature (e.g., Davies et al., 2022; Moriya et al., 2023). We also calculate the time in which the mass was removed $t_{removal} \sim R_{CSM}/v_{wind}$. While M23 explored $R_{\rm CSM}$ from 10^{14} – 10^{15} cm, we cannot uniquely determine $\dot{M}$ from our observations alone. For comparison with previous studies, we adopt a fiducial value of $R_{\rm CSM} = 5{\times}10^{14}$ cm.

3.6.3 Progenitor Property Volume Corrected Distributions

After weighting the distributions, we create weighted KDEs for empirically derived progenitor properties $M_{\rm CSM}$, $\dot{M}$ and $R_{\rm CSM}$ – see Figs. 3.14, 3.15 and 3.16 respectively.

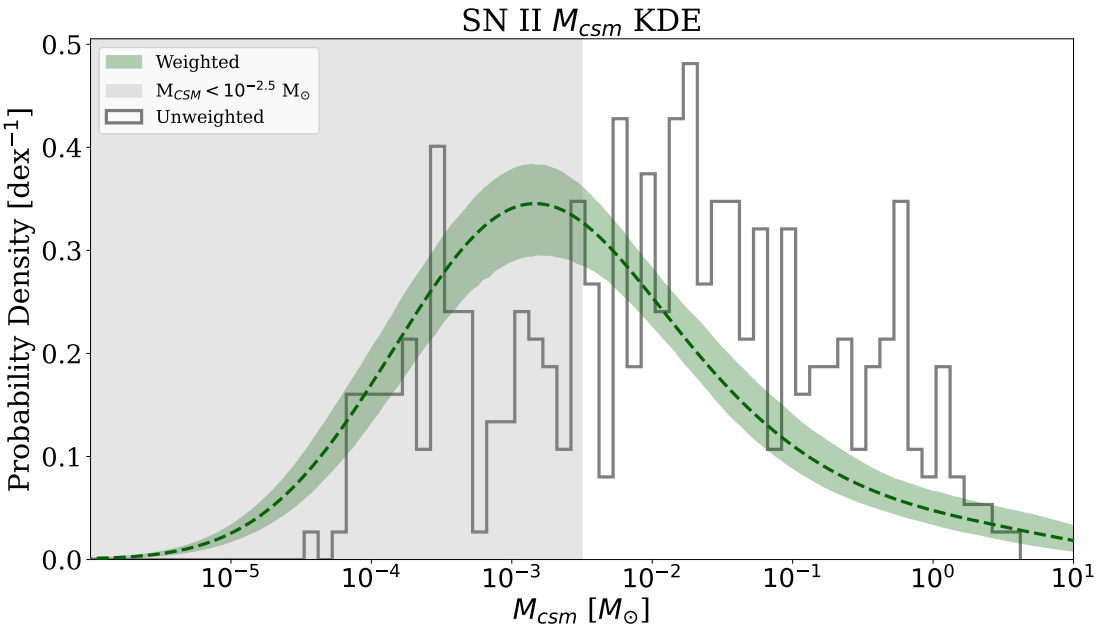

FIGURE 3.14: $M_{\rm CSM}$ KDE distribution along with the associated 80% CI. The weighted distribution is in dark green (*dashed* line) and the unweighted normalised histogram is in *black*. The shaded region on the KDE shows the region below $10^{-2.5}$ $M_\odot$ (or corresponding to) where we find CSM does not impact observables.

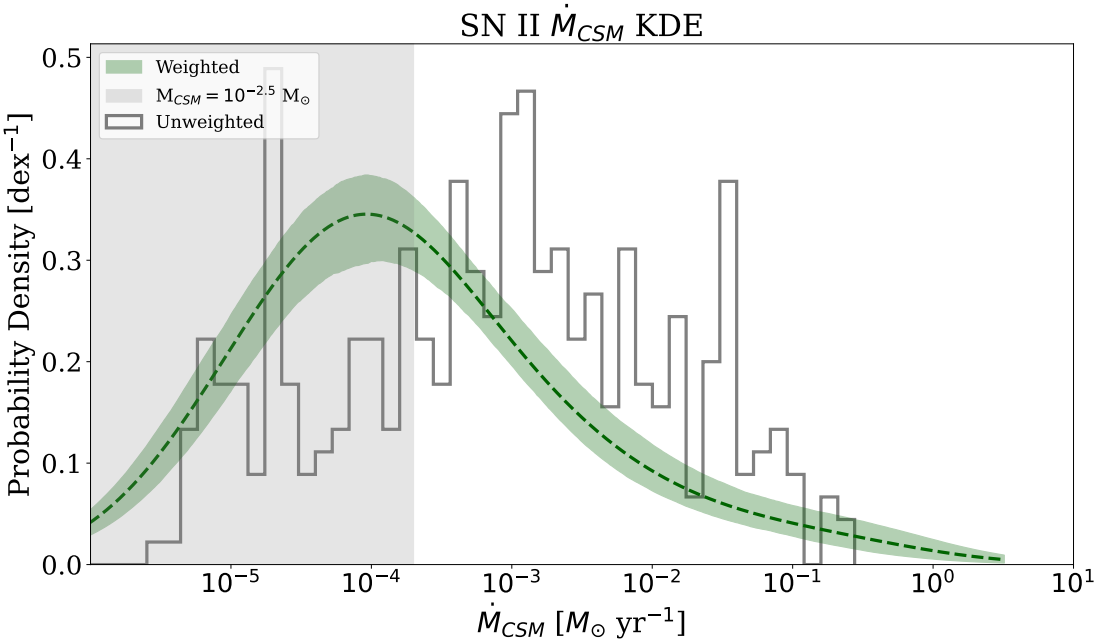

FIGURE 3.15: $\dot{M}$ KDE distribution along with the associated 80% CI. Shading is the same as described in Fig. 3.14.

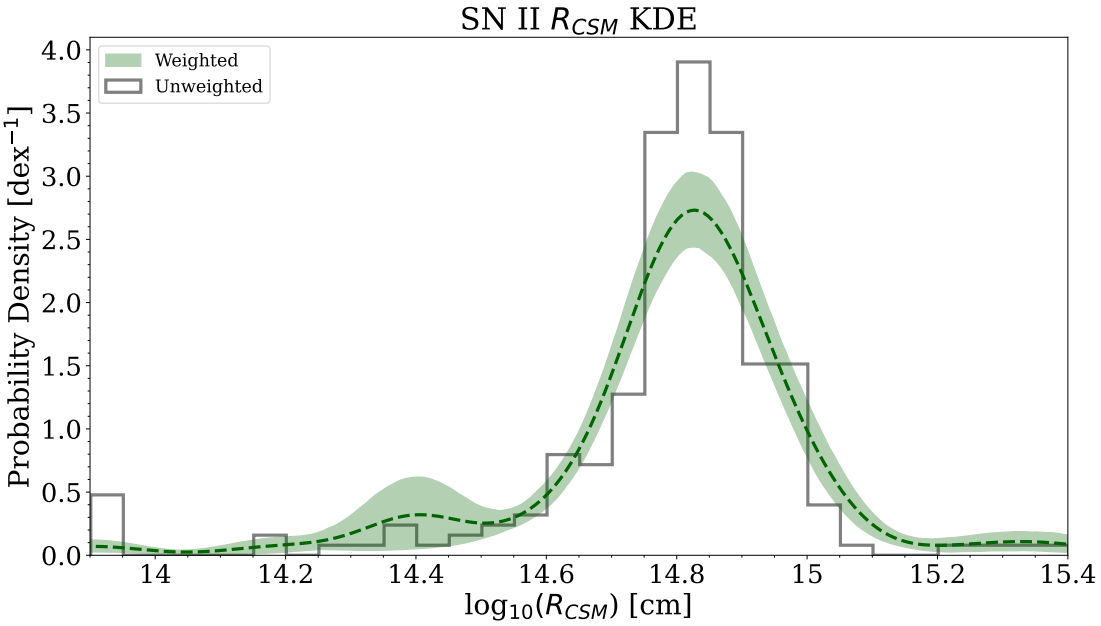

FIGURE 3.16: $R_{\rm CSM}$ KDE distribution along with the associated 80% CI.

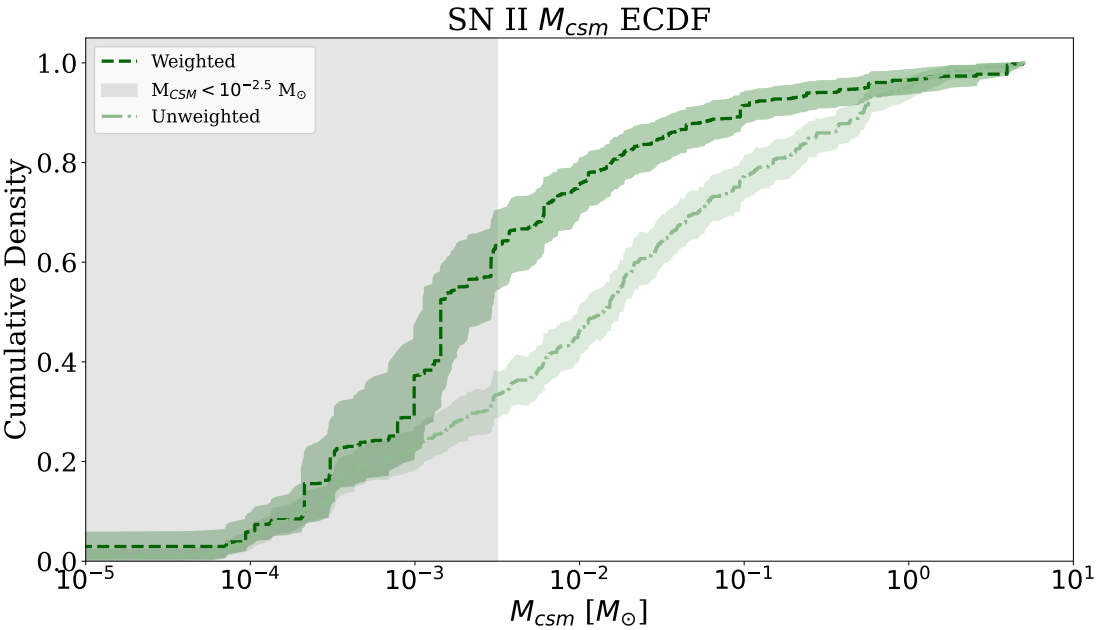

FIGURE 3.17: Type II $M_{\rm CSM}$ weighted (*dark green*) and unweighted (*light green*) ECDF. We plot the 80% CI for the weighted ECDF and the 95% CI for the unweighted ECDF. The shaded region on the ECDF is the same as applied in Figs. 3.14 and 3.15.

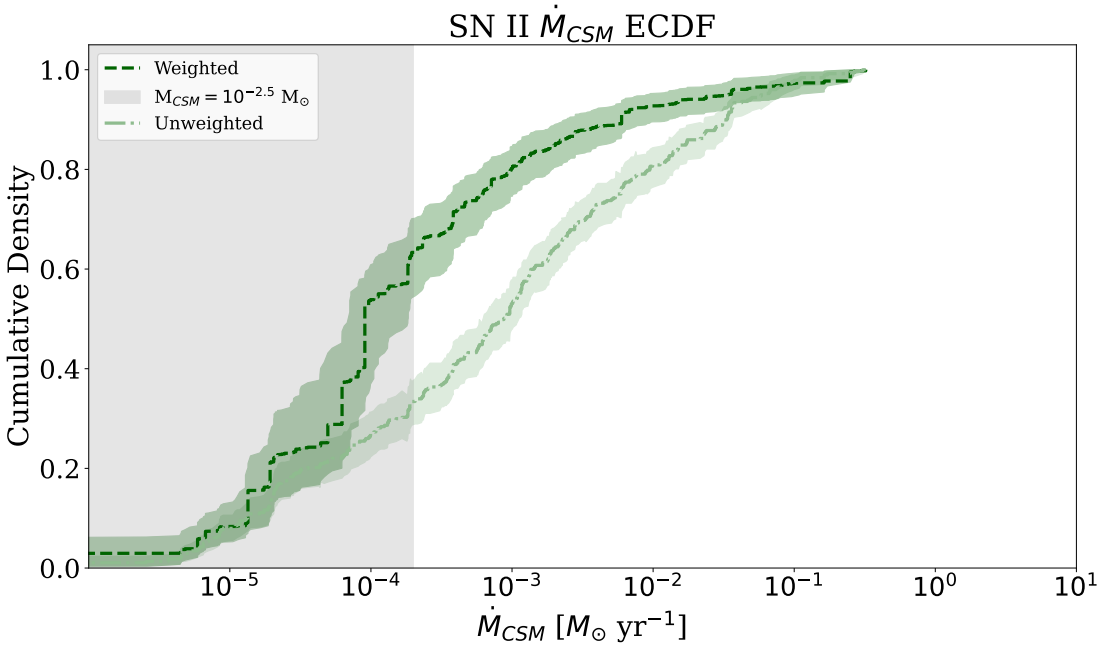

FIGURE 3.18: Type II $\dot{M}$ weighted (*dark green*) and unweighted (*light green*) ECDF. CI's and shading described in Fig. 3.17.

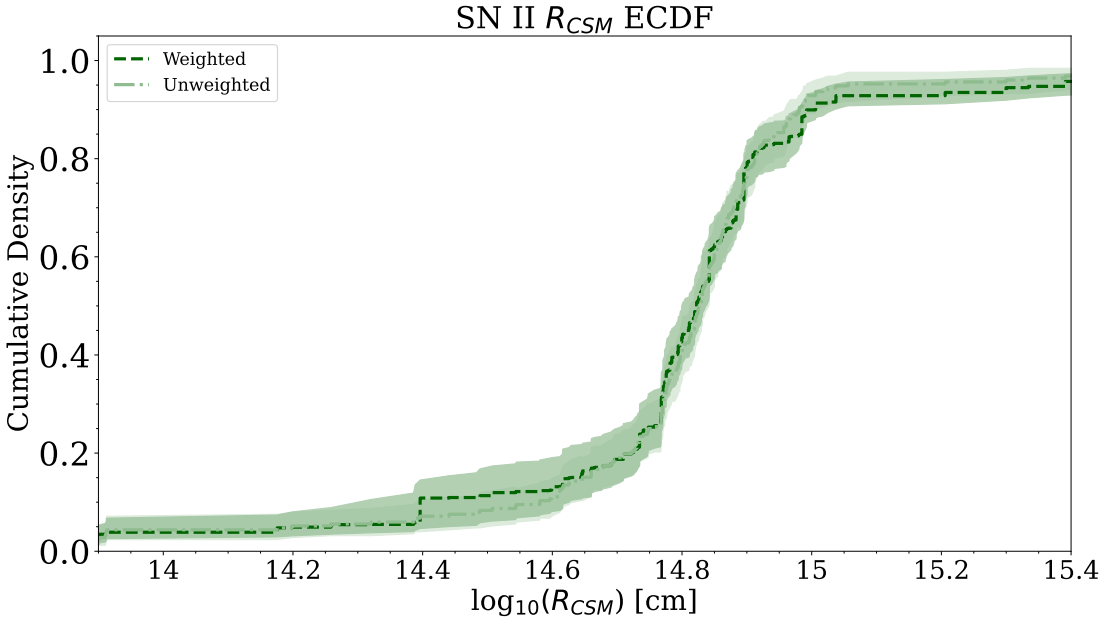

FIGURE 3.19: Type II $R_{\rm CSM}$ weighted (*dark green*) and unweighted (*light green*) ECDF. For $R_{\rm CSM}$, we exclude data where the corresponding $M_{\rm CSM} < 10^{-2.5}$ $M_\odot$ as we consider $M_{\rm CSM}$ lower than this to have a negligible effect on the observable parameters.

For comparison, recent studies of SN 2023ixf (e.g., Hosseinzadeh et al., 2023; Hiramatsu et al., 2023; Jencson et al., 2023; Jacobson-Galán et al., 2023; Li et al., 2024; Zimmerman et al., 2024) and SN 2024ggi (e.g., Jacobson-Galán et al., 2024b; Shrestha et al., 2024; Chen et al., 2025, 2024) prefer $\dot{M}$ between 10^{-3} – 10^{-2} $M_\odot$ yr^{-1} calculated by photometric and/or spectroscopic modelling of the event and its environment. For SN 2023ixf, we find $M_{CSM} \sim 0.1$ $M_\odot$, $R_{CSM} \sim 6{\times}10^{14}$ cm and $\dot{M} \sim 1{\times}10^{-2}$ $M_\odot$ yr^{-1} respectively. Singh et al. (2024) and Moriya & Singh (2024) conduct a similar exercise, finding the best fitting M23 models to SN 2023ixf, and measure similar values for $\dot{M}$, 10^{-3} –10^{-2} $M_\odot$ yr^{-1} and $R_{CSM} \sim 5$–$10{\times}10^{14}$ cm. For SN 2024ggi, we find $M_{CSM} \sim 5{\times}10^{-3}$ $M_\odot$, $R_{CSM} \sim 3{\times}10^{14}$ cm and $\dot{M} \sim 2{\times}10^{-4}$ $M_\odot$ yr^{-1} respectively.

Parameter	Units	Mean	25th%ile	50th%ile	75th%ile	Range	No.
				Weighted			
$M_{\rm CSM}$	$\times 10^{-3}$ M$_\odot$	–	–	–	$9.55^{+3.48}_{-5.79}$	[0.11,1.05$\times 10^3$][1]	377
$\dot{M}$	$\times 10^{-4}$ M$_\odot$ yr^{-1}	–	–	–	$6.03^{+2.20}_{-3.61}$	[3.22,8.16$\times 10^2$][1]	377
$R_{\rm CSM}$	10^{14} cm	6.69 ± 0.92	$5.58^{+0.28}_{-0.28}$	6.56 ± 0.25	$7.84^{+0.19}_{-0.11}$	[1.98,14.11]	253
				Unweighted			
$M_{\rm CSM}$	$\times 10^{-3}$ M$_\odot$	$10.61^{+1.79}_{-1.54}$	$1.34^{+1.91}_{-2.05}$	$11.62^{+2.05}_{-1.74}$	$93.87^{+36.22}_{-45.90}$	-	-
$\dot{M}$	$\times 10^{-4}$ M$_\odot$ yr^{-1}	$6.70^{+1.15}_{-0.98}$	$0.85^{+0.41}_{-0.49}$	$7.54^{+1.40}_{-1.18}$	$59.25^{+25.22}_{-30.85}$	-	-
$R_{\rm CSM}$	10^{14} cm	6.55 ± 0.44	$5.72^{+0.51}_{-0.18}$	6.63 ± 0.12	$7.90^{+0.33}_{-0.31}$	-	-

[1] The ranges reported are the 5th and 95th percentiles to remove outliers beyond the limits of the original dataset.

TABLE 3.6: Mean and median of the volume corrected KDE for $M_{\rm CSM}$, $\dot{M}$ and $R_{\rm CSM}$ in the final sample. $M_{\rm CSM}$, $\dot{M}$ and $R_{\rm CSM}$ were inferred via linear relations involving GPR parameters. For $R_{\rm CSM}$, we exclude data where the corresponding $M_{\rm CSM} < 10^{-2.5}$ M$_\odot$ as we consider $M_{\rm CSM}$ lower than this to have a negligible effect on the observable parameters and cannot constrain $R_{\rm CSM}$ for lower $M_{\rm CSM}$. Values for $\dot{M}$ use a fiducial value of 5×10^{14} cm for $R_{\rm CSM}$. Uncertainties reported here are the standard deviation of the bootstrapped values. The mean, 25th percentile and median values for $M_{\rm CSM}$ are not reported here as they are below $10^{-2.5}$ M$_\odot$ and we cannot confidently constrain below this threshold. For the same reason, we do not report the mean, 25th percentile or median for $\dot{M}$ as this is below the $\dot{M}$ corresponding to $M_{\rm CSM} = 10^{-2.5}$ M$_\odot$.

We report the key statistics for measured $M_{\rm CSM}$, $\dot{M}$ and $R_{\rm CSM}$ in Table 3.6 derived from their weighted respective KDEs. For the uncertainties on $M_{\rm CSM}$ and $R_{\rm CSM}$ quoted either in Table 3.6 or later, we use Eq. 4 for $M_{\rm CSM}$ and $R_{\rm CSM}$ and resample each parameter 1,000 times within their uncertainties using a uniform distribution – bounds set to be, for example, $[M_{g,\rm peak} - \sigma_{M_{g,\rm peak}}, M_{g,\rm peak} + \sigma_{M_{g,\rm peak}}]$. We then find the 1 σ standard deviation. This method is repeated for $\dot{M}$ using Eq. 3.6.2.

Figs. 3.17 and 3.18 and 3.19 are the ECDFs for $M_{\rm CSM}$, $\dot{M}$ and $R_{\rm CSM}$ which show the empirical distribution of parameters for the weighted and unweighted samples. For the weighted ECDFs, we show the 80% CI via the same bootstrapping method as previously described. For the unweighted ECDF, we perform a similar bootstrap with replacement to select from the sample and find the 95% CI empirically following a similar routine of finding the difference between the 2.5th and 97.5th percentiles.

3.7 Discussion

3.7.1 Luminosity and Rise Distributions

The volume-corrected sample of 377 Type II SNe yields a mean peak absolute magnitude in rest-frame ZTF g-band of $M_{g,\rm peak} = -16.59 \pm 0.29$ mag, with a median of $M_{g,\rm peak} = -16.71 \pm 0.25$ mag. To place these results in the context of previous studies, we compile peak luminosities from recent surveys in Table 3.7. While direct comparison is limited by filter differences – earlier surveys typically used $UBVRI$ rather than Sloan or ZTF filters – our mean and median weighted measurements in ZTF g can be broadly compared with Johnson-Cousins B and V-band values, and show agreement within 1.5 σ across all studies.

Reference	$M_{B,peak}$ [mag]	$M_{V,peak}$ [mag]	No.	Extinction	Vol.	Class Sys.	Surveys
Anderson et al. (2014)	-	-16.74 ± 1.01	68	MW & Host	No	Spec + Phot	CT; CTSN; SOIRS; CATS; CSP
Richardson et al. (2014)	-16.80 ± 0.37	-	74	MW & Host	Yes	Spec	ASC
Galbany et al. (2016a)	-16.43 ± 1.19	-16.89 ± 0.98	51	MW	No	Spec	C&T; CTSN; SOIRS; CATS
de Jaeger et al. (2019)	-16.57 ± 1.14	-16.74 ± 0.92	23	MW	No	Spec	LOSS

TABLE 3.7: Previous measurements of the mean AB peak absolute magnitudes for Type II SNe. Uncertainties are those reported in the study. Extinction refers to whether the magnitudes were corrected for MW and host extinction, or for MW extinction only, with no host correction. Vol. refers to whether there is a volume correction applied to the statistic. Classification refers to how the final samples were selected, all chose to spectroscopically (spec) classify, with Anderson et al. (2014) performing some photometric (phot) typing to remove Type IIb, IIn and 1987A-like SNe. Survey refers to which surveys the samples belong to: CT – Cerro Tololo SN program. CTSN – Calán/Tololo SN. SOIRS – Optical and Infrared Supernova Survey. CATS – Carnegie Type II Supernova Program. CSP – Carnegie Supernova Program. C&T – Calán/Tololo Supernova Program. LOSS – Lick Observatory Supernova Search.

When comparing our volume corrected mean $M_{g,\mathrm{peak}}$ to the entire M23 model grid (no weighting applied), we find the theoretical predictions are systematically brighter: mean $M_{g,\mathrm{peak}} = -17.88$ mag and median $M_{g,\mathrm{peak}} = -18.11$ mag. This luminosity difference reflects the ability of our volume-complete sample to naturally capture the full diversity of Type II SNe, with the M23 grid focusing on systematically exploring parameter space rather than matching the observed luminosity distribution or the IMF.

We compared our sample with that of Das et al. (2025)), using the ZTF Census of the Local Universe survey (CLU; De et al., 2020), and we are consist in the key overlapping measurement between the studies, with the luminosity distributions, Fig. 3.6, being in strong agreement.

We have limited overlap with Pessi et al. (2025), studying Type II SLSNe from ZTF, though we find 23^{+9}_{-7}% Type IIn SNe in our weighted sample have $M_{g,\mathrm{peak}}$ brighter than -19 mag – this is the most appropriate as we grouped Type IIn and SLSNe together – with a large range in $M_{g,\mathrm{peak}}$ -17.01 to -22.20 mag. Our unweighted median $M_{g,\mathrm{peak}}$ for Type IIn, -19.32 ± 0.13 mag, agrees with median values in Hiramatsu et al. (2024).

The observed correlation between $M_{g,\mathrm{peak}}$ and t_{25_75} for Type II SNe (excluding Types IIn and IIb) revealed in Section §3.4.1 is likely to be driven by a deficit of slow-rising, low-luminosity events. This weak correlation, also noted by Valenti et al. (2016), presents an intriguing discrepancy with theoretical predictions. While the M23 models (Fig. 3.11) predict this region of parameter space to be populated by explosions from low-mass progenitors, our BTS sample shows noticeably fewer such events than theoretically expected. Although we do detect some low-luminosity SNe with extended rise times ($t_{25\_75} \gtrsim 15$ d), their relative scarcity compared to model predictions is significant. Section 3.7.2 quantifies this population's occurrence rate relative to the broader Type II population.

Type II SNe exhibit diverse rise times, with their distribution (Fig. 3.4) suggesting a continuous rather than bi-modal range of progenitor properties. The lack of bi-modality in the observed t_{25_75} distributions is significant and likely reflects an overabundance of these events compared to their representation in the M23 grid. This continuous distribution is seen before and after the volume correction, Fig. 3.8, suggesting this is not a result of lacking observations of a particular population. The prevalence of events with both rapid rise times and high luminosities provides compelling evidence for dense CSM being common among Type II SNe. These characteristics are consistent with SBO

within circumstellar material (e.g., Moriya et al., 2011; Chevalier, 2012; Das & Ray, 2017; Moriya et al., 2018; Tinyanont et al., 2022; Pearson et al., 2023; Li et al., 2024), as models without significant CSM struggle to simultaneously produce such fast rise times and enhanced peak brightness.

To investigate whether our results depend on the extinction correction, we also examined the distributions of all parameters if no extinction correction was applied. $M_{g,\mathrm{peak}}$, t_{25_75} and CSM parameters estimates changed by no more than 1 σ. Since the host extinction correction affects only a small fraction of our sample, our conclusions about the physical parameter distributions remain largely unaffected. The $1/V_{\mathrm{max}}$ correction we apply to our observational sample addresses potential observational bias, but significant uncertainties remain in the faint end of the luminosity function – explored in detail by Das et al. (2025).

3.7.2 Long Rising Type II SNe

Of note in Fig. 3.4 are the events with long rise times, $\gtrsim$ 25 d. These events are slowly evolving, seemingly in the gap between Type IIn and the region of space the long-simulated Type II light curves from Moriya (2023) occupy. There are 5 events in our sample with rise times $\geq$ 25 d that all have non-standard Type II light curves. Some of these SNe show resemblance to SN 1987A where the rise to peak is a slow hump or they have an early peak fainter than the main peak – see ZTF18acbwaxk/SN 2018hna in Fig. 3.3 for an example. To confirm the absence of narrow lines and rule out misclassification of Type IIn SNe, we checked the classifying spectra and confirmed there were no narrow lines present in their spectral series – most have multiple high-resolution spectra.

When comparing the magnitude-limited BTS sample with the volume-limited ZTF CLU, only one event overlaps with the Sit et al. (2023) study – ZTF18acbwaxk/SN 2018hna ($t_{25\_75} \sim 35$ d, $M_{g,\mathrm{peak}} \sim -15.99$ mag uncorrected). This limited overlap stems from different selection criteria: BTS captures brighter events (peak magnitudes < 18.5 mag) while CLU focuses on lower luminosity events in nearby galaxies. For Type II SNe with rise times > 25 d, we compute a rate relative to the CCSN rate found in Perley et al. (2020).

Before applying a magnitude cut for completeness, we identify 5/481 Type II SNe with $t_{25\_75} \geq 25$ d from our sample. Accounting for observational bias, we find these long-rising events constitute $2.16^{+1.93}_{-0.60}\%$ of the Type II SN population, with a weighted mean $M_{g,\mathrm{peak}} = -16.33$ mag, compared to -16.59 mag for the overall sample. After implementing an 18.5 mag completeness cut, we retain 4 long-rising events in our sample of 377 SNe, corresponding to a bias-corrected fraction of $1.43^{+1.28}_{-0.15}\%$ with no significant change in $M_{g,\mathrm{peak}}$. These low rates, though limited by small statistics, confirm these events are rare and align with previous findings: Sit et al. (2023) report that SNe with $t_{25\_75} > 40$ d comprise $1.4 \pm 0.3\%$ of all CCSNe, while earlier studies found rates of 1.5 – 3% (Smartt, 2009; Kleiser et al., 2011; Pastorello et al., 2012).

3.7.3 CSM Mass and Radial Extent

Our Type II SN sample reveals widespread evidence for substantial CSM present at the time of explosion. Accounting for observational biases through a volumetric weighting, $36^{+5}_{-7}\%$ of events have $M_{\mathrm{CSM}} \geq 10^{-2.5}$ $\mathrm{M}_\odot$, with the 80th percentile of the full sample being $1.56^{+1.12}_{-0.54} \times 10^{-2}$ $\mathrm{M}_\odot$. In the unweighted sample, $67 \pm 6\%$ of events show significant M_{CSM} ($\geq 10^{-2.5}$ $\mathrm{M}_\odot$). These M_{CSM} estimates, and the corresponding R_{CSM}, remain consistent when analysed without host-extinction corrections.

For events with massive CSM shells ($M_{\mathrm{CSM}} \geq 10^{-2.5}$ $\mathrm{M}_\odot$), our weighted sample shows a median R_{CSM} of $\sim 6 \times 10^{14}$ cm, with nearly all events having inferred radii $\leq 10^{15}$ cm and a well-defined peak around this median (Figs. 3.16 and 3.19). The upper limit of $R_{\mathrm{CSM}} \leq 10^{15}$ cm in our sample reflects the parameter space explored by M23, with this particular methodology being insensitive to larger radii – like those expected in Type IIn SNe. However, our analysis reveals a physically meaningful result: the rapid rise times observed in most events require both sufficient M_{CSM} and relatively compact radii ($\sim 6 \times 10^{14}$ cm median for $M_{\mathrm{CSM}} > 10^{-2.5}$ $\mathrm{M}_\odot$) to effectively trap energy and accelerate the early light curve evolution.

The high M_{CSM} ($\geq 10^{-1} \mathrm{M}_\odot$) and $\dot{M}$ ($\geq 10^{-2}$ $\mathrm{M}_\odot$ yr^{-1}) we infer for a fraction of our sample (Figs. 3.14 and 3.17) likely produce distinctive spectroscopic signatures from compact and dense CSM, such as flash features typically lasting $\leq$1 week. While our study focuses on CSM shells with specific density profiles affecting early light curves ($\rho \propto r^{-2}$; Moriya et al., 2023), Dessart & Jacobson-Galán (2023) demonstrate that

different CSM configurations can produce similar photometric evolution while predicting different spectroscopic features (see Moriya, 2023; Khatami & Kasen, 2024; Jacobson-Galán et al., 2024a). Spectroscopy is required to aid in breaking these degeneracies as it becoming clear that large amounts of CSM represent a common phenomenon rather than exceptional cases (e.g., Förster et al., 2018; Hosseinzadeh et al., 2022; Kozyreva et al., 2022; Jacobson-Galán et al., 2023; Hiramatsu et al., 2023; Jencson et al., 2023; Hosseinzadeh et al., 2023; Irani et al., 2024; Li et al., 2024; Zimmerman et al., 2024; Andrews et al., 2024; Shrestha et al., 2024; Pessi et al., 2024; Xiang et al., 2024; Chen et al., 2024; Jacobson-Galán et al., 2024b; Rehemtulla et al., 2025).

For events with lower inferred $M_{\rm CSM}$ ($< 10^{-2.5}$ M$_\odot$), the impact of CSM on the early light curve is too weak to constrain $R_{\rm CSM}$. While many of these SNe are likely to possess non-negligible CSM, material at larger radii would likely not influence the early evolution, and would be too diffuse to influence the later light curve evolution in a clearly discernible way unless the mass is extremely high (e.g., Irani et al., 2024).

A limitation of the approach from this work is that for the fastest rising events (≤ 1 d), which likely require dense, compact CSM to achieve such rapid evolution, our measured rise times would represent upper limits, unresolved fast rises might require more substantial $M_{\rm CSM}$ or closer and more compact CSM. While individual CSM parameters may have uncertainties due to model assumptions, observational constraints and scatter present in relationships, this frequency of substantial CSM in our volume corrected sample represents a robust statistical result, independent of the precise CSM parameterisation. Our analysis is further constrained by confidence in classifications, an issue we explore in greater detail in appendix B.11.

3.7.4 Implications for Mass-Loss Mechanisms

With a minimum $M_{\rm CSM}$, $10^{-2.5}$ M$_\odot$ and observationally supported fiducial values for v_{wind} and $R_{\rm CSM}$ of 10 km s^{-1} and 5×10^{14} cm respectively, we find a characteristic $\dot{M}$ of $2{\times}10^{-4}$ M$_\odot$ yr^{-1}. This characteristic value is higher, by $\sim$ two orders of magnitude, than values inferred from observations of local group RSGs e.g., $\dot{M} \sim 10^{-6}$ M$_\odot$ yr^{-1} (e.g., Vink et al., 2001; Smith, 2014; Beasor & Davies, 2018; Beasor et al., 2020).

Our findings are instead closer to studies such as Morozova et al. (2017); Moriya et al. (2018); Bruch et al. (2021, 2023); Irani et al. (2024); Jacobson-Galán et al. (2024a) that estimate $\dot{M}$ to be $\sim 10^{-4}$ – 10^{-1} $M_\odot$ yr^{-2} based on detailed analysis of spectroscopy and photometry of early SNe. Like Jacobson-Galán et al. (2024a), we find that Type II SNe exhibit a continuum of $\dot{M}$, representative of the heterogeneous morphology of light curves, with 46^{+5}_{-13}% of the corrected population having $\dot{M} \geq 1{\times}10^{-4}$ $M_\odot$ yr^{-1} in the last several decades before core-collapse.

Given a v_{wind} of 10 km s^{-1} and the minimum and maximum values of $R_{\rm CSM}$, 10^{14} – 10^{15} cm, we calculate the range of timescales in which the material is removed to be 3 – 32 yrs. The distinctly short timescales of mass-loss, compared to the lifespan of this evolutionary stage, further supports the need for a period of 'enhanced' mass-loss. We argue the higher rates of mass-loss estimated from early photometry found here and by other studies (e.g., Irani et al., 2024; Jacobson-Galán et al., 2024b; Silva-Farfán et al., 2024) are probing the end-of-life mass-loss rather than the typical $\dot{M}$ of RSGs.

Any viable mass-loss mechanism must maintain sufficient CSM density at compact radii while preventing complete shell detachment. The mechanism must operate on timescales consistent with our inferred $\dot{M}$ ($\geq 10^{-4}$ $M_\odot$ yr^{-1}) and produce velocities that allow the material to remain within $R_{\rm CSM} \leq 10^{15}$ cm. Higher ejection velocities or more extended distributions would result in CSM densities too low to effectively interact with the SN ejecta and SBO during the early light curve evolution.

As an alternative to 'enhanced' $\dot{M}$ in the centuries before core-collapse, the dense chromosphere model of Fuller & Tsuna (2024) offers a compelling explanation for the apparent disparity between observed RSG mass-loss rates and those inferred from early SN evolution (see Fuller & Tsuna, 2024). A chromosphere exists in approximate hydrostatic equilibrium, with significantly higher densities above the stellar surface than predicted by constant or β-law wind velocity models, despite maintaining $\dot{M}$ more consistent with local group RSG measurements (see Fig. 4 in Fuller & Tsuna, 2024). This model is able to naturally produce the rapid photometric and spectroscopic evolution observed in fast-rising SNe while preserving realistic progenitor properties. While our $M_{\rm CSM}$ estimates would remain largely unaffected, the inferred $\dot{M}$ would decrease substantially due to the significantly different velocity structure in Fuller & Tsuna (2024) compared to those used in M23. Thus, the chromosphere model represents a promising alternative to

'enhanced' $\dot{M}$, potentially resolving a tension between $\dot{M}$ measured from local RSGs and early SN evolution, though additional development is required to fully understand the impact of chromospheres on the photometric and spectroscopic evolution across diverse SN populations.

3.8 Conclusions

In this work, we have presented forced photometry and Gaussian process analysis of all spectroscopically classified H-rich SNe from the ZTF Bright Transient Survey, 1802 objects up to the 31st of December 2023, 981 of which pass various quality cuts outlined in BTS sample paper (Perley et al., 2020). We have modelled the light curves with GPR to return various empirical light curve parameters, with a focus on the rise times of 639 Type II SNe. Using various light curve parameters, we have created volume corrected ($V_{\rm max}$ method) distributions from the BTS sample, allowing us to confidently report the following main conclusions for a highly complete sample of 377 Type II SNe (excluding Type IIn and IIb SNe, and after a magnitude cut at ≤ 18.5 mag for completeness):

- We see large diversity in Type II light curve demographics but no clear separation in the luminosity-rise phase-space. The predicted bi-modality that appears when we measure the distributions of rise times, t_{25_75}, from the simulated light curves of Moriya et al. (2023) is not seen in our observed light curves.
- Based on the $1/V_{\rm max}$ weighted sample of Type II SNe from this study, we find $36^{+5}_{-7}\%$ of Type II SN progenitors have $M_{\rm CSM} \geq 10^{-2.5}$ M$_\odot$ at the time of core-collapse. We find this is the minimum amount of $M_{\rm CSM}$ needed to impact the observables like the rise time and peak magnitude, based on Moriya et al. (2023) models.
- For an assumed progenitor wind velocity of 10 km s^{-1}, a maximum CSM radius of $R_{\rm CSM} \approx 5 \times 10^{14}$ cm and $M_{\rm CSM} = 10^{-2.5}$ M$_\odot$, we estimate mass-loss rates of $\dot{M} \sim 2 \times 10^{-4}$ M$_\odot$ yr^{-1} for events showing CSM-affected light curves. We constrain the period of this to occur within the last 3 – 32 years, consistent with recent findings from Bruch et al. (2021), Bruch et al. (2023) and Jacobson-Galán et al. (2024a), which suggest 'enhanced' mass-loss is a common feature of RSG evolution in the final decades before core-collapse.

This supports findings in recent literature that CSM interactions contribute significantly to the early light curve and are prevalent in a large set of Type II SNe. While not ubiquitous across Type II SNe, we show possessing large amounts of CSM in common amongst Type II SNe progenitors. For the ∼36% of Type II SNe (excluding Types IIn and IIb SNe) where CSM interactions dominate, we find that dense CSM both shortens the rise time to peak luminosity and enhances the early-time brightness. We have further highlighted the need to reconcile and address the disparity between light curve derived $\dot{M}$ values and $\dot{M}$ from RSG observations – which are typically larger by ≈ 2 orders of magnitudes than the rates inferred from local group RSG observations (e.g., Levesque et al., 2005; Mauron & Josselin, 2011; Smith, 2014; Beasor et al., 2020; Stroh et al., 2021; Strotjohann et al., 2024a).

Mapping the true distribution of CSM properties and establishing robust connections between SNe and their progenitors requires deeper observations over longer baselines than currently available. The Vera Rubin Observatory, ZTF-III, and upcoming IR/UV missions will provide unprecedented multi-wavelength coverage with the depth and cadence needed to probe fainter CSM signatures and earlier epochs, essential for reconstructing progenitor mass-loss histories and understanding how they shape the observed diversity of Type II SNe.

3.9 Acknowledgements

Based on observations obtained with the Samuel Oschin Telescope 48-inch and the 60-inch Telescope at the Palomar Observatory as part of the Zwicky Transient Facility project. ZTF is supported by the National Science Foundation under Grants No. AST-1440341 and AST-2034437 and a collaboration including current partners Caltech, IPAC, the Oskar Klein Center at Stockholm University, the University of Maryland, University of California, Berkeley, the University of Wisconsin at Milwaukee, University of Warwick, Ruhr University, Cornell University, Northwestern University and Drexel University. Operations are conducted by COO, IPAC, and UW.

SED Machine is based upon work supported by the National Science Foundation under Grant No. 1106171. The ZTF forced-photometry service was funded under the Heising-Simons Foundation grant #12540303 (PI: Graham). The Gordon and Betty Moore

Foundation, through both the Data-Driven Investigator Program and a dedicated grant, provided critical funding for SkyPortal.

Numerical computations were in part carried out on PC cluster at the Center for Computational Astrophysics, National Astronomical Observatory of Japan.

This research has made use of the SVO Filter Profile Service "Carlos Rodrigo", funded by MCIN/AEI/10.13039/501100011033/ through grant PID2023-146210NB-I00 .

This research has made use of the NASA/IPAC Extragalactic Database (NED), which is funded by the National Aeronautics and Space Administration and operated by the California Institute of Technology.

3.10 Data Availability

There will be a large data release of the ZTF P48 light curves used in this work in the upcoming publication, A. A. Miller et al. (2025, in prep.).

The light curves and empirical properties measured for the SNe, as they relate to this work, can be found here: [https://doi.org/10.5281/zenodo.15229515].

Access to the public Bright Transient Survey sample explorer can be found here: [https://sites.astro.caltech.edu/ztf/bts/explorer.php].

Chapter 4

Inferring Nickel Mass Properties of Type II SNe Using a Magnitude-Limited ZTF Sample

4.1 Introduction

As was briefly mentioned in Chapter 1, Section §1.5, the nickel synthesised in the explosive shell burning plays a critical role in shaping the light curves of Type II SNe past the photospheric (plateau) phase (e.g., Woosley & Weaver, 1986; Woosley, 1988; Arnett, 1996). Explosive nuclear burning efficiently produces heavy elements from silicon to zinc, though ^{56}Ni and other iron-group elements dominate the production of nuclear species in the inner ejecta (e.g., Woosley & Weaver, 1995; Thielemann et al., 1996).

There is significant interest in characterising the distribution of ^{56}Ni masses ($M_{\rm Ni}$) across different SN subtypes due to the fundamental role of this particular isotope in shaping observable properties and its diagnostic power for explosion physics (e.g., Chugai, 1991; Nadyozhin, 1994; Hamuy, 2003; Spiro et al., 2014; Pejcha & Prieto, 2015a,b; Valenti et al., 2016; Yuan et al., 2016; Nakar et al., 2016; Müller et al., 2017; Anderson, 2019; Kozyreva et al., 2019; Goldberg et al., 2019, 2020; Rodríguez et al., 2021; Utrobin et al., 2021; Martinez et al., 2022a; Martinez et al., 2022b; Fang et al., 2025b). The amount of ^{56}Ni synthesised during core-collapse is highly sensitive to the explosion energy and the structure of the progenitor's core at the time of collapse (e.g., Ugliano et al., 2012;

Sukhbold et al., 2016; Suwa et al., 2019). Since the decay of ^{56}Ni and its daughter nuclei dominates the power source of the light curve at late times, measurements of $M_{\rm Ni}$ provide a direct window into the internal conditions of the explosion. Furthermore, the degree of mixing and fallback can influence the observed luminosity and spectral evolution, making $M_{\rm Ni}$ a key parameter for connecting theoretical models with observations of late-time supernova behaviour.

The observed distribution of $M_{\rm Ni}$ within a given SN class can be compared to predictions from neutrino-driven explosion models to assess their validity and guide refinements in the physical treatment of explosion mechanisms and progenitor structure (e.g., Sukhbold et al., 2016; Anderson, 2019; Rodríguez et al., 2021). Such comparisons help constrain key parameters like core compactness, energy deposition, and mixing processes, ultimately improving our theoretical understanding of SN morphology. Additionally, comparing ^{56}Ni yields across different CCSN types – particularly between hydrogen-rich and hydrogen-poor events – provides valuable insights into distinct progenitor evolutionary pathways. A key result from Anderson (2019) is that on average, SESNe produce significantly more ^{56}Ni than their hydrogen-rich counterparts, suggesting that their progenitors either retain more compact cores or experience more energetic explosions – possibly due to differences in initial mass, mass-loss history, or binary interaction. This result places meaningful constraints on the range of progenitor structures and evolutionary channels that can lead to different explosion outcomes.

Previous studies have reported a range of ^{56}Ni mass estimates for Type II SNe using various methodologies. Pejcha & Thompson (2015) applied the physically-motivated relationship between $M_{\rm Ni}$ and late-time bolometric luminosity from Hamuy (2003) to 21 SNe, finding a median $M_{\rm Ni}$ of 3 $\times 10^{-2}$ M$_\odot$ with a range spanning 0.45 – 28 $\times 10^{-2}$ M$_\odot$. Valenti et al. (2016) employed a scaling relation comparing late-time luminosities to SN 1987A at comparable phases (following Spiro et al., 2014), yielding $M_{\rm Ni}$ values from 0.01–20 $\times 10^{-2}$ M$_\odot$. In the meta-analysis combining such previous literature measurements, Anderson (2019) compiled a heterogeneous sample of 115 Type II SNe and found a median $M_{\rm Ni} = 3.2 \times 10^{-2}$ M$_\odot$.

Hydrodynamic modelling of the light curves has produced consistent results. Sukhbold et al. (2016), Müller et al. (2017), Kozyreva et al. (2019), Martinez et al. (2020), and Martinez et al. (2022b) all found similar mean and median values between 2 – 6 $\times 10^{-2}$ M$_\odot$

across different SN samples. The largest simulation-based study, Rodríguez et al. (2021), analysed 110 SNe with detailed physical modelling, finding a mean $M_{\rm Ni} = 4.2 \times 10^{-2}$ M$_\odot$.

While these studies report consistent characteristic values (medians and means), their upper limits diverge significantly – non-hydrodynamic modelling approaches (e.g., Hamuy, 2003; Pejcha & Prieto, 2015b) yield larger maximum $M_{\rm Ni}$ values (~ 30 – 40×10^{-2} M$_\odot$) compared to hydrodynamic modelling methods ($\lesssim 10 \times 10^{-2}$ M$_\odot$). Pejcha & Thompson (2015) attributed this discrepancy to uncertainties in distance estimates, which propagate into $M_{\rm Ni}$ calculations when overestimated distances artificially inflate absolute luminosities. Crucially, non-hydrodynamic methods often rely on scaling relations where higher luminosities – resulting from overestimated distances – directly translate into higher $M_{\rm Ni}$ values. In contrast, hydrodynamic modelling self-consistently compute luminosity from the underlying explosion physics (e.g., mass, energy, radius, and $M_{\rm Ni}$), meaning that distance-induced luminosity shifts do not map linearly onto $M_{\rm Ni}$ estimates[1].

Additionally, most existing samples (except for the CSP-based study by Martinez et al. 2022c) suffer from heterogeneity (they are assembled from diverse sources with inconsistent selection criteria and observational strategies) and often lack corrections for observational biases that inherently favour more luminous events. This selection effect potentially skews reported distributions toward higher values. Since $M_{\rm Ni}$ determinations fundamentally depend on accurate bolometric luminosity measurements, which themselves rely on precise distance estimates, understanding these systematic uncertainties is essential for interpreting the true physical distribution of $M_{\rm Ni}$ across core-collapse events.

In hydrogen-rich CCSNe, the contribution of ^{56}Ni to the observed emission during the photospheric phase is subdominant ($\sim$30%) as the primary energy source is hydrogen recombination (Nakar et al., 2016). However, the degree of ^{56}Ni mixing and its spatial distribution can significantly influence the plateau, particularly its duration. High $M_{\rm Ni}$ is thought to extend the plateau phase by $\sim$20% (e.g., Chugai, 1991; Young, 2004; Kasen & Woosley, 2009; Bersten et al., 2011; Kozyreva et al., 2019; Goldberg et al., 2019; Fang et al., 2025b), primarily by providing additional heating to the ejecta – see Fig.4.1.

[1]Such models explore a multidimensional parameter space where the relationship between parameters and luminosity is more complex, potentially dampening the effect of distance errors.

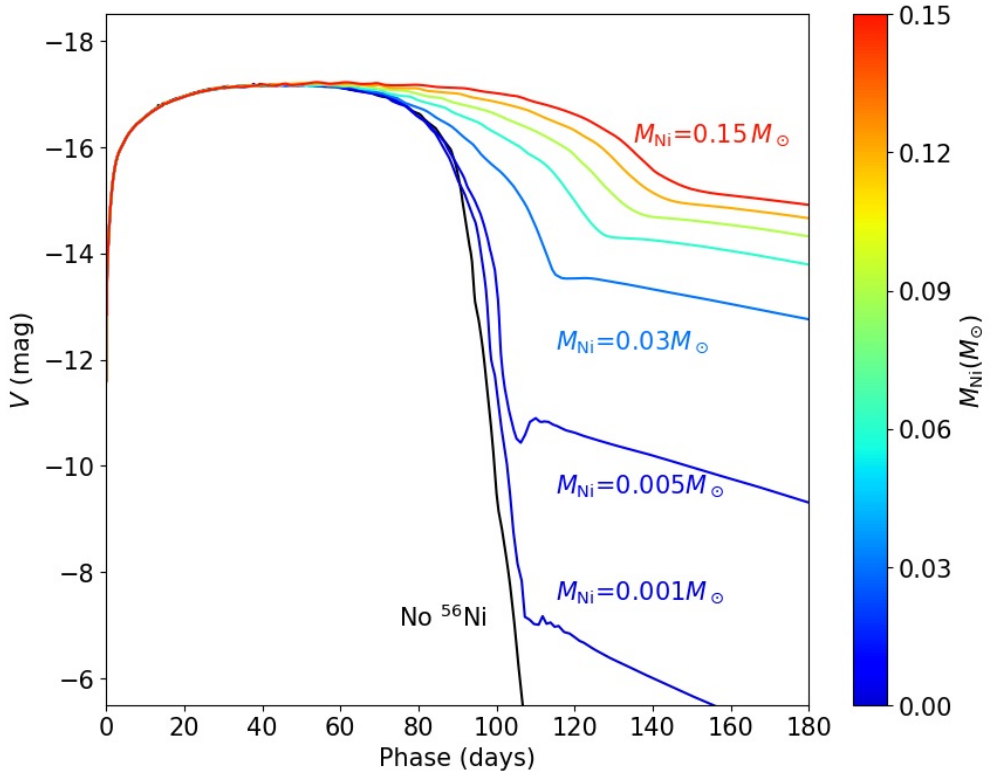

FIGURE 4.1: V-band light curve model for a STELLA model ($\alpha_{\rm mlt} = 2.0$, $M_{\rm ZAMS} = 15\,M_\odot$, $M_{\rm Henv} = 8.0\,M_\odot$, and $E = 10^{51}$ ergs) with varying $M_{\rm Ni}$, colour-coded (and labelled) by the colour-bar on the plot. This depicts the increase in plateau length with increasing $M_{\rm Ni}$. Figure from Fang et al. (2025b).

In Type II SNe, the luminosity at 50 d post-explosion, $L_{50\,\rm d}$, is also known to correlate strongly with $M_{\rm Ni}$ estimates derived from their radioactive tail (e.g., Hamuy, 2003; Spiro et al., 2014; Pejcha & Prieto, 2015b; Valenti et al., 2016; Rodríguez et al., 2021). This empirical relationship – where brighter SNe tend to synthesise more ^{56}Ni – is supported by theory. At these epochs, photons from the ^{56}Ni decay chain likely have enough time to begin to diffuse through the ejecta and contribute meaningfully to the observed luminosity (e.g., Kasen & Woosley, 2009; Dessart et al., 2013). The correlation may also reflect a more fundamental link between explosion energy and ^{56}Ni production (e.g., Sukhbold et al., 2016): more energetic explosions both elevate plateau luminosities and trigger more extensive nucleosynthesis in the inner silicon-rich layers, enhancing ^{56}Ni synthesis (e.g., Müller et al., 2017; Burrows & Vartanyan, 2021).

However, as shown in Fig. 4.1, the plateau magnitude does not appear to vary significantly, despite expectations from these correlations. This remains a point of contention. While several studies report strong links between plateau luminosity and $M_{\rm Ni}$ (e.g., Hamuy, 2003; Spiro et al., 2014; Pejcha & Prieto, 2015b; Valenti et al., 2016; Rodríguez

et al., 2021), others suggest a different role for ^{56}Ni heating. For instance, Fang et al. (2025b) argue that the primary effect of ^{56}Ni is to extend the plateau duration – an effect not yet conclusively observed (e.g., Valenti et al., 2016; Martinez et al., 2022c; Jacobson-Galán et al., 2025).

In this chapter, I build on the theoretical motivation outlined above by using the highly complete and magnitude-limited BTS sample of Type II SNe to constrain the distribution $M_{\rm Ni}$ across the Type II population. Unlike many previous studies, which were often limited by heterogeneous or biased samples, this work leverages the homogeneity of the BTS to enable volume-corrected inferences about the underlying $M_{\rm Ni}$ distribution. This is particularly important for addressing ongoing questions about how explosion energy and progenitor structure vary within the hydrogen-rich CCSN population, and how these compare with hydrogen-poor SESNe.

Light curves are modelled using GPR on FP from the ZTF, supplemented with additional data from ATLAS, the Liverpool Telescope (LT), and the Nordic Optical Telescope (NOT). Bolometric light curves are constructed using the empirical bolometric corrections developed by Martinez et al. (2022a), and the late-time bolometric luminosity is used to estimate $M_{\rm Ni}$ via two independent methods. By analysing a statistically representative and highly complete sample, this preliminary study aims to provide robust, volume-corrected constraints on the distribution of $M_{\rm Ni}$ in Type II SNe.

4.2 Bolometric Light Curves

After the transition from recombination-powered to radioactively powered emission (^{56}Ni $\rightarrow$ ^{56}Co $\rightarrow$ ^{56}Fe; see Eqs. 1.7 and 1.8), the luminosity declines exponentially with time (linearly in magnitude space). During this phase, the dominant energy sources are gamma rays and positrons from the decay of ^{56}Co. Since this decay directly powers the emission, the luminosity at this stage provides a robust estimate of the $M_{\rm Ni}$ ejected in the explosion.

Therefore, to measure $M_{\rm Ni}$, the bolometric luminosity at some epoch, $L_{\rm bol}(t)$, is used in either a physically informed equation (Eq. 4.1; Hamuy, 2003) or a scaling relation (Eq. 4.2; Spiro et al., 2014; Valenti et al., 2016) relative to a well-observed SN (e.g. SN 1987A).

$$M_{\rm Ni}\,[{\rm M}_\odot] = 7.866 \times 10^{-44} \times L_{\rm bol}(t)\,[{\rm erg\ s^{-1}}] \times \exp\left(\frac{t\ [{\rm d}]/(1+{\rm z}) - 6}{112\ [{\rm d}]}\right) \tag{4.1}$$

In Eq. 4.1, 6 is the half-life of ^{56}Ni and 112 is the e-folding time (in d) of the ^{56}Co decay.

$$M_{\rm Ni}\ \ [{\rm M}_\odot] = 0.075 \times \frac{L_{\rm bol}(t)\,[{\rm erg\ s^{-1}}]}{L_{\rm 87A}(t)\ [{\rm erg\ s^{-1}}]} \tag{4.2}$$

In Eq. 4.2, $L_{\rm bol}(t)$ is compared to $L_{\rm 87A}(t)$ as similar epochs.

The key challenge lies in constructing the bolometric light curve, which represents the total radiated energy across all wavelengths as a function of time. This is achieved either by integrating flux over available photometric bands with corrections for unobserved spectral regions, or more commonly, by applying bolometric corrections (BCs) to transform multi-band photometry into $L_{\rm bol}(t)$. The former is preferred when time and wavelength coverage are sufficient to constrain the SED; the latter must account for missing emission, especially in the NUV and NIR, and gaps between filter bands (e.g., between g and r).

For Type II SNe, where the emission evolves significantly over time – from X-ray/FUV (SC and CSM interaction) to optical and finally IR (radioactive decay) – the choice and implementation of BCs are particularly critical. As the blackbody (BB) peak shifts redward over months, the relative contribution of different spectral regions changes substantially.

Full integration over ZTF $gr(i)$ filters is insufficient for constructing bolometric light curves, particularly at early times (UV-dominated) and late times (IR-dominated) due to no coverage at these key wavelengths. Similarly, BCs based on ZTF data alone would be inadequate at early and late times as ZTF provides coverage primarily in the g and r-bands, with limited access to i-band[2].

BCs based on optical colours have been proposed for the photospheric phase (e.g., Bersten & Hamuy, 2009; Lyman et al., 2014; Pejcha & Prieto, 2015b); however, they do

[2]ZTF i-band data is partnership-specific and lacks full-sky coverage like public gr-band data.

not completely account for the early cooling or late radioactive phases and should be phase-dependent. Martinez et al. (2022a) addressed this by analysing 74 high-quality Type II SN light curves with extensive coverage in optical ($uBgVri$) and NIR (YJH) bands from CSP. They compute pseudo-bolometric fluxes via broadband integration and apply corrections for unobserved UV and IR contributions – particularly important at early times ($\lesssim 20$ d) and late times ($\gtrsim 100$ d), respectively.

As expected, the UV contributes significantly early on – between 50% and 80% of the total flux (Bersten & Hamuy, 2009; Martinez et al., 2022a) – and the full SED is well-described by a BB. As the SN expands and cools, the UV flux drops sharply, making its contribution negligible during the plateau. At these times, the BB approximation also begins to break down. Importantly, Martinez et al. (2022a) show that the i-band becomes the most critical optical contributor as time progresses, and that IR emission can account for up to ∼50% of the total flux around 100 d post-explosion, underscoring the need for NIR coverage or appropriate corrections when estimating $L_{\rm bol}(t)$.

For example, the BC for g-band based on the $g - i$ colour is defined as:

$$\mathrm{BC}_{g(g-i)} = m_{\rm bol} - m_g \tag{4.3}$$

where BC and m are the BC and extinction corrected magnitude in g-band and $m_{\rm bol}$ is the bolometric magnitude. The absolute bolometric magnitude, $M_{\rm bol}$, is defined by:

$$M_{\rm bol} = M_{\odot,\rm bol} - 2.5 \log_{10}\left(\frac{L_{\rm bol}}{L_{\odot,\rm bol}}\right) \tag{4.4}$$

where $L_{\odot,\rm bol} = 3.845 \times 10^{33}$ erg s^{-1} and $M_{\odot,\rm bol} = 4.74$ mag are the bolometric luminosity and magnitude of the sun (Drilling & Landolt, 2000).

Using the comprehensive photometric data from CSP, Martinez et al. (2022a) calculate BC, as a function of colour, splitting the data into phases, cooling, plateau and tail to represent the different power mechanisms. The cooling phase is typically ∼20 d after

Colour	Phase	Range	c_0	c_1	c_2	c_3	c_4	σ
$g-r$	Cooling	$(-0.26, 1.09)$	-0.352	1.753	-4.078	1.961	—	0.11
	Plateau	(0.01, 2.17)	-0.219	0.813	-2.194	1.205	-0.305	0.14
	Tail	(0.78, 2.07)	-9.994	21.507	-15.343	3.273	—	0.22
$g-i$	Cooling	$(-0.50, 1.15)$	-0.214	0.789	-2.357	1.097	—	0.11
	Plateau	$(-0.10, 2.79)$	-0.140	0.292	-1.224	0.522	-0.090	0.07
	Tail	(0.86, 2.43)	-0.263	-0.154	-0.256	—	—	0.08

TABLE 4.1: Coefficients of the polynomial fits to the BC versus different colours from Martinez et al. (2022a). These are the parameters used with $g-i$ or $g-r$ colours in Eqs. 4.3 and 4.4 to generate bolometric luminosities.

explosion (before the transition to the radioactive tail) and the plateau phase is between the cooling and transition (see Martinez et al., 2022a, for details).

4.3 LT Photometry

As ZTF alone would provide suboptimal and inconsistent colour information (i.e., not all SNe would have ZTF i coverage), I supplement the ZTF data with additional photometry from other sources to enhance BCs. Starting in the 2024A semester (and continuing over two successive semesters), I have led a proposal on the LT to obtain multi-band photometry with the optical imager IO:O (see Chapter 5 for details) for Type II SNe on their radioactive tail.

The LT, a fully robotic 2 m-class telescope, is well suited for follow-up observations of transient events. It is particularly effective in complementing wide-field survey telescopes, as the radioactive tail phase of SNe often fades beyond the typical ZTF survey depth of $\sim$20.5 mag. The LT can reach limiting magnitudes of 22.5 – 23 mag (during dark time with an integration time of 120 s in r-band), making it ideal for capturing late-time emission. Additionally, the LT provides broader colour coverage, extending into the NUV and NIR through its *urgiz* filter set. This extended wavelength coverage, combined with flexible cadence and deeper sensitivity, is essential for confirming their nebular behaviour.

The LT program selects Type II SNe based on the following selection criteria: (1) peak magnitude < 18 mag, (2) at least one spectroscopic classification confirming Type II classification (rejecting ambiguous spectra), (3) resolved plateau end, (4) adequate cadence ($< 4-5$ d on average in any filter) along the plateau, and (5) not be lost to

visibility within 2 months of the plateau end – SNe with a gap of ≥ 2 months must be rejected largely due to an inability to confidentially measure the luminosity of the tail at the start.

46 Type II (excluding IIn and IIb) SNe found by or saved to the BTS in 2024 peaked above 18 mag in any filter. Of these 46, 2 did not pass the criteria due to poor coverage along the plateau or being lost to visibility close to the start of the tail.

Objects meeting these criteria receive follow-up *griz* observations, beginning around the start of the tail and progressing through this phase. A minimum of three epochs are scheduled: one near the plateau-to-tail transition and two subsequent observations during the established tail. The cadence is based on the ^{56}Co decay timescale ($\tau_{\rm Co} = 77$ d), with the first observation typically occurring when the SN reached approximately 19 mag in *riz*-bands and 21 mag in g (for a SN peaking at 18 mag). A second epoch followed $\sim$7 d later (weather permitting), and a final observation is scheduled approximately 30 d after the initial measurement – corresponding to $\sim$half the ^{56}Co decay timescale. This both confirms the SN has entered the radioactive decay phase and aims to provide multiple colour measurements – particularly the critical $g - i$ colour identified by Martinez et al. (2022a). Fig. 4.2 demonstrates typical examples of SN targeted by this program, illustrating both the selection criteria and the timing of complementary *griz* observations.

Since the beginning of March 2024, the programme has taken constraining late-time observations in *griz* for 65 Type II SNe that were all on or close to beginning their radioactive tail – including SN 2023ixf (Michel et al., 2025). LT photometry was processed using a `python` based image subtraction pipeline, `subphot`, I developed – see Chapter 5.

4.4 ZTF Bright Transient Survey Sample

See Chapter 3, Section §3.3 for an overview of the BTS and FP. Since beginning in 2018, the BTS has catalogued 360 Type II SNe[3] that peak (in any filter) brighter than 18 mag – this excludes Type IIn, Type IIb and SLSNe.

[3]These all pass the criteria in Perley et al. (2020) and were downloaded from the BTS Sample Explorer.

Out of these 360 events, 306 have significant plateaus observed and measured, found using a gradient analysis along the plateau of the GP model. The start and end are estimated based on a dynamically calculated gradient threshold in regime from initially around $T = 0-100$ d, but extends to either side where appropriate. A cutoff of 150 d was enforced as the method to measure the plateau becomes unreliable for longer plateaus if the GP light curve is particularly smooth or linearly declines.

The plateau measurement requires a well-defined peak (detections both before and after the peak) and a well-defined end of the plateau. For the peak coverage constraint, I require the first criterion from Chapter 3, Section 3.3.5.1 which states at least one measurement in the regime $T_{g,75} - 4 \leq T \leq T_{g,75} + 4$ [d] is required, where $T_{g,75}$ is the time at ZTF g peak flux $\times$ 0.75 before peak. Additionally, I require that there is at least one detection (not upper limit) in each of the following regimes:

- $T_{\rm plat,end} + 10 \leq T \leq T_{\rm plat,end} + 30$ [d]
- $T \geq T_{\rm plat,end} + 50$ [d]

This ensures the fitting processes are constrained by multiple measurements post-plateau. This selection criterion does not remove any events as events that peak <18 mag will typically have detections during the fall from the plateau from either ZTF or other surveys (e.g. ATLAS). The mean change in luminosity from ZTF r peak to the end of the plateau +20 d is 1.99 mag ($\sigma_{\rm std} = 0.67$ mag), $\sim$0.5 mag brighter than the nominal survey limit and $\sim$1 mag brighter than the typical limiting magnitude of ZTF FP.

Of the 54 without plateau measurements, visual inspections reveal that most have a clear plateau phase; however, most also have poor coverage pre-peak, so both the GP light curve is unconstrained and the plateau finding method cannot establish a start, even if an end is found. In some cases, the first half of the plateau is caught and there are no observations beyond, so the end of the plateau is not accurate to the plateau phase, resulting in plateau durations >300 d. Also within this 54 are unique light curves that show no clear plateau phase (e.g., ZTF20aatqesi, ZTF22aaspkif and ZTF22abybbud in Figs. C.1, C.1 and C.1, respectively).

195 of the remaining 305 pass the peak coverage level cut, and 136/195 pass the end of plateau cuts. Of the 136 in this final sample, 120 have ZTF FP, 81 have ATLAS

FP, 77 have P60 photometry, and 31 have LT photometry. The number of events with LT photometry listed here differs from the 44 that passed the selection criteria in 2024, as most of the 2024 events currently have only alert photometry available. For such cases, it is more difficult to satisfy the rise-time selection criterion given that Type II SNe typically rise rapidly, and alert photometry only includes detections above a 3σ threshold. As a result, these light curves often lack the earlier, fainter detections needed to characterise the rise. In contrast, FP, when available, provides deeper flux limits and can recover sub-threshold activity, increasing the likelihood that an event meets the rise requirement. Therefore, once FP becomes available for these events, the number passing the rise criterion is expected to increase.

4.5 Constructing Bolometric Light Curves

With the BC from Martinez et al. (2022a) and additional late-time photometry from the LT, the bolometric light curves of Type II SNe can be computed. The SN light curves are modelled using similar methods to those described in Chapter 3, Section 3.3.3, but with a multiplicative kernel, defined as kernel **K** (see Chapter 2) chosen based on the minimum of AIC and BIC values[4]. **K** is multiplied by a Squared Exponential kernel (with a larger length scale) in the temporal direction to better handle non-stationarity and smooth late time behaviour. The use of photometry from P60, ATLAS[5] and the NOT enhances training the GP by extending the coverage in wavelength space.

For the BC, I base phase definitions (cooling, plateau, tail) on the plateau phase as it provides the most straightforward measurement and clearly relates to the other regimes. I define the cooling phase as beginning at T = max[ZTF g-band peak time +10 d, plateau start time], ensuring this phase does not end before plateau onset – the g-band turnover generally indicates the beginning of hydrogen recombination while showing no regular plateau itself.

Following Martinez et al. (2022a), I define the transition time ($T_{\rm trans}$) as plateau end +20 d, recognising that the transition to the radioactive tail occurs during the post-plateau luminosity drop rather than precisely at plateau end. To avoid unphysical

[4]If the same kernel does not have the minimum AIC and BIC value, the kernel with the minimum BIC is chosen as I prefer BIC as a metric of model complexity.

[5]Binned into 2.5 d bins.

undulations in the GP model during the tail phase (which would create highly uncertain colour estimates), I instead fit an exponential decay of the form:

$$F(t) = A \times \exp\left(-\frac{t - t_0}{\tau}\right) \tag{4.5}$$

to the post-$T_{\rm trans}$ light curve in each filter, spanning the range $T_{\rm trans}$ to $T_{\rm trans}$+450 d, using `scipy.optimize.curve_fit`. Here, t_0 is a temporal offset, A is a normalisation constant, and τ is the exponential decay timescale [6].

This exponential fit is only applied when there are ≥ 3 detections (not non-detections) post-$T_{\rm trans}$. For bands with < 3 detections in bands (excluding ZTF r), I use the $r - B_i$ colour at $T_{\rm trans}$ to scale the ZTF r-band flux to band B_i flux, as r-band measurements typically maintain the highest SNR during this phase due to increasing IR contributions. While this assumes constant colour evolution, it provides a reasonable approximation for the early tail. Figs. 4.2 and 4.3 demonstrate this methodology for ZTF23abnogui and ZTF24aaqajjb (with complementary LT observations), and ZTF19aapafit and ZTF19aadnxnl (ZTF and ATLAS data only).

The error envelope in Figs. 4.2 and 4.3 is propagated through from $3\times\sigma_{RMS}$ in the exponential fit. The envelope is conservative to account for the assumption of constant colour evolution (where relevant) and no additional power contributed from other sources (e.g. CSM).

Where possible, the SDSS g − SDSS i colour from LT photometry is used to compute the bolometric luminosity following:

$$m_{g,\rm bol} = \mathrm{BC}_{g(g\ -\ i)} + m_{\rm g} \tag{4.6}$$

$$M_{g,\rm bol} = m_{g,\rm bol} - 5\log(\frac{d_l\,[\mathrm{Mpc}]}{10}) + 2.5\log(1+z) - A_V \tag{4.7}$$

[6] Interpreted as the characteristic time over which the flux decreases by a factor of e due to the radioactive decay of ^{56}Co to ^{56}Fe

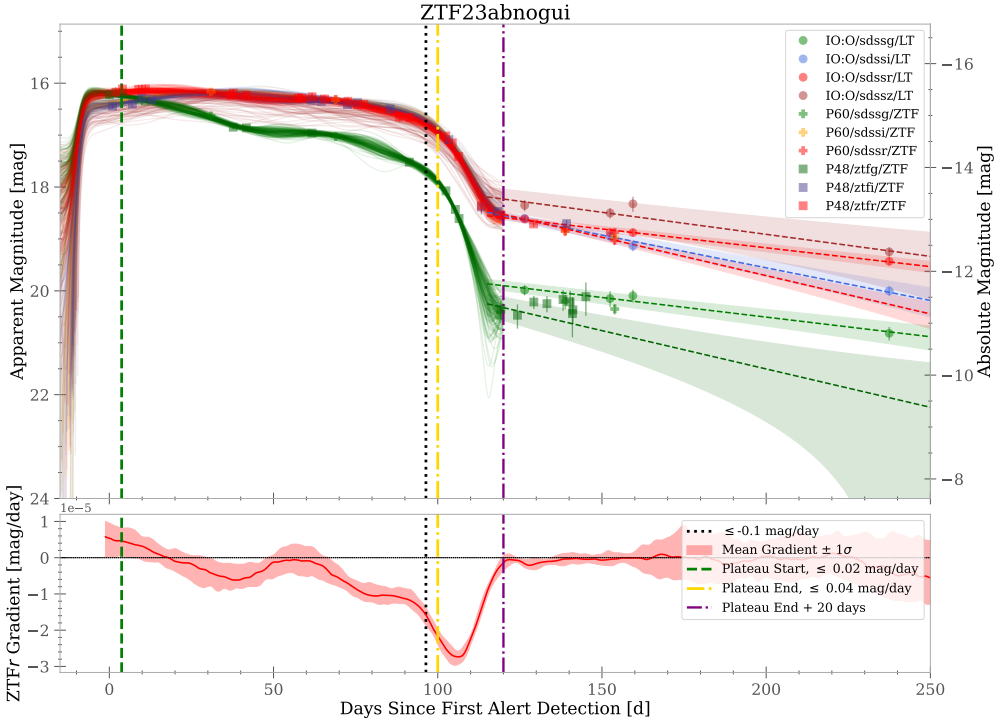

Figure 4.2.1: ZTF23abnogui ZTF (*gri*) light curves with P60 (*gri*) and LT (*griz*) photometry.

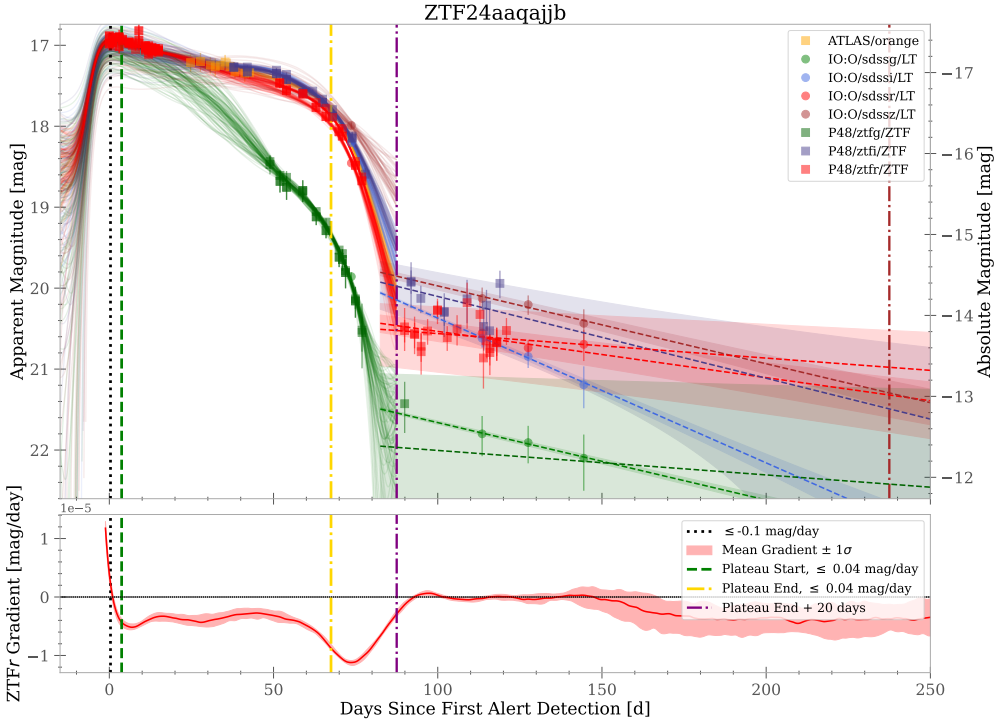

Figure 4.2.2: ZTF24aaqajjb ZTF (*gri*) light curves with ATLAS (*o*) and LT (*griz*) photometry.

FIGURE 4.2: ZTF23abnogui (*top*) and ZTF24aaqajjb (*bottom*) – Examples of Type II SN light curves with complementary LT (*circles*) and alert ZTF (*squares*) observations showing the well-defined plateaus and the radioactive tails. Note the high SNR in SDSS *g* from the LT at late times. Solid lines representing the GP fits during the cooling and plateau phases, transitioning to exponential decay fits (*dashed lines*) during the radioactive tail. Vertical dotted lines mark key plateau phases: plateau start (*green*), plateau end (*yellow*), and the approximate transition time $T_{\rm trans}$ (*purple*) where the SN enters the radioactive tail phase.

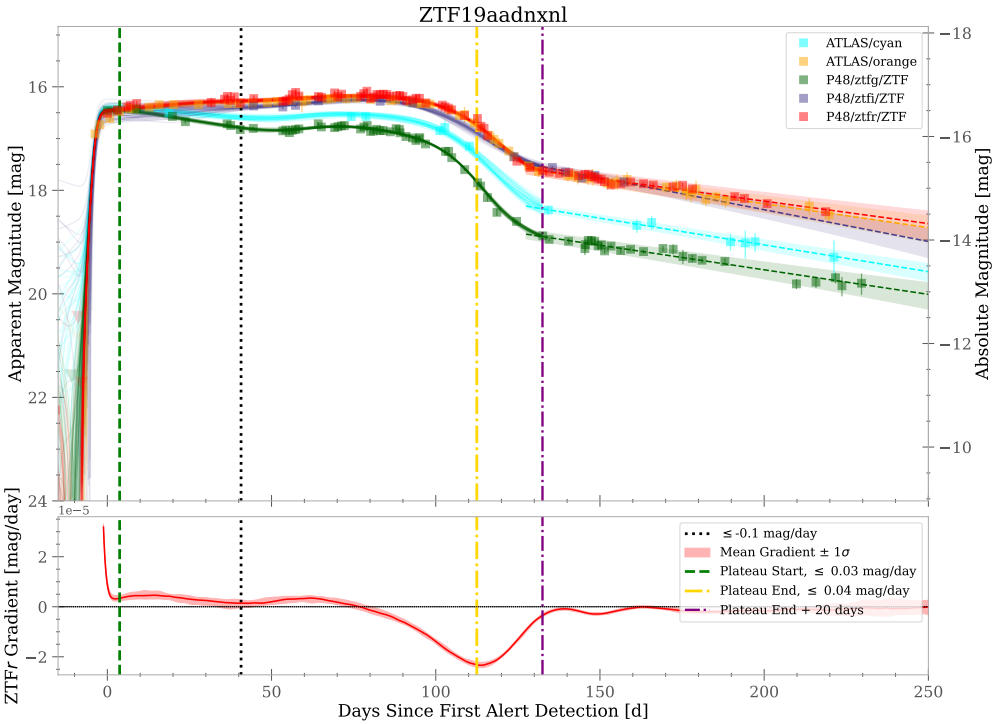

Figure 4.3.1: ZTF19aadnxnl ZTF (*gri*) light curves with ATLAS (*co*) photometry.

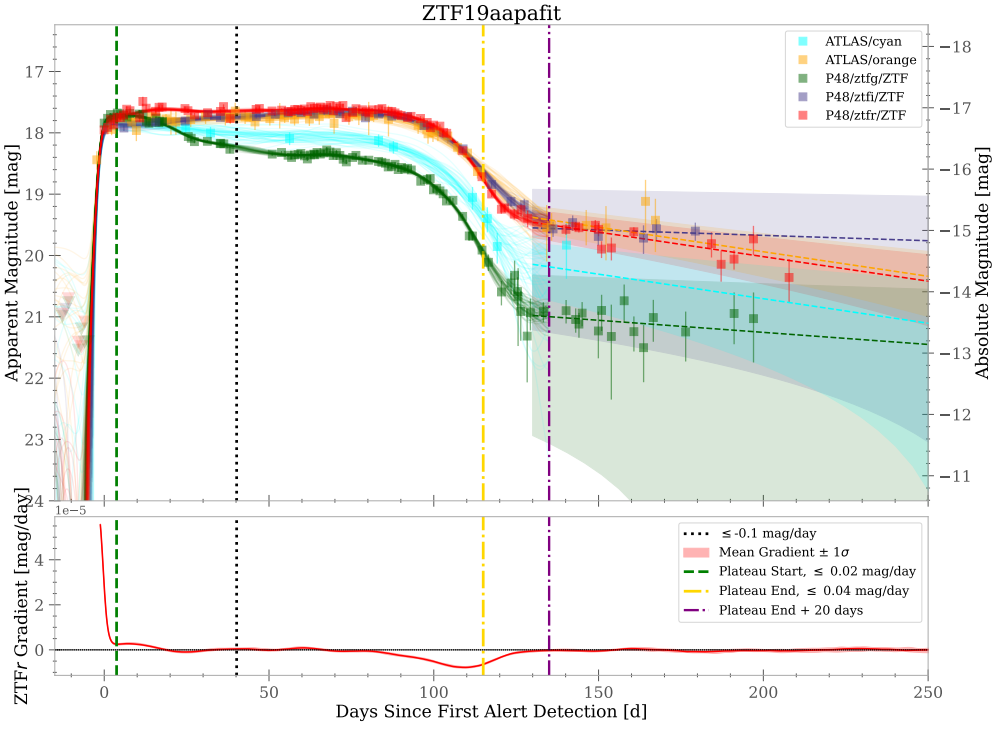

Figure 4.3.2: ZTF19aapafit ZTF (*gri*) light curves with ATLAS (*co*) photometry.

FIGURE 4.3: ZTF19aadnxnl (*top*) and ZTF19aapafit (*bottom*) – Examples of Type II SN light curves with ZTF and ATLAS showing well-defined plateau and the radioactive tail. The same as Fig. 4.2 but for light curves with FP.

$$L_{\rm bol}\,[\rm erg\ s^{-1}] = 10^{0.4\left(M_{\odot,\rm bol} - M_{\rm g,bol}\right)} \times L_{\odot,\rm bol}\,[\rm erg\ s^{-1}] \tag{4.8}$$

In the absence of SDSS i-band observations, first ZTF i is used (e.g., ZTF g − ZTF i) or ZTF r is used (e.g., ZTF g − ZTF r) if there are no i-band observations from either available.

To construct a continuous bolometric light curve that smoothly spans all phases of SN evolution, I model each regime (cooling, plateau, and radioactive tail) separately and combine them using sigmoid weighting functions. The final composite light curve is computed as a weighted sum, with the weights defined by:

$$\sigma(t) = \frac{1}{1 + \exp\left(\frac{t - T_i}{\omega_i}\right)} \tag{4.9}$$

where T_i [d] is the transition time between phases and ω_i [d] controls the smoothness of the transition.

For the transition from the initial cooling phase to the plateau, I set the midpoint at $T = \max[\text{ZTF } g\text{-band peak time} + 10\,\text{d}, \text{plateau start time}]$, with $\omega = 3\,\text{d}$, ensuring a seamless shift as hydrogen recombination begins to dominate. For the plateau-to-tail transition, the sigmoid is centred at the measured transition time $T = T_{\rm trans}$, with $\omega = 5\,\text{d}$, allowing for a gradual blend as the ejecta becomes optically thin and the light curve becomes powered primarily by radioactive decay.

For uncertainties on both the colour and bolometric luminosity, I use the ability to draw samples from the GP and calculate the 68% CI. Shown in Fig. 4.4 are the bolometric light curves for ZTF19aapafit and ZTF19aadnxnl.

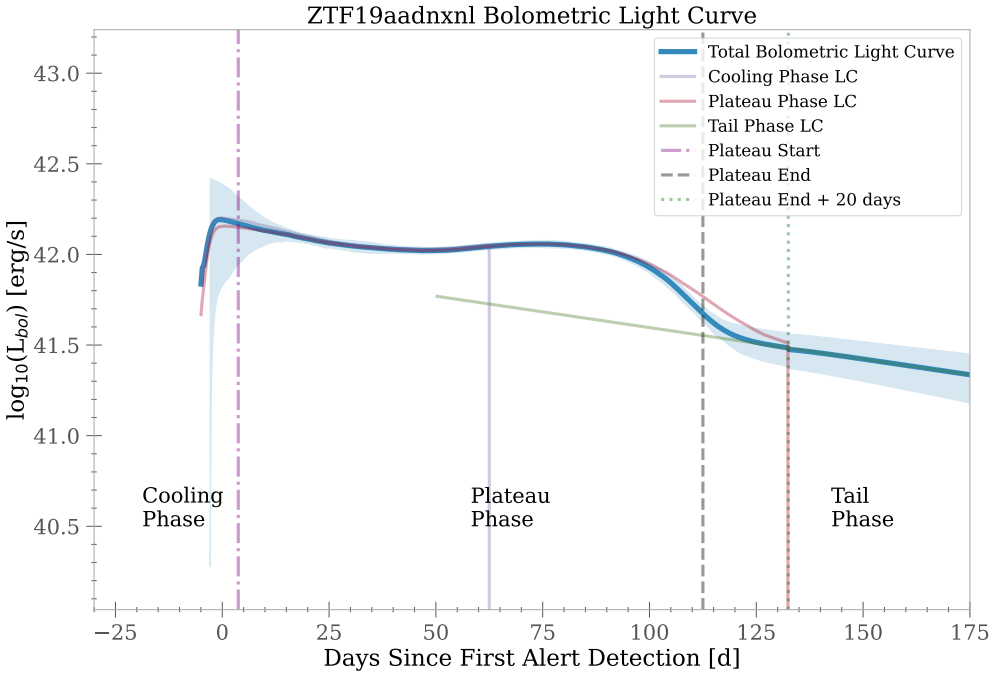

Figure 4.4.1: ZTF19aadnxnl bolometric light curve.

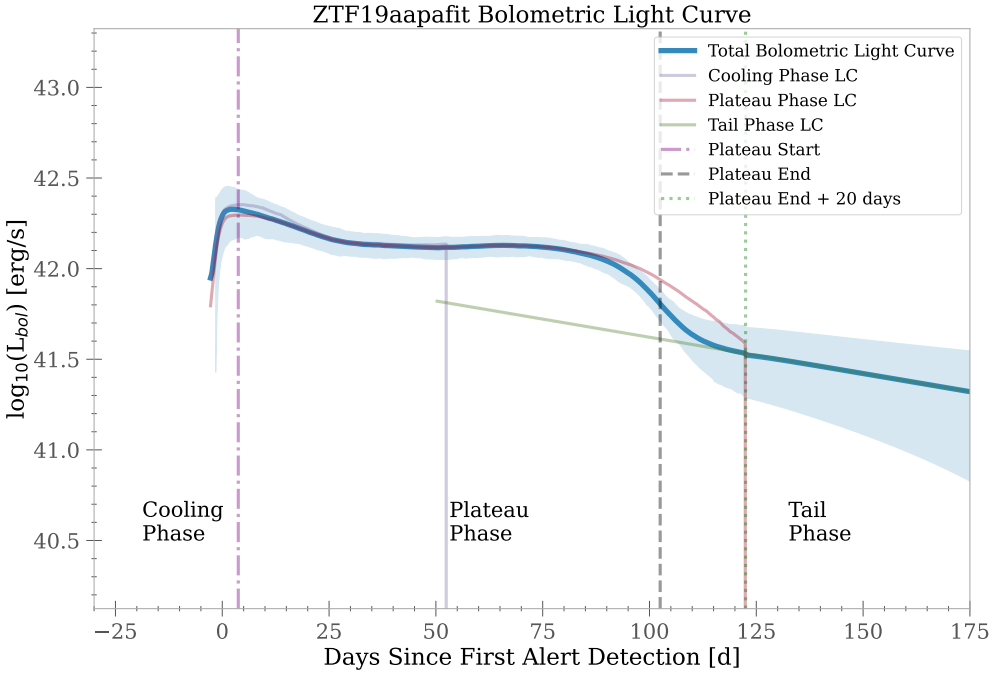

Figure 4.4.2: ZTF19aapafit bolometric lightcurve.

FIGURE 4.4: ZTF19aadnxnl (*top*) and ZTF19aapafit (*bottom*) – Example bolometric light curves Type II SNe using phase-specific bolometric corrections from Martinez et al. (2022a). The bolometric light curves are divided into three distinct evolutionary phases (cooling, plateau, and radioactive tail), each requiring independent BC parameters. Individual phase-specific bolometric light curves are shown in different colours, with vertical dotted lines marking the transition boundaries between phases. The final combined bolometric light curve (*blue*) and error envelope incorporates sigmoid weighting functions at the transitions to ensure continuity while preserving the physical characteristics of each phase. The optical light curves for these SNe can be seen in Fig. 4.3.

4.6 Results

As the BTS is a highly complete, magnitude-limited sample, I apply a correction to account for those events missed due to peaking fainter than the limiting magnitude of 18 mag required for the sample. The core principle is the same as described in Chapter 3, Section §3.4.2, correcting for intrinsic observational biases that favour the detection of more luminous events since they can be observed to greater distances in a magnitude-limited survey (Malquist bias; Malmquist, 1920).

Based on the sample selection criteria described in Section 4.4, the limiting magnitude for the $V_{\rm max}$ correction is set by the peak brightness, with a threshold of $m_{\rm peak} = 18$ mag. However, because the analysis also requires measurements during the radioactive tail phase, the survey's nominal limiting magnitude of ∼20.5 mag introduces an additional constraint. For some SNe, the tail magnitude ($m_{\rm Tail}$) – used to calculate $M_{\rm Ni}$ – may fall below the detection threshold (i.e., $m_{\rm Tail} > 20.5$ mag), resulting in a bias against SNe with intrinsically faint tails, as these events are more likely to be excluded from the sample due to insufficient late-time coverage.

To account for this, a conservative approach is adopted: when $m_{\rm Tail} \geq 20.5$ mag, the SN is excluded from the volume correction (e.g., $1/V_{\rm max} = 0$), as its tail would not be reliably detectable across the survey volume. For all other cases, $V_{\rm max}$ is computed as:

$$V_{\rm max} = \frac{d_{l,\rm max}^3}{(1+z)^3} \tag{4.10}$$

where $d_{l,\rm max} = \min[d_{l,\rm peak}, d_{l,\rm Tail}]$ and the factor (1+z) coverts this to the comoving distance – $1/V_{\rm max}$ is used for weighting after being normalised to unity. These distances represent the maximum redshift-limited luminosity distances at which the SN could be observed given either its peak brightness or tail brightness, and are calculated using the relations:

$$d_{l,\mathrm{peak}}\,[\mathrm{Mpc}] = 10^{(18.5-M_{r,\mathrm{peak}}-A_V)/5} \tag{4.11}$$

$$d_{l,\mathrm{Tail}}\,[\mathrm{Mpc}] = 10^{(20.5-M_{r,\mathrm{Tail}}-A_V)/5} \tag{4.12}$$

For the 136 in the sample, $m_{\mathrm{Tail}} > 20.5$ mag occurs in $5 \pm 3\%$ of the population (uncertainty is the 95% CI), and thus, this excludes only a small portion of events.

In addition to volume-corrections, corrections for host extinction must be carefully considered, as extinction can systematically reduce the observed fluxes, leading to underestimated bolometric luminosities. So far, all analyses have assumed zero host galaxy extinction ($A_V = 0$). Given that BCs are applied to broadband photometry, any uncorrected extinction can propagate non-linearly into the derived M_{Ni}, potentially biasing estimates.

To quantify this effect, I selected a representative subset of SNe spanning a wide range of M_{Ni} values ($0.9 - 30 \times 10^{-2}$ $\mathrm{M}_\odot$) and re-measured M_{Ni} assuming different host extinctions: $A_V = [0.1, 0.3, 0.7, 1.5]$ mag. Extinction in the g, r, and i -bands were computed using a standard Milky Way reddening law ($R_V = 3.1$) following Cardelli et al. (1989), implemented via the `extinction` `python` package (see Table C.1). Each light curve was first corrected for extinction before recalculating M_{Ni} using the same method.

The results, presented in Table C.2, show that even in the case of significant host extinction ($A_V = 1.5$ mag), changes in M_{Ni} remain within a factor of $\sim$2. For typical extinctions ($A_V \lesssim 0.3$ mag), the effect is minimal. This demonstrates that while extinction introduces some additional uncertainty, it does not dominate the error budget for most events. Consequently, host extinction can be considered a secondary effect for the majority of the sample.

To maintain consistency with previous analysis (Chapter 3, Section 3.3.4), I apply an empirical extinction correction based on colour excesses at peak. Assuming $A_g/A_V = 1.19$, $A_r/A_V = 0.84$, and $A_i/A_V = 0.61$ (again neglecting redshift effects), I estimate extinction from observed colours. For a $g - r$ reddening of 1 mag, the corresponding extinction values are $A_g = 3.37$ mag and $A_r = 2.41$ mag. Similarly, for $g - i$ reddening of 1 mag, $A_i = 2.03$ mag. To correct for extinction, I multiply the colour excess at peak

by these coefficients and apply the correction to the corresponding magnitudes. These adjustments then propagate into the bolometric luminosities.

Importantly, the resulting shifts in $M_{\rm Ni}$ remain small, confirming that host extinction does not significantly bias the derived $M_{\rm Ni}$ in most cases.

For the 136 SNe in the final sample, I show the weighted KDE distributions (refer to Chapter 3, Section §3.4.2), unweighted histograms and the ECDFs of tail luminosities, $L_{\rm bol}(t = T_{\rm trans}) = L_{\rm Tail}$, in Fig. 4.5.

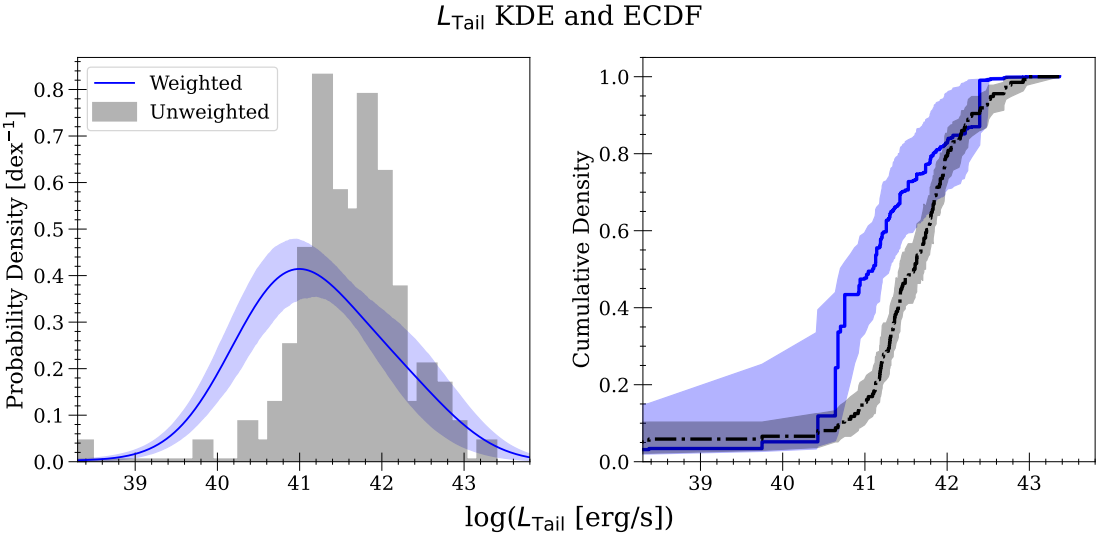

FIGURE 4.5: KDE distribution (*left*) and ECDF (*right*) for the bolometric luminosity on the tail, $L_{\rm Tail}$. This is taken at the end of the plateau + 20d ($T_{\rm trans}$). In grey are the unweighted distributions, and in blue are the volume-corrected distributions. The KDE and ECDFs are plotted with their associated 80% CIs.

Based on the relationships commonly used to calculate $M_{\rm Ni}$ (Eqs. 4.1 and 4.2), I show the weighted and unweighted KDEs and ECDFs in Fig. 4.6. The mean, median and other characteristic values of the distributions in Figs. 4.5 and 4.6 are in Table 4.2.

In Fig. 4.7, I show the bolometric luminosity at 50 d, $L_{50\,\rm d}$, vs $M_{\rm Ni}$ in the upper panel as well as the bolometric luminosity at a time after explosion equal to half of the plateau duration, $L_{t_p/2}$, vs $M_{\rm Ni}$ in the lower panel. A Spearman's rank test between $L_{50\,\rm d}$ and $M_{\rm Ni}$ for both methods of calculating $M_{\rm Ni}$ reveal strong, positive correlations, with the coefficients, R_{sp}, > 0.70 and $p \ll 10^{-5}$. Linear regression, using `scipy.stats linregress`, defines these relationships in Eqs. 4.13 and 4.14.

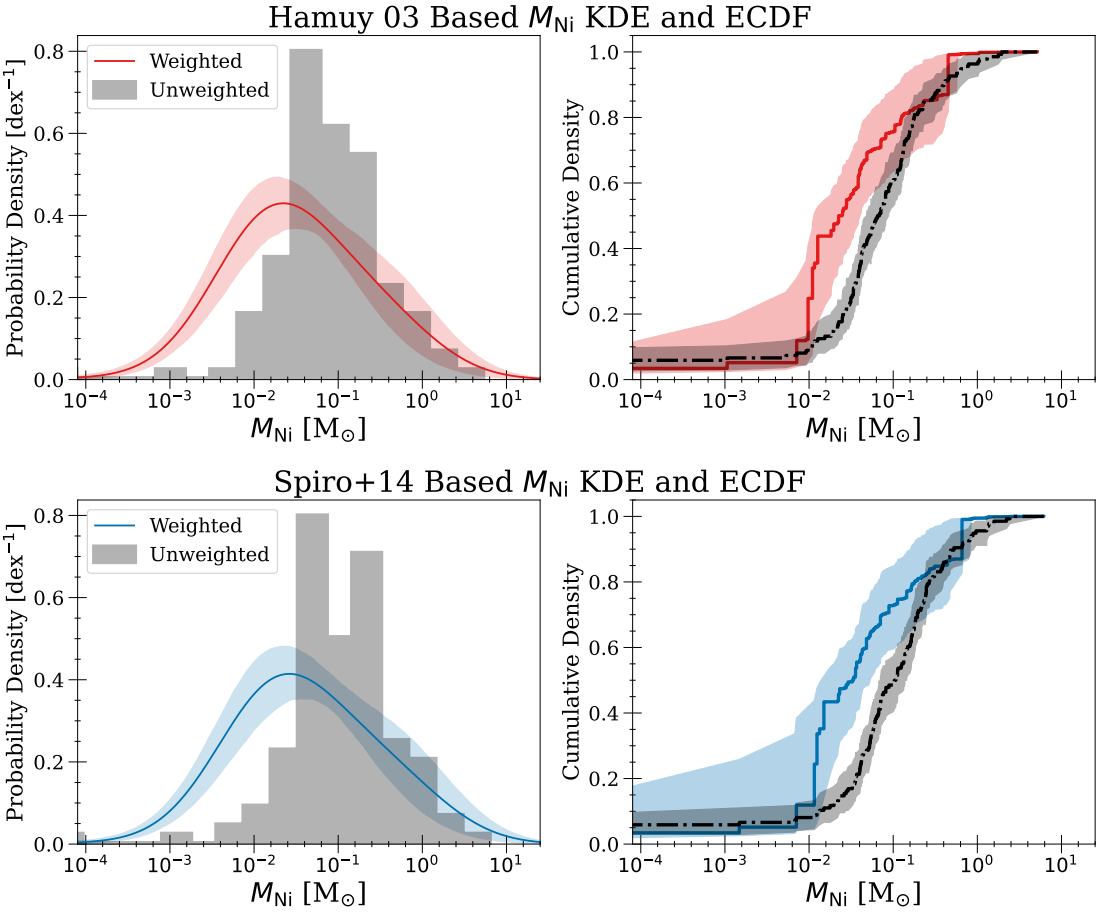

FIGURE 4.6: KDE distribution (*left column*) and ECDF (*right column*) for $M_{\rm Ni}$, calculated based on Hamuy (2003) (Eq. 4.1; *top row*) and Spiro et al. (2014) (Eq. 4.2; *bottom row*). In grey are the unweighted distributions, and in red/blue are the volume-corrected distributions. The KDE and ECDFs are plotted with their associated 80% CIs.

Parameter	Units	Mean	25th%ile	50th%ile	75th%ile	Range
			Weighted			
$M_{\rm Ni}$[1]	$\times 10^{-2}$ M$_\odot$	$2.50^{+1.26}_{-0.68}$	$1.07^{+0.41}_{-0.47}$	$3.08^{+1.66}_{-1.08}$	$8.39^{+4.33}_{-23.34}$	[0.84, 79.58][3]
$M_{\rm Ni}$[2]	$\times 10^{-2}$ M$_\odot$	$2.91^{+1.50}_{-0.84}$	$1.13^{+0.99}_{-0.71}$	$3.82^{+2.04}_{-1.33}$	$12.80^{+7.33}_{-20.98}$	[0.94, 129.30]
$L_{\rm Tail}$	$\times 10^{41}$ erg s^{-1}	$0.85^{+0.58}_{-0.32}$	$0.42^{+0.36}_{-0.27}$	$1.50^{+0.84}_{-0.54}$	$5.42^{+3.10}_{-8.88}$	[0.37, 48.95]
			Unweighted			
$M_{\rm Ni}$[1]	$\times 10^{-2}$ M$_\odot$	$6.26^{+1.22}_{-0.62}$	$2.83^{+0.61}_{-0.77}$	$7.42^{+0.88}_{-0.79}$	$15.36^{+3.30}_{-4.20}$	–
$M_{\rm Ni}$[2]	$\times 10^{-2}$ M$_\odot$	$7.81^{+1.75}_{-0.89}$	$3.81^{+0.82}_{-1.05}$	$10.61^{+1.36}_{-1.20}$	$23.48^{+5.06}_{-6.45}$	–
$L_{\rm Tail}$	$\times 10^{41}$ erg s^{-1}	$4.68^{+0.67}_{-0.34}$	$1.43^{+0.44}_{-0.39}$	$4.17^{+0.53}_{-0.47}$	$8.81^{+1.90}_{-2.42}$	–

[1] Calculated using Eq. 4.1, based on Hamuy (2003).
[2] Calculated using Eq. 4.2, based on Spiro et al. (2014); Valenti et al. (2016).
[3] The ranges reported are the 5th and 95th percentiles to remove outliers beyond the limits of the original dataset.

TABLE 4.2: Mean and median of the volume corrected KDE for $M_{\rm Ni}$ and $L_{\rm Tail}$ in the final sample of 136. 25th and 75th percentiles are calculated using the ECDFs.

$$\log(M_{\rm Ni}\,[{\rm M}_\odot]) = 0.81^{+0.11}_{-0.10} \times \log(L_{50\,\rm d}\ \ [{\rm L}_\odot]) - 8.10^{+0.84}_{-0.93} \quad (\sigma_{\rm SE} = 0.07) \tag{4.13}$$

$$\log(M_{\rm Ni}\,[{\rm M}_\odot]) = 0.79\,(\pm 0.11) \times \log(L_{50\,\rm d}\ \ [{\rm L}_\odot]) - 7.77^{+0.93}_{-0.97} \quad (\sigma_{\rm SE} = 0.08) \tag{4.14}$$

A Spearman's rank test between $L_{t_p/2}$ and $M_{\rm Ni}$ for both methods of calculating $M_{\rm Ni}$ reveal stronger positive correlations in both cases, with R_{sp}, > 0.75 and $p \ll 10^{-5}$. Linear regression defines these relationships in Eqs. 4.15 and 4.16.

$$\log(M_{\rm Ni}\,[{\rm M}_\odot]) = 0.59\,(\pm 0.11) \times \log(L_{t_p/2}\ \ [{\rm L}_\odot]) - 6.38^{+0.94}_{-0.97} \quad (\sigma_{\rm SE} = 0.08) \tag{4.15}$$

$$\log(M_{\rm Ni}\,[{\rm M}_\odot]) = 0.66^{+0.12}_{-0.11} \times \log(L_{t_p/2}\ \ [{\rm L}_\odot]) - 6.84^{+0.98}_{-1.06} \quad (\sigma_{\rm SE} = 0.08) \tag{4.16}$$

Uncertainties on the linear regression parameters are estimated through a two-step Monte Carlo approach. First, bootstrapping is used to account for sampling variability by randomly resampling the dataset with replacement. Second, within each bootstrap sample, the individual measurements are resampled based on their reported uncertainties. Linear regression is then performed on each bootstrapped resampled dataset, and this process is repeated 1000 times. The 68% CI on the regression parameters are derived from the resulting distributions, capturing both measurement uncertainty and sampling error. $\sigma_{\rm SE}$ is the standard error on the linear regression.

4.7 Discussion

For the volume-corrected sample of 136 Type II SNe, the weighted median $M_{\rm Ni}$ is $3.08^{+1.66}_{-1.08} \times 10^{-2}$ M$_\odot$ and $3.82^{+2.04}_{-1.33} \times 10^{-2}$ M$_\odot$ using Eqs. 4.1 and 4.2, respectively (calculated using the ECDFs in Fig. 4.6). These values align well with those reported in the literature: hydrodynamic modelling typically yields medians in the range of [2, 6] $\times 10^{-2}$ M$_\odot$ (e.g., Sukhbold et al., 2016; Müller et al., 2017; Kozyreva et al., 2019; Martinez et al., 2020; Martinez et al., 2022b), while non-hydrodynamic methods – similar

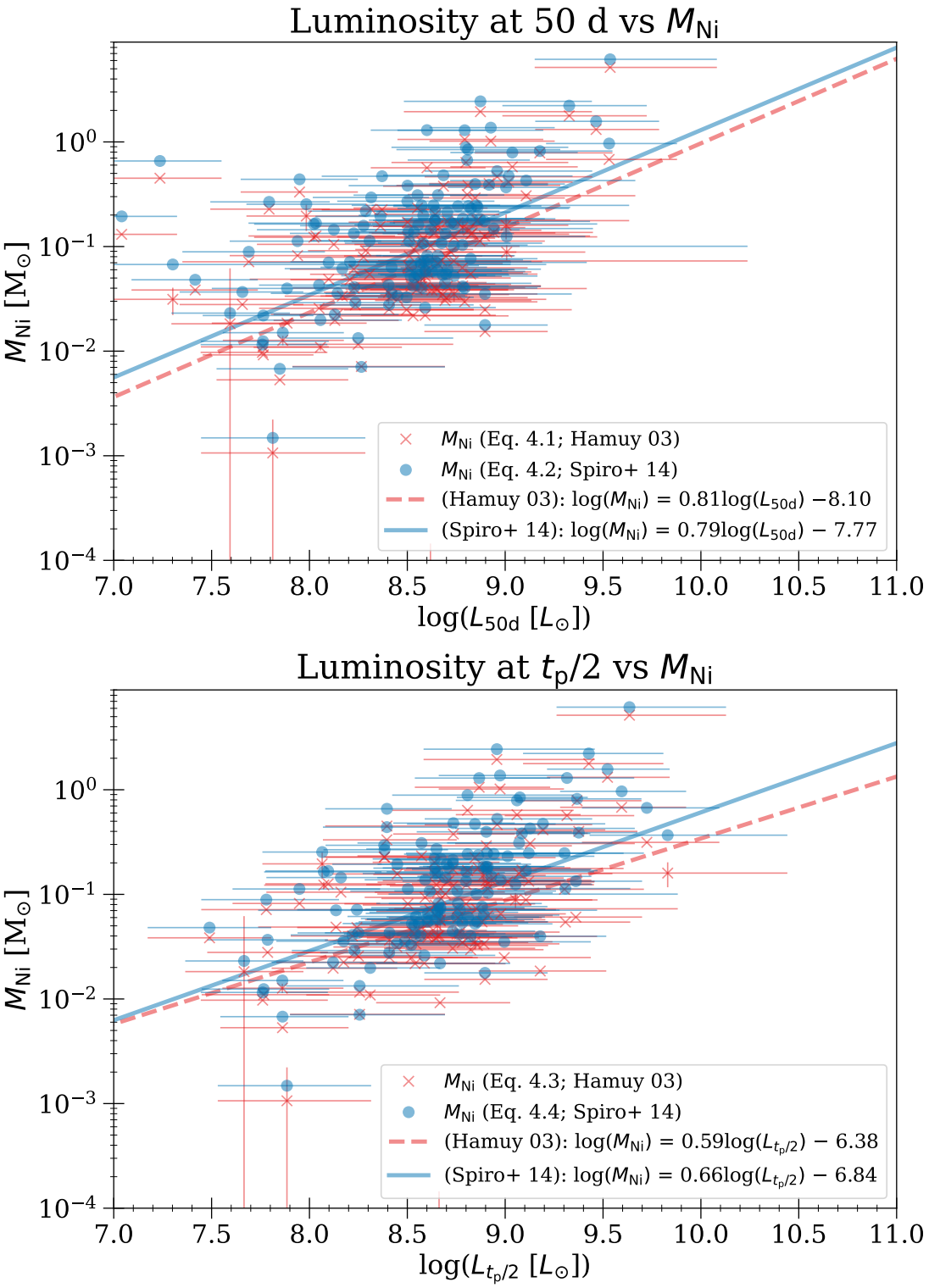

FIGURE 4.7: $M_{\rm Ni}$ vs $L_{50\,\rm d}$ (*top*) and $M_{\rm Ni}$ vs $L_{t_{p/2}}$ (*bottom*). The correlation between both sets of parameter shows high strength and significance, with Spearman rank coefficients > 0.70 and $p \ll 10^{-5}$ when considering both methods of calculating $M_{\rm Ni}$. The parameters for the linear regression are in the legend of the figures.

to those employed here – report a broader range extending up to 30 $\times 10^{-2}$ $M_\odot$ (e.g., Hamuy, 2003; Spiro et al., 2014; Pejcha & Prieto, 2015b; Valenti et al., 2016).

Like previous studies on $M_{\rm Ni}$, I find a continuous distribution across the volume-corrected sample (Fig. 4.6). A notable point of comparison is the upper limit for $M_{\rm Ni}$ where a discrepancy emerges as hydrodynamical modelling studies (e.g., Müller et al., 2017; Martinez et al., 2022b) typically yield lower maximum values than analytical approaches (e.g., Pejcha & Prieto, 2015b; Valenti et al., 2016) similar to those employed here. The 5th and 95th percentiles in this study are $\sim 0.1 \times 10^{-2}$ and $\sim 90 \times 10^{-2}$ $M_\odot$ respectively, though the upper boundary likely suffers from luminosity measurement uncertainties.

Whilst there is no theoretical limit of the maximum mass of ^{56}Ni synthesised in hydrogen-rich CCSNe, it is important to consider the unbiased range to, for example, asses how progenitor properties translate to SN evolution. For hydrogen-rich and hydrogen-poor CCSNe alike, the key physical factors that limit ^{56}Ni production include: (1) incomplete silicon burning efficiency due to finite explosion timescales and temperature gradients, (2) neutronisation at high densities that shifts nucleosynthesis toward neutron-rich isotopes rather than ^{56}Ni, (3) the finite mass of the silicon/oxygen shell available for explosive burning (typically 1 – 3 $M_\odot$in Type II progenitors), and (4) competition between different burning modes during the shock passage.

Given that BCs are used to recover unobserved flux, it is important to account for both the intrinsic uncertainty in the BC relations and their inability to capture all missing flux. I estimate the total systematic uncertainty on the $M_{\rm Ni}$ measurements by combining contributions from the uncertainties in: tail luminosities, BC, extinction, and incomplete gamma-ray trapping.

The average uncertainty on the measured tail luminosities is $\sim$ 0.03 dex, while the typical uncertainty on tail magnitudes is $\sim$ 0.3 mag, corresponding to $\sim$ 0.12 dex in flux. Adding this $\sim$ 0.12 dex measurement term in quadrature with the $\sim$ 0.1 dex calibration uncertainty of the $g - i$ bolometric correction from Martinez et al. (2022a) gives a combined BC-related systematic of $\sim$ 0.16 dex, equivalent to approximately 40% uncertainty in $M_{\rm Ni}$.

Extinction increases this uncertainty: the peak-colour based correction has a typical uncertainty of $\sim$ 0.1 mag, which corresponds to $\sim$ 10% in luminosity, still subdominant

to the BC term.

Incomplete gamma-ray trapping introduces an additional systematic. While not accounted for here, reduced trapping efficiencies would bias $M_{\rm Ni}$ downward, particularly for low-mass ejecta. CMFGEN models of 9 – 29 $M_\odot$ RSG explosions show trapping efficiencies $\gtrsim 60\%$ during the plateau and early tail phases (Dessart et al., 2021), with Jacobson-Galán et al. (2025) finding 60 – 100% at 100 – 150 d in their CMFGEN grids and $\sim 100\%$ for most observed SNe given gamma-leakage timescales > 450 d. Adopting a representative 90% efficiency implies tail luminosities could be underluminous by $\sim 10\%$, corresponding to $\log_{10}(1/0.9) \approx 0.04$ dex. For an 80% efficiency, this rises to ~ 0.1 dex. I fold this range in quadrature with the BC and measurement terms.

Combining these effects yields a total systematic uncertainty of ~ 0.18 – 0.2 dex (approximately 55 – 60%) on the $M_{\rm Ni}$ estimates. This budget captures the dominant contributions from bolometric calibration, measurement scatter, extinction, and possible incomplete gamma-ray trapping.

I infer that $24.3^{+11.2}_{-10.3}\%$ of the SN population possess $M_{\rm Ni} \geq 0.1$ $M_\odot$ using Eq. 4.1, this increases slightly to $27.1^{+9.6}_{-10.3}\%$ using Eq. 4.2. This confirms that high $M_{\rm Ni}$ mass events are exceptions, though there exist some examples: SN 1992am ($M_{\rm Ni} \sim 0.3$ $M_\odot$ Schmidt et al., 1994; Hamuy, 2001) and SN 2009kf ($M_{\rm Ni} \gtrsim 0.25 M_\odot$ Botticella et al., 2010; Ouchi & Maeda, 2020).

Of interest is the potential existence of a subpopulation of Type II SNe with extremely low $M_{\rm Ni}$, defined here as $M_{\rm Ni} \leq 1 \times 10^{-3}$ $M_\odot$. Based on Eqs. 4.1 and 4.2, these make up $4.3^{+8.6}_{-2.4}\%$ and $4.3^{+3.6}_{-1.6}\%$ of the volume-corrected sample, respectively. Although a minority, this subpopulation is notable for its characteristically low tail luminosities, with an unweighted median $\log(L_{\rm Tail}\ [\rm erg\ s^{-1}]) = 37.62$ and a standard deviation of 1.68, as expected from their low $M_{\rm Ni}$. This stems from the initial theoretical expectations that reduced ^{56}Ni synthesis leads to a fainter light curve at late times, since the radioactive decay of ^{56}Ni is the dominant power source during the nebular phase.

Interestingly, when comparing peak-to-tail declines in r-band magnitudes, these low-$M_{\rm Ni}$ SNe do not show a significantly greater drop relative to higher $M_{\rm Ni}$ counterparts. The median luminosity drop from peak to tail is $\sim$1.92 mag across the samples with $M_{\rm Ni}$ above or below 1×10^{-3} $M_\odot$, with a standard deviation of 0.60 mag, showing

no statistically meaningful difference between the subgroups. While one might expect a larger decline in cases of lower $M_{\rm Ni}$, due to reduced radioactive heating during the tail, this signal may be obscured by other factors such as variations in explosion energy, envelope mass, or dust formation at late times.

Overall, these findings are consistent with theoretical models where greater progenitor core compactness leads to more energetic explosions with enhanced explosive nucleosynthesis. Quantities are derived from the ECDFs in Fig. 4.6 with uncertainties representing the 80% confidence interval.

The correlations between luminosity on the plateau and $M_{\rm Ni}$ found here are significant given $p \ll 10^{-5}$, confirming the findings by Hamuy (2003); Spiro et al. (2014); Pejcha & Prieto (2015b); Valenti et al. (2016); Müller et al. (2017); Fang et al. (2025b). Like these studies, I find that SNe which produce larger $M_{\rm Ni}$ are more luminous on the plateau, whether considering $L_{50\,\rm d}$ or $L_{t_p/2}$.

Pejcha & Prieto (2015b) expresses the correlation (see their Fig. 1)[7] between $M_{\rm Ni}$ by Eq. 4.17.

$$\log\left(M_{\rm Ni}\,[\rm M_\odot]\right) = 1.53^{+0.18}_{-0.17} \times \log\left(L_{\rm pl}\,[\rm L_\odot]\right) - 14.3^{+1.40}_{-1.50} \tag{4.17}$$

where $L_{\rm pl}$ is the bolometric luminosity at 50 d (calculated by integrating the SED from ~ 0.19 – 2.2 μm).

When comparing the slope and intercepts found by Pejcha & Prieto (2015b), I find both quantities are inconsistent at a >3 σ level across Eqs. 4.13 – 4.16. I speculate that this is in large part due to the uncertainty in measuring the bolometric luminosity on the tail when there are only ZTF g and r-bands available. Additionally, as indicated by Valenti et al. (2016), the scatter in the relationships between the luminosity and $M_{\rm Ni}$ is likely more complicated than a simple 2d parameter space. This is evidenced by the correlation between the $M_{\rm Ni}$ and the explosion energy (Popov, 1993; Hamuy, 2003; Pejcha & Prieto, 2015b) as well as well the correlation between the plateau luminosity

[7] Pejcha & Prieto (2015b) expresses the relationship as usually presented, assuming uncorrelated uncertainties, in addition to accounting for spread in the covariance as a result of distance uncertainties. For consistency, I compare to the standard relationship.

and expansion velocity of Fe II λ5169 line (e.g., Hamuy, 2003; Martinez et al., 2022c). The bolometric luminosity on the tail is also strongly correlated with the explosion energy (Martinez et al., 2022c).

Altogether, the complex dependency of plateau luminosity on the tail luminosity, expansion velocity, explosion energy, and $M_{\rm Ni}$ suggests that the observed correlations (both here and in previous studies) are not artefacts of methodological bias or sample selection, but are instead caused by the underlying physics of CCSNe. This conclusion stems from the fact that these parameters are theoretically expected to be interrelated through the explosion physics itself. For instance, higher explosion energies – often associated with progenitors having more compact or evolved cores (e.g., Anderson, 2019) – result in higher post-shock temperatures and densities, particularly in the inner ejecta. Since the production of radioactive ^{56}Ni requires heating material above $\sim 5 \times 10^9$ K (e.g., Woosley & Weaver, 1995; Martinez et al., 2022c), more energetic explosions naturally yield greater amounts of ^{56}Ni. This, in turn, powers brighter plateau luminosities and more luminous tails due to increased radioactive heating. The "complexity" here is not random or confounding, but rather a signature of coherent physical coupling between progenitor structure, explosion dynamics, and radiative output – further suggesting that the relationships are fundamentally real and causally driven.

When examining the relationship between plateau duration (t_p) and $M_{\rm Ni}$, Spearman rank correlation tests yielded correlation coefficent $R_{sp} = -0.10$ with p-value $= 0.23$ for $M_{\rm Ni}$ calculated using Eq. 4.1, and $R_{sp} = -0.24$ with $p = 0.006$ for Eq. 4.2 (see Fig. 4.8).

For the former, the high p-value ($p > 0.05$) indicates no statistically significant correlation. For the latter, while the p-value ($p < 0.05$) suggests a significant trend, the negative correlation implies that larger $M_{\rm Ni}$ values are associated with shorter plateau durations – contrary to theoretical expectations that higher ^{56}Ni yields should extend the plateau by up to $\sim$20% (e.g., Kasen & Woosley, 2009; Bersten et al., 2011; Kozyreva et al., 2019).

This lack of consistency with theory, and the absence of a strong or positive correlation is in line with previous findings by Martinez et al. (2022c) and Jacobson-Galán et al. (2025), who similarly report no clear trend between these quantities. Given the broad distribution of t_p in the BTS sample, these results support the conclusion that there is no robust correlation between plateau duration and $M_{\rm Ni}$.

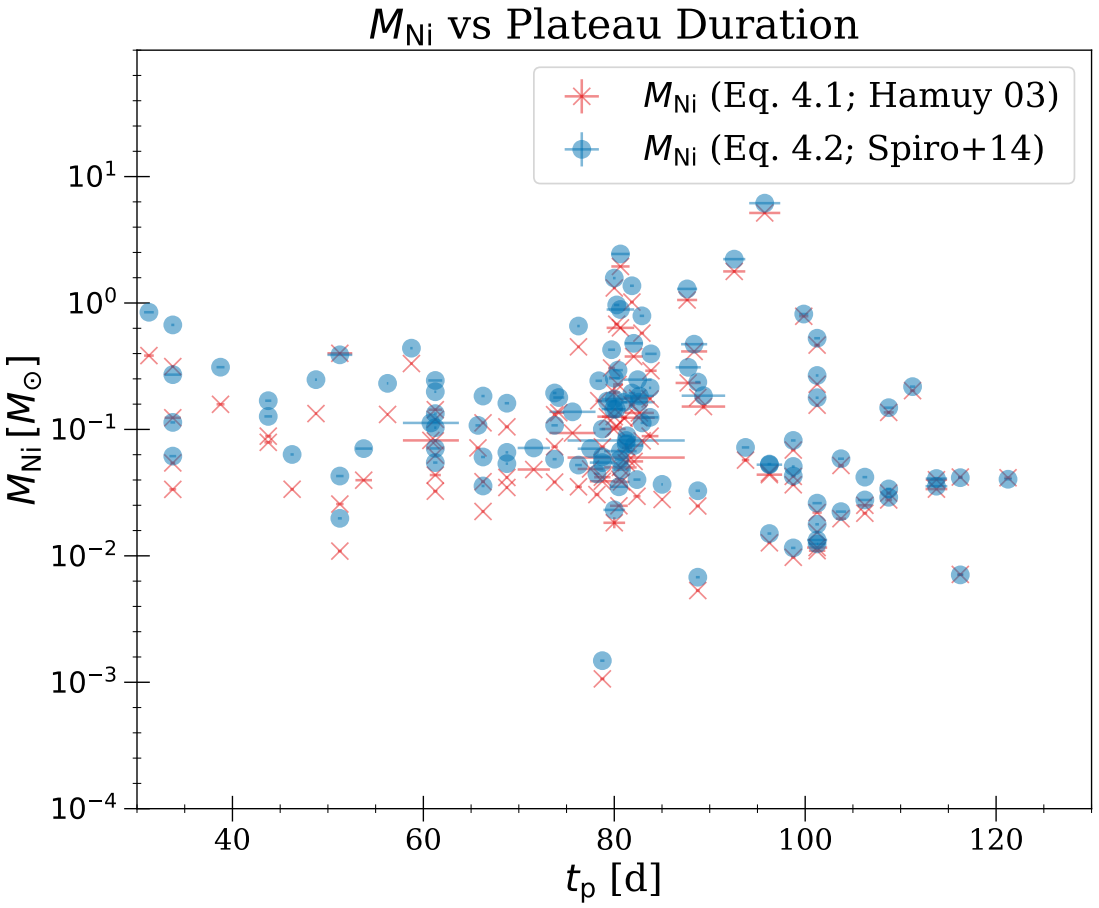

FIGURE 4.8: Correlation between $M_{\rm Ni}$ and plateau duration (t_p) for the BTS Type II SN sample. $M_{\rm Ni}$ from Eq. 4.1 and from Eq. 4.2 are shown as *red crosses* and *blue circles*, respectively. Despite a statistically significant result for $M_{\rm Ni}$ from Eq. 4.2 ($p < 0.05$), the correlation is weak and negative, opposite to the expected trend, suggesting no physically meaningful trend.

4.8 Nickel Mass Summary

In this preliminary investigation, I have used Type II SNe from the highly complete ZTF BTS sample to infer the ^{56}Ni mass from their well-sampled light curves. I find the weighted median mass of ^{56}Ni in a volume-corrected sample of 136 SNe from the ZTF BTS to be $M_{\rm Ni} = 3.08^{+1.66}_{-1.08} \times 10^{-2}$ M$_\odot$ and $3.82^{+2.04}_{-1.33} \times 10^{-2}$ M$_\odot$ from Eqs. 4.1 and 4.2 respectively. This is consistent with previous findings that estimate the median $M_{\rm Ni}$ to be between 2 and $30{\times}10^{-2}$ M$_\odot$.

I find a strong and statistically significant correlation between $M_{\rm Ni}$ and the luminosity at 50 d as well as a slightly stronger correlation between $M_{\rm Ni}$ and the plateau luminosity at the midway point. Both correlations have been previously found and are attributed

to the ^{56}Ni decay into ^{56}Co providing a noticeable boost in luminosity. The point at which this occurs is at 50 d or a time since the explosion equal to half of the plateau duration, and likely indicates the increasing contribution from the decay of radioactive material as the onset of radioactive phase begins in earnest.

Though the correlation between plateau duration and $M_{\rm Ni}$ returns $p < 0.05$, there is significant scatter in the relationship and the relationship is negative, indicating that SNe producing large $M_{\rm Ni}$ are fainter on the plateau, in contradiction with theoretical expectations. This is likely driven to the large heterogeneity in the plateau durations and shapes of Type II SNe. Thus, it is not clear whether $M_{\rm Ni}$ does increase the plateau duration.

Whilst the study has proved successful, there are several improvements that this study would benefit from. The most important would be to increase the number of SNe in the study. This can easily be done by requesting FP from ZTF and ATLAS for the entire sample (this not being possible at the time of writing). Late-time detections are crucial for improving both the GPR fits and the linear fits, enabling smoother transitions between distinct phases of the bolometric light curve. Additionally, extended photometric coverage at late times allows for more reliable and constraining colour measurements, which are essential for accurate BC. The continuation of the LT follow-up programme will significantly aid this effort, particularly for newly discovered SNe, by extending light curves deeper into the radioactive tail phase where constraints are otherwise limited.

An avenue worth exploring in the future is the ability to stack ZTF FP to increase the limiting depth from the nominal ∼20.5 mag to between 21.5 – 22 mag. This would recover the behaviour of the tail close to the transition from the photospheric phase to the tail phase, where the measurement of colour and magnitude is critical for calculating the tail luminosity and $M_{\rm Ni}$.

4.9 Data Availability

The light curves and empirical properties measured for the SNe, as they relate to this work, can be found here: [https://hpc.ljmu.ac.uk/~arikhind/Hinds_Thesis_Ni_Mass.html].

Chapter 5

Liverpool Telescope Image Subtraction and the Zwicky Transient Facility

5.1 Introduction

The increased rate of discovery of transients has driven the continued development of image subtraction techniques and software. The community has progressed greatly from photographic plates to CCDs, as explored in Chapter 1, Section §1.7, and with this shift and increased complexity of detectors, there has been a push to greatly improve transient detection and photometric measurements.

The increased rates necessitated an improvement on aperture photometry that was both more careful and more systematic, taking into account the PSF of the telescope and instrument in addition to varying seeing conditions, prompting PSF photometry. Image subtraction or difference imaging (e.g., Phillips & Davis, 1995; Naylor, 1998; Heasley, 1999; Alard & Lupton, 1998; Alard, 2000; Becker, 2015; Zackay et al., 2016b; Hu et al., 2022), using the PSF of the instrument, quickly became the standard after being introduced by Phillips & Davis (1995), Alard & Lupton (1998) and Gal-Yam et al. (2008).

This technique addresses several critical challenges in transient detection: it effectively removes contributions from host galaxies, attempts to mitigate blended contaminants,

compensates for varying observing conditions, and isolates absolute flux changes between epochs – enabling the detection of faint or subtly varying transients that would otherwise be overwhelmed by host galaxy light. Most simply explained, image subtraction hinges on subtracting a high-quality "template image" (obtained on in photometric conditions) from a "newer science" image after aligning, scaling, and PSF-matching the two. The residual "difference image" isolates flux changes between epochs, enabling precise detection of variable sources – even in complex environments. Subsequent refinements, such as the adaptive convolution kernels of Alard (2000), the computational efficiency of `HOTPANTS` (Becker, 2015), and the statistically rigorous framework of Zackay et al. (2016b), have cemented its indispensability in surveys like ZTF, Rubin-LSST, and Roman.

During this PhD, I have developed and actively maintained a new, `python` based photometry pipeline, `subphot`, which handles various datasets and performs image subtraction of new science images relative to Pan-STARRS, SDSS or custom reference images using PSF photometry methods, similar to those described in Gal-Yam et al. (2008) and Fremling et al. (2016). The pipeline, originally created in Taggart (2020), has been updated and installed on local servers to automatically download, perform image subtraction and PSF photometry in addition to upload the results rapidly to Fritz (the primary ZTF Marshal; Duev et al., 2019; van der Walt et al., 2019; Duev & van der Walt, 2021; Coughlin et al., 2023) for the purposes of chasing fast transients in addition to general purpose photometry.

`subphot` was originally designed for the fully robotic LT (Steele et al., 2004). Since taking over its development, I have improved the pipeline, increasing the versatility to provide more utility for the general community. In this chapter, I review PSF photometry and present the fully automated `subphot` image subtraction pipeline, including the development and integration into ZTF as well as its extension to new instruments, namely the Palomar-60 inch Telescope.

5.2 Modern All-Sky Surveys

Modern all-sky surveys employ sophisticated transient discovery pipelines that integrate advanced PSF photometry methods (e.g., Bailey et al., 2007; Bramich, 2008; Bramich

et al., 2013; Zackay et al., 2016b; Liu et al., 2024; Thomas et al., 2025) and noise-optimised algorithms (e.g., Liu et al., 2024), with ML classifiers to distinguish astrophysical transients from instrumental artefacts or atmospheric phenomena (e.g., Bloom et al., 2012; Cabrera-Vives et al., 2017; Acero-Cuellar et al., 2023). These pipelines, deployed in surveys like ZTF, Pan-STARRS, and the upcoming Rubin-LSST, generate real-time data streams distributed via standardised alert systems. Each alert packet typically includes the new science image, a reference template, and a difference image produced through PSF-matched subtraction (Masci et al., 2019), enabling the identification of point-like sources against crowded stellar fields or variable backgrounds, utilising both real-time and historical contextual information.

In high-cadence surveys like ZTF, nightly alert volumes exceed 100,000 detections, a figure projected to grow 10 – 100 fold for Rubin-LSST. However, reliance on fixed detection thresholds (e.g., $\sim 3\sigma$ for ZTF) risks missing faint or marginally significant transients. Alerts are triggered only when sources surpass these thresholds, and positional uncertainties or low signal-to-noise ratios (SNR) can lead to incomplete light curves or fragmented transient histories.

Thus, to address these limitations, forced photometry (FP) has emerged as a critical tool. Unlike traditional methods that couple detection and measurement, FP performs photometric measurements at fixed coordinates – often derived from prior detections or external catalogues – regardless of whether a source is visibly detected in a given image. This technique decouples measurement from detection, enabling: earlier detection of transients (hours – days before meeting the pipeline thresholds, see Strotjohann et al., 2021) capturing the crucial early moments before peak; deeper light curves with measurements 1 – 2 mag fainter than typical limits, revealing both early- and late-time behaviour that normally surpass survey limits; and more stringent upper limits typically 2 – 3 mag deeper than catalog-based limits when no flux is detected.

FP achieves this by leveraging precise astrometric priors and PSF models to measure fluxes at SNR levels as low as 1 – 2 sigma, compared to the 3 – 5 sigma thresholds of standard pipelines. Major surveys now offer FP services, allowing users to extract light curves across entire survey archives. These services have proven indispensable for studies of low-luminosity transients, TDE's, and KNe, where marginal detections carry significant physical meaning.

5.3 Photometric Pipelines

While modern all-sky surveys operate sophisticated, dedicated photometric pipelines, smaller observatories and individual researchers face more limited options, with many relying predominantly on aperture or PSF photometry without image subtraction. This approach introduces subtle but scientifically significant limitations, particularly for transient sources. Although astronomically classified as "point sources", stars and transients are inevitably affected by atmospheric turbulence and optical imperfections that spread their flux beyond the idealised point-like distribution. Consequently, circular apertures that sum flux within a central region while subtracting background from an annulus frequently miss extended flux in the wings of the PSF – an effect that becomes progressively more pronounced under degraded seeing conditions or for transients embedded in crowded fields. PSF photometry partially mitigates this by modelling with enhanced deblending through multi-PSF fitting for overlapping sources – e.g., SNOoPY[1].

Even for high SNR or particularly bright sources, where photometry with and without image subtraction may exhibit seemingly marginal differences, these systematic effects can compromise precise light curve characterisation. To maximise scientific return despite these challenges, the transient astronomy community has developed a multi-tiered observational strategy, coupling wide-field survey facilities with more specialised follow-up instruments offering complementary capabilities in depth, wavelength coverage, and instrumental flexibility – while simultaneously developing more sophisticated photometric extraction methods to address the inherent limitations of traditional aperture photometry.

ZTF exemplifies this collaborative approach through strategic partnerships with 2 – 3-meter-class telescopes distributed globally. This network provides enhanced scientific flexibility through higher-cadence observations, deeper photometric limits, and expanded spectroscopic capabilities spanning UV – IR wavelengths. Synergies with complementary facilities prove particularly valuable during critical phases of transient evolution: the earliest epochs where rapid evolution occurs, and late-time observations when emission transitions to the nebular phase and approaches host galaxy brightness levels.

[1] SNOoPy is a package for SN photometry using PSF fitting and/or template subtraction developed by E. Cappellaro. A package description can be found at http://sngroup.oapd.inaf.it/ecsnoopy.html.

While most observatories provide basic data reduction services (bias subtraction, dark correction, and flat-fielding), the responsibility for extracting precise photometric measurements typically falls to individual researchers, as standardised analysis procedures remain fairly elusive across diverse sets of instruments. Historically, photometric analysis centred around `DAOPHOT` (Stetson, 1987) within the Image Reduction and Analysis Facility (`IRAF`; Tody, 1986; Tody, 1993). However, as `IRAF` support diminished and data volumes expanded, the community developed alternative systems with enhanced capabilities for modern observational challenges. Source Extractor (`SExtractor`; Bertin & Arnouts, 1996) emerged as a powerful alternative, particularly excelling at automated source detection and deblending in crowded fields, though it too has now reached end-of-support status. Its algorithmic approach nonetheless inspired numerous modern photometric systems (e.g., Zackay et al., 2016b; Mommert, 2017). Despite the proliferation of astronomical data and increasing standardisation of formats, truly comprehensive pipelines capable of handling heterogeneous datasets while maintaining consistent photometric precision remain surprisingly scarce. Notable exceptions include `HOTPANTS` (Becker, 2015) for image subtraction, `PhotometryPipeline` (Mommert, 2017), `A-Phot` (Merlin et al., 2019), and `AUTOPHOT` (Brennan & Fraser, 2022) for various photometric purposes, including transient follow-up campaigns – each addressing specific observational niches but none providing the universal solution increasingly required by time-domain astronomy.

Addressing the challenges of heterogeneous data processing outlined above requires not only versatile software solutions but also access to complementary observational facilities that can provide the rapid-response, multi-wavelength data needed for comprehensive transient characterisation. The LT represents a prime example of such a facility – a purpose-built robotic observatory specifically designed for time-domain astronomy that exemplifies the ideal follow-up instrument to complement survey telescopes. Its automated operations system and diverse instrument suite directly address the observational flexibility gap identified above, while its data products present precisely the type of heterogeneous datasets that modern photometric pipelines must accommodate. As a key component of the global follow-up network supporting ZTF and other surveys, the LT has become instrumental in extending the temporal and spectral coverage of newly discovered transients, particularly during their critical early evolutionary phases.

5.4 The Liverpool Telescope

The LT (Steele et al., 2004) is a fully robotic, 2-m telescope located at the Roque de Los Muchachos Observatory on La Palma, Canary Islands. LT's robotic nature makes it particularly well suited for time-critical observations and rapid follow-up of transient phenomena discovered by surveys such as ZTF. Current instrumentation on LT includes:

- An optical wide-field imager (IO:O)[2] providing deep imaging across the optical spectrum.
- A fast-readout wide-field optical camera (RISE; Steele et al., 2008).
- A low-resolution (R $\simeq$ 350, 18 Å) Spectrograph for the Rapid Acquisition of Transients (SPRAT; Piascik et al., 2014).
- A Multicolour OPTimised Optical Polarimeter for time-resolved polarimetric and colour observations (MOPTOP; Jermak et al., 2016).
- A near-infrared camera operating in the 1.1 –1.16 μm (Barr J – H-band) range (LIRIC; Batty et al., 2022)[3].
- A separate wide-field imager (SkyCam)[4] mounted on the side wall of the LT enclosure.

These instruments collectively provide comprehensive coverage across the optical and near-infrared spectrum, enabling rapid follow-up observations of various time-domain and transient phenomena. For this PhD, both SPRAT and IO:O have been extensively used for transient classification and characterisation.

IO:O uses Sloan-like *ugriz* filters (see Fig. 5.1 for comparisons of filter transmission between SDSS/Pan-STARRS and ZTF) for multi-colour observations. As ZTF is primarily a survey in ZTF g and r, the capability of the LT to produce wider colour coverage, particularly into the NUV and NIR, is extremely complementary to ZTF. Additionally, the LT being a 2 m telescope allows it to push the limiting depths of 22.5 – 23 mag, close to 2 mag deeper than the nominal depth of 20.5 for ZTF (which is usually limited

[2] https://telescope.livjm.ac.uk/TelInst/Inst/IO0/
[3] https://telescope.livjm.ac.uk/TelInst/Inst/LIRIC/
[4] https://telescope.livjm.ac.uk/TelInst/Inst/SkyCam/

to 30 s exposures). The combined colour coverage, flexible cadences and deeper limiting magnitudes are critical for constraining the temperature of transients and confirming that they've faded. This has been critical for the BTS, where the aim is to classify transients peaking < 18.5 mag to characterise behaviour around peak, filling in survey cadence and providing enhanced colour diagnostics ($u - z$) to aid in assess spectroscopic classifications – useful for blue, featureless transients like TDEs which remain blue and hot compared to SNe that cool and become red.

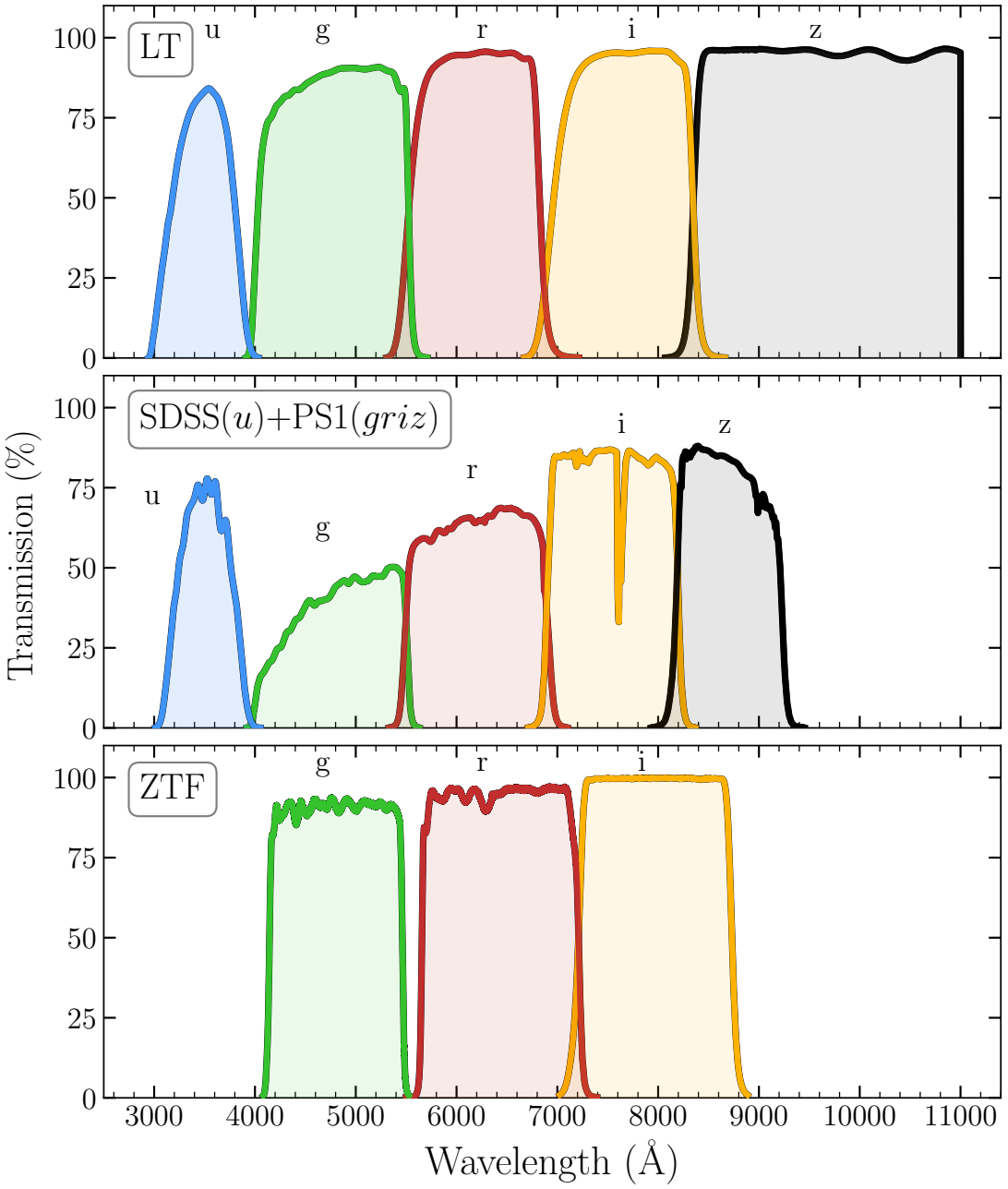

FIGURE 5.1: Transmission profiles for the LT filters on IO:O (*ugriz*) compared to the profiles from SDSS (*u*) and PS1 (*griz*) used as templates in addition to ZTF *gri*.

Exposure times typically range from 30 –120 s, although shorter exposures are possible for exceptional cases like SN 2023ixf and SN 2024ggi, the Type II SNe at $\sim$7 Mpc (Bostroem et al., 2023; Hosseinzadeh et al., 2023; Hiramatsu et al., 2023; Jencson et al., 2023; Jacobson-Galán et al., 2023; Li et al., 2024; Singh et al., 2024; Zimmerman et al., 2024; Chen et al., 2024, 2025; Xiang et al., 2024; Pessi et al., 2024; Jacobson-Galán et al., 2024b; Shrestha et al., 2024), that peaked around 11 mag, saturating ZTF. Single exposures reach r-band limiting magnitudes of $\sim$22 mag in dark time, while stacked images can achieve $\sim$23 mag, with noise reduced by $1/\sqrt{\mathrm{N}}$ for N exposures. Bright time observations typically reach $\sim$20 mag depth. u-band observations are approximately 1 mag shallower than r-band[5]. Note that for targets with complex host galaxies, subtraction residuals may dominate the noise floor, limiting the benefits of increased exposure time.

5.5 Image Subtracted Photometry

For a more in depth review of IO:O, the original description and performance analysis of the pipeline, see Taggart (2020). Briefly, the `subphot` pipeline implements a robust image differencing technique for transient photometry, following the methodologies established by Gal-Yam et al. (2008) and Fremling et al. (2016). This approach employs cross-convolution of PSFs to create difference images, as described by:

$$\mathrm{I_{Sub}}(x,y) = \mathrm{PSF_{Ref}}(x,y) \otimes \mathrm{I_{Sci}}(x,y) - \mathrm{PSF_{Sci}}(x,y) \otimes \mathrm{I_{Ref}}(x,y) \tag{5.1}$$

where $\mathrm{I_D}(x,y)$ is the Image and $\mathrm{PSF_D}(x,y)$ is the PSF [D = Subtracted, Science or Reference data]. Despite its advantages, this method introduces notable drawbacks. When the science and reference PSFs are nearly identical, this method unnecessarily degrades image quality and increases noise by convolving both images with kernel functions that effectively blur the data twice. However, cross-convolution has remained a standard method for decades because it elegantly handles the asymmetric problem of difference imaging while being computationally tractable. See later sections for a more in-depth discussion.

The pipeline architecture consists of five primary stages: (1) image preparation, which includes stacking multiple exposures, background modelling and subtraction, and cosmic

[5] u-band limiting magnitudes: $\sim$20 mag for single exposures, $\sim$21 mag for stacked images.

ray rejection; (2) reference image preparation and image alignment; (3) PSF modelling and cross-convolution; (4) photometric calibration against standard catalogs; and (5) difference image generation and transient photometry.

5.5.1 Initial Preparation and Stacking

The pipeline extracts metadata from FITS headers and processes sequences of multiple exposures using SWarp (Bertin, 2010). SWarp aligns the images using their World Coordinate System (WCS) information, resamples pixels, and combines them with a median algorithm to reject transient artefacts and improves the SNR by approximately $\sqrt{N}$ for N combined frames.

5.5.2 Background Subtraction

The pipeline removes the sky background from science images using sigma-clipped statistics and the `photutils` `SExtractorBackground` and `Background2D` estimators. These create a 2D background model with a filter size of 150×150 pixels, which is then subtracted from the original image.

5.5.3 Cosmic Ray Removal

Cosmic rays are identified and removed using the `astroscrappy.detect_cosmic` algorithm. The pipeline employs exposure time-dependent parameters, with longer exposures receiving more aggressive cosmic ray rejection. The process utilises instrument-specific parameters including gain, read noise, and saturation level, combined with 3 σ sigma-clipping and a median filtering method.

5.5.4 Reference Image and Alignment

For the image subtraction, the pipeline retrieves appropriate reference images based on filter selection. For *griz* filters, references are obtained from the Pan-STARRS DR1 survey using the `panstamps` API. For SDSS u filter observations, references are sourced from SDSS DR16 via direct server queries, with SWarp handling the mosaic combination using WCS information. In both cases, the pipeline requests a field of view

significantly larger than the science image (typically 1.5 × wider) to ensure sufficient overlap for robust alignment.

The alignment process employs a two-stage approach for optimal precision. First, a coarse alignment is performed using WCS header information. This is followed by a refined "relative nudge" correction. This approach accommodates small WCS inaccuracies, resulting in science and reference images precisely aligned.

The final alignment is performed using SWarp with an image centre defined at the image's geometric centre. For LT images, which typically have the target positioned within 100 pixels of the centre, this approach works well. The pipeline uses a standardised output size of 1500×1500 pixels to optimise overlap. When alignment fails due to minimal overlap, the science image is padded with NaN values or zeros to maintain consistent dimensions.

5.5.5 PSF Modelling and Cross-Convolution

PSF models are created for both science and reference images using PSFEx (Bertin, 2011). The process begins with SExtractor generating a catalogue of stars, which PSFEx uses to construct a model PSF. As shown in Eq. 5.1, the science PSF is convolved with the aligned reference image, the reference PSF is convolved with the aligned science and the PSFs are convolved together to create a combined PSF so subsequent photometry – convolutions handled with `scipy.signal.convolve`

5.5.6 Photometric Calibration

Whether the reference is from Pan-STARRS, SDSS or custom, the methodology is the same in that a reference catalogue is downloaded (or input) and cleaned based on quality flags to remove low-quality stars. Stars are then located in the science image using `photutils.IRAFStarFinder` and matched to reference catalogue stars with a default tolerance of 1 arcsecond, which is adaptively increased if insufficient matches (≤ 3) are found. For each matched star, FP is performed in the science and reference convolved images using the convolved PSF by fitting the PSF without positional shifts using `scipy.stats.linregress`. During the fitting process, a goodness of fit measurement is returned, informing on how well the PSF fit to the image (1 for perfect, 0 for failed).

This metric allows filtering based on how well the PSF fit and is set higher for *griz* as there typically are more stars in the images than for u, allowing for more stringent constraints on the goodness of fit.

At this stage, at least 3 stars are required to have a metric $>$ threshold. If ≥ 5 stars pass, sigma-clipping is performed to remove outliers. Once the final matched stars are found, the science and reference zeropoints, $Z_{\rm Sci}$ and $Z_{\rm Ref}$ respectively, and their associated 1 σ standard deviations are found.

5.5.7 Image Subtraction and Photometry

The final stage performs scaled subtraction and photometry on the difference image. The convolved reference image is scaled to the convolved science image using:

$$\text{scale} = 10^{(Z_{\rm Sci} - Z_{\rm Ref})/2.5} \tag{5.2}$$

The scaled reference image is subtracted from the science image. A cutout of the target region is created and the combined PSF is fit to the image, initially with free position parameters. If the best-fit position deviates from the catalogue coordinates by more than 0.5 arcseconds (the nominal astrometric precision of ZTF, which calculates coordinates from the median of all alerts and updates them with new detections), I deem the free-position solution as potentially spurious (likely fitting to dipoles as a result of inaccuracies in the subtraction). In these instances, I perform FP (no positional freedom) at the catalogue location.

For uncertainties in the photometry, artificial sources are placed on a grid spanning $\pm$ 50 pixels from the target position and PSF fitting is performed on each artificial source. The standard deviation of artificial source flux measurements (after sigma-clipping) determines the photometric uncertainty.

The pipeline calculates detection limits by placing artificial sources in background regions of the subtracted image and measuring their detection significance. Specifically, it determines the 3 σ and 5 σ limits by adding 3 or 5 times the standard deviation of

the background flux measurements to the median background flux, then converting to magnitudes using the zero point.

Fig. 5.1 are demonstrations of the pipeline, showing cutouts at various stages for several transients in some particularly challenging environments (e.g., bright hosts, low SNR or deep limiting magnitudes).

5.6 Performance

The `subphot` pipeline is deployed as a fully automated system on Liverpool John Moores University's (LJMU) high-performance computing cluster, Prospero, utilising scheduled cron jobs to manage workload distribution via the SLURM queue management system. This end-to-end infrastructure provides near-real-time processing capabilities, automatically retrieving new observations from the LT Quicklook service[6] at 5-minute intervals, performing image subtraction and photometric analysis, and disseminating results.

The pipeline interfaces directly with Fritz, uploading processed photometry immediately upon completion, while also compiling daily summary reports distributed to collaboration members each morning. This automated infrastructure supports time-critical science across multiple transient categories, including BTS sources, SLSNe, FBOTs, GRB afterglows, and GW electromagnetic counterparts.

As the primary developer and maintainer, I have continuously enhanced the pipeline's capabilities (detailed in the following section) while performing daily quality assurance of outputs. To ensure sustainability and reproducibility, the codebase is version-controlled through GitHub with documentation[7]. Ongoing development includes containerisation via Docker to facilitate deployment across different computing environments, aligning with modern scientific software distribution practices and enabling broader community adoption.

This containerisation approach is particularly valuable as several critical dependencies, including the Astromatic software suite (SExtractor, SWarp, and PSFEx), are no longer actively maintained and present significant installation challenges across different

[6]The Quicklook service delivers bias-, dark-subtracted and flat-fielded data approximately 5 minutes after observation completion: https://telescope.livjm.ac.uk/DataProd/quicklook/

[7]https://github.com/kryanhinds/subphot_pipe

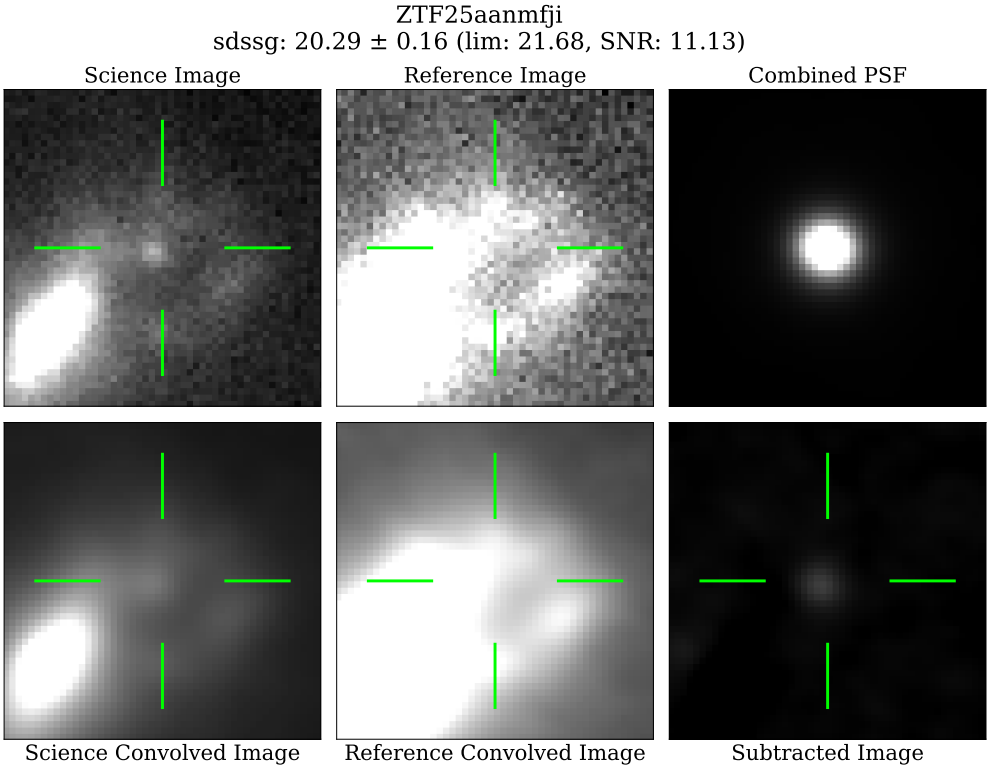

Figure 5.1.1: ZTF25aanmfji – Type Ib SN in a complex, diffuse host. g-band observation taken $\sim$ 10 d pre-peak. This SN suffers from significant host extinction ($g - r \sim 1.4$ mag at peak).

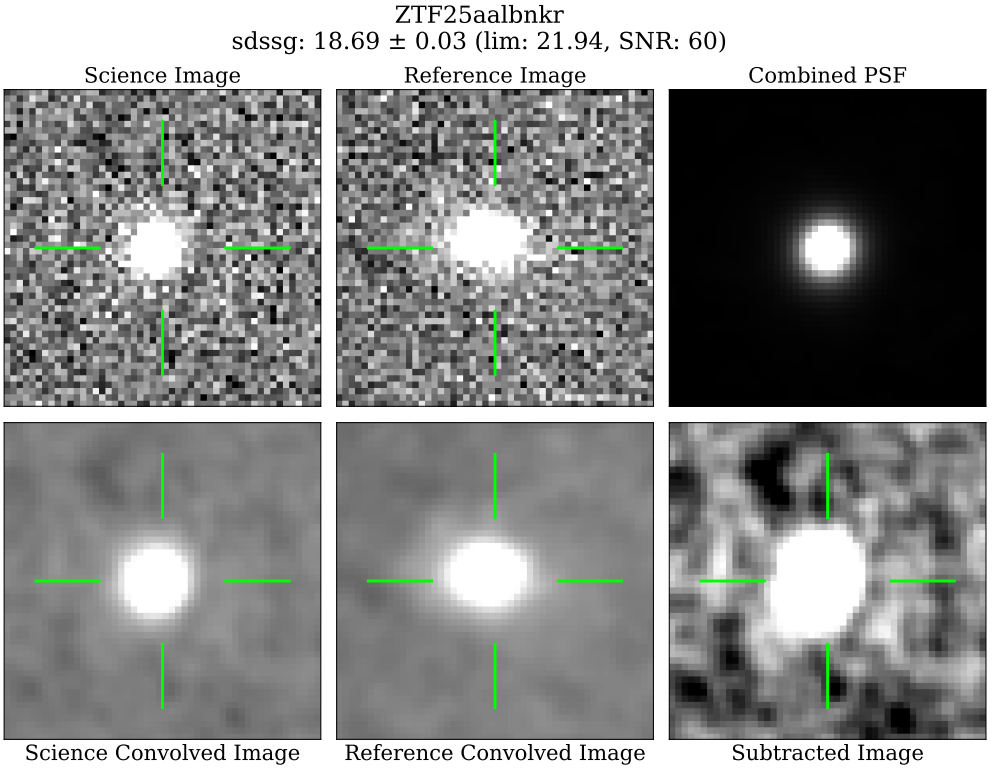

Figure 5.1.2: ZTF25aalbnkr – Type II SN centrally located within a bright host. g-band observation taken $\sim$ 20 d post-peak.

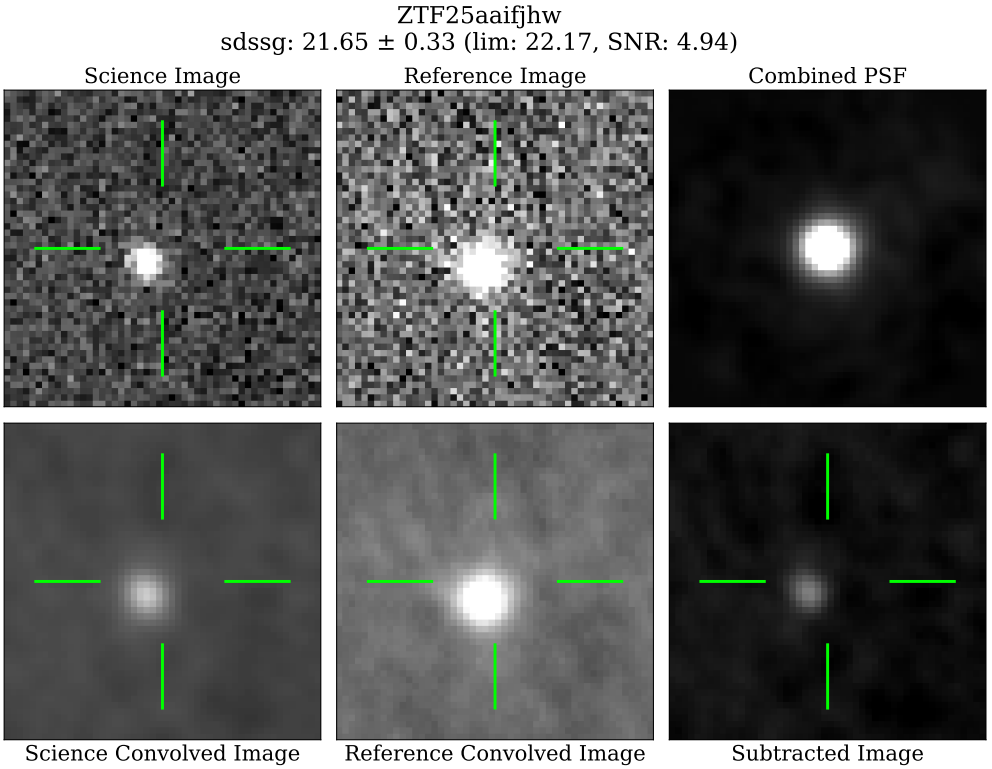

Figure 5.1.3: ZTF25aaifjhw – slow rising ambiguous nuclear transient centrally located with a bright host. g-band observation taken $\sim$ 60 d post peak.

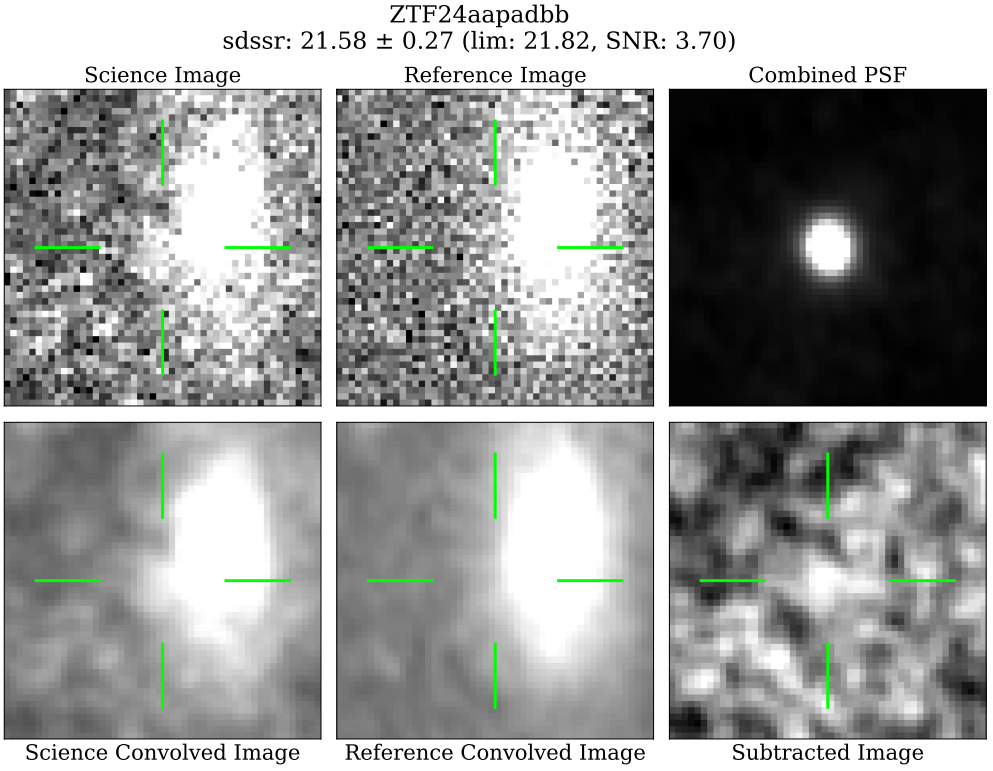

Figure 5.1.4: ZTF24aapadbb – nearby Type Ic SLSN in a diffuse host. r-band observation taken $\sim$ 300 d post peak.

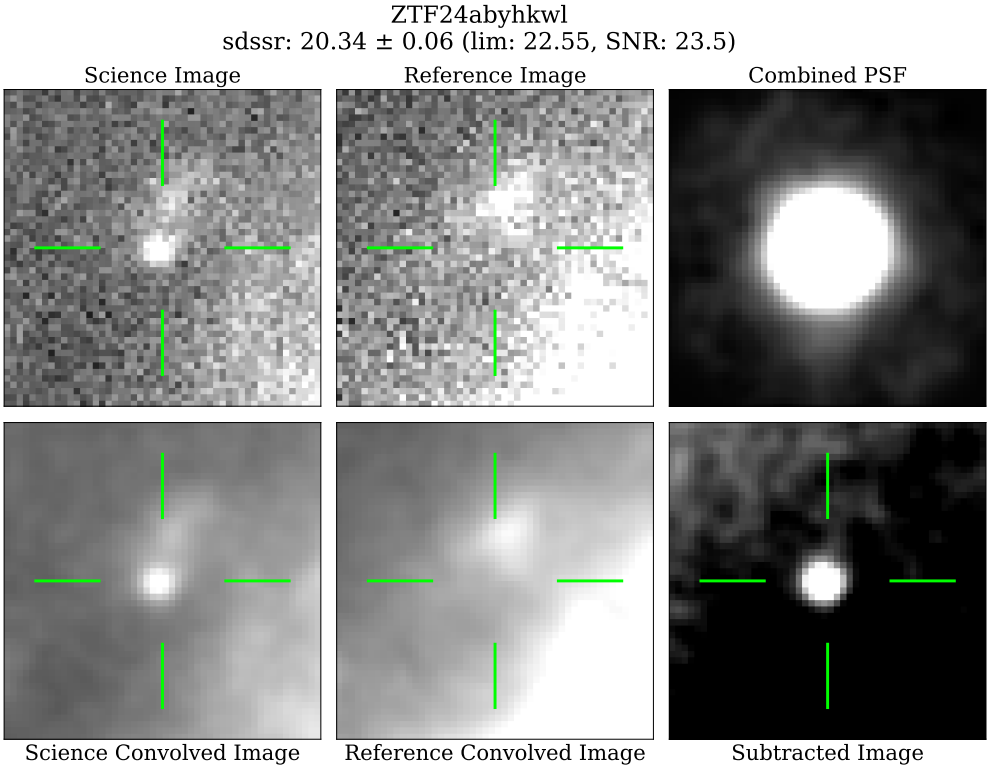

Figure 5.1.5: ZTF24abyhkwl – Type II SN between the spiral arms of a diffuse galaxy. *r*-band observation taken ∼ 160 d post-peak during the radioactive tail.

FIGURE 5.1: Demonstrations of `subphot`, showing (from *top left* to *bottom right* in each panel) the aligned science and reference images, the combined PSF, the science image convolved with the reference PSF, the reference image convolved with the science PSF and the subtracted image.

operating systems. Docker containerisation effectively addresses these dependency issues by encapsulating the precise software environment required for operation, ensuring consistent performance regardless of the host system configuration.

To date, the `subphot` pipeline has produced publication-quality photometry for numerous papers – see light curves that include LT photometry in Figs. 5.2. As mentioned, the nightly routine runs on the Quicklook images and uploads these results. For publications, I use the fully reduced images[8] that are available the following morning – typically identical to the Quicklook reductions, therefore tailoring prior to publication is usually unnecessary.

[8] Available in the mornings at: https://telescope.livjm.ac.uk/DataProd/RecentData/

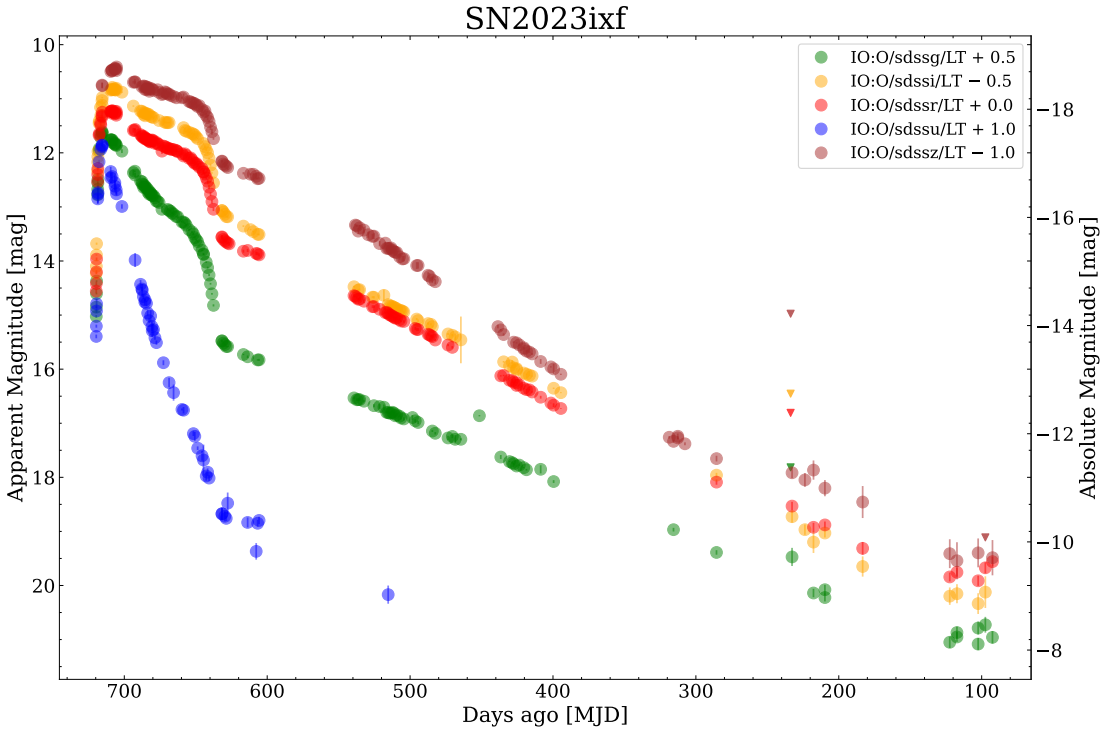

Figure 5.2.1: SN 2023ixf – Type II SN at ∼ 7 Mpc. One of the closest SN discovered to date, prompting extensive global follow-up campaigns. This dataset, analysed with `subphot`, was used for a nebular phase modelling in Michel et al. (2025).

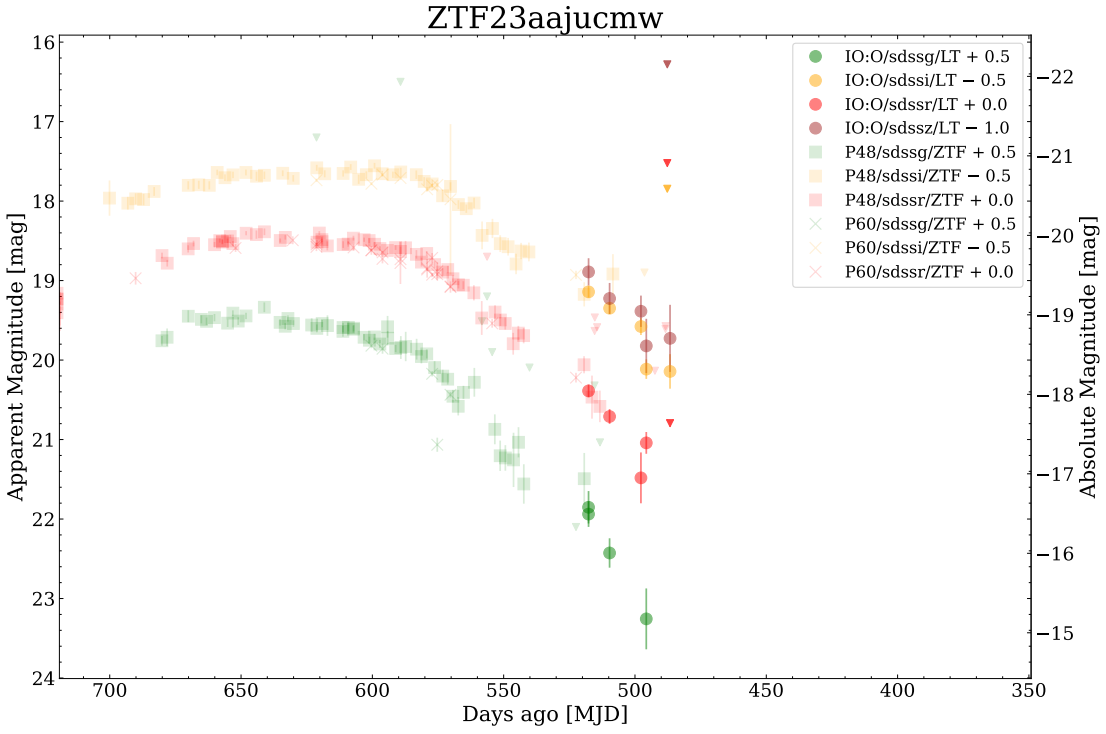

Figure 5.2.2: ZTF23aajucmw – luminous Type II SN with a peak magnitude ∼ −20.1 mag, a rise time ∼100 d, with a relatively slow and linear decline.

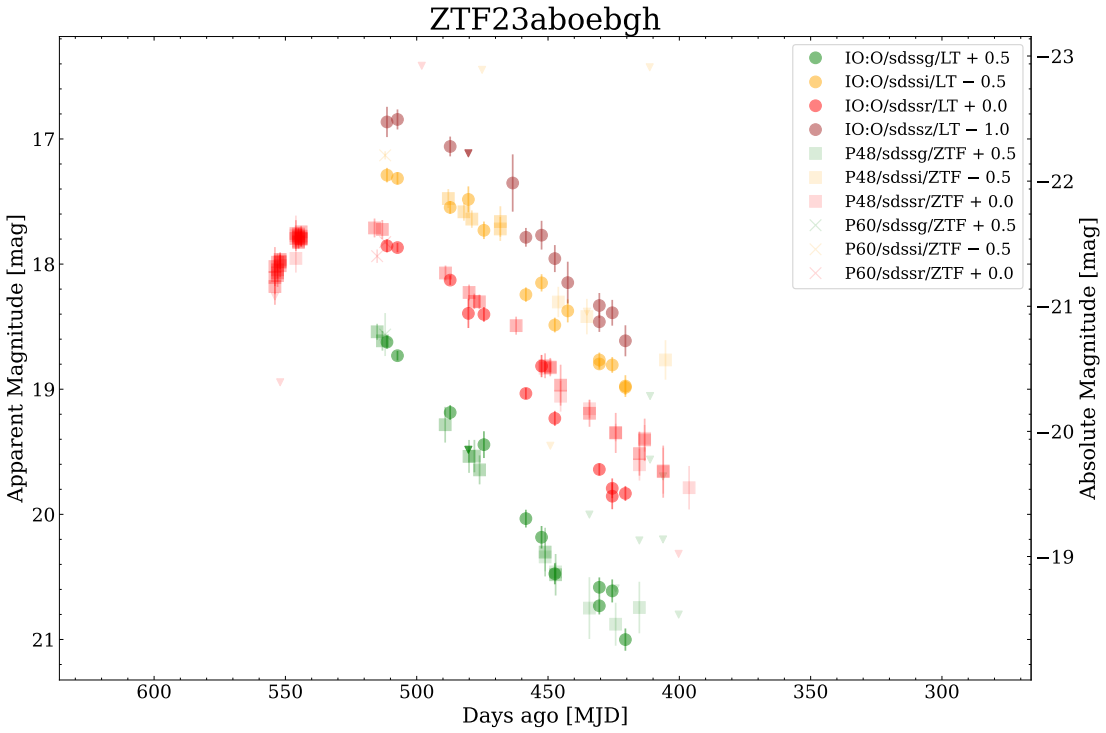

Figure 5.2.3: ZTF23aboebgh – Type Ic SLSN.

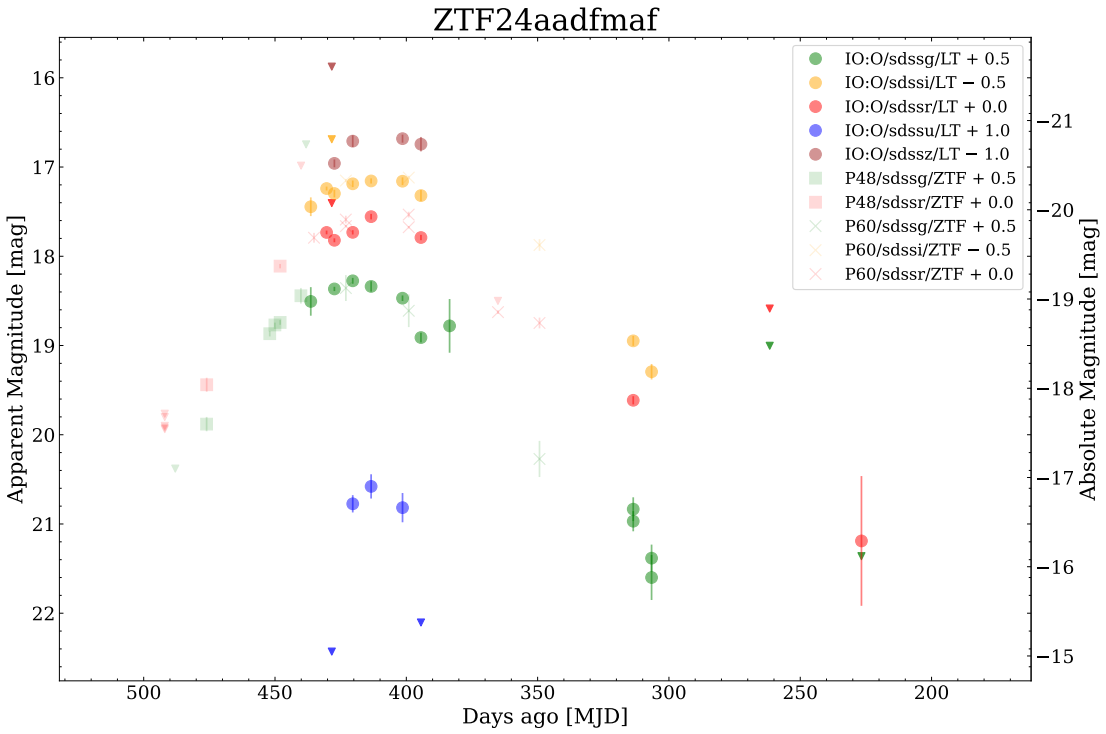

Figure 5.2.4: ZTF24aadfmaf – Type Ic SLSN.

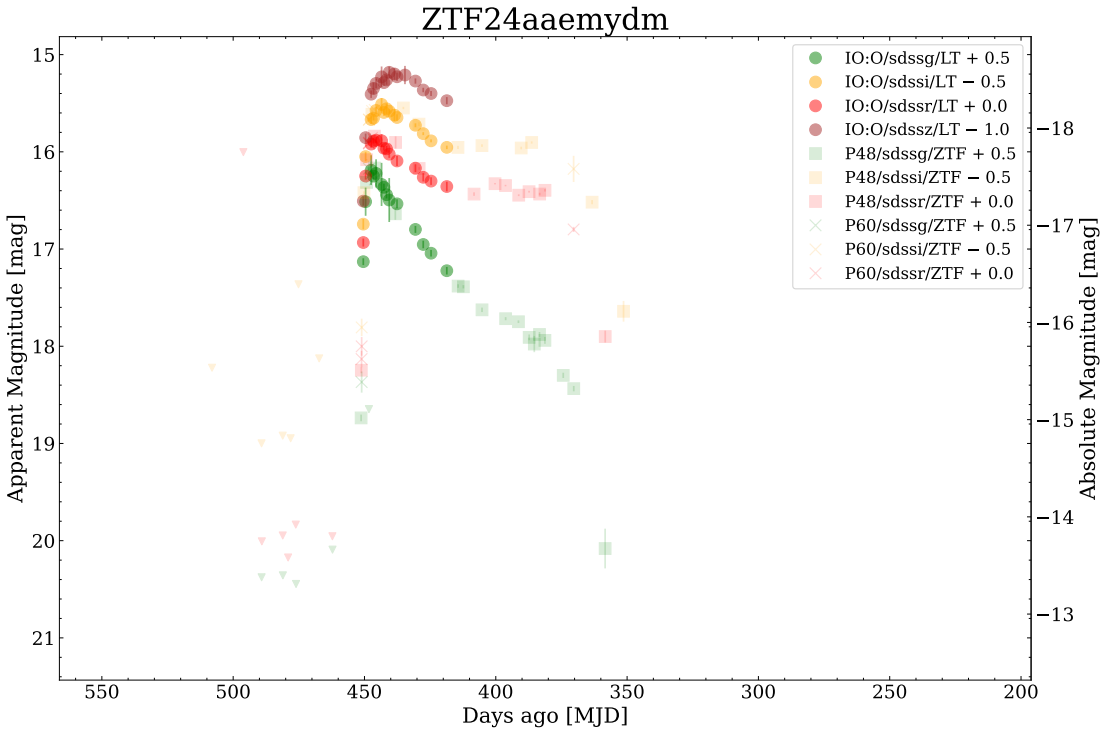

Figure 5.2.5: ZTF24aaemydm – Type II SN.

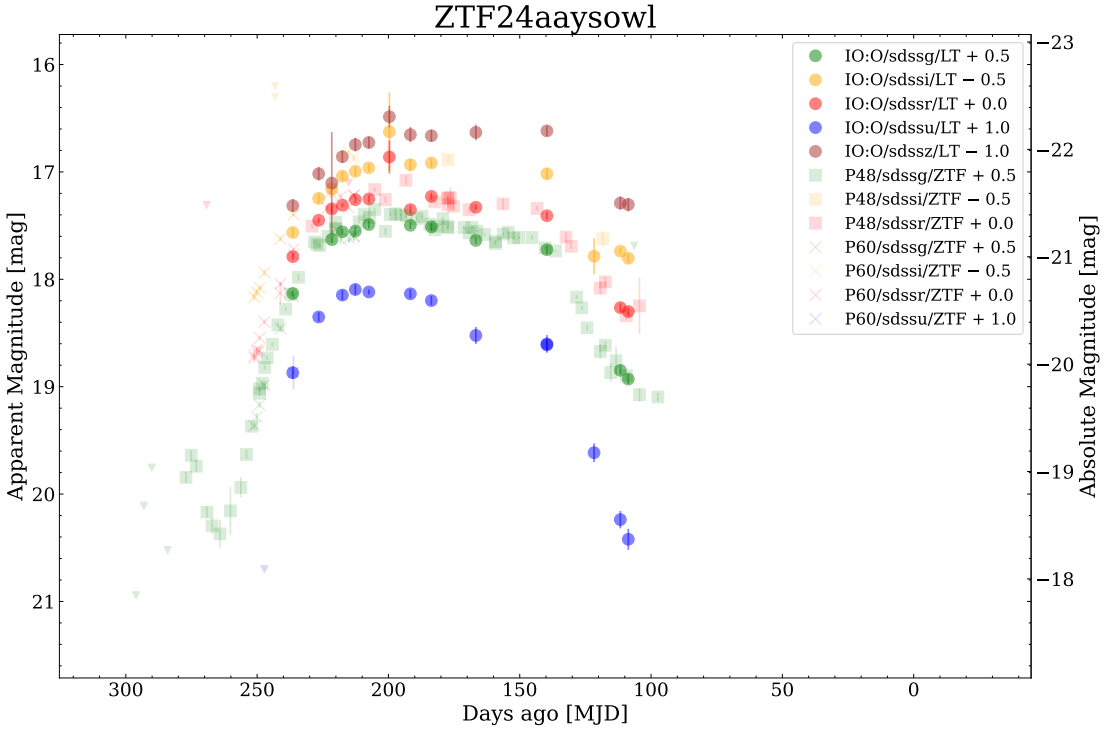

Figure 5.2.6: ZTF24aaysowl – Type Ic SLSN.

FIGURE 5.2: Mutli-band light curves of six ZTF transients with photometry from the LT processed using `subphot`. From *top* to *bottom*: (a) SN 2023ixf (Type II SN), (b) ZTF23aajucmw (Type II SN), (c) ZTF23aboebgh (SLSN Ic), (d) ZTF24aadfmaf (SLSN Ic), (e) ZTF24aaemydm (Type II SN), (f) ZTF24aaysowl SLSN Ic). LT observations are the solid colours, ZTF P48 and P60 observations are slightly transparent. Upper limits are inverted triangles.

`subphot` delivers robust, automated photometry for transient sources by adapting to diverse observing conditions, variable seeing, and instrument-specific calibration requirements across different filters. A key advantage of this approach is its minimal parameter tuning – requiring only specification of the PSF measurement aperture – which affords users considerable flexibility in star selection for PSF modelling. Unlike kernel-based methods (e.g., Alard, 2000; Bramich, 2008) that necessitate explicit kernel definitions and optimisation, `subphot`'s cross-convolution technique inherently handles seeing variations without manual intervention. This also allows a consistent platform to perform large sets of photometry at once, rather than on a case-by-case basis, ensuring reproducibility and robustness.

However, this approach carries certain trade-offs. The cross-convolution process deliberately degrades the better-seeing image to match the quality of the poorer one, resulting in a broader combined PSF and consequently some loss of spatial resolution. This degradation can reduce detection sensitivity for faint transients and increase photometric uncertainties. This resolution sacrifice, while reducing the SNR compared to optimal image subtraction methods (Zackay et al., 2016b), enables significantly greater versatility across heterogeneous datasets. Additionally, the pipeline's performance can degrade when handling images with substantially different PSF shapes (not just widths) or with strong optical distortions. When processing data from different instruments, careful attention must be paid to astrometric registration and photometric scaling, as systematic errors in either can introduce subtraction artefacts that may be misinterpreted as transient signals.

The simplicity of implementation and reliability across diverse observing conditions outweighed the noise penalty until more sophisticated methods like Zackay et al. (2016b) developed statistically optimal approaches that minimise noise amplification while maintaining the benefits of difference imaging. Such a drawback would be significant for ZTF and other all-sky surveys that use their own survey-built references in image subtraction, prompting the creation of more sophisticated methods (e.g., `ZOGY` and LSST-specific pipelines[9]).

Thus, despite these caveats, `subphot`'s balance of automation, reliability, and adaptability makes it particularly well-suited for time-domain astronomy campaigns that process

[9]See `https://github.com/lsst` and `https://github.com/LSSTDESC/dia_pipe`

large volumes of follow-up observations from diverse telescope facilities.

5.7 Pipeline Development and Enhancements

Since taking over development from Taggart (2020) at the start of my PhD in 2021, I have expanded the pipeline and continued its development. These enhancements fall into several key categories:

5.7.1 Architectural Improvements

- **Object-Oriented Redesign:** Restructured the codebase following object-oriented programming principles, improving maintainability and enabling more modular development.
- **Python Modernisation:** Migrated legacy code components by providing a completely `python`-based version.
- **Version Control:** Established GitHub repository with continuous integration, issue tracking, and documentation.
- **Multiprocessing:** Implemented parallel processing capabilities to allow quicker processing of large datasets

5.7.2 Image Handling and Processing

- **Image Sorting:** Developed algorithms for consistent and automatic sorting and filtering of incoming images.
- **Distortion Correction:** Added specialised correction routines for optical distortions in P60 data, improving cross-instrument compatibility.
- **Multi-Facility Support:** Extended the pipeline to handle data from diverse telescope facilities with instrument-specific calibration routines, currently including: P60 RCAM, Super Light Telescope (SLT) Astrodon, Gran Telescopio Canarias (GTC) Osiris and HiPERCAM, Nordic Optical Telescope (NOT) ALFOSC and European Southern Observatory-New Technology Telescope (ESO-NTT) EFOSC2.

5.7.3 Photometric Quality Enhancements

- **Dynamic Zeropoint Determination:** Improved photometric calibration with saturation detection and exclusion during zeropoint calculations.
- **Adaptive PSF Quality Metrics:** Implemented automatic threshold adjustment based on available calibration stars.
- **Outlier Rejection:** Added statistical identification and removal of outlier zeropoint measurements that disproportionately increase scatter.
- **Local Residual Analysis:** Developed quality checks for subtraction artefacts in the vicinity of transient locations.

5.7.4 Usability and Configurability

- **Command-Line Interface:** Implemented comprehensive argument parsing (with `argparse`) system allowing flexible operation from the command line with customisable parameters (e.g., running `subphot` on specific filters, downloading data from a specific night, multiprocessing).
- **Optional Astrometric Error:** Incorporated propagation of astrometric uncertainties into final photometric error budgets when requested.
- **General Logging:** Developed a sophisticated logging system that captures detailed information at each processing stage, facilitates debugging, and provides a comprehensive processing history for reproducibility and quality assessment.

These improvements have transformed `subphot` from a specialised tool into a versatile, production-grade pipeline capable of handling heterogeneous datasets from multiple facilities while maintaining consistent photometric precision. The redesigned architecture also facilitates ongoing development, with modular components that can be independently upgraded as new techniques and requirements emerge in time-domain astronomy.

5.8 Application to P60

Most recently, I have extended `subphot` to process data from the P60, the robotic facility that serves as a dedicated follow-up instrument for transients discovered by ZTF. The P60 has been operational since ZTF's commissioning in 2018, utilising a photometric pipeline initially developed by Fremling et al. (2016). My adaptation enables real-time processing of P60 data within the same framework used for LT observations, offering a more robust alternative – see Fig. 5.3 for an example.

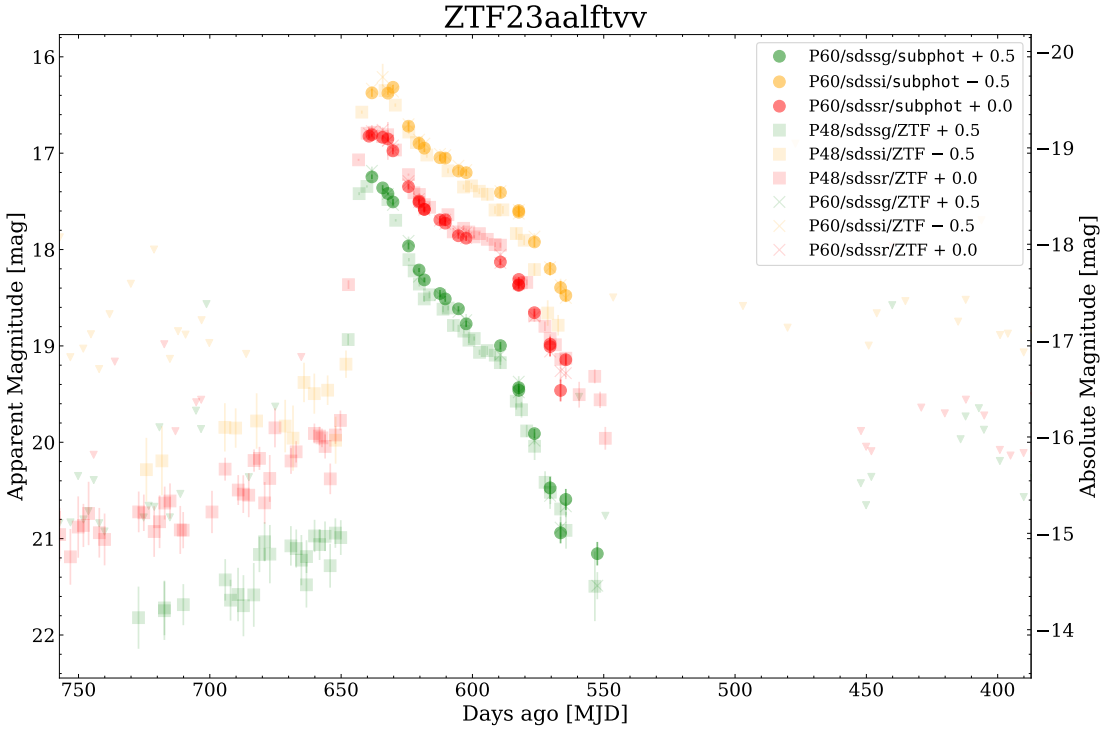

FIGURE 5.3: Mutli-band light curves of ZTF23aalftvv with photometry from P60 (*solid*), processed using `subphot`, and ZTF P48 (*faded*).

The P60's primary imaging instrument, Rainbow Camera (RCAM; Blagorodnova et al., 2018), employs a 2048×2048 pixel CCD array with SDSS *ugri* filters and a 13×13 arcmin field-of-view. However, RCAM presents unique challenges compared to conventional imaging instruments. Unlike most telescope configurations, RCAM occupies a secondary port, as the primary focal position is dedicated to the SEDM. This arrangement necessitates an unusual optical design wherein the incoming light is divided across four quadrants of the detector using a dichroic beam-splitter system, with each quadrant simultaneously imaging the field through a different filter. This configuration limits the field-of-view to a 6×6 arcmin field-of-view and creates a distinctive pattern where the

central region of the image contains the shadow of the filter holder. (Blagorodnova et al., 2018). Images are obtained in each filter by offsetting the centre of the telescope to a new quadrant – a raw SEDM image is shown in Fig. 5.4.

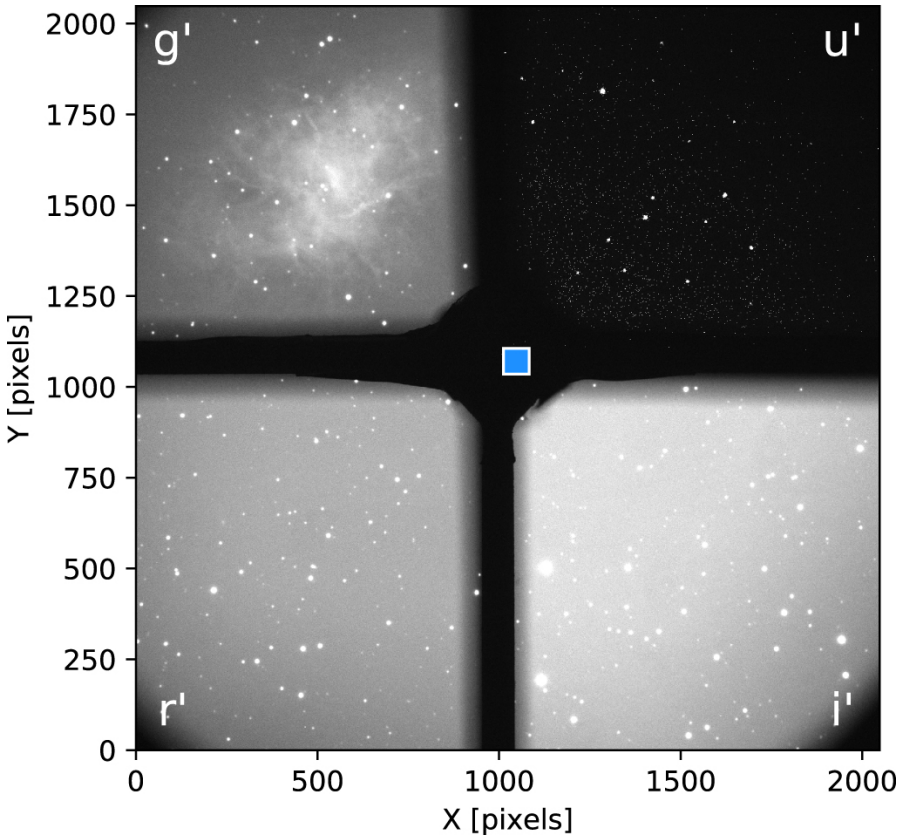

FIGURE 5.4: Raw sdss*g* RC image of the Crab Nebula (*upper left corner*). The various level of background for each filter is a function of sky colour and filter-detector throughput. The blue square indicates which part of the field is directed to the IFU by a pick off prism. Figure from Blagorodnova et al. (2018).

A significant challenge in processing P60/RCAM images is the complex optical distortion that varies as a function of telescope altitude. This distortion induces non-linear astrometric solutions that standard linear WCS transformations cannot adequately address. The severity of this effect increases toward the edges of each quadrant, causing systematic positional errors that propagate into photometric measurements and can lead to subtraction artefacts near transient locations.

SWARP can natively handle certain types of distortion corrections if properly specified in the FITS headers. For P60/SEDM images, I convert the WCS representation from the instrument's native Polynomial Distortion format to the TPV convention (Tangent Plane projection with distortion polynomial), then extract and transform the Simple Imaging Polynomial (SIP) coefficients present in the headers to equivalent TPV coefficients using

$CD_{ij} = PC_{ij} \times CDELT_i$ [i=1,2, j=1,2]. The conversion from SIP to TPV uses the new CD matrix and `sip_to_tpv` from `sip_tpv` to perform this transformation and correct distortions.

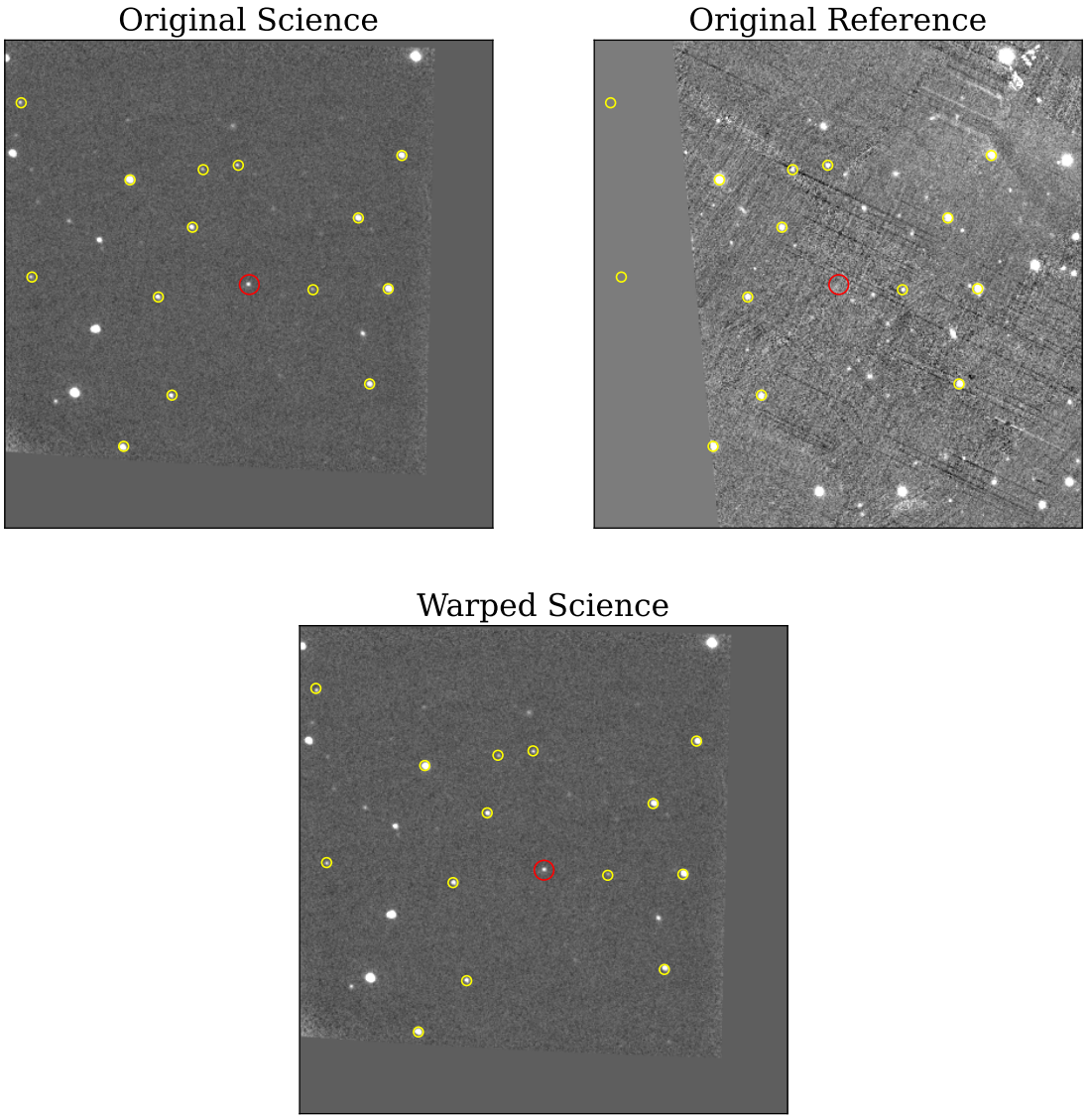

FIGURE 5.5: Collage of the distortion correction process for P60 RCam images relative to the reference image. *Top left* and *right* – the distorted aligned science and (assumed) not-distorted reference images in sdss*g* with 20 matching stars (yellow circles) identified in each – red circles indicate the transient's location. *Bottom*: the warped and aligned science image, which has been transformed based on the reverse mapping from the matched science stars to reference stars.

While SWARP's distortion correction is effective for global alignment, residual local distortions often remain, particularly in regions far from the optical axis. To address these, I implemented an additional transformation step based on matched star positions. Using `transform` from `sci-kit image`, I find the transform between the stars' pixel coordinates in the reference and science pixel and to the science image to remove additional

warping not captured in the SWarp's correction – see Fig. 5.5. The transformation is assumed to be a first-order polynomial and does not alter the image significantly. Further testing is required to find the optimal method to correct for the distortion in a consistent manner, given that the degree of field distortion is a function of the telescope position.

5.9 Photometry Summary

The future of astronomy is to become highly synergistic with the era of Rubin-LSST + ZTF-III commencing imminently. The advent of the Rubin-LSST promises a new era of discovery, with unprecedented depth and sky coverage. However, Rubin-LSST's cadence – prioritising wide-field coverage over high temporal sampling – creates a complementary dynamic with higher-cadence surveys like ZTF. While Rubin-LSST will excel in detecting faint transients at high redshifts and probing larger volumes, ZTF's rapid observational cadence remains critical for capturing fast-evolving phenomena (e.g., KNe, FBOTs) – representing critically undersampled regions of parameter space – and triggering timely follow-up.

In future work, I plan to implement automated triggering capabilities for high-priority events based on real-time alert stream classification. This system will leverage machine learning algorithms already in place (e.g., Rehemtulla et al., 2025) to identify scientifically valuable targets – including nearby SNe, KNe, GRB afterglows, and other rare transients – and autonomously initiate follow-up observations for the LT without the need for human intervention.

This synergy extends to multi-tiered observational networks: ZTF's discoveries are augmented by follow-up facilities (e.g., the LT and NOT), which provide high-cadence multi-wavelength data (e.g., Swift, EP, SVOM, the VLA[10], NOEMA[11] and ALMA[12], among others), while Rubin-LSST's deep, wide-field observations will anchor population studies and statistical analyses. For example, ZTF's rapid identification of SN 2023ixf enabled LT to trace its shock-cooling phase with sub-day cadence (Zimmerman et al., 2024).

[10] National Radio Astronomy Observatory Very Large Array.
[11] The Northern Extended Millimetre Array.
[12] Atacama Large Millimeter Array.

Chapter 6

Summary

6.1 Conclusions

In the course of this thesis, I have presented detailed analysis of 639 Type II SNe from the ZTF Bright Transient Survey. These objects, with high-cadenced forced photometry light curves, allowed for the construction of this dataset and analysis. I have modelled the light curves with GPR to return various empirical light curve parameters, with a focus on the rise times as they are sensitive to progenitor properties, namely $M_{\rm CSM}$ and $R_{\rm CSM}$. Building on this, I developed new empirical relations to infer these and other physical properties from the observed light curve features, enabling a quantitative connection between light curve morphology and progenitor characteristics across the sample. Using the various light curve parameters I measured, I created volume corrected ($V_{\rm max}$ method) distributions from the BTS sample, allowing determination of the following main conclusions for a highly complete sample of 377 Type II SNe (excluding Type IIn and IIb SNe, and after a magnitude cut at $\leq$ 18.5 mag for completeness):

- There is large diversity in Type II light curve demographics, but no clear separation in the luminosity-rise phase-space. The predicted bi-modality that appears when I measure the distributions of rise times, t_{25_75}, from the simulated light curves of Moriya et al. (2023) is not seen in our observed light curves.

- Based on the $1/V_{max}$ weighted sample of Type II SNe from this study, I find 36^{+5}_{-7}% of Type II SN progenitors have $M_{\rm CSM} \geq 10^{-2.5}$ M$_{\odot}$ at the time of core-collapse. I

find this is the minimum amount of $M_{\rm CSM}$ needed to impact the observables like the rise time and peak magnitude, based on Moriya et al. (2023) models.

- For an assumed progenitor wind velocity of 10 km s^{-1}, a maximum CSM radius of $R_{\rm CSM} \approx 5 \times 10^{14}$ cm and $M_{\rm CSM} = 10^{-2.5}$ M$_{\odot}$, I estimate mass-loss rates of $\dot{M} \sim 2 \times 10^{-4}$ M$_{\odot}$ yr^{-1} for events showing CSM-affected light curves. I constrain the period of this to occur within the last 3 – 32 years, consistent with recent findings from Bruch et al. (2021), Bruch et al. (2023) and Jacobson-Galán et al. (2024a), which suggest 'enhanced' mass-loss is a common feature of RSG evolution in the final decades before core-collapse.

This analysis contributes to the mounting evidence that CSM interaction plays a significant role in shaping the early light curves of Type II SNe, revealing that dense CSM is a common feature among their progenitors. While not ubiquitous, this analysis finds that 36^{+5}_{-7}% of Type II SNe (excluding Types IIn and IIb) exhibit clear signatures of CSM interaction, characterised by rapid rise times and enhanced early-time luminosity – attributed to efficient conversion of kinetic energy to thermal energy. These systems favour progenitors with confined CSM envelopes ($R_{\rm CSM} \leq 10^{15}$ cm), indicative of elevated mass-loss in the final years ($\leq$ 100 yrs) before explosion.

The observed fraction of Type II SNe with significant $M_{\rm CSM}$ likely reflects fundamental physical processes in late-stage stellar evolution rather than purely observational biases. This dichotomy – where approximately 1/3 of progenitors show evidence for undergoing extreme pre-explosion mass-loss while 2/3 maintain relatively modest circumstellar environments[1] – suggests multiple evolutionary pathways for RSGs approaching core-collapse.

A possible explanation is that the binary interactions might trigger enhanced mass-loss in a large set of progenitors. Given the high efficiency of CE interactions to remove material, the 36% of SNe with evidence of dense surrounding CSM could be reconciled with estimates of the fraction of massive stars in binary systems with orbital periods tight enough to induce significant interaction (e.g., Sana et al., 2012; Sana et al., 2013; Zapartas et al., 2019). Recent population synthesis studies suggest that $\geq$ 30 – 50% of massive stars experience binary mass transfer during their evolution (e.g., Zapartas

[1]To the extent that can be confidently detected with current surveys.

et al., 2019; Farrell et al., 2020; Zapartas et al., 2021), aligning well with the observed fraction. However, for such CSM to affect the SN observables, the mass transfer must occur during the very final stages of stellar evolution – shortly before core-collapse – such that the ejected material remains nearby, avoiding fallback into the CE and remaining confined within radii of $\lesssim 10^{15}$ cm. Late-stage evolution could trigger orbital instabilities through angular momentum transfer, potentially initiating episodes of enhanced mass-loss shortly before core-collapse.

Understanding whether this 36% fraction varies with metallicity, initial mass, or other parameters will be crucial for distinguishing between these possibilities in future studies. If this fraction remains constant across diverse stellar populations, it would suggest a universal physical mechanism inherent to late-stage stellar evolution rather than environmentally dependent processes.

The critical tension that emerges when comparing light curve-derived mass-loss rates ($\dot{M} \sim 10^{-4} - 10^{-1}$ M$_\odot$ yr^{-1}) to those observed in RSGs ($\dot{M} \sim 10^{-6} - 10^{-5}$ M$_\odot$ yr^{-1}). This $\approx$ 2 orders of magnitude discrepancy (Levesque et al., 2005; Beasor et al., 2020) challenges standard stellar evolutionary models, suggesting either enhanced pre-SN mass-loss or observational biases in local RSG studies. Resolving this requires: 1) deeper and earlier multi-colour pre-SN observations to capture short-term mass-loss variations and 2) hydrodynamical modelling of large SN samples linking CSM properties to photometric signatures.

For volume-corrected sample of 136 Type II SNe (excluding Type IIn and IIb SNe) used to calculate the $M_{\rm Ni}$, I find:

- The continuous distribution of $M_{\rm Ni}$ measurements suggests a log-normal distribution of $M_{\rm Ni}$. The weighted median ^{56}Ni mass from our sample is $M_{\rm Ni} = 3.08^{+1.66}_{-1.08} \times 10^{-2}$ M$_\odot$ or $3.82^{+2.04}_{-1.33} \times 10^{-2}$ M$_\odot$ (across two methodologies), aligning with literature values of 2 – 30 $\times 10^{-2}$ M$_\odot$ and supporting a continuum of explosion mechanisms rather than distinct categories.
- The bolometric luminosity at 50 d strongly correlates with $M_{\rm Ni}$, with correlation strength increasing when measured at the plateau midpoint. This robust relationship confirms that higher ^{56}Ni yields produce more luminous plateaus, reflecting

the growing contribution of radioactive decay energy to the photospheric emission during this transitional phase.

Looking forward, Rubin-LSST will revolutionise transient astronomy with its unprecedented combination of depth, colour coverage and area ($M_{\rm lim} \sim 24-25$ mag and coverage in *ugrizy*). Specialised facilities like the Gravitational-wave Optical Transient Observer (GOTO; Dyer et al., 2018; Steeghs et al., 2022), WINTER and BlackGEM will target specific science cases from GW counterparts to IR transients. Space missions including ULTRASAT (Shvartzvald et al., 2024), the Nancy Grace Roman Space Telescope (Troxel et al., 2021; Wang et al., 2023) and the UltraViolet EXplorer (UVEX; Kulkarni et al., 2021) will extend these capabilities drastically into ultraviolet and infrared wavelengths.

The imminent commencement of the Rubin-LSST marks the beginning of an unprecedented era in time-domain astronomy. The synergy between LSST's deep, wide-field observations and complementary surveys – ZTF-III, LS4, ATLAS, and BlackGEM – will create a unique multi-facility ecosystem that largely overcomes traditional cadence and depth limitations. This coordinated network will be further enhanced by expanded wavelength coverage from space-based facilities like ULTRASAT and UVEX in the UV and Roman in the NIR, collectively spanning the electromagnetic spectrum from NUV through optical to NIR with high temporal resolution.

This observational framework will greatly transform our understanding of transient phenomena across multiple dimensions: SC emission captured within hours of explosion will probe progenitor envelope structures; multi-year pre-explosion monitoring will definitively constrain mass-loss episodes occurring $\lesssim 10$ years before core-collapse; and homogeneous samples exceeding 10^5 SNe will provide statistical power sufficient to identify rare subclasses, map volumetric rates as a function of host properties, and accurately measure the stellar death rate across cosmic time. Perhaps most significantly, the systematic nature of these observations will eliminate many of the historical selection biases that have complicated demographic analyses, enabling robust population studies across the largest accessible volume to date.

6.2 Future Work

A central tension the analysis in this thesis has not addressed is the RSG problem. The apparent dearth of high-mass Type II SN progenitors remains a highly contested subject (e.g., Strotjohann et al., 2024b; Beasor et al., 2025; Fang et al., 2025a). Whilst novel methods (e.g., nebular phase spectroscopy in Fang et al., 2025a) have seen success in calculating upper limits on M_{ZAMS}, there is yet to be a large, definitive study to confirm whether the dearth exists. Moreover, if the dearth does exist, is this a purely observational bias? If not, what physical mechanism is causing this?

Among the most compelling physical explanations for the observed dearth of high-mass RSG progenitors is the possibility of failed SNe – massive stars that collapse directly to BH without producing the outward-propagating shock necessary to unbind the stellar envelope (e.g., Kochanek et al., 2008; Kochanek, 2011; Adams et al., 2017b). This phenomenon would render such terminal stellar events essentially invisible in traditional transient surveys, creating a systematic observational bias against detecting the deaths of the most massive progenitors. This scenario reinforces the paradigm of "islands of explodability", wherein cores with specific physical characteristics are more likely to produce successful explosions and observable SNe, while others preferentially implode and form BH without luminous counterparts (e.g., Maltsev et al., 2025).

Recent simulation studies have provided compelling theoretical support for these non-monotonic explosion landscapes, identifying specific mass ranges that fail to consistently produce successful explosions despite seemingly modest differences in progenitor properties (e.g., O'Connor & Ott, 2011; Pejcha & Thompson, 2015; Sukhbold et al., 2016; Byrne & Fraser, 2022; Heger et al., 2023; Laplace et al., 2025). Direct observational programs searching for failed SNe through the disappearance of RSGs have recently yielded promising candidates (e.g., Beasor et al., 2024; Kochanek et al., 2024), potentially validating this theoretical framework (see also Kochanek et al., 2008; Adams et al., 2017b). If the RSG problem indeed reflects a genuine physical mechanism rather than an observational artefact, it represents a fundamental gap in our understanding of core-collapse physics – one that bridges stellar evolution, explosion mechanisms, and compact object formation through a single observational constraint.

Thus, resolving the RSG problem remains a critical objective in stellar evolution theory. While this thesis made significant strides by empirically inferring $M_{\rm CSM}$ from the early-time light curve, this approach was limited. Notably, I did not estimate $M_{\rm ZAMS}$, and I did not model the full range of explosion and progenitor parameters.

Improvements to this study would come in the form of utilising recent theoretical advances to enable a more holistic and systematic investigation. In particular, an emulator framework based on the expansive $>300{,}000$ model grid of radiative-hydrodynamic SN simulations by Moriya et al. (2023) offers a transformative opportunity. These models incorporate detailed physics, including atomic opacities and shock-CSM interaction, and span a wide range of input parameters – $M_{\rm ZAMS}$, $R_\star$, envelope mass ($H_{\rm env}$), $M_{\rm Ni}$, $E_{\rm exp}$, and $\dot{M}$. Unlike the empirical estimates employed here, an emulator will allow robust inference of *measured* progenitor properties – rather than approximate or inferred quantities – by enabling comparisons across the full multi-dimensional parameter space.

Developing a machine learning surrogate model – using GP techniques similar to those demonstrated in this thesis – and applying it to large, complete samples represents a powerful next step. Such a surrogate would encode the complex, non-linear mapping between physical parameters (e.g., $M_{\rm ZAMS}$, $R_\star$, $H_{\rm env}$, $E_{\rm exp}$, $M_{\rm Ni}$, CSM properties) and observable SN signatures (e.g., peak luminosity, spectral signatures). Unlike the original discrete model grid, the emulator would allow continuous exploration of parameter space, enabling rapid predictions for arbitrary combinations via interpolation, while preserving the underlying physics. This approach, similar to that implemented for Type Ia SNe by Kerzendorf et al. (2021), would dramatically reduce computation time without compromising physical fidelity.

When coupled with Bayesian inference, this emulator framework would enable rapid, systematic fitting of observed SNe, yielding joint constraints on both progenitor and CSM properties. Crucially, it addresses the core limitations of this study – namely, the absence of direct $M_{\rm ZAMS}$ estimates and limited coverage of the explosion parameter space. By unifying sophisticated theoretical models with large-scale observational datasets, this method offers a self-consistent, physically grounded pathway to resolving the RSG problem.

The forthcoming data from Rubin-LSST, ZTF-III, and other next-generation surveys necessitates computationally efficient methods for extracting physical parameters from

large samples. Applied to these datasets, the surrogate model would facilitate the determination of progenitor properties for thousands of Type II SNe. This approach would produce a statistically robust, bias-corrected distribution of progenitor properties. The first application would be to create a representative distribution of $M_{\rm ZAMS}$ from a magnitude-limited survey, enabling a quantitative assessment of the apparent high-mass progenitor deficiency. Additionally, the model's capacity to predict early light curve evolution would provide insight into pre-explosion mass-loss mechanisms, as Rubin-LSST and ULTRASAT observations investigate the earliest post-explosion phases where CSM most significantly affects photometric behaviour.

In summary, the confluence of next-generation observational facilities, advanced computational techniques, and sophisticated theoretical models presents an unprecedented opportunity to resolve longstanding questions in SN science. By combining ML approaches with physically-motivated models, efficient extraction of physical progenitor properties from the vast datasets soon to be available will be possible, potentially closing the gap between theory and observation regarding the $M_{\rm ZAMS}$ distribution of CCSN progenitors. The resolution of the RSG problem would not only address a persistent discrepancy in stellar evolution theory but also provide crucial insight into the fundamental physics governing the final moments of massive stars – ultimately advancing our understanding of stellar endpoints across cosmic time.

Appendix A

A.1 CSM Flash Ionisation

This appendix supplements Chapter 1, Section §1.5, by showing the detailed filter transmission functions of the China Space Station Telescope (CSST) overlaid with model SN spectra at different evolutionary phases, illustrating the observational signatures of CSM flash ionisation events.

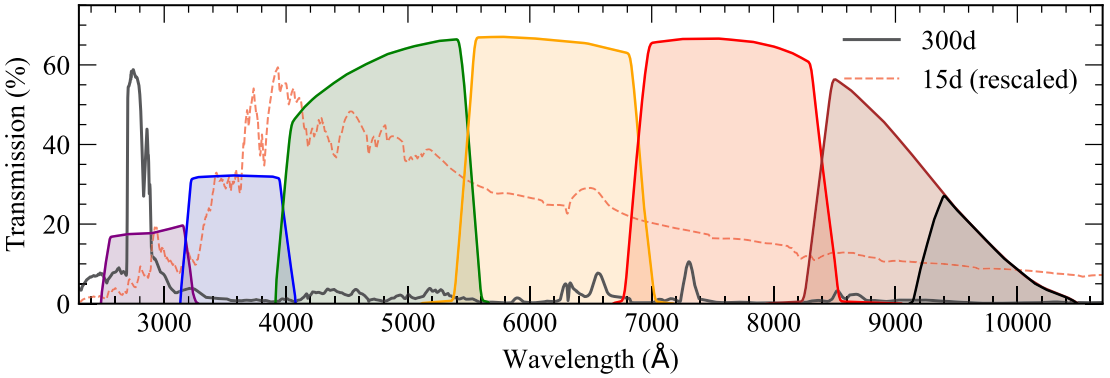

FIGURE A.1: Normalised spectra of model Pwr1e41 from Dessart & Hillier (2022) plotted over the filter transmission function of the China Space Station Telescope (CSST) sky survey. The purple line and shaded region under it denote the transmission function of the NUV band. The red dashed line is the SN spectrum 15 d after the explosion (rescaled by a factor of 0.3), when most of the power is released in the optical range. The solid black line is the model spectrum at 300 d after explosion, when reprocessed shock power dominates the UV luminosity in the form of Lyα (falling in the FUV and thus not shown) and the Mg II $\lambda\lambda$ 2795, 2802 doublet in NUV band. The other shaded regions are transmission functions of $u/g/r/i/z/Y$ bands. Figure from Luo et al. (2024).

Appendix B

B.1 Heavily Host-Extinguished

Table B.1 contains significantly dust-extinguished Type II SNe we identify in our sample. These events are characterised by distinctly red colours, $(g - r)_{g,\max} \geq 0.25$ mag, at peak and moderate rise times, $t_{25\_75} \leq 20$ d, placing them in a unique region of parameter space as illustrated in Fig. 3.2. We correct for host extinction using $(g - r)_{g,\max}$ and apply this correction to these SNe only, as described in Chapter 3, Section §3.3.4.

ZTF	TNS ID	Type	z	$M_{g,\mathrm{peak}}$ [mag]	t_{25_75} [d]	$(g-r)_{g,\mathrm{max}}$ [mag]	A_g^{host} [mag]
ZTF18abdbysy	2018cyg	II	0.01127	-14.40 ± 0.02	1.70 ± 0.18	0.71 ± 0.03	2.38
ZTF18abvvmdf	2018gts	II	0.029597	-16.70 ± 0.02	2.00 ± 0.14	0.59 ± 0.03	1.97
ZTF19aamkmxv	2019bxq	IIn	0.014	-16.66 ± 0.02	3.41 ± 0.16	0.77 ± 0.02	2.61
ZTF19aamvape	2019cjx	II	0.03	-17.69 ± 0.02	8.43 ± 0.39	0.30 ± 0.02	1.01
ZTF19aayrosj	2019hrb	II	0.015064	-15.86 ± 0.02	1.83 ± 0.14	0.27 ± 0.03	0.90
ZTF19abgfuhh	2019lgc	IIb	0.0354	-17.35 ± 0.02	3.99 ± 0.19	0.37 ± 0.03	1.26
ZTF19abxtcio	2019pof	IIb	0.0155	-15.79 ± 0.02	14.30 ± 0.68	0.46 ± 0.03	1.57
ZTF20aaetrle	2020sy	II	0.02	-16.99 ± 0.02	6.97 ± 0.68	0.47 ± 0.04	1.60
ZTF20aaurfwa	2020hem	IIn	0.0935	-20.37 ± 0.01	16.86 ± 0.51	0.32 ± 0.01	1.09
ZTF20abfcrzj	2020mob	IIb	0.023244	-16.86 ± 0.06	10.01 ± 0.68	0.26 ± 0.08	0.87
ZTF20abpmqnr	2020qmj	IIn	0.022	-18.53 ± 0.01	7.47 ± 0.18	0.42 ± 0.01	1.41
ZTF20abwzqzo	2020sbw	IIb	0.023033	-16.64 ± 0.07	7.97 ± 2.60	0.38 ± 0.10	1.27
ZTF20aclkhnm	2020xql	II	0.036	-17.07 ± 0.04	12.93 ± 1.61	0.56 ± 0.06	1.90
ZTF20acnzkxb	2020ykd	II	0.02690421	-16.95 ± 0.01	5.65 ± 0.28	0.40 ± 0.02	1.33
ZTF20acpgokr	2020yzi	II	0.027	-16.72 ± 0.02	2.08 ± 0.15	0.34 ± 0.03	1.15
ZTF20acrzwvx	2020aatb	II	0.009954	-16.41 ± 0.01	7.70 ± 0.52	0.45 ± 0.02	1.51
ZTF20actqnhg	2020aaxf	IIb	0.014813	-16.55 ± 0.02	5.01 ± 0.35	0.38 ± 0.03	1.27
ZTF20acvevsn	2020abqw	II	0.01417	-14.96 ± 0.02	1.73 ± 0.22	0.42 ± 0.04	1.42

Continued on next page

Table B.1 – *Continued from previous page*

ZTF	TNS ID	Type	z	$M_{g,\mathrm{peak}}$ [mag]	t_{25_75} [d]	$(g-r)_{g,\mathrm{max}}$ [mag]	A_g^{host} [mag]
ZTF21aajgdeu	2021cjd	II	0.027929	-16.71 ± 0.04	1.76 ± 0.19	0.36 ± 0.05	1.22
ZTF21aakupth	2021cvd	IIn	0.023483	-16.11 ± 0.02	4.33 ± 0.32	0.52 ± 0.03	1.76
ZTF21aamwqim	2021dru	II	0.025878	-16.51 ± 0.05	4.17 ± 0.70	0.46 ± 0.07	1.57
ZTF21aavuqzr	2021kat	IIn	0.1013	-20.24 ± 0.01	16.78 ± 0.50	0.35 ± 0.01	1.19
ZTF21aaydxoo	2021kwc	IIn	0.021759	-17.53 ± 0.01	4.85 ± 0.15	0.59 ± 0.01	1.99
ZTF21aayfnjz	2021kww	II	0.023	-17.52 ± 0.01	6.31 ± 0.13	0.31 ± 0.02	1.04
ZTF21abfoyac	2021pni	II	0.033	-18.27 ± 0.01	7.40 ± 0.25	0.38 ± 0.01	1.27
ZTF21abujgmr	2021wrr	IIn	0.048	-17.95 ± 0.01	6.86 ± 0.37	0.44 ± 0.01	1.47
ZTF21abviabc	2021wyn	II	0.053467	-18.20 ± 0.02	3.32 ± 0.39	0.75 ± 0.02	2.54
ZTF21abyqrli	2021ybc	IIb	0.02925	-17.29 ± 0.09	6.15 ± 1.26	0.29 ± 0.04	0.99
ZTF22aagvxjc	2022iep	IIn	0.025	-17.00 ± 0.01	16.40 ± 0.60	0.28 ± 0.01	0.95
ZTF22aalorla	2022lix	II	0.06804	-18.66 ± 0.01	5.52 ± 0.13	0.46 ± 0.01	1.54
ZTF22aamjqvc	2018elp	IIb	0.030089	-17.57 ± 0.01	5.56 ± 0.20	0.29 ± 0.02	0.99
ZTF22aaotgrc	2022ngb	IIb	0.00965	-16.18 ± 0.02	6.96 ± 0.13	0.66 ± 0.03	2.23
ZTF22aapqaqe	2022npv	II	0.025177	-17.32 ± 0.01	3.21 ± 0.12	0.46 ± 0.02	1.54
ZTF22aawptbl	2022pzh	II	0.045	-18.20 ± 0.02	5.79 ± 0.48	0.44 ± 0.02	1.49
ZTF22ablvnwa	2022xae	IIb	0.045229	-18.09 ± 0.04	4.64 ± 0.57	0.26 ± 0.05	0.87

Continued on next page

Table B.1 – *Continued from previous page*

ZTF	TNS ID	Type	z	$M_{g,\mathrm{peak}}$ [mag]	t_{25_75} [d]	$(g-r)_{g,\mathrm{max}}$ [mag]	A_g^{host} [mag]
ZTF22abnejmu	2022ycs	II	0.01	-15.50 ± 0.02	9.14 ± 1.46	0.48 ± 0.02	1.61
ZTF22abssiet	2022zmb	II	0.01449	-15.41 ± 0.02	1.73 ± 0.11	0.25 ± 0.03	0.85
ZTF23aaawbsc	2023aew	IIb	0.025	-18.55 ± 0.03	7.41 ± 0.22	0.30 ± 0.03	1.01
ZTF23aaesmsf	2023fsc	IIb	0.02	-17.81 ± 0.01	11.13 ± 0.41	0.34 ± 0.02	1.13
ZTF23aazqmwp	2023qec	II	0.02079	-17.50 ± 0.01	6.88 ± 0.21	0.26 ± 0.02	0.88
ZTF23abjrolf	2023uvh	II	0.02676	-16.69 ± 0.07	4.81 ± 1.15	0.46 ± 0.10	1.54

TABLE B.1: Properties of heavily dust-extinguished Type II SNe, identified by their red colours, $(g-r)_{g,\mathrm{max}} \geq 0.25$ mag, and moderate rise times, $t_{25\_75} \leq 20$ d, as shown in Fig. 3.2. Table contains: ZTF object name; TNS name; spectroscopic classification; redshift; $M_{g,\mathrm{peak}}$ in ZTF g at rest-frame and uncertainty; t_{25_75} rise time [d] in ZTF g at rest-frame wavelength and uncertainty; $g-r$ colour at ZTF g peak time and uncertainty; host galaxy extinction in ZTF g band, method described in Section §3.3.4.

B.2 Rise Time Recovery

To assess the impact of the sampling function on our GPR measurements, we conducted a systematic resampling experiment using well-sampled light curves with well-constrained t_{25_75} values. This involved taking thoroughly observed events (e.g., ZTF18aacnlxz/SN 2020aavr) and resampling their light curves (simulating alternative sampling functions) to match the observation cadence of more sparsely observed light curves in our sample. Figure B.1 illustrates the resulting distribution of measured rise times across different intrinsic t_{25_75} values.

Our analysis demonstrates that the GPR process reliably distinguishes between fast-rising ($t_{25\_75} \leq 5$ d) and slower-rising ($t_{25\_75} > 5$ d) events. For the fastest risers (t_{25_75} between 1–2 d), we observe substantial uncertainty with a spread of ≈ 0.7 dex. This improves to ≈ 0.4 dex for moderate risers (t_{25_75} between 3 – 5 d) and further to ≈ 0.2 dex for slower-rising events ($t_{25\_75} > 5$ d).

B.3 Sample Redshift Distribution

In Fig. B.2, we show the distribution of redshift, z, across our SN sample. The upper panel shows the z distribution for our full dataset, and the lower panel displays the highly complete ($\sim 95\%$) sample limited to events with peak apparent magnitudes $m_{peak} \leq 18.5$ mag.

B.4 Peak Colours

In Figs. B.3 – B.8, we present the KDE distributions (*left*) and ECDFs (*right*) of peak $g-r$ colours ($(g-r)_{g,\mathrm{max}}$) for Type II, Type IIn and Type IIb SNe. The panels display distributions for standard Type II (*top*), Type IIn (*middle*), and Type IIb (*bottom*) SNe. We show various statistical quantities for each distribution in Table 3.4.

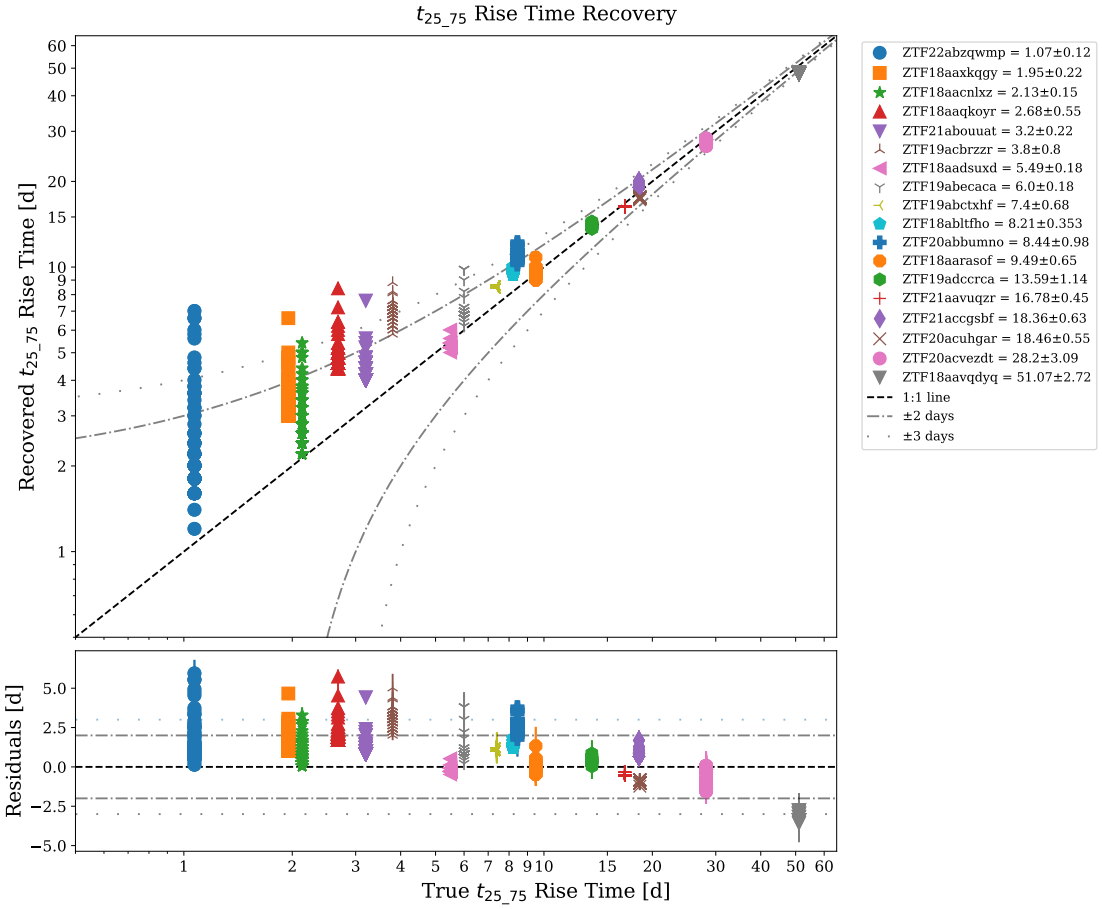

FIGURE B.1: t_{25_75} rise time recovery exploring the impact of resampling high cadenced light curve (see in the legend) to the sampling function of less well sampled light curves. The diagonal dashed line is the 1:1 line, the dot-dashed line encloses ± 2 d and the dotted line encloses ± 3 d. The bottom plot shows the residual between the 'true' rise time of each event vs the measurements from resampling.

B.5 V_{max} Verification

We performed several tests to verify that the $V_{\rm max}$ correction was functioning as intended. First, following the methodology of Schmidt (1968), we examined the distribution of $V/V_{\rm max}$ values, where V is the volume out to which a transient with peak apparent magnitude m_i could be detected in the absence of extinction and cosmological effects. For a complete and unbiased sample, the expected distribution of $V/V_{\rm max}$ is uniform between 0 and 1, with a mean value of approximately 0.5. Our distribution has a mean of 0.45 and a standard deviation of 0.29 (Fig. B.10), which is consistent with a uniform distribution and supports both the completeness of the sample and the reliability of the $V_{\rm max}$ correction.

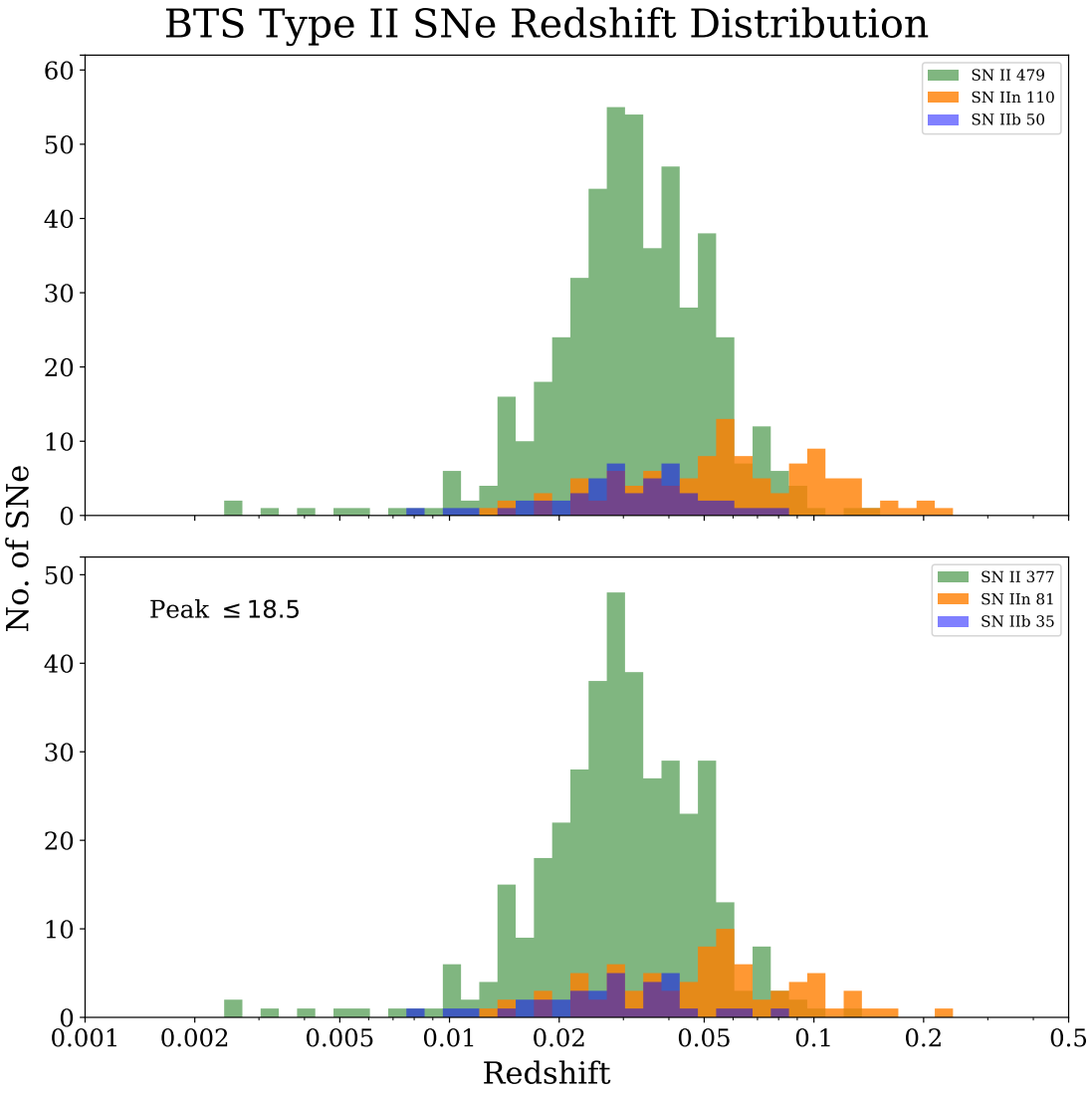

FIGURE B.2: Distribution of redshift, z, across the for the whole sample (*top*) and for the sample with a $m_{peak} \leq 18.5$ mag (*bottom*).

To quantify this, we performed a one-sample Kolmogorov–Smirnov (KS) test comparing the empirical $V/V_{\max}$ distribution to a uniform distribution over the interval [0, 1]. The resulting p-value of 0.43 indicates no statistically significant deviation from uniformity. We therefore cannot reject the null hypothesis that the $V/V_{\max}$ values are drawn from a uniform distribution. This result, together with the ECDF shown in Fig. B.11, confirms the consistency of the corrected sample with theoretical expectations.

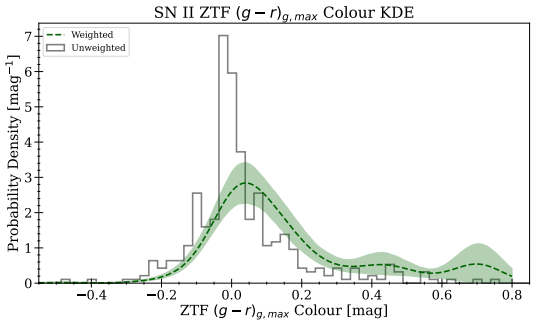

FIGURE B.3: Type II Peak Colour, $(g - r)_{g,\mathrm{max}}$, KDE.

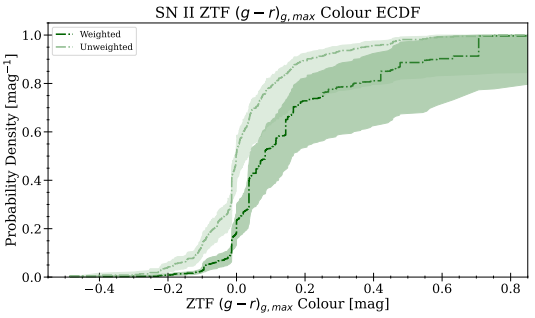

FIGURE B.4: Type II Peak Colour, $(g - r)_{g,\mathrm{max}}$, ECDF.

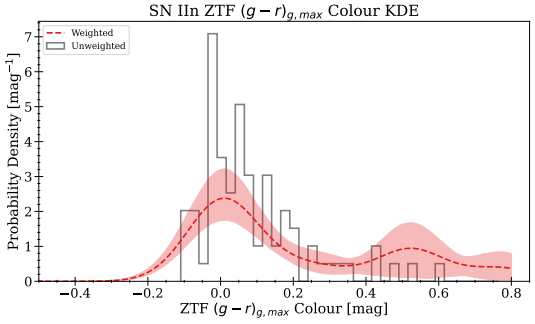

FIGURE B.5: Type IIn Peak Colour, $(g - r)_{g,\mathrm{max}}$, KDE.

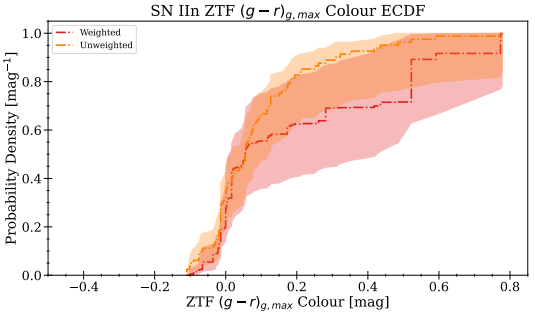

FIGURE B.6: Type IIn Peak Colour, $(g - r)_{g,\mathrm{max}}$, ECDF.

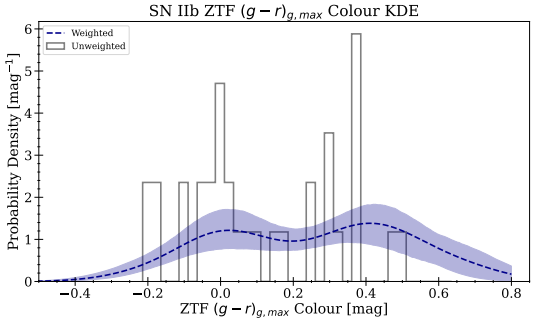

FIGURE B.7: Type IIb Peak Colour, $(g - r)_{g,\mathrm{max}}$, KDE.

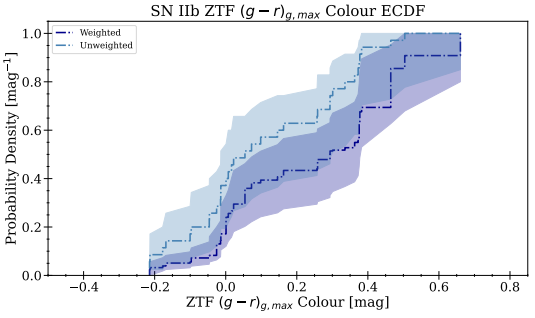

FIGURE B.8: Type IIb Peak Colour, $(g - r)_{g,\mathrm{max}}$, ECDF.

FIGURE B.9: KDE (*left*) and ECDF (*right*) for Type II (*top*), Type IIn (*middle*) and Type IIb (*bottom*) showing the ZTF $g - r$ colour at ZTF g peak, $(g - r)_{g,\mathrm{max}}$, for the purposes of correcting for host extinction using the colour at peak. A correction, detailed if Chapter 3, Section §3.3.4 is applied to events with a $g - r \geq 0.25$ mag and $t_{25\_75} < 20$ d.

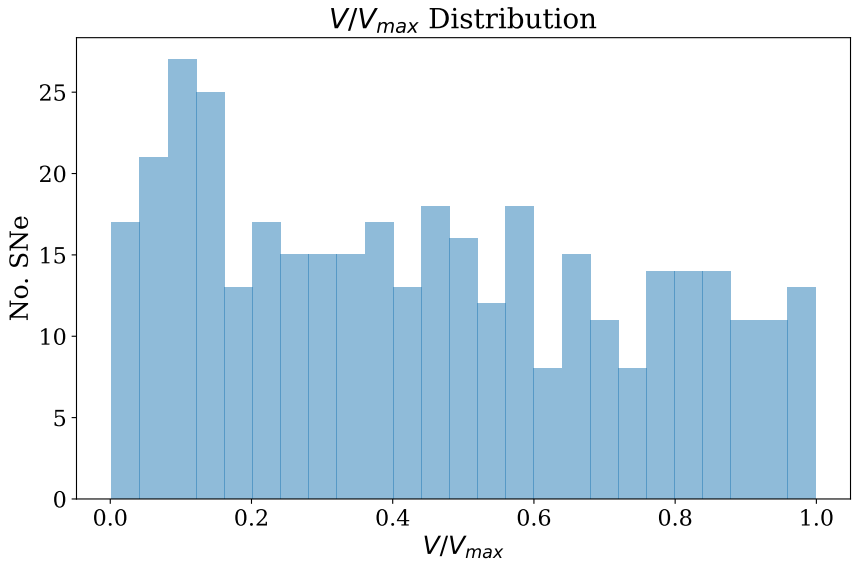

FIGURE B.10: V/V_{max} histrogram.

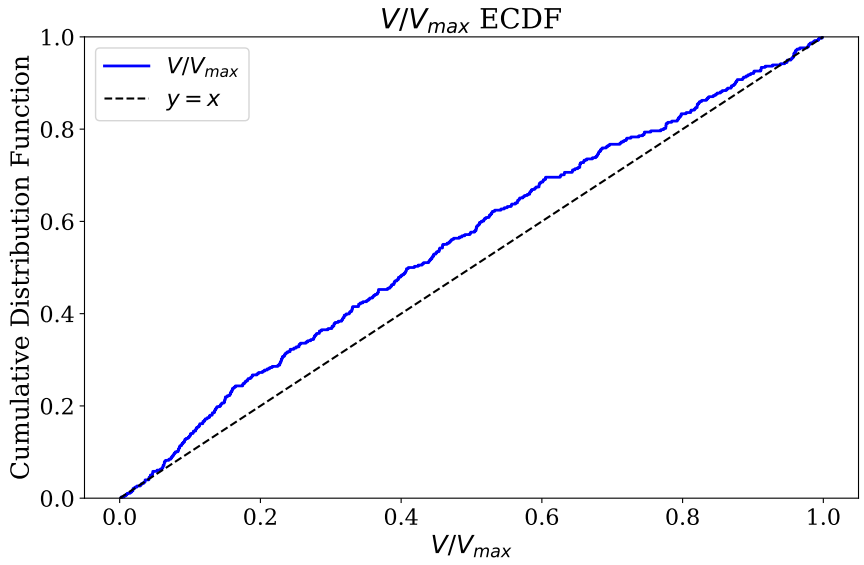

FIGURE B.11: V/V_{max} ECDF.

FIGURE B.12: Histogram (*left*) and ECDF (*right*) of V/V_{max} showing the distribution. For a complete and unbiased sample, the $V/V_{\max}$ distribution is expected to be uniform over [0, 1], with a mean of 0.5; the corresponding ECDF should follow a straight diagonal line. A one-sample Kolmogorov–Smirnov (KS) test comparing the observed distribution to a uniform distribution yields a p-value of 0.43, indicating no statistically significant deviation. This supports the completeness of the sample and the effectiveness of the $V_{\max}$ correction.

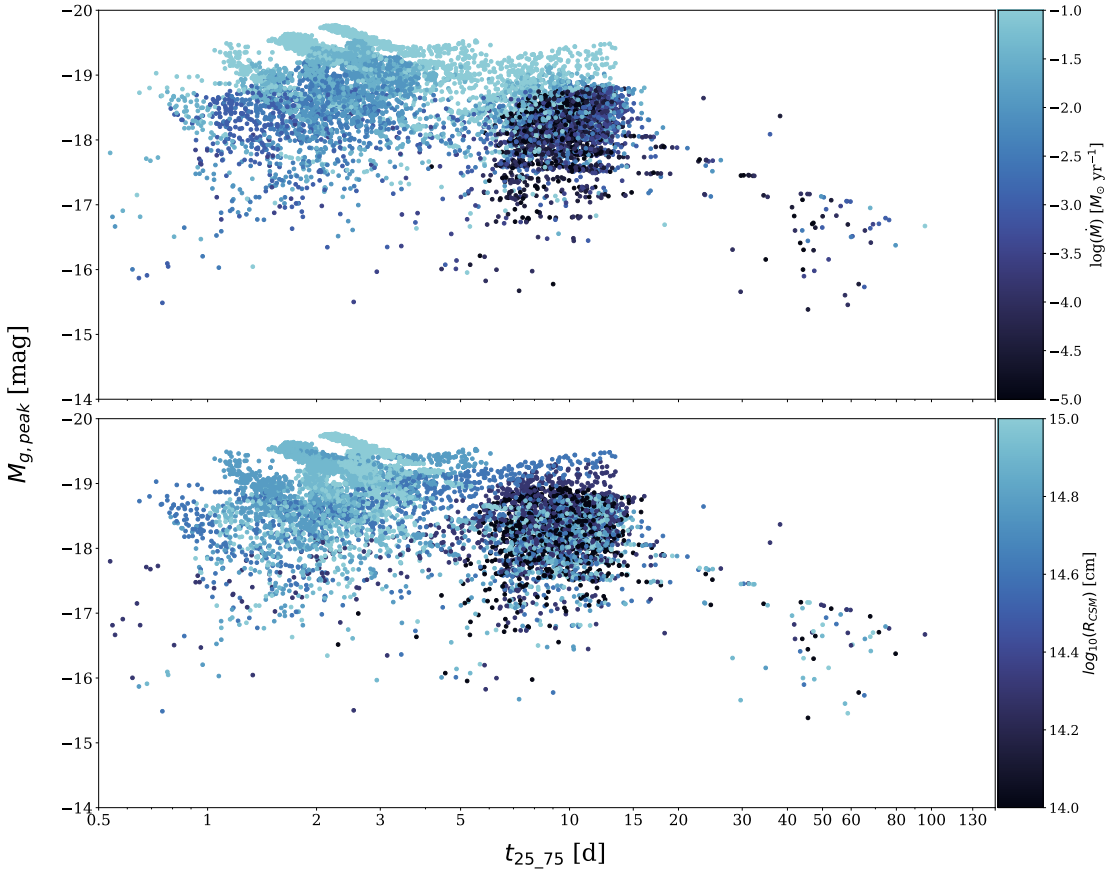

FIGURE B.13: t_{25_75} vs $M_{g,\mathrm{peak}}$ distribution for the theoretical light curve grid from M23, with points drawn from a sample of 10,000 models, colour-coded by $\dot{M}$ (*top*) and $\log(R_{\mathrm{CSM}})$ (*bottom*). The weighting is the same as applied in Fig. 3.11.

B.6 M23 Luminosity-Rise

Fig. B.13 shows the distribution of t_{25_75} vs. $M_{g,\mathrm{peak}}$ for the theoretical light curve grid from M23. We present 10,000 model points using the same $V_{max} \times M_{ZAMS}^{-2.35}$ weighting scheme applied in Fig. 3.11, which accounts for both observational selection effects and the IMF (e.g., Salpeter, 1955). The top panel colour-codes data by $\dot{M}$, while the bottom panel uses R_{CSM}.

This visualisation reveals how CSM properties strongly influence the distribution of SNe in the t_{25_75}-$M_{g,\mathrm{peak}}$ plane. Fast risers ($t_{25\_75} \leq 5$ d) typically have confined, dense CSM characterised by higher $\dot{M}$ and smaller R_{CSM}, producing moderately more luminous peaks. In contrast, slower risers ($t_{25\_75} > 5$ d) typically exhibit less confined and less dense CSM with lower overall M_{CSM} values and larger R_{CSM}. Notably, even within the slower-rising population, the most luminous events still require substantial CSM masses,

confirming that CSM mass remains a fundamental driver of peak luminosity across the distribution.

The clear separation between these populations emerges naturally from the underlying physics rather than from arbitrary parameter choices, suggesting fundamental differences in mass-loss mechanisms or progenitor structures. This bi-modality provides valuable context for interpreting the observed distribution of Type II SNe in our sample.

B.7 $M_{\mathrm{Fe,Core}}$ Measurements

We extend the predictive capabilities of multi-output GPR extend to estimating the iron core mass, $M_{\mathrm{Fe,Core}}$, of the progenitor through Eq. 1, which exploits a tight correlation between $M_{\mathrm{Fe,Core}}$ and the plateau luminosity at 50 d in simulated Type IIP light curves (e.g., Barker et al., 2022; Barker et al., 2023). The theoretical correlation indicates that more massive stellar cores lead to more energetic and luminous SNe, notably enhancing the bolometric luminosity during the plateau phase at approximately 50 d post-explosion (Barker et al., 2022). To quantify this relationship, we utilise the bolometric plateau luminosity at 50 d, $L_{\mathrm{bol,50d}}$. The plateau length is measured by analysing the gradient along the light curve and identifying significant changes in the slope. The ZTF g and r band magnitudes are measured at 50 d after the plateau onset. A bolometric correction is then applied to convert these magnitudes into bolometric luminosity – we adopt the methodology described by Lyman et al. (2014).

$$\frac{M_{Fe,Core}}{\mathrm{M}_{\odot}} = 0.0978 \times \left(\frac{L_{\mathrm{bol,50\ d}}}{10^{42}\ \mathrm{erg\ s^{-1}}} \right) + 1.29 \tag{1}$$

The KDE distribution for $M_{\mathrm{Fe,Core}}$, Fig. B.14, shows a sharp cutoff at 1.3 $\mathrm{M}_{\odot}$, reflecting the lower limit of iron core masses in the models from which the correlation was derived (Barker et al., 2022). Since the KDE smoothing kernel could not properly handle this abrupt transition, we truncate the distribution at 1.3 $\mathrm{M}_{\odot}$ and normalise the probability density to unity.

The weighted mean $M_{\mathrm{Fe,Core}}$ of 1.36 ± 0.01 $\mathrm{M}_{\odot}$ is consistent with the mean found in Barker et al. (2022) and Barker et al. (2023) of 1.4 ± 0.05 $\mathrm{M}_{\odot}$ to within 1 σ – see

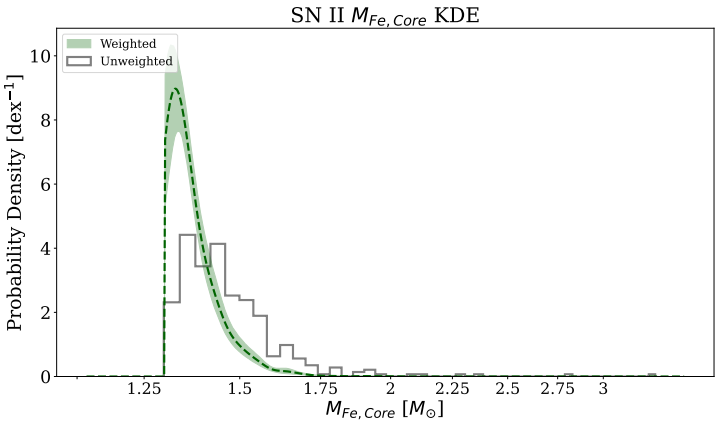

FIGURE B.14: Type II KDE for $M_{\mathrm{Fe,Core}}$ along with the associated 80% CI. The weighted distribution is in dark green (dashed line) and the unweighted normalised histogram is in black.

Parameter	Units	Mean	25th%ile	50th%ile	75th%ile	Range	No.
			Weighted				
$M_{\mathrm{Fe,Core}}$	$\mathrm{M}_\odot$	1.36 ± 0.01	$1.31^{+0.02}_{-0.01}$	1.34 ± 0.01	$1.38^{+0.01}_{-0.04}$	[1.30,3.31]	354
			Unweighted				
$M_{\mathrm{Fe,Core}}$	$\mathrm{M}_\odot$	1.49 ± 0.01	$1.38^{+0.02}_{-0.01}$	1.45 ± 0.01	$1.53^{+0.01}_{-0.02}$	-	-

[1] The ranges reported are the 5th and 95th percentiles to remove outliers beyond the limits of the original dataset.

TABLE B.2: Mean and median of the volume corrected KDE for $M_{\mathrm{Fe,Core}}$ in the final sample. The uncertainties reported here are the standard deviations of the bootstrapped values.

Table B.2. The distribution appears to be in agreement with the distribution created by Barker et al. (2022) and Barker et al. (2023), as they find a range in $M_{\mathrm{Fe,Core}}$ (1.3 – 1.5 $\pm$ 0.05 $\mathrm{M}_\odot$) after applying Eq. 1 to CCSN samples from Anderson et al. (2014) and Gutiérrez et al. (2017a,b).

While this correlation provides a useful estimate of the core mass, it assumes a direct relationship between core mass and explosion energy that, in reality, may be complicated by ejecta properties (mass and H-richness). Higher ejecta masses or more H-richness can extend and diminish the plateau luminosity independent of core mass (e.g., Goldberg, 2022). The use of luminosity at 50 d may be particularly sensitive to hydrogen envelope mass variations, as it assumes complete H retention (e.g., Goldberg, 2022; Fang et al., 2025b). A more robust approach might utilise the luminosity at half the plateau duration, which better accounts for diversity in envelope masses and better isolates the core mass contribution to the light curve evolution (Fang et al., 2025b).

B.8 M23 Relations

$$\log_{10}(\mathrm{U}) = C_0 \ + C_1 \times \mathrm{V} \ + C_2 \times \mathrm{W} + C_3 \times \mathrm{X} \ + C_4 \times \mathrm{Y} \ + C_5 \times \mathrm{Z} \tag{2}$$

$$\begin{aligned}\log_{10}(\mathrm{U}) = C_0 + C_1 \times \mathrm{V}^2 + C_2 \times (\mathrm{V} \times \mathrm{W}) \ + C_3 \times (\mathrm{V} \times \mathrm{X}) \ + C_4 \times (\mathrm{V} \times \mathrm{Y}) \ + \\ C_5 \times (\mathrm{V} \times \mathrm{Z}) \ + C_6 \times \mathrm{W}^2 + C_7 \times (\mathrm{W} \times \mathrm{X}) \ + C_8 \times (\mathrm{W} \times \mathrm{Y}) \ + C_9 \times (\mathrm{W} \times \mathrm{Z}) \ + \\ C_{10} \times \mathrm{X}^2 + C_{11} \times (\mathrm{X} \times \mathrm{Y}) \ + C_{12} \times (\mathrm{X} \times \mathrm{Z}) \ + C_{13} \times \mathrm{Y}^2 + C_{14} \times (\mathrm{Y} \times \mathrm{Z}) \ + C_{15} \times \mathrm{Z}^2\end{aligned} \tag{3}$$

$$\begin{aligned}\log_{10}(\mathrm{U}) = C_0 + C_1 \times \mathrm{V}^3 + C_2 \times \left(\mathrm{V}^2 \times \mathrm{W}\right) \ + C_3 \times \left(\mathrm{V} \times \mathrm{W}^2\right) \ + C_4 \times \mathrm{W}^3 + \\ C_5 \times \left(\mathrm{V}^2 \times \mathrm{X}\right) + C_6 \times (\mathrm{V} \times \mathrm{W} \times \mathrm{X}) + C_7 \times \left(\mathrm{W}^2 \times \mathrm{X}\right) + C_8 \times \left(\mathrm{V} \times \mathrm{X}^2\right) + C_9 \times \left(\mathrm{W} \times \mathrm{X}^2\right) \ + \\ C_{10} \times \mathrm{X}^3 + C_{11} \times \left(\mathrm{V}^2 \times \mathrm{Y}\right) + C_{12} \times (\mathrm{V} \times \mathrm{W} \times \mathrm{Y}) + C_{13} \times \left(\mathrm{W}^2 \times \mathrm{Y}\right) + C_{14} \times (\mathrm{V} \times \mathrm{X} \times \mathrm{Y}) \ + \\ C_{15} \times (\mathrm{W} \times \mathrm{X} \times \mathrm{Y}) + C_{16} \times \left(\mathrm{X}^2 \times \mathrm{Y}\right) + C_{17} \times \left(\mathrm{V} \times \mathrm{Y}^2\right) + C_{18} \times \left(\mathrm{W} \times \mathrm{Y}^2\right) + C_{19} \times \left(\mathrm{X} \times \mathrm{Y}^2\right) \ + \\ C_{20} \times \mathrm{Y}^3 + C_{21} \times \left(\mathrm{V}^2 \times \mathrm{Z}\right) + C_{22} \times (\mathrm{V} \times \mathrm{W} \times \mathrm{Z}) + C_{23} \times \left(\mathrm{W}^2 \times \mathrm{Z}\right) + C_{24} \times (\mathrm{V} \times \mathrm{X} \times \mathrm{Z}) \ + \\ C_{25} \times (\mathrm{W} \times \mathrm{X} \times \mathrm{Z}) \ + C_{26} \times \left(\mathrm{X}^2 \times \mathrm{Z}\right) \ + C_{27} \times (\mathrm{V} \times \mathrm{Y} \times \mathrm{Z}) \ + C_{28} \times (\mathrm{W} \times \mathrm{Y} \times \mathrm{Z}) \ + \\ C_{29} \times (\mathrm{X} \times \mathrm{Y} \times \mathrm{Z}) + C_{30} \times \left(\mathrm{Y}^2 \times \mathrm{Z}\right) + C_{31} \times \left(\mathrm{V} \times \mathrm{Z}^2\right) + C_{32} \times \left(\mathrm{W} \times \mathrm{Z}^2\right) + C_{33} \times \left(\mathrm{X} \times \mathrm{Z}^2\right) \ + \\ C_{34} \times \left(\mathrm{Y} \times \mathrm{Z}^2\right) \ + C_{35} \times \mathrm{Z}^3\end{aligned} \tag{4}$$

For M_{CSM}, $\mathrm{U} = M_{\mathrm{CSM}}$, $\mathrm{V} = M_{g,\mathrm{peak}}$, $\mathrm{W} = \log_{10}(t_{20\_60})$, $\mathrm{X} = \log_{10}(t_{60\_90})$, $\mathrm{Y} = (g-r)_{g,\mathrm{max}}$ & $\mathrm{Z} = M_{g,10\mathrm{d}}$.
For R_{CSM}, $\mathrm{U} = R_{\mathrm{CSM}}$, $\mathrm{V} = M_{g,\mathrm{peak}}$, $\mathrm{W} = \log_{10}(t_{20\_50})$, $\mathrm{X} = \log_{10}(t_{50\_80})$, $\mathrm{Y} = (g-r)_{g,\mathrm{max}}$ & $\mathrm{Z} = M_{g,5\mathrm{d}}$.

	C_0	C_1	C_2	C_3	C_4	C_5	C_6	C_7	C_8	C_9	C_{10}	C_{11}
$M_{\rm CSM} \leq 5$ d	-4.51	2.28	2.07	-0.24	1.07	-2.88	-0.19	0.0823	2.10	-1.24	-0.16	-12.35
$M_{\rm CSM} > 5$ d	-3.54	13.24	-3.85	5.94	0.22	-30.16	-9.55	-1.10	4.64	4.31	-2.26	42.92
$R_{\rm CSM} \leq 5$ d	0.65	0.43	-2.91	0.51	0.14	1.93	0.57	0.18	-1.04	0.039	-0.071	-10.05
$R_{\rm CSM} > 5$ d	-0.41	30.75	0.24	-4.57	0.29	5.67	5.47	-0.042	-4.65	-0.18	0.22	0.055
	C_{12}	C_{13}	C_{14}	C_{15}	C_{16}	C_{17}	C_{18}	C_{19}	C_{20}	C_{21}	C_{22}	C_{23}
$M_{\rm CSM} \leq 5$ d	-16.12	-2.31	5.66	2.76	-0.13	8.06	-2.24	2.19	0.84	-6.88	-3.95	0.20
$M_{\rm CSM} > 5$ d	5.95	1.44	10.72	-8.35	4.53	-29.78	5.17	3.19	-10.21	-42.38	7.66	-6.04
$R_{\rm CSM} \leq 5$ d	3.82	-0.16	3.71	-0.41	0.29	2.89	0.54	-0.46	-0.46	-1.03	5.83	-0.46
$R_{\rm CSM} > 5$ d	6.36	0.0098	-7.77	0.64	-0.49	-4.28	-0.59	0.22	-0.13	-93.03	-0.35	4.6
	C_{24}	C_{25}	C_{26}	C_{27}	C_{28}	C_{29}	C_{30}	C_{31}	C_{32}	C_{33}	C_{34}	C_{35}
$M_{\rm CSM} \leq 5$ d	5.85	0.085	-2.11	25.25	16.32	-5.72	-8.03	6.91	1.87	-2.97	-12.91	-2.31
$M_{\rm CSM} > 5$ d	61.57	9.91	-5.03	-86.78	-6.18	-10.02	29.54	45.11	-3.81	-31.43	43.9	-15.97
$R_{\rm CSM} \leq 5$ d	-3.99	-0.55	1.03	20.35	-3.84	-3.69	-2.94	0.77	-2.92	2.07	-10.30	-0.17
$R_{\rm CSM} > 5$ d	-11.87	-5.48	4.68	-0.54	-6.38	7.74	4.31	93.82	0.11	6.21	0.49	-31.53

TABLE B.3: $M_{\rm CSM}$ and $R_{\rm CSM}$ coefficients.

B.9 M23 Radial Extent Predictions

Fig. B.15 shows the multivariate analysis comparing our polynomial regression-predicted CSM radial extent values (y-axis) against the corresponding M23 model values (x-axis), following an approach similar to Figure 3.13. This systematic evaluation examines the performance of polynomial fits across different degrees (1st, 2nd, and 3rd order) and specific parameter regimes to determine the optimal method for characterising this relationship. Unlike our $M_{\rm CSM}$ analysis, this investigation of $R_{\rm CSM}$ is restricted to M23 models with $M_{\rm CSM} \geq 1 \times 10^{-2.5}$ $\rm M_{\odot}$, which Section §3.6.1 identifies as the threshold above which CSM significantly influences both $M_{g,\rm peak}$ and t_{25_75}. The results demonstrate that $R_{\rm CSM}$ can only be reliably constrained for events with substantial $M_{\rm CSM}$.

B.10 M23 $M_{\rm CSM}$ Lower Limit

Accurate measurements of $R_{\rm CSM}$ becomes challenging when $M_{\rm CSM}$ is insufficient to significantly influence observables such as $M_{g,\rm peak}$ and t_{25_75}. To establish a critical threshold below which CSM becomes virtually undetectable in early light curves, we systematically analysed how variations in key physical parameters – $\dot{M}$, $R_{\rm CSM}$ and β – affect observable properties.

We systematically varied these parameters while holding other key physical parameters constant (e.g., nickel mass). Our investigation revealed that when $M_{\rm CSM}$ falls below approximately $10^{-2.5}$ $\rm M_{\odot}$, the CSM becomes too diffuse to meaningfully influence early light curve evolution. This threshold is evidenced by minimal variations in $M_{g,\rm peak}$ below $10^{-2.5}$ $\rm M_{\odot}$ and increasingly significant variations above this mass – a pattern consistent across all progenitor masses. At this critical point, we observe a transition to a regime where CSM interaction becomes negligible in shaping the observable properties of the supernova. This theoretical expectation is strongly supported by the distinct bimodal distribution observed in the M23 models (Fig. B.13).

Given this fundamental limitation in detecting and characterising low-mass CSM environments, we restrict our subsequent analysis of $R_{\rm CSM}$ to events where the predicted $M_{\rm CSM}$ exceeds $10^{-2.5}$ $\rm M_{\odot}$.

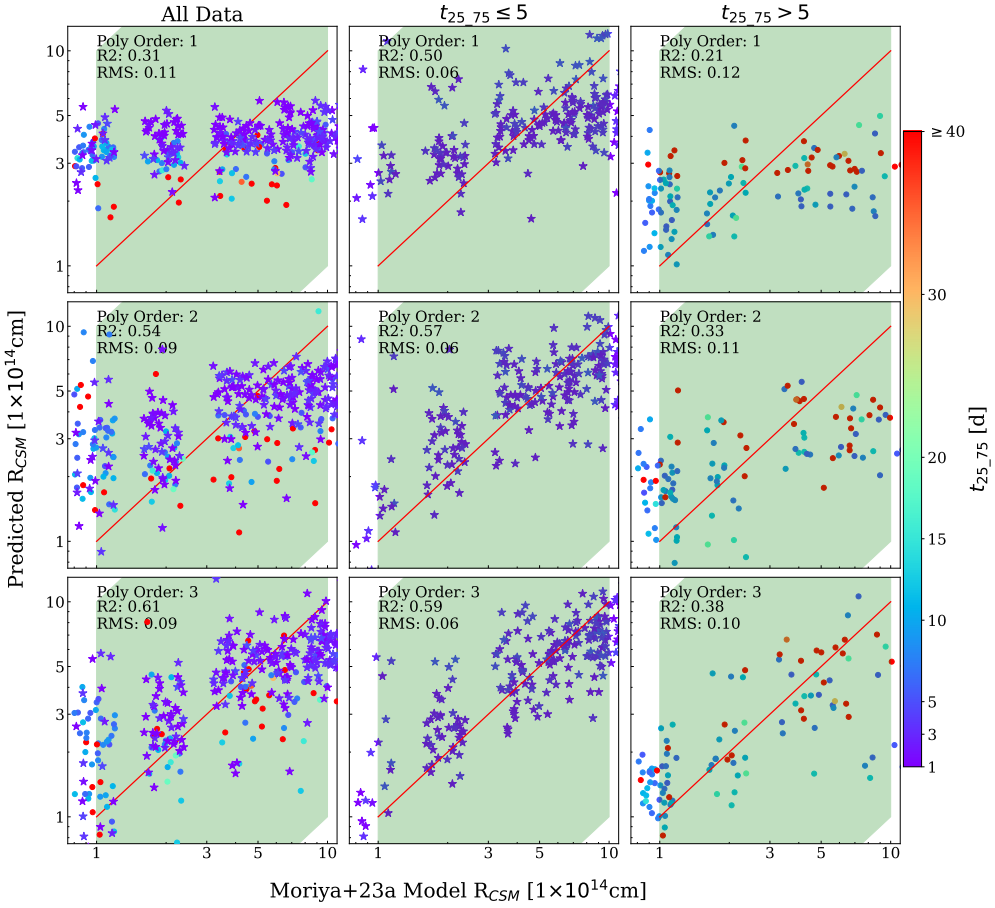

FIGURE B.15: Multivariate analysis results of the predicted $R_{\rm CSM}$ radial extent (y-axis) vs. the M23 $R_{\rm CSM}$ radial extent (x-axis). The top, middle and bottom rows are polynomial orders 1, 2 and 3, respectively. The first column contains all the data and stars are those with $t_{25\_75} \leq 5$ d, with the 2nd and 3rd rows containing only data with $t_{25\_75} \leq 5$ d and $t_{25\_75} > 5$ d to show how the correlations' predictive power decreases significantly for events with $t_{25\_75} \geq 5$ d. The diagonal red line is the 1:1 line, with the green shaded region showing 1 order of magnitude above and below. This is run only on M23 models where $M_{\rm CSM} \geq 1\times10^{-2.5}$ $M_\odot$ as we identify in Chapter 3, Section §3.6.1 this to be the lower limit, above which $M_{g,\rm peak}$ and t_{25_75} were influenced.

B.11 Impact of Systematic Misclassifications

Most SN classifications from the BTS rely on the low-resolution SEDM spectrograph (R $\sim$100). The limited spectral resolution and typically single-epoch observations near maximum light can make distinguishing certain SN subclasses challenging, particularly Type IIb from Type II and, to a lesser extent, Type IIn from Type II or host emission. Consequently, our Type II sample might contain some level of contamination from misclassified events, a consideration we quantitatively address here.

To quantify potential classification biases, we conducted Kolmogorov-Smirnov (KS) tests

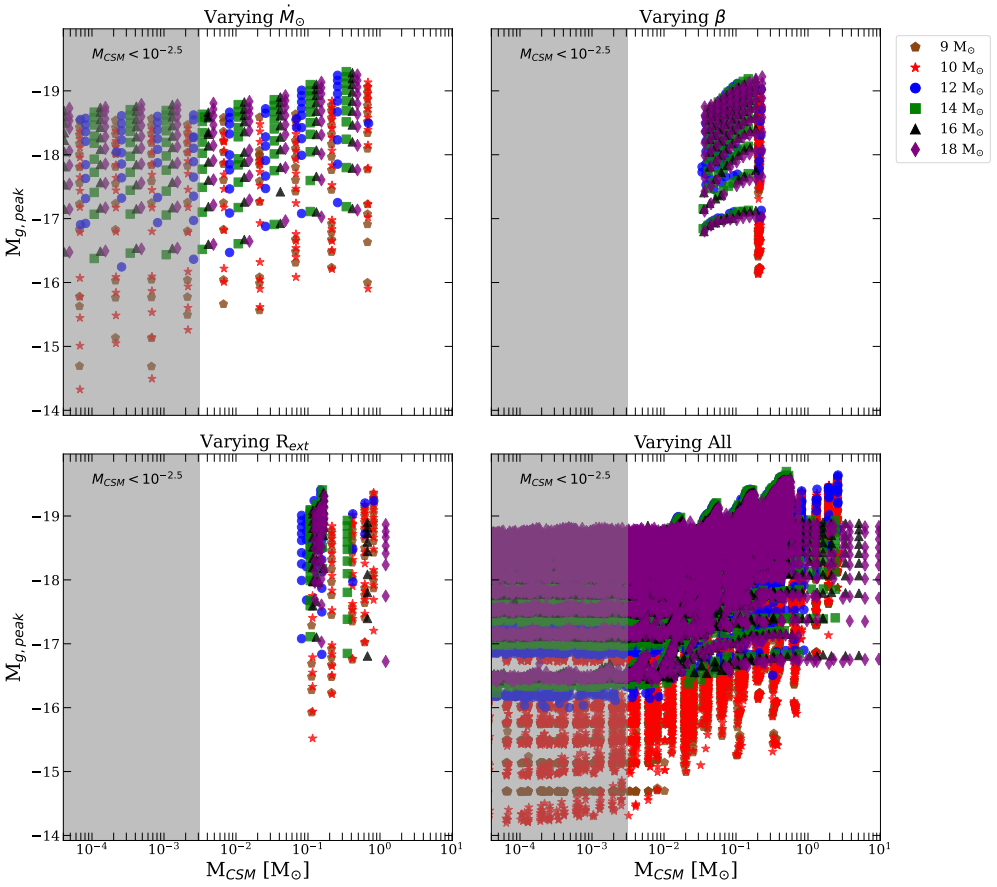

FIGURE B.16: Dependence of $M_{g,\mathrm{peak}}$ on M_{CSM} under different parameter variations, with fixed Ni mass and explosion energy. Top left: Varying $\dot{M}$ with fixed β and R_{CSM}. Top right: Varying β with fixed $\dot{M}$ and R_{CSM}. Bottom left: Varying R_{CSM} with fixed $\dot{M}$ and β. Bottom right: Combined variation of all CSM parameters ($\dot{M}$, β, R_{CSM}). Each panel shows results for different progenitor masses (10 – 18 $\mathrm{M}_{\odot}$). Below $M_{\mathrm{CSM}} \approx 10^{-2.5}$ $\mathrm{M}_{\odot}$, CSM properties do not significantly influence the peak magnitude, indicating a transition to CSM-negligible evolution.

comparing Type II and Type IIb populations. KS tests of the unweighted $M_{g,\mathrm{peak}}$ and t_{25_75} distributions yielded p-values of 0.038 and 0.0030, respectively, indicating statistically significant differences between these populations. We identified an approximately 5% shortfall of Type IIb SNe in our sample ($7.22^{+2.40}_{-1.84}$% versus the expected $\sim$12.5% from the Shivvers et al. 2017 volume-complete sample). To assess the impact of possible misclassifications, we applied a conservative approach by removing the fastest-rising 5% of Type II SNe – those most likely to be misclassified Type IIbs and have the largest impact on our results – and recalculated the M_{CSM} KDE distribution. The fraction of Type II SNe with $M_{\mathrm{CSM}} \geq 10^{-2.5}$ $\mathrm{M}_{\odot}$ remained consistent (38 – 41%) with our original finding ($\sim$36%). This represents the most extreme scenario, confirming that potential misclassifications affect our results by less than 1 σ.

Similarly, our analysis yields a Type IIn rate of $4.34^{+1.49}_{-1.09}\%$ relative to Type II SNe, consistent with Shivvers et al. (2017). We consider the possibility of misclassification between regular Type II SNe and Type IIn events to be minimal for several reasons: (1) Type IIn SNe typically exhibit higher luminosities and represent a small fraction of the overall population, resulting in negligible statistical impact after $V_{\rm max}$ weighting; (2) BTS routinely conducts follow-up observations using higher-resolution spectrographs for suspected Type IIn events to refine classification; and (3) wee see that $< 2\%$ of our Type IIn sample exhibits photometric characteristics resembling typical Type II events (i.e., $t_{25\text{-}75} \leq 3$ d and $M_{g,\rm peak} > -18$ mag, which represent the median values for our unweighted Type II sample; Table 3.4). Our robust classification methodology ensures complete Type IIn identification, and our focus on CSM around fast-rising SNe means the longer evolution timescales of Type IIn events minimally impact our conclusions.

We have also considered the potential impact of peculiar events resembling SN 1987A on our results. Such objects, characterised by moderate peak luminosities combined with unusually slow rise times (e.g., ZTF18acbwaxk), represent rare occurrences in the local universe. If several such events were misclassified or included within our sample, their statistical contribution would remain minimal given our V_{max} weighting and large sample size.

Appendix C

C.1 Unique Type II Light Curves

The following SNe, ZTF20aatqesi, ZTF22aaspkif and ZTF22abybbud, are examples of spectroscopically classified Type II SNe that show no obvious plateau. Both ZTF20aatqesi and ZTF22abybbud show resemblance to SN 1987A with an initial peak and then a much slower, wider peak with similar peak magnitudes. These and similar SNe were excluded from the sample as the plateau finding algorithm was unable to identify significant plateaus in these cases. Amongst the unique SNe were other Type II SNe showing a plateau phase that was only partially caught (either the start or the end of the plateau was missed), resulting in uncertain measurements and failure to meet the quality cuts outlined in Chapter 4, Section §4.4.

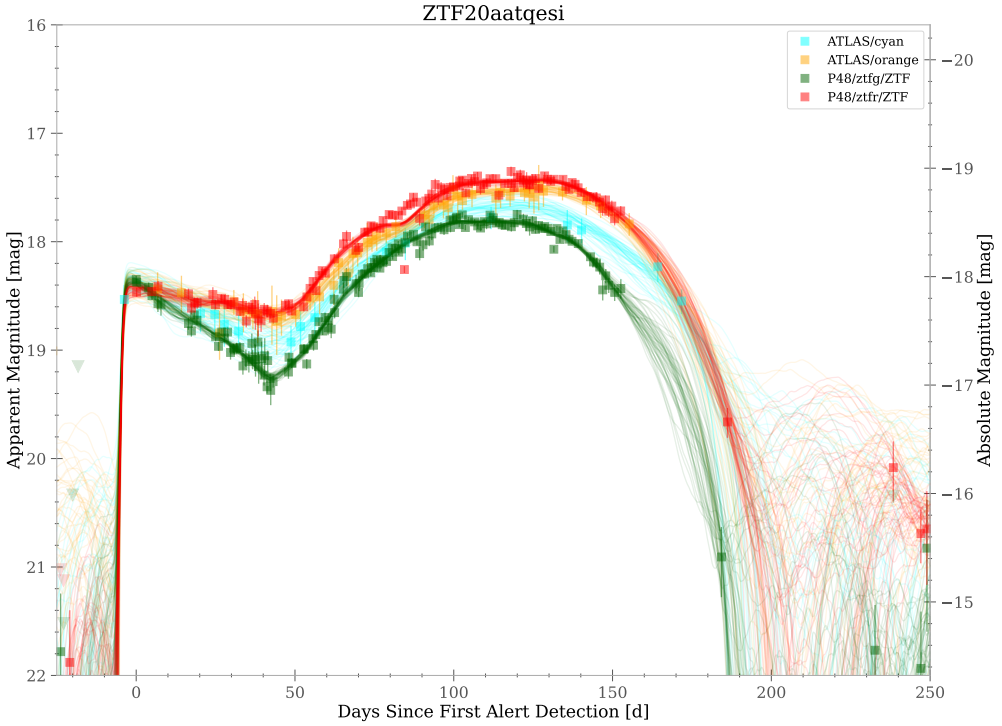

FIGURE C.1: ZTF20aatqesi – Type II SN with no obvious plateau.

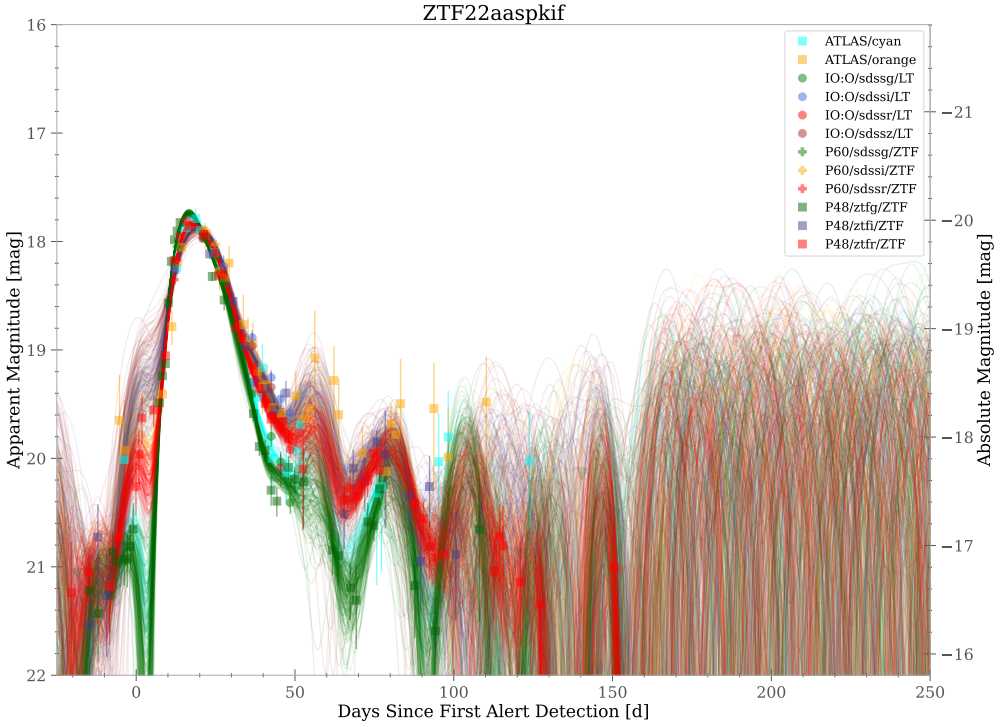

FIGURE C.1: ZTF22aaspkif – Type II SN with no obvious plateau phase

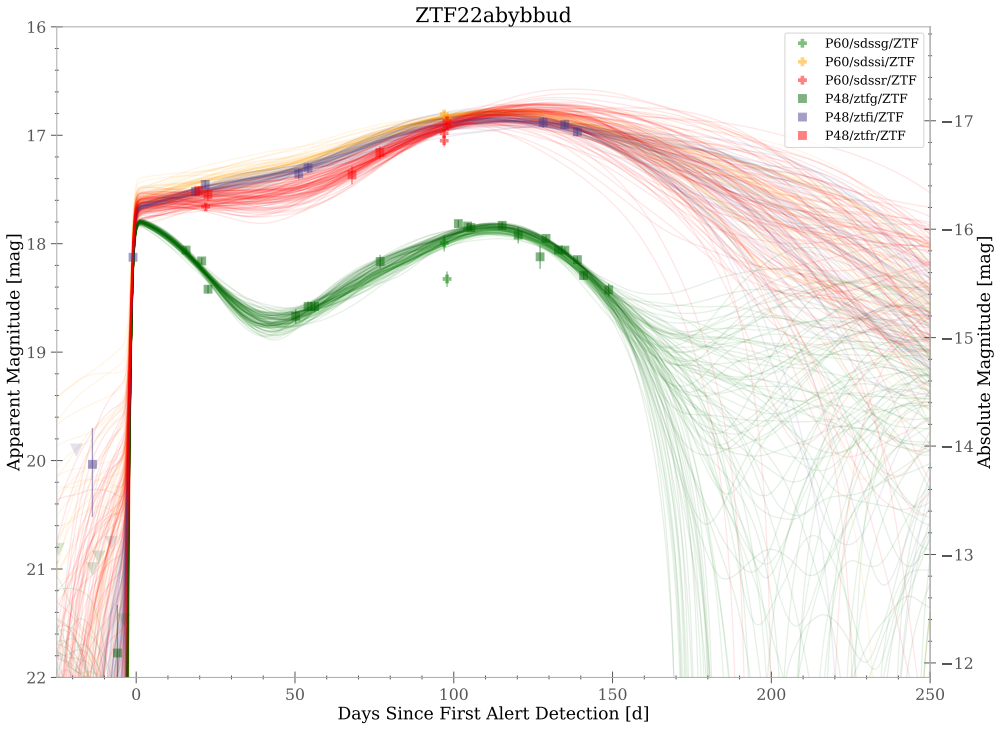

FIGURE C.1: ZTF22abybbud – Type II SN with no obvious plateau phase.

Figure C.1: Examples of spectroscopically classified Type II SNe within the BTS that show no obvious plateau phase synonymous with Type II SNe. These were removed from the sample as the plateau finding algorithm was unable to identify a clear plateau.

C.2 Impact of Host Extinction

To assess the sensitivity of $M_{\rm Ni}$ estimates on host galaxy extinction, a representative subset of SNe was selected spanning a wide range of $M_{\rm Ni}$ values ($0.9 - 30 \times 10^{-2}$ $M_\odot$). For each event, $M_{\rm Ni}$ was recalculated assuming varying levels of host extinction: $A_V = [0.1, 0.3, 0.7, 1.5]$ mag. Band-specific extinctions in g, r, and i were derived using a Milky Way extinction law with $R_V = 3.1$ (Cardelli et al., 1989), implemented via the `extinction python` package. Extinction corrections were applied to the light curves prior to re-estimating $M_{\rm Ni}$ using the same procedure described in the main analysis.

The corresponding extinction factors are listed in Table C.1, and the resulting $M_{\rm Ni}$ estimates for each extinction level are presented in Table C.2. Even under substantial extinction ($A_V = 1.5$ mag), the inferred $M_{\rm Ni}$ values varied by no more than a factor of $\sim$2. For more typical extinction values ($A_V \lesssim 0.3$ mag), the impact was negligible. These results confirm that while host extinction introduces additional uncertainty, it does not significantly bias $M_{\rm Ni}$ estimates for most SNe in the sample.

A_V	A_g	A_r	A_i
0.1	0.12	0.085	0.061
0.3	0.36	0.25	0.18
0.7	0.84	0.59	0.43
1.5	1.80	1.27	0.91

TABLE C.1: Extinction values in different bands derived using a Milky Way extinction law with $R_V = 3.1$. Wavelengths for g, r and i are based on ZTF filters e.g., 4753.15 Å, 6369.99 Å and 7915.49 Å respectively (Rodrigo & Solano, 2020; Rodrigo et al., 2024).

SN	Parameter	Units	$A_V = 0.0$	0.1	0.3	0.7	1.5
ZTF19aadnxog	$\log(L_{\rm Tail})$	erg s^{-1}	41.60	41.60	41.61	41.61	41.73
	$M_{\rm Ni}$[1]	$\times 10^{-2}$ M$_\odot$	9.64	9.58	9.82	9.83	13.00
	$M_{\rm Ni}$[2]	$\times 10^{-2}$ M$_\odot$	10.51	10.44	10.70	10.71	14.17
ZTF19abbnamr	$\log(L_{\rm Tail})$	erg s^{-1}	42.06	42.04	41.99	41.91	41.74
	$M_{\rm Ni}$[1]	$\times 10^{-2}$ M$_\odot$	30.63	29.01	26.10	21.26	14.67
	$M_{\rm Ni}$[2]	$\times 10^{-2}$ M$_\odot$	26.15	24.77	22.28	18.15	12.53
ZTF20abjonjs	$\log(L_{\rm Tail})$	erg s^{-1}	41.02	40.99	40.94	40.86	40.89
	$M_{\rm Ni}$[1]	$\times 10^{-2}$ M$_\odot$	2.77	2.58	2.28	1.90	2.05
	$M_{\rm Ni}$[2]	$\times 10^{-2}$ M$_\odot$	2.58	2.41	2.12	1.77	1.91
ZTF22abtjefa	$\log(L_{\rm Tail})$	erg s^{-1}	40.57	40.56	40.54	40.52	40.48
	$M_{\rm Ni}$[1]	$\times 10^{-2}$ M$_\odot$	0.98	0.96	0.93	0.87	0.79
	$M_{\rm Ni}$[2]	$\times 10^{-2}$ M$_\odot$	0.86	0.85	0.82	0.77	0.70
ZTF22abtspsw	$\log(L_{\rm Tail})$	erg s^{-1}	40.50	40.58	40.58	40.56	40.57
	$M_{\rm Ni}$[1]	$\times 10^{-2}$ M$_\odot$	0.83	1.00	0.99	0.96	0.98
	$M_{\rm Ni}$[2]	$\times 10^{-2}$ M$_\odot$	0.84	0.99	0.98	0.95	0.97
ZTF23abbzdoj	$\log(L_{\rm Tail})$	erg s^{-1}	41.19	41.18	41.15	41.12	41.05
	$M_{\rm Ni}$[1]	$\times 10^{-2}$ M$_\odot$	4.11	3.96	3.77	3.45	2.99
	$M_{\rm Ni}$[2]	$\times 10^{-2}$ M$_\odot$	2.47	2.38	2.27	2.07	1.79

[1] Calculated using Eq. 4.1, based on Hamuy (2003).
[2] Calculated using Eq. 4.2, based on Spiro et al. (2014); Valenti et al. (2016).

TABLE C.2: $M_{\rm Ni}$ estimates for several SNe under different extinction assumptions. For $\log(L_{\rm Tail})$, the units represent the linear space $L_{\rm Tail}$ units and not the transformed value.

Bibliography

Abbott D. C., Beiging J. H., Churchwell E., Torres A. V., 1986, ApJ, 303, 239

Acero-Cuellar T., Bianco F., Dobler G., Sako M., Qu H., LSST Dark Energy Science Collaboration 2023, AJ, 166, 115

Adams S. M., Kochanek C. S., Gerke J. R., Stanek K. Z., Dai X., 2017a, MNRAS, 468, 4968

Adams S. M., Kochanek C. S., Gerke J. R., Stanek K. Z., 2017b, MNRAS, 469, 1445

Aigrain S., Foreman-Mackey D., 2023, ARA&A, 61, 329

Akaike H., 1974, IEEE Transactions on Automatic Control, 19, 716

Alard C., 2000, A&AS, 144, 363

Alard C., Lupton R. H., 1998, ApJ, 503, 325

Aldering G., Humphreys R. M., Richmond M., 1994, AJ, 107, 662

Álvarez M., Rosasco L., Lawrence N., 2012, Kernels for Vector-Valued Functions: A Review. Foundations and Trends® in Machine Learning Series, Now Publishers, https://books.google.co.uk/books?id=2A5hLwEACAAJ

Ambikasaran S., Foreman-Mackey D., Greengard L., Hogg D. W., O'Neil M., 2015, IEEE transactions on pattern analysis and machine intelligence, 38, 252

Anderson J. P., 2019, A&A, 628, A7

Anderson J. P., Covarrubias R. A., James P. A., Hamuy M., Habergham S. M., 2010, MNRAS, 407, 2660

Anderson J. P., et al., 2014, ApJ, 786, 67

Anderson J. P., et al., 2016, A&A, 589, A110

Andreoni I., et al., 2021, ApJ, 918, 63

Andrews J. E., et al., 2024, ApJ, 965, 85

Angus C. R., et al., 2019, MNRAS, 487, 2215

Arcavi I., 2017, Handbook of Supernovae, pp 239–276

Arcavi I., et al., 2010, ApJ, 721, 777

Arcavi I., et al., 2011, ApJ, 742, L18

Arcavi I., et al., 2012, ApJ, 756, L30

Arnett W. D., 1966, Canadian Journal of Physics, 44, 2553

Arnett W. D., 1972, ApJ, 176, 681

Arnett W. D., 1980, ApJ, 237, 541

Arnett D., 1996, Supernovae and Nucleosynthesis: An Investigation of the History of Matter from the Big Bang to the Present. Princeton University Press

Arnett W. D., Meakin C., 2011, ApJ, 733, 78

Arnett W. D., Bahcall J. N., Kirshner R. P., Woosley S. E., 1989, ARA&A, 27, 629

Ayala B., et al., 2025, arXiv e-prints, p. arXiv:2503.05909

Baade W., Zwicky F., 1934, Proceedings of the National Academy of Science, 20, 254

Bailer-Jones C. A. L., 2012, A&A, 546, A89

Bailey S., Aragon C., Romano R., Thomas R. C., Weaver B. A., Wong D., 2007, ApJ, 665, 1246

Barbon R., Ciatti F., Rosino L., 1979, Astronomy and Astrophysics, vol. 72, no. 3, Feb. 1979, p. 287-292. Research supported by the Consiglio Nazionale delle Ricerche., 72, 287

Barkat Z., Rakavy G., Sack N., 1967, Phys. Rev. Lett., 18, 379

Barker B. L., Harris C. E., Warren M. L., O'Connor E. P., Couch S. M., 2022, ApJ, 934, 67

Barker B. L., O'Connor E. P., Couch S. M., 2023, ApJ, 944, L2

Batty K., Steele I., Copperwheat C., 2022, PASP, 134, 065001

Bazin G., et al., 2009, A&A, 499, 653

Bazin G., et al., 2011, A&A, 534, A43

Beasor E. R., Davies B., 2016, MNRAS, 463, 1269

Beasor E. R., Davies B., 2018, MNRAS, 475, 55

Beasor E. R., Smith N., 2022, ApJ, 933, 41

Beasor E. R., Davies B., Smith N., van Loon J. T., Gehrz R. D., Figer D. F., 2020, MNRAS, 492, 5994

Beasor E. R., Hosseinzadeh G., Smith N., Davies B., Jencson J. E., Pearson J., Sand D. J., 2024, ApJ, 964, 171

Beasor E. R., Smith N., Jencson J. E., 2025, ApJ, 979, 117

Becker A., 2015, HOTPANTS: High Order Transform of PSF ANd Template Subtraction, Astrophysics Source Code Library, record ascl:1504.004

Bellm E. C., et al., 2019a, PASP, 131, 018002

Bellm E. C., et al., 2019b, PASP, 131, 068003

Ben-Ami S., et al., 2015, ApJ, 803, 40

Benson P. J., et al., 1994, AJ, 107, 1453

Bersten M. C., Hamuy M., 2009, ApJ, 701, 200

Bersten M. C., Benvenuto O., Hamuy M., 2011, ApJ, 729, 61

Bersten M. C., Tanaka M., Tominaga N., Benvenuto O. G., Nomoto K., 2013, ApJ, 767, 143

Bersten M. C., et al., 2018, Nature, 554, 497

Bertin E., 2010, SWarp: Resampling and Co-adding FITS Images Together (ascl:1010.068)

Bertin E., 2011, in Evans I. N., Accomazzi A., Mink D. J., Rots A. H., eds, Astronomical Society of the Pacific Conference Series Vol. 442, Astronomical Data Analysis Software and Systems XX. p. 435

Bertin E., Arnouts S., 1996, A&AS, 117, 393

Bestenlehner J. M., et al., 2014, A&A, 570, A38

Bethe H. A., 1990, Rev. Mod. Phys., 62, 801

Bethe H. A., Wilson J. R., 1985, ApJ, 295, 14

Bionta R. M., et al., 1987, Phys. Rev. Lett., 58, 1494

Blagorodnova N., et al., 2018, PASP, 130, 035003

Blinnikov S. I., Bartunov O. S., 1993, A&A, 273, 106

Blinnikov S. I., Eastman R., Bartunov O. S., Popolitov V. A., Woosley S. E., 1998, ApJ, 496, 454

Blinnikov S., Lundqvist P., Bartunov O., Nomoto K., Iwamoto K., 2000, ApJ, 532, 1132

Blinnikov S. I., Röpke F. K., Sorokina E. I., Gieseler M., Reinecke M., Travaglio C., Hillebrandt W., Stritzinger M., 2006, A&A, 453, 229

Bloemen S., et al., 2016, in Hall H. J., Gilmozzi R., Marshall H. K., eds, Society of Photo-Optical Instrumentation Engineers (SPIE) Conference Series Vol. 9906, Ground-based and Airborne Telescopes VI. p. 990664, doi:10.1117/12.2232522

Bloom J. S., et al., 2012, PASP, 124, 1175

Boccioli L., Roberti L., 2024, Universe, 10, 148

Bollig R., Yadav N., Kresse D., Janka H.-T., Müller B., Heger A., 2021, ApJ, 915, 28

Boone K., 2019, AJ, 158, 257

Bose S., et al., 2018, ApJ, 862, 107

Bostroem K. A., et al., 2023, ApJ, 956, L5

Botticella M. T., et al., 2010, ApJ, 717, L52

Bowers R., Wilson J. R., 1982, ApJ, 263, 366

Boyle W. S., Smith G. E., 1970, The Bell System Technical Journal, 49, 587

Bramich D. M., 2008, MNRAS, 386, L77

Bramich D. M., et al., 2013, MNRAS, 428, 2275

Braun T., Kvellestad A., De Bin R., 2024, arXiv e-prints, p. arXiv:2410.01024

Brennan S. J., Fraser M., 2022, A&A, 667, A62

Brown T. M., et al., 2013, PASP, 125, 1031

Bruch R. J., et al., 2021, ApJ, 912, 46

Bruch R. J., et al., 2023, ApJ, 952, 119

Burbidge E. M., Burbidge G. R., Fowler W. A., Hoyle F., 1957, Rev. Mod. Phys., 29, 547

Burnham K. P., Anderson D. R., 2004, Sociological Methods & Research, 33, 261

Burrows A., 1987, ApJ, 318, L57

Burrows A., Lattimer J. M., 1987, ApJ, 318, L63

Burrows A., Vartanyan D., 2021, Nature, 589, 29

Burrows A., Hayes J., Fryxell B. A., 1995, ApJ, 450, 830

Byrne R. A., Fraser M., 2022, MNRAS, 514, 1188

Cabrera-Vives G., Reyes I., Förster F., Estévez P. A., Maureira J.-C., 2017, ApJ, 836, 97

Cappellaro E., Turatto M., Benetti S., Tsvetkov D. Y., Bartunov O. S., Makarova I. N., 1993, A&A, 268, 472

Cappellaro E., Turatto M., Tsvetkov D. Y., Bartunov O. S., Pollas C., Evans R., Hamuy M., 1997, A&A, 322, 431

Cardelli J. A., Clayton G. C., Mathis J. S., 1989, ApJ, 345, 245

Carrasco-Davis R., et al., 2021, AJ, 162, 231

Castor J. I., Abbott D. C., Klein R. I., 1975, ApJ, 195, 157

Catchpole R. M., 1989, Highlights of Astronomy, 8, 185

Chambers K. C., et al., 2016, arXiv e-prints, p. arXiv:1612.05560

Chandra P., 2018, Space Science Reviews, 214

Chen Z. H., et al., 2023, ApJ, 943, 41

Chen X., et al., 2024, ApJ, 971, L2

Chen T.-W., et al., 2025, ApJ, 983, 86

Chevalier R. A., 1976, ApJ, 207, 872

Chevalier R. A., 1992, ApJ, 394, 599

Chevalier R. A., 2012, ApJ, 752, L2

Chevalier R. A., Fransson C., 2008, ApJ, 683, L135

Chevalier R. A., Irwin C. M., 2011, ApJ, 729, L6

Chieffi A., Domínguez I., Höflich P., Limongi M., Straniero O., 2003, MNRAS, 345, 111

Chugai N. N., 1991, Soviet Astronomy Letters, 17, 210

Chugai N. N., 2001, MNRAS, 326, 1448

Chugai N. N., Danziger I. J., 1994a, MNRAS, 268, 173

Chugai N. N., Danziger I. J., 1994b, MNRAS, 268, 173

Claeys J. S. W., de Mink S. E., Pols O. R., Eldridge J. J., Baes M., 2011, A&A, 528, A131

Clayton D. D., Craddock W. L., 1965, ApJ, 142, 189

Clayton D., Fowler W., Hull T., Zimmerman B., 1961, Annals of Physics, 12, 331

Cohen J. G., Darling J., Porter A., 1995, AJ, 110, 308

Colgate S. A., 1975, ApJ, 198, 439

Colgate S. A., Johnson M. H., 1960, Phys. Rev. Lett., 5, 235

Colgate S. A., White R. H., 1966, ApJ, 143, 626

Conti P. S., 1984, in Maeder A., Renzini A., eds, IAU Symposium Vol. 105, Observational Tests of the Stellar Evolution Theory. p. 233

Coppejans D. L., et al., 2020, ApJ, 895, L23

Coughlin M. W., et al., 2023, ApJS, 267, 31

Crockett R. M., Smartt S. J., Pastorello A., Eldridge J. J., Stephens A. W., Maund J. R., Mattila S., 2011, MNRAS, 410, 2767

Crowther P. A., 2007, ARA&A, 45, 177

Das S., Ray A., 2017, ApJ, 851, 138

Das K. K., et al., 2025, PASP, 137, 044203

Davies B., Beasor E. R., 2017, MNRAS, 474, 2116

Davies B., Plez B., Petrault M., 2022, MNRAS, 517, 1483

Davis S., et al., 2019, ApJ, 887, 4

De K., et al., 2020, ApJ, 905, 58

Dekany R., et al., 2020, PASP, 132, 038001

Dessart L., Hillier D. J., 2011, MNRAS, 410, 1739

Dessart L., Hillier D. J., 2019, A&A, 625, A9

Dessart L., Hillier D. J., 2022, A&A, 660, L9

Dessart L., Jacobson-Galán W. V., 2023, A&A, 677, A105

Dessart L., Burrows A., Livne E., Ott C. D., 2008, ApJ, 673, L43

Dessart L., Hillier D. J., Gezari S., Basa S., Matheson T., 2009, MNRAS, 394, 21

Dessart L., Hillier D. J., Waldman R., Livne E., 2013, MNRAS, 433, 1745

Dessart L., Audit E., Hillier D. J., 2015, MNRAS, 449, 4304

Dessart L., Hillier D. J., Audit E., 2017, A&A, 605, A83

Dessart L., Hillier D. J., Sukhbold T., Woosley S. E., Janka H. T., 2021, A&A, 652, A64

Doherty C. L., Gil-Pons P., Siess L., Lattanzio J. C., 2017, Publ. Astron. Soc. Australia, 34, e056

Dong Y., et al., 2024, ApJ, 977, 254

Drilling J. S., Landolt A. U., 2000, in Cox A. N., ed., , Allen's Astrophysical Quantities. New York, p. 381

Duev D. A., van der Walt S. J., 2021, arXiv e-prints, p. arXiv:2111.12142

Duev D. A., et al., 2019, MNRAS, 489, 3582

Dyer M. J., Dhillon V. S., Littlefair S., Steeghs D., Ulaczyk K., Chote P., Galloway D., Rol E., 2018, in Observatory Operations: Strategies, Processes, and Systems VII. p. 107040C (arXiv:1807.01614), doi:10.1117/12.2311865

Eggleton P. P., 1983, ApJ, 268, 368

Ekström S., et al., 2012, A&A, 537, A146

El Eid M. F., Langer N., 1986, A&A, 167, 274

Eldridge J. J., Tout C. A., 2004, MNRAS, 353, 87

Eldridge J. J., Izzard R. G., Tout C. A., 2008, MNRAS, 384, 1109

Eldridge J. J., Fraser M., Smartt S. J., Maund J. R., Crockett R. M., 2013, MNRAS, 436, 774

Eldridge J. J., Xiao L., Stanway E. R., Rodrigues N., Guo N. Y., 2018, Publ. Astron. Soc. Australia, 35, e049

Elias-Rosa N., et al., 2009, ApJ, 706, 1174

Ensman L., Burrows A., 1992, ApJ, 393, 742

Falk S. W., Arnett W. D., 1977, ApJS, 33, 515

Fang Q., Moriya T. J., Maeda K., 2025a, Red Supergiant problem viewed from the nebular phase spectroscopy of type II supernovae (arXiv:2504.14502), https://arxiv.org/abs/2504.14502

Fang Q., Maeda K., Ye H., Moriya T. J., Matsumoto T., 2025b, ApJ, 978, 35

Faran T., et al., 2014, MNRAS, 445, 554

Farrell E. J., Groh J. H., Meynet G., Eldridge J. J., 2020, MNRAS, 494, L53

Fassia A., et al., 2000, MNRAS, 318, 1093

Filippenko A. V., 1992, in Filippenko A. V., ed., Astronomical Society of the Pacific Conference Series Vol. 103, Robotic Telescopes in the 1990s. pp 55–66

Filippenko A. V., 1997, ARA&A, 35, 309

Filippenko A. V., Li W. D., Treffers R. R., Modjaz M., 2001, Astronomical Society of the Pacific Conference Series, 246, 121

Foreman-Mackey D., 2015, George: Gaussian Process regression, Astrophysics Source Code Library, record ascl:1511.015

Foreman-Mackey D., Agol E., Ambikasaran S., Angus R., 2017, AJ, 154, 220

Förster F., et al., 2018, Nature Astronomy, 2, 808

Fox O. D., et al., 2014, ApJ, 790, 17

Fraley G. S., 1968, Ap&SS, 2, 96

Fransson C., Gilmozzi R., Groeningsson P., Hanuschik R., Kjaer K., Leibundgut B., Spyromilio J., 2007, The Messenger, 127, 44

Fransson C., et al., 2014, ApJ, 797, 118

Fransson C., et al., 2015, ApJ, 806, L19

Fraser M., et al., 2012, ApJ, 759, L13

Fraser M., et al., 2013, ApJ, 779, L8

Fremling C., et al., 2016, A&A, 593, A68

Fremling C., et al., 2020, ApJ, 895, 32

Frieman J. A., et al., 2007, AJ, 135, 338

Fryer C. L., 1999, ApJ, 522, 413

Fuller J., 2017, MNRAS, 470, 1642

Fuller J., Tsuna D., 2024, The Open Journal of Astrophysics, 7, 47

Gal-Yam A., 2012, Science, 337, 927

Gal-Yam A., 2017a, Handbook of Supernovae, pp 195–237

Gal-Yam A., 2017b, Handbook of Supernovae, p. 195–237

Gal-Yam A., 2019a, ARA&A, 57, 305

Gal-Yam A., 2019b, ARA&A, 57, 305

Gal-Yam A., Leonard D. C., 2009, Nature, 458, 865

Gal-Yam A., et al., 2007, ApJ, 656, 372

Gal-Yam A., Maoz D., Guhathakurta P., Filippenko A. V., 2008, ApJ, 680, 550

Gal-Yam A., et al., 2009, Nature, 462, 624

Gal-Yam A., et al., 2014, Nature, 509, 471

Galbany L., et al., 2016a, AJ, 151, 33

Galbany L., et al., 2016b, A&A, 591, A48

Gall E. E. E., et al., 2015, A&A, 582, A3

Garnavich P. M., Tucker B. E., Rest A., Shaya E. J., Olling R. P., Kasen D., Villar A., 2016, ApJ, 820, 23

Georgy C., 2012, A&A, 538, L8

Georgy C., Ekström S., Meynet G., Massey P., Levesque E. M., Hirschi R., Eggenberger P., Maeder A., 2012, A&A, 542, A29

Gerke J. R., Kochanek C. S., Stanek K. Z., 2015, MNRAS, 450, 3289

Gezari S., et al., 2008, ApJ, 683, L131

Gezari S., et al., 2010, ApJ, 720, L77

Gezari S., et al., 2015, ApJ, 804, 28

Gibbs M. N., 1998, PhD thesis, Citeseer

Gibson B. K., Loewenstein M., Mushotzky R. F., 1997, MNRAS, 290, 623

Gibson N. P., Aigrain S., Roberts S., Evans T. M., Osborne M., Pont F., 2012, MNRAS, 419, 2683

Gilkis A., Laplace E., Arcavi I., Shenar T., Schneider F. R. N., 2025, MNRAS,

Gilmozzi R., et al., 1987, Nature, 328, 318

Ginolin M., et al., 2025, A&A, 695, A140

Goldberg J., 2022, Understanding Type II-Plateau Supernovae and the Red Supergiants that Cause Them., https://escholarship.org/uc/item/65m867f0

Goldberg J. A., Bildsten L., Paxton B., 2019, ApJ, 879, 3

Goldberg J. A., Bildsten L., Paxton B., 2020, ApJ, 891, 15

González-Gaitán S., et al., 2015, MNRAS, 451, 2212

Goobar A., et al., 2023, Nature Astronomy, 7, 1098

Gordon T. A., Agol E., Foreman-Mackey D., 2020, AJ, 160, 240

Graham M. J., et al., 2019, PASP, 131, 078001

Grassberg E. K., Imshennik V. S., Nadyozhin D. K., 1971, Ap&SS, 10, 28

Graur O., Bianco F. B., Huang S., Modjaz M., Shivvers I., Filippenko A. V., Li W., Eldridge J. J., 2017a, ApJ, 837, 120

Graur O., Bianco F. B., Modjaz M., Shivvers I., Filippenko A. V., Li W., Smith N., 2017b, ApJ, 837, 121

Groh J. H., 2014a, A&A, 572, L11

Groh J. H., 2014b, A&A, 572

Groh J. H., Meynet G., Georgy C., Ekström S., 2013, A&A, 558, A131

Groot P. J., et al., 2024, PASP, 136, 115003

Gräfener G., Vink J. S., 2015, MNRAS, 455, 112

Gutiérrez C. P., et al., 2017a, ApJ, 850, 89

Gutiérrez C. P., et al., 2017b, ApJ, 850, 90

Gutiérrez C. P., et al., 2020a, MNRAS, 496, 95

Gutiérrez C. P., et al., 2020b, MNRAS, 499, 974

Gutiérrez C. P., et al., 2017, ApJ, 850, 90

Hachisu I., Matsuda T., Nomoto K., Shigeyama T., 1991, ApJ, 368, L27

Hamuy M. A., 2001, PhD thesis, University of Arizona

Hamuy M., 2003, ApJ, 582, 905

Hamuy M., et al., 2012, Mem. Soc. Astron. Italiana, 83, 388

Han Z., Podsiadlowski P., 2004, MNRAS, 350, 1301

Heasley J. N., 1999, in Craine E. R., Crawford D. L., Tucker R. A., eds, Astronomical Society of the Pacific Conference Series Vol. 189, Precision CCD Photometry. p. 56

Heger A., Woosley S. E., 2002, ApJ, 567, 532

Heger A., Jeannin L., Langer N., Baraffe I., 1997, A&A, 327, 224

Heger A., Langer N., Woosley S. E., 2000, ApJ, 528, 368

Heger A., Fryer C. L., Woosley S. E., Langer N., Hartmann D. H., 2003, ApJ, 591, 288

Heger A., Woosley S. E., Spruit H. C., 2005, ApJ, 626, 350

Heger A., Müller B., Mandel I., 2023, arXiv e-prints, p. arXiv:2304.09350

Heinonen M., Mannerström H., Rousu J., Kaski S., Lähdesmäki H., 2015, arXiv e-prints, p. arXiv:1508.04319

Helou G., Madore B. F., Schmitz M., Bicay M. D., Wu X., Bennett J., 1991, in Albrecht M. A., Egret D., eds, Astrophysics and Space Science Library Vol. 171, Databases and On-line Data in Astronomy. pp 89–106, doi:10.1007/978-94-011-3250-3˙10

Hendry M. A., et al., 2006, MNRAS, 369, 1303

Hillier D. J., Dessart L., 2012, MNRAS, 424, 252

Hillier D. J., Dessart L., 2019, A&A, 631, A8

Hillier D. J., Lanz T., 2001, in Ferland G., Savin D. W., eds, Astronomical Society of the Pacific Conference Series Vol. 247, Spectroscopic Challenges of Photoionized Plasmas. p. 343

Hillier D. J., Miller D. L., 1998, ApJ, 496, 407

Hinds K.-R., et al., 2025, arXiv e-prints, p. arXiv:2503.19969

Hiramatsu D., et al., 2021, ApJ, 913, 55

Hiramatsu D., et al., 2023, ApJ, 955, L8

Hiramatsu D., Berger E., Gomez S., Blanchard P. K., Kumar H., Athukoralalage W., 2024, arXiv e-prints, 2411.07287

Hirata K., et al., 1987, Phys. Rev. Lett., 58, 1490

Hirschi R., Meynet G., Maeder A., 2004, A&A, 425, 649

Hložek R., et al., 2023, ApJS, 267, 25

Ho A. Y. Q., et al., 2020, ApJ, 895, 49

Ho A. Y. Q., et al., 2023a, Nature, 623, 927

Ho A. Y. Q., et al., 2023b, ApJ, 949, 120

Horiuchi S., Beacom J. F., Kochanek C. S., Prieto J. L., Stanek K. Z., Thompson T. A., 2011, ApJ, 738, 154

Hosseinzadeh G., et al., 2018, ApJ, 861, 63

Hosseinzadeh G., et al., 2022, ApJ, 935, 31

Hosseinzadeh G., et al., 2023, ApJ, 953, L16

Hoyle F., Fowler W. A., 1960, ApJ, 132, 565

Hu L., Wang L., Chen X., Yang J., 2022, ApJ, 936, 157

Huang F., et al., 2018, MNRAS, 475, 3959

Hubble E., Sandage A., 1953, ApJ, 118, 353

Humphreys R. M., 1975, ApJ, 200, 426

Humphreys R. M., Helmel G., Jones T. J., Gordon M. S., 2020, AJ, 160, 145

Hurley J. R., Tout C. A., Pols O. R., 2002, MNRAS, 329, 897

Iben Jr. I., Tutukov A. V., 1984, ApJS, 54, 335

Inserra C., et al., 2016, MNRAS, 459, 2721

Irani I., et al., 2024, ApJ, 970, 96

Ivanova N., et al., 2013, A&A Rev., 21, 59

Ivezić Ž., et al., 2019, ApJ, 873, 111

Jacobson-Galán W. V., et al., 2022, ApJ, 924, 15

Jacobson-Galán W. V., et al., 2023, ApJ, 954, L42

Jacobson-Galán W. V., et al., 2024a, ApJ, 970, 189

Jacobson-Galán W. V., et al., 2024b, ApJ, 972, 177

Jacobson-Galán W. V., et al., 2025, arXiv e-prints, p. arXiv:2505.04698

Janka H.-T., 2012, Annual Review of Nuclear and Particle Science, 62, 407

Janka H.-T., 2017, Neutrino Emission from Supernovae. Springer International Publishing, p. 1575–1604, doi:10.1007/978-3-319-21846-5˙4, http://dx.doi.org/10.1007/978-3-319-21846-5_4

Janka H. T., 2025, arXiv e-prints, p. arXiv:2502.14836

Janka H. T., Langanke K., Marek A., Martínez-Pinedo G., Müller B., 2007, Phys. Rep., 442, 38

Jencson J. E., et al., 2023, ApJ, 952, L30

Jerkstrand A., Ergon M., Smartt S. J., Fransson C., Sollerman J., Taubenberger S., Bersten M., Spyromilio J., 2015, A&A, 573, A12

Jerkstrand A., Milisavjlevic D., Müller B., 2025, arXiv

Jermak H., Steele I. A., Smith R. J., 2016, in Evans C. J., Simard L., Takami H., eds, Society of Photo-Optical Instrumentation Engineers (SPIE) Conference Series Vol. 9908, Ground-based and Airborne Instrumentation for Astronomy VI. p. 99084I, doi:10.1117/12.2232324

Jones D. O., et al., 2021, ApJ, 908, 143

Kaiser N., et al., 2002, in Tyson J. A., Wolff S., eds, Society of Photo-Optical Instrumentation Engineers (SPIE) Conference Series Vol. 4836, Survey and Other Telescope Technologies and Discoveries. pp 154–164, doi:10.1117/12.457365

Kangas T., et al., 2022, MNRAS, 516, 1193

Kare J. T., Pennypacker C. R., Muller R. A., Mast T. S., Crawford F. S., Burns M. S., 1981, The Berkeley automated supernova search, Presented at the NATO Advan. Study Inst. on Supernova, Cambridge, 28 Jun. - 10 Jul. 1981

Kare J. T., Pennypacker C. R., Muller R. A., Mast T. S., Crawford F. S., Burns M. S., 1982, in Rees M. J., Stoneham R. J., eds, NATO Advanced Study Institute (ASI) Series C Vol. 90, Supernovae: A Survey of Current Research. pp 319–232, doi:10.1007/978-94-009-7876-8˙20

Kasen D., Woosley S. E., 2009, ApJ, 703, 2205

Kasliwal M. M., et al., 2019, PASP, 131, 038003

Kasliwal M. M., et al., 2020, ApJ, 905, 145

Kelly P. L., Kirshner R. P., 2012, ApJ, 759, 107

Kerzendorf W. E., Vogl C., Buchner J., Contardo G., Williamson M., van der Smagt P., 2021, ApJ, 910, L23

Kessler R., et al., 2019, PASP, 131, 094501

Khatami D. K., Kasen D. N., 2024, ApJ, 972, 140

Khazov D., et al., 2016, ApJ, 818, 3

Kiewe M., et al., 2012, ApJ, 744, 10

Kilpatrick C. D., et al., 2023, ApJ, 952, L23

Kim Y. L., et al., 2022, PASP, 134, 024505

Kirshner R. P., Kwan J., 1974, ApJ, 193, 27

Kirshner R. P., Oke J. B., Penston M. V., Searle L., 1973, ApJ, 185, 303

Klein R. I., Chevalier R. A., 1978, ApJ, 223, L109

Kleiser I. K. W., et al., 2011, MNRAS, 415, 372

Kobayashi C., Karakas A. I., Lugaro M., 2020, ApJ, 900, 179

Kochanek C. S., 2011, ApJ, 743, 73

Kochanek C. S., 2015, MNRAS, 446, 1213

Kochanek C. S., 2019, MNRAS, 483, 3762

Kochanek C. S., 2020, MNRAS, 493, 4945

Kochanek C. S., Beacom J. F., Kistler M. D., Prieto J. L., Stanek K. Z., Thompson T. A., Yüksel H., 2008, ApJ, 684, 1336

Kochanek C. S., Khan R., Dai X., 2012, ApJ, 759, 20

Kochanek C. S., et al., 2017, MNRAS, 467, 3347

Kochanek C. S., Neustadt J. M. M., Stanek K. Z., 2024, ApJ, 962, 145

Kolb E. W., Turner M. S., 1987, Phys. Rev. D, 36, 2895

Kornilov M. V., Semenikhin T. A., Pruzhinskaya M. V., 2023, MNRAS, 526, 1822

Kotak R., et al., 2009, ApJ, 704, 306

Kozyreva A., Nakar E., Waldman R., 2019, MNRAS, 483, 1211

Kozyreva A., Klencki J., Filippenko A. V., Baklanov P., Mironov A., Justham S., Chiavassa A., 2022, ApJ, 934, L31

Kulkarni S. R., et al., 2021, arXiv e-prints, p. arXiv:2111.15608

Kulkarni S. R., et al., 2023, Science with the Ultraviolet Explorer (UVEX) (arXiv:2111.15608), https://arxiv.org/abs/2111.15608

Kuncarayakti H., et al., 2013, AJ, 146, 31

Kuncarayakti H., et al., 2018, A&A, 613, A35

LSST Science Collaboration Abell P. A., Allison J., Anderson S. F., Andrew J. R., Angel J. R. P., 2009, arXiv e-prints, p. arXiv:0912.0201

Langer N., 2012, ARA&A, 50, 107

Laplace E., Schneider F. R. N., Podsiadlowski P., 2025, A&A, 695, A71

Law N. M., et al., 2009, PASP, 121, 1395

Law N. M., et al., 2022a, PASP, 134, 035003

Law N., Soto A. V., Corbett H., Galliher N., Gonzalez R., Machia L., Walters G., 2022b, in Ground-based and Airborne Telescopes IX. pp 1390–1399

Leaman J., Li W., Chornock R., Filippenko A. V., 2011, MNRAS, 412, 1419

Leonard D. C., Gal-Yam A., Fox D. B., Cameron P. B., Johansson E. M., Kraus A. L., Le Mignant D., van Dam M. A., 2008, PASP, 120, 1259

Leung S.-C., Fuller J., 2020, ApJ, 900, 99

Leung S.-C., Nomoto K., Blinnikov S., 2019, ApJ, 887, 72

Levesque E. M., Massey P., Olsen K. A. G., Plez B., Josselin E., Maeder A., Meynet G., 2005, ApJ, 628, 973

Li Y., Gong Z. G., 1994, A&A, 289, 449

Li X. D., van den Heuvel E. P. J., 1997, A&A, 322, L9

Li W., Van Dyk S. D., Filippenko A. V., Cuillandre J., 2005, PASP, 117, 121

Li W., Chornock R., Leaman J., Filippenko A. V., Poznanski D., Wang X., Ganeshalingam M., Mannucci F., 2011, MNRAS, 412, 1473

Li G., et al., 2024, Nature, 627, 754

Liddle A. R., 2007, MNRAS: Letters, 377, L74–L78

Liu S., Wood-Vasey W. M., Armstrong R., Narayan G., Sánchez B. O., Dark Energy Science Collaboration 2024, ApJ, 967, 10

Lochner M., McEwen J. D., Peiris H. V., Lahav O., Winter M. K., 2016, ApJS, 225, 31

Lourie N. P., et al., 2020, in Evans C. J., Bryant J. J., Motohara K., eds, Society of Photo-Optical Instrumentation Engineers (SPIE) Conference Series Vol. 11447, Ground-based and Airborne Instrumentation for Astronomy VIII. p. 114479K (arXiv:2102.01109), doi:10.1117/12.2561210

Lucy L. B., Solomon P. M., 1970, ApJ, 159, 879

Luger R., Foreman-Mackey D., Hedges C., 2021, AJ, 162, 124

Luo J., Dessart L., Chen X., Liu Z., 2024, A&A, 689, A246

Luo J., et al., 2025, ApJ, 982, L55

Lyman J. D., Bersier D., James P. A., 2014, MNRAS, 437, 3848

Lyman J. D., Bersier D., James P. A., Mazzali P. A., Eldridge J. J., Fraser M., Pian E., 2016, MNRAS, 457, 328

MacFadyen A. I., Woosley S. E., 1999, ApJ, 524, 262

Maeda K., 2013, ApJ, 762, 14

Malmquist K. G., 1920, Meddelanden fran Lunds Astronomiska Observatorium Serie I, 96, 1

Maltsev K., Schneider F. R. N., Mandel I., Müller B., Heger A., Röpke F. K., Laplace E., 2025, arXiv e-prints, p. arXiv:2503.23856

Maoz D., Graur O., 2017, ApJ, 848, 25

Margutti R., et al., 2017, ApJ, 835, 140

Martinez L., Bersten M. C., Anderson J. P., González-Gaitán S., Förster F., Folatelli G., 2020, A&A, 642, A143

Martinez L., et al., 2022a, A&A, 660, A40

Martinez L., et al., 2022b, A&A, 660, A41

Martinez L., et al., 2022c, A&A, 660, A42

Masci F. J., et al., 2019, PASP, 131, 018003

Masci F. J., et al., 2023, arXiv e-prints, p. arXiv:2305.16279

Matheson T., et al., 2021, AJ, 161, 107

Matsumoto J., Takiwaki T., Kotake K., Asahina Y., Takahashi H. R., 2020, MNRAS, 499, 4174

Matsumoto T., Metzger B. D., Goldberg J. A., 2025, ApJ, 978, 56

Matsuura M., et al., 2011, Science, 333, 1258

Matthews D., et al., 2023, Research Notes of the AAS, 7, 126

Mattila S., Smartt S. J., Eldridge J. J., Maund J. R., Crockett R. M., Danziger I. J., 2008, ApJ, 688, L91

Matzner C. D., McKee C. F., 1999, ApJ, 510, 379

Maund J. R., Smartt S. J., Kudritzki R. P., Podsiadlowski P., Gilmore G. F., 2004, Nature, 427, 129

Maund J. R., Smartt S. J., Danziger I. J., 2005, MNRAS: Letters, 364, L33

Maund J. R., et al., 2011, ApJ, 739, L37

Maund J. R., et al., 2013, MNRAS: Letters, 431, L102

Maund J. R., Fraser M., Reilly E., Ergon M., Mattila S., 2015, MNRAS, 447, 3207

Maund J. R., et al., 2021, MNRAS, 503, 312–323

Mauron N., Josselin E., 2011, A&A, 526, A156

McLaughlin S. A. J., Mullaney J. R., Littlefair S. P., 2024, MNRAS, 529, 2877

Medler K., et al., 2022, MNRAS, 513, 5540

Merlin E., Pilo S., Fontana A., Castellano M., Paris D., Roscani V., Santini P., Torelli M., 2019, A&A, 622, A169

Meyer B. S., 1994, ARA&A, 32, 153

Mezzacappa A., Endeve E., Messer O. E. B., Bruenn S. W., 2020, Living Reviews in Computational Astrophysics, 6, 4

Michel P. D., Mazzali P. A., Perley D. A., Hinds K. R., Wise J. L., 2025, MNRAS, 539, 633

Miller A. C., Anderson L., Leistedt B., Cunningham J. P., Hogg D. W., Blei D. M., 2022, arXiv e-prints, p. arXiv:2202.06797

Miller A. A., et al., 2025, arXiv e-prints, p. arXiv:2503.14579

Milne E., 1926, MNRAS, Vol. 86, p. 459-473, 86, 459

Miyaji S., Nomoto K., Yokoi K., Sugimoto D., 1980, PASJ, 32, 303

Modjaz M., et al., 2009, ApJ, 702, 226

Möller A., et al., 2021, MNRAS, 501, 3272

Mommert M., 2017, Astronomy and Computing, 18, 47

Morag J., Sapir N., Waxman E., 2023, MNRAS, 522, 2764

Morales-Garoffolo A., et al., 2014, MNRAS, 445, 1647

Morales-Garoffolo A., et al., 2015, MNRAS, 454, 95

Moriya T. J., 2023, MNRAS, 524, 5309

Moriya T. J., Singh A., 2024, PASJ, 76, 1050

Moriya T., Tominaga N., Blinnikov S. I., Baklanov P. V., Sorokina E. I., 2011, MNRAS, 415, 199

Moriya T. J., et al., 2016, MNRAS, 466, 2085

Moriya T. J., Yoon S.-C., Gräfener G., Blinnikov S. I., 2017, MNRAS, 469, L108

Moriya T. J., Förster F., Yoon S.-C., Gräfener G., Blinnikov S. I., 2018, MNRAS, 476, 2840

Moriya T. J., Subrayan B. M., Milisavljevic D., Blinnikov S. I., 2023, PASJ, 75, 634

Morozova V., Piro A. L., Renzo M., Ott C. D., Clausen D., Couch S. M., Ellis J., Roberts L. F., 2015, ApJ, 814, 63

Morozova V., Piro A. L., Renzo M., Ott C. D., 2016, ApJ, 829, 109

Morozova V., Piro A. L., Valenti S., 2017, ApJ, 838, 28

Morozova V., Piro A. L., Valenti S., 2018, ApJ, 858, 15

Morozova V., Piro A. L., Fuller J., Van Dyk S. D., 2020, ApJ, 891, L32

Morris T., Podsiadlowski P., 2007, Science, 315, 1103

Müller E., 1987, Computer Physics Communications, 44, 271

Müller T., Prieto J. L., Pejcha O., Clocchiatti A., 2017, ApJ, 841, 127

Myra E. S., Bludman S. A., Hoffman Y., Lichenstadt I., Sack N., van Riper K. A., 1987, ApJ, 318, 744

Müller B., 2020, Living Reviews in Computational Astrophysics, 6

Müller B., et al., 2019, MNRAS, 484, 3307

Nadyozhin D. K., 1994, ApJS, 92, 527

Nakar E., Piro A. L., 2014, ApJ, 788, 193

Nakar E., Sari R., 2010, ApJ, 725, 904–921

Nakar E., Poznanski D., Katz B., 2016, ApJ, 823, 127

Narayan G., et al., 2018, ApJS, 236, 9

Nayana A. J., et al., 2024, arXiv e-prints, p. arXiv:2411.02647

Naylor T., 1998, MNRAS, 296, 339

Nelemans G., Yungelson L. R., Portegies Zwart S. F., Verbunt F., 2001, A&A, 365, 491

Neustadt J. M. M., Kochanek C. S., Smith M. R., 2024, MNRAS, 527, 5366

Ni Y. Q., et al., 2025, ApJ, 983, 3

Niemela V. S., Ruiz M. T., Phillips M. M., 1985, ApJ, 289, 52

Nieuwenhuijzen H., de Jager C., 1990, A&A, 231, 134

Niu Z., Sun N.-C., Maund J. R., Zhang Y., Zhao R., Liu J., 2023, ApJ, 955, L15

Noack M. M., Sethian J. A., 2021, arXiv e-prints, p. arXiv:2102.03432

Noack M. M., Luo H., Risser M. D., 2024, APL Machine Learning, 2, 010902

Nomoto K., Hashimoto M., 1988, Phys. Rep., 163, 13

Nomoto K., Thielemann F. K., Yokoi K., 1984, ApJ, 286, 644

Nomoto K., Suzuki T., Shigeyama T., Kumagai S., Yamaoka H., Saio H., 1993, Nature, 364, 507

Nomoto K., Kobayashi C., Tominaga N., 2013, ARA&A, 51, 457

Nugis T., Lamers H. J. G. L. M., 2000, A&A, 360, 227

Nyholm A., et al., 2020, A&A, 637, A73

O'Neill D., et al., 2019, A&A, 622, L1

O'Neill D., Kotak R., Fraser M., Mattila S., Pietrzyński G., Prieto J. L., 2021, A&A, 645, L7

Ofek E. O., et al., 2007, ApJ, 659, L13

Ofek E. O., et al., 2010, ApJ, 724, 1396–1401

Ofek E. O., et al., 2013, Nature, 494, 65–67

Ofek E. O., et al., 2014, ApJ, 789, 104

Ofek E. O., et al., 2021, ApJ, 922, 247

Oke J. B., Gunn J. E., 1982, PASP, 94, 586

Oppenheimer J. R., Volkoff G. M., 1939, Physical Review, 55, 374

Ott C. D., 2009, Classical and Quantum Gravity, 26, 063001

Ouchi R., Maeda K., 2020, MNRAS, 500, 1889–1894

O'Connor E. P., Couch S. M., 2018, ApJ, 865, 81

O'Connor E., Ott C. D., 2011, ApJ, 730, 70

Paciorek C., Schervish M., 2003, Advances in neural information processing systems, 16

Paczyński B., 1971, ARA&A, 9, 183

Paczyński B., 2000, PASP, 112, 1281

Pastorello A., et al., 2005, MNRAS, 360, 950

Pastorello A., et al., 2008, MNRAS, 389, 955

Pastorello A., et al., 2012, A&A, 537, A141

Patat F., Barbon R., Cappellaro E., Turatto M., 1993, A&AS, 98, 443

Patat F., Barbon R., Cappellaro E., Turatto M., 1994, A&A, 282, 731

Patterson M. T., et al., 2019, PASP, 131, 018001

Paxton B., et al., 2015, ApJS, 220, 15

Pearson J., et al., 2023, ApJ, 945, 107

Pejcha O., Prieto J. L., 2015a, ApJ, 799, 215

Pejcha O., Prieto J. L., 2015b, ApJ, 806, 225

Pejcha O., Thompson T. A., 2015, ApJ, 801, 90

Pellegrino C., et al., 2022, ApJ, 938, 73

Perets H. B., et al., 2010, Nature, 465, 322

Perley D. A., et al., 2019, MNRAS, 484, 1031

Perley D. A., et al., 2020, ApJ, 904, 35

Perley D. A., et al., 2021a, MNRAS, 508, 5138

Perley D. A., et al., 2021b, MNRAS, 508, 5138

Perley D. A., et al., 2022, ApJ, 927, 180

Perlmutter S., Muller R. A., Newberg H. J. M., Pennypacker C. R., Sasseen T. P., Smith C. K., 1989, in Norman E. B., ed., Particle Astrophysics: Forefront Experimental Issues. p. 196

Perlmutter S., Muller R. A., Newberg H. J. M., Pennypacker C. R., Sasseen T. P., Smith C. K., 1992, in Filippenko A. V., ed., Astronomical Society of the Pacific Conference Series Vol. 103, Robotic Telescopes in the 1990s. pp 67–71

Pessi P. J., et al., 2019, MNRAS, 488, 4239

Pessi P. J., et al., 2023a, MNRAS, 523, 5315

Pessi T., et al., 2023b, A&A, 677, A28

Pessi T., Anderson J. P., Lyman J. D., Prieto J. L., Galbany L., Kochanek C. S., Sánchez S. F., Kuncarayakti H., 2023c, ApJ, 955, L29

Pessi T., et al., 2024, A&A, 688, L28

Pessi P. J., et al., 2025, A&A, 695, A142

Phillips A. C., Davis L. E., 1995, in Astronomical Data Analysis Software and Systems IV. p. 297

Piascik A. S., Steele I. A., Bates S. D., Mottram C. J., Smith R. J., Barnsley R. M., Bolton B., 2014, in Proc. SPIE. p. 91478H, doi:10.1117/12.2055117

Pickering E. C., 1897, Popular Astronomy, 5, 411

Pignata G., et al., 2009, in Giobbi G., Tornambe A., Raimondo G., Limongi M., Antonelli L. A., Menci N., Brocato E., eds, American Institute of Physics Conference Series Vol. 1111, Probing Stellar Populations Out to the Distant Universe: Cefalu 2008, Proceedings of the International Conference. AIP, pp 551–554 (arXiv:0812.4923), doi:10.1063/1.3141608

Piro A. L., 2015, ApJ, 808, L51

Piro A. L., Haynie A., Yao Y., 2021, ApJ, 909, 209

Pledger J. L., Shara M. M., 2023, ApJ, 953, L14

Podsiadlowski P., Joss P. C., Hsu J. J. L., 1992, ApJ, 391, 246

Podsiadlowski P., Hsu J. J. L., Joss P. C., Ross R. R., 1993, Nature, 364, 509

Podsiadlowski P., Morris T. S., Ivanova N., 2007, in Immler S., Weiler K., McCray R., eds, American Institute of Physics Conference Series Vol. 937, Supernova 1987A: 20 Years After: Supernovae and Gamma-Ray Bursters. AIP, pp 125–133, doi:10.1063/1.3682893

Popov D. V., 1993, ApJ, 414, 712

Prentice S. J., et al., 2018, ApJ, 865, L3

Prentice S. J., et al., 2020, MNRAS, 499, 1450

Press W. H., 1997, Understanding data better with Bayesian and global statistical methods.. Unsolved problems in astrophysics, pp 49–60 (arXiv:astro-ph/9604126), doi:10.48550/arXiv.astro-ph/9604126

Press W. H., Rybicki G. B., Hewitt J. N., 1992, ApJ, 385, 404

Puls J., Vink J. S., Najarro F., 2008, A&A Rev., 16, 209

Pumo M. L., Zampieri L., 2011, ApJ, 741, 41

Pumo M. L., Zampieri L., Spiro S., Pastorello A., Benetti S., Cappellaro E., Manicò G., Turatto M., 2017, MNRAS, 464, 3013

Pursiainen M., et al., 2018, MNRAS, 481, 894

Qin Y.-J., et al., 2024, MNRAS, 534, 271

Qu H., Sako M., Möller A., Doux C., 2021, AJ, 162, 67

Quataert E., Shiode J., 2012, MNRAS, 423, L92

Quataert E., Fernández R., Kasen D., Klion H., Paxton B., 2016, MNRAS, 458, 1214

Quimby R. M., 2006, PhD thesis, University of Texas, Austin

Quimby R. M., Wheeler J. C., Höflich P., Akerlof C. W., Brown P. J., Rykoff E. S., 2007a, ApJ, 666, 1093

Quimby R. M., Aldering G., Wheeler J. C., Höflich P., Akerlof C. W., Rykoff E. S., 2007b, ApJ, 668, L99

Quimby R. M., Yuan F., Akerlof C., Wheeler J. C., 2013, MNRAS, 431, 912

Rabinak I., Waxman E., 2011, ApJ, 728, 63

Rakavy G., Shaviv G., 1967, ApJ, 148, 803

Rakavy G., Shaviv G., Zinamon Z., 1967, ApJ, 150, 131

Ransome C. L., Habergham-Mawson S. M., Darnley M. J., James P. A., Filippenko A. V., Schlegel E. M., 2021, MNRAS, 506, 4715

Rasmussen C. E., 2004, Gaussian Processes in Machine Learning. Springer Berlin Heidelberg, Berlin, Heidelberg, pp 63–71, doi:10.1007/978-3-540-28650-9˙4, https://doi.org/10.1007/978-3-540-28650-9_4

Rau A., et al., 2009, PASP, 121, 1334

Ravi A. P., et al., 2025, ApJ, 982, 12

Reguitti A., et al., 2024, A&A, 692, A26

Rehemtulla N., et al., 2025, arXiv e-prints, p. arXiv:2501.18686

Reimers D., 1975, Memoires of the Societe Royale des Sciences de Liege, 8, 369

Rest A., et al., 2011, ApJ, 729, 88

Reynolds T. M., et al., 2020, MNRAS, 493, 1761

Richardson D., III R. L. J., Wright J., Maddox L., 2014, AJ, 147, 118

Richmond M., Treffers R. R., Filippenko A. V., 1993, PASP, 105, 1164

Richmond M. W., Treffers R. R., Filippenko A. V., Paik Y., Leibundgut B., Schulman E., Cox C. V., 1994, AJ, 107, 1022

Rigault M., et al., 2019, A&A, 627, A115

Rigault M., et al., 2025, A&A, 694, A1

Roberts S., Osborne M., Ebden M., Reece S., Gibson N., Aigrain S., 2012, Philosophical Transactions of the Royal Society of London Series A, 371, 20110550

Rodrigo C., Solano E., 2020, in XIV. 0 Scientific Meeting (virtual) of the Spanish Astronomical Society. p. 182

Rodrigo C., et al., 2024, A&A, 689, A93

Rodríguez Ó., 2022, MNRAS, 515, 897

Rodríguez Ó., Meza N., Pineda-García J., Ramirez M., 2021, MNRAS, 505, 1742

Rosino L., 1964, Annales d'Astrophysique, 27, 313

Rubin A., Gal-Yam A., 2017, ApJ, 848, 8

Rubin A., et al., 2016, ApJ, 820, 33

Rui L., et al., 2019, MNRAS, 485, 1990

Salasnich B., Bressan A., Chiosi C., 1999, A&A, 342, 131

Salmaso I., et al., 2023, A&A, 673, A127

Salpeter E. E., 1955, ApJ, 121, 161

Sana H., et al., 2012, Science, 337, 444

Sana H., et al., 2013, A&A, 550, A107

Sánchez-Sáez P., et al., 2021, AJ, 161, 141

Sanders N. E., et al., 2015, ApJ, 799, 208

Sargent W. L. W., Searle L., Kowal C. T., 1974, Astrophysics and Space Science Library

Schaeffer R., Declais Y., Jullian S., 1987, Nature, 330, 142

Schaeffer R.and Cassé M., Mochkovitch R., Cahen S., Nomoto K., 1988, in Atmospheric Diagnostics of Stellar Evolution: Chemical Peculiarity, Mass Loss, and Explosion. Springer Berlin Heidelberg, Berlin, Heidelberg, pp 438–439

Schawinski K., et al., 2008, Science, 321, 223

Schaye J., et al., 2015, MNRAS, 446, 521

Schlafly E. F., Finkbeiner D. P., 2011, ApJ, 737, 103

Schlegel E. M., 1990, MNRAS, 244, 269

Schmidt M., 1968, ApJ, 151, 393

Schmidt B. P., et al., 1993, Nature, 364, 600

Schmidt B. P., et al., 1994, AJ, 107, 1444

Schulze S., et al., 2024, arXiv e-prints, p. arXiv:2409.02054

Schwarz G., 1978, The annals of statistics, pp 461–464

Seeger M., 2004, International Journal of Neural Systems, 14, 69

Seeger P. A., Fowler W. A., Clayton D. D., 1965, ApJS, 11, 121

Seikel M., Clarkson C., Smith M., 2012, Journal of Cosmology and Astroparticle Physics, 2012, 036

Sfaradi I., Horesh A., Fender R., Rhodes L., Bright J., Williams-Baldwin D., Green D. A., 2025, ApJ, 979, 189

Shappee B. J., et al., 2014, ApJ, 788, 48

Shigeyama T., Suzuki T., Kumagai S., Nomoto K., Saio H., Yamaoka H., 1994, ApJ, 420, 341

Shiode J. H., Quataert E., 2014, ApJ, 780, 96

Shivvers I., et al., 2017, PASP, 129, 054201

Shrestha M., et al., 2024, ApJ, 972, L15

Shvartzvald Y., et al., 2024, ApJ, 964, 74

Silva-Farfán J., et al., 2024, ApJ, 969, 57

Singh A., et al., 2019, ApJ, 882, L15

Singh A., et al., 2024, ApJ, 975, 132

Sit T., et al., 2023, ApJ, 959, 142

Smartt S. J., 2009, ARA&A, 47, 63

Smartt S. J., 2015, Publ. Astron. Soc. Australia, 32, e016

Smartt S. J., Gilmore G. F., Trentham N., Tout C. A., Frayn C. M., 2001, ApJ, 556, L29

Smartt S. J., Maund J. R., Hendry M. A., Tout C. A., Gilmore G. F., Mattila S., Benn C. R., 2004, Science, 303, 499

Smartt S. J., Eldridge J. J., Crockett R. M., Maund J. R., 2009, MNRAS, 395, 1409

Smith N., 2011, Bulletin de la Societe Royale des Sciences de Liege, 80, 322

Smith N., 2014, ARA&A, 52, 487

Smith N., 2017a, Handbook of Supernovae, pp 403–429

Smith N., 2017b, Philosophical Transactions of the Royal Society A: Mathematical, Physical and Engineering Sciences, 375, 20160268

Smith N., Arnett W. D., 2014, ApJ, 785, 82

Smith N., et al., 2007, ApJ, 666, 1116

Smith N., Chornock R., Silverman J. M., Filippenko A. V., Foley R. J., 2010, ApJ, 709, 856

Smith N., Li W., Silverman J. M., Ganeshalingam M., Filippenko A. V., 2011, MNRAS, 415, 773

Smith N., et al., 2015, MNRAS, 449, 1876

Smith K. W., et al., 2019, Research Notes of the AAS, 3, 26

Soderberg A. M., et al., 2008, Nature, 453, 469

Sollerman J., et al., 2019, A&A, 621, A30

Sonneborn G., Altner B., Kirshner R. P., 1987, ApJ, 323, L35

Soraisam M. D., et al., 2023, ApJ, 957, 64

Spiro S., et al., 2014, MNRAS, 439, 2873

Sravan N., Marchant P., Kalogera V., 2019, ApJ, 885, 130

Stathakis R. A., Sadler E. M., 1991, MNRAS, 250, 786

Steeghs D., et al., 2022, MNRAS, 511, 2405

Steele I. A., et al., 2004, in Oschmann Jacobus M. J., ed., Society of Photo-Optical Instrumentation Engineers (SPIE) Conference Series Vol. 5489, Ground-based Telescopes. pp 679–692, doi:10.1117/12.551456

Steele I. A., Bates S. D., Gibson N., Keenan F., Meaburn J., Mottram C. J., Pollacco D., Todd I., 2008, in Proc. SPIE. p. 70146J, doi:10.1117/12.787889

Stetson P. B., 1987, PASP, 99, 191

Stevance H. F., Lee A., 2023, MNRAS, 518, 5741

Stritzinger M., et al., 2002, AJ, 124, 2100

Stroh M. C., et al., 2021, ApJ, 923, L24

Strolger L.-G., et al., 2015, ApJ, 813, 93

Strotjohann N. L., et al., 2021, ApJ, 907, 99

Strotjohann N. L., et al., 2024a, ApJ, 960, 72

Strotjohann N. L., Ofek E. O., Gal-Yam A., 2024b, ApJ, 964, L27

Sukhbold T., Adams S., 2020, MNRAS, 492, 2578

Sukhbold T., Ertl T., Woosley S. E., Brown J. M., Janka H.-T., 2016, ApJ, 821, 38

Sullivan M., 2013, Astronomy & Geophysics, 54, 6.17

Sundqvist J. O., Owocki S. P., 2013, MNRAS, 428, 1837

Suntzeff N. B., 1997, arXiv e-prints, pp astro–ph/9707324

Suntzeff N., Bouchet P., 1990, AJ, 99, 650

Suntzeff N. B., Phillips M. M., Elias J. H., Depoy D. L., Walker A. R., 1992, ApJ, 384, L33

Suwa Y., Tominaga N., Maeda K., 2019, MNRAS, 483, 3607

Svirski G., Nakar E., Sari R., 2012, ApJ, 759, 108

Szalai T., et al., 2024, A&A, 690, A17

Taddia F., et al., 2013, A&A, 555, A10

Taddia F., et al., 2016, A&A, 588, A5

Taggart K., 2020, PhD thesis, Liverpool John Moores University, doi:10.24377/LJMU.t.00014104, http://researchonline.ljmu.ac.uk/id/eprint/14104/

Takáts K., et al., 2015, MNRAS, 450, 3137

Tartaglia L., et al., 2018, ApJ, 853, 62

Theureau G., et al., 2005, A&A, 430, 373

Theureau G., Hanski M. O., Coudreau N., Hallet N., Martin J. M., 2007, A&A, 465, 71

Thévenot M., 2020, Research Notes of the AAS, 4, 243

Thielemann F.-K., Nomoto K., Hashimoto M.-A., 1996, ApJ, 460, 408

Thomas A., et al., 2025, arXiv e-prints, p. arXiv:2501.18142

Thompson T. A., Burrows A., Pinto P. A., 2003, ApJ, 592, 434

Thornton I., Villar V. A., Gomez S., Hosseinzadeh G., 2024, Research Notes of the AAS, 8, 48

Tinyanont S., et al., 2021, Nature Astronomy, 5, 544

Tinyanont S., et al., 2022, MNRAS, 512, 2777

Tody D., 1986, in Instrumentation in astronomy VI. pp 733–748

Tody D., 1993, in Hanisch R. J., Brissenden R. J. V., Barnes J., eds, Astronomical Society of the Pacific Conference Series Vol. 52, Astronomical Data Analysis Software and Systems II. p. 173

Tokunaga A. T., Vacca W. D., 2005, PASP, 117, 421

Tomasella L., et al., 2013, MNRAS, 434, 1636

Tominaga N., Blinnikov S., Baklanov P., Morokuma T., Nomoto K., Suzuki T., 2009, ApJ, 705, L10

Tominaga N., Morokuma T., Blinnikov S. I., Baklanov P., Sorokina E. I., Nomoto K., 2011, ApJS, 193, 20

Tonry J. L., et al., 2018, PASP, 130, 064505

Troxel M. A., et al., 2021, MNRAS, 501, 2044

Turatto M., Cappellaro E., Danziger I. J., Benetti S., Gouiffes C., della Valle M., 1993, MNRAS, 262, 128

Ugliano M., Janka H.-T., Marek A., Arcones A., 2012, ApJ, 757, 69

Underhill A. B., 1969, in Hack M., ed., Mass Loss from Stars. Springer Netherlands, Dordrecht, pp 17–25

Utrobin V. P., Chugai N. N., 2009, A&A, 506, 829

Utrobin V. P., Wongwathanarat A., Janka H. T., Müller E., 2017, ApJ, 846, 37

Utrobin V. P., et al., 2021, MNRAS, 505, 116

Valenti S., et al., 2016, MNRAS, 459, 3939

Valerin G., et al., 2022, MNRAS, 513, 4983

Vallely P. J., Kochanek C. S., Stanek K. Z., Fausnaugh M., Shappee B. J., 2021, MNRAS, 500, 5639

Van Dyk S. D., 2017, Philosophical Transactions of the Royal Society of London Series A, 375, 20160277

Van Dyk S. D., Li W., Filippenko A. V., 2003, PASP, 115, 1289

Van Dyk S. D., et al., 2012, ApJ, 756, 131

Van Dyk S. D., et al., 2014, AJ, 147, 37

Van Dyk S. D., et al., 2019, ApJ, 875, 136

Van Dyk S. D., et al., 2023, MNRAS, 524, 2186

Van Dyk S. D., et al., 2024, ApJ, 968, 27

Vanbeveren D., De Loore C., Van Rensbergen W., 1998, A&A Rev., 9, 63

Van Bemmel N., et al., 2025, MNRAS, 537, 3332

Villar V. A., Berger E., Metzger B. D., Guillochon J., 2017, ApJ, 849, 70

Villar V. A., et al., 2019, ApJ, 884, 83

Villar V. A., et al., 2020, ApJ, 905, 94

Villar V. A., Cranmer M., Berger E., Contardo G., Ho S., Hosseinzadeh G., Lin J. Y.-Y., 2021, ApJS, 255, 24

Vink J. S., 2008, New Astronomy Reviews, 52, 419

Vink J. S., 2018, A&A, 615, A119

Vink J. S., 2022, ARA&A, 60, 203

Vink, Jorick S. Sabhahit, Gautham N. 2023, A&A, 678, L3

Vink J. S., de Koter A., Lamers H. J. G. L. M., 2000, A&A, 362, 295

Vink J. S., de Koter A., Lamers H. J. G. L. M., 2001, A&A, 369, 574

Vink J. S., Muijres L. E., Anthonisse B., de Koter A., Gräfener G., Langer N., 2011, A&A, 531, A132

Vogl C., Kerzendorf W. E., Sim S. A., Noebauer U. M., Lietzau S., Hillebrandt W., 2020, A&A, 633, A88

Wanajo S., Nomoto K., Janka H. T., Kitaura F. S., Müller B., 2009, ApJ, 695, 208

Wang L. J., et al., 2018, ApJ, 865, 95

Wang L.-J., Liu L.-D., Lin W.-L., Wang X.-F., Dai Z.-G., Li B., Song L.-M., 2022, ApJ, 933, 102

Wang K. X., et al., 2023, MNRAS, 523, 3874

Warwick B., et al., 2025, MNRAS, 536, 3588

Waxman E., Katz B., 2017, in Alsabti A. W., Murdin P., eds, , Handbook of Supernovae. Springer, Cham, p. 967, doi:10.1007/978-3-319-21846-5˙33

Waxman E., Mészáros P., Campana S., 2007, ApJ, 667, 351

Webbink R. F., 1984, ApJ, 277, 355

Weil K. E., Fesen R. A., Patnaude D. J., Raymond J. C., Chevalier R. A., Milisavljevic D., Gerardy C. L., 2020, ApJ, 891, 116

Whelan J., Iben Jr. I., 1973, ApJ, 186, 1007

Wilson J. R., 1971, ApJ, 163, 209

Wolf C. J. E., Rayet G., 1867, Academie des Sciences Paris Comptes Rendus, 65, 292

Wongwathanarat A., Müller E., Janka H. T., 2015, A&A, 577, A48

Woosley S. E., 1988, ApJ, 330, 218

Woosley S. E., 2017, ApJ, 836, 244

Woosley S., Bloom J., 2006, ARA&A, 44, 507

Woosley S. E., Weaver T. A., 1986, ARA&A, 24, 205

Woosley S. E., Weaver T. A., 1995, ApJS, 101, 181

Woosley S. E., Eastman R. G., Weaver T. A., Pinto P. A., 1994, ApJ, 429, 300

Woosley S. E., Heger A., Weaver T. A., 2002, Rev. Mod. Phys., 74, 1015

Woosley S. E., Blinnikov S., Heger A., 2007, Nature, 450, 390

Wu C. O., 1997, Journal of Multivariate Analysis, 61, 38

Wu S., Fuller J., 2021, ApJ, 906, 3

Xiang D., et al., 2023, MNRAS, 520, 2965

Xiang D., et al., 2024, ApJ, 969, L15

Yamanaka M., Nagayama T., Horikiri T., 2025, PASJ,

Yang S., et al., 2017, ApJ, 851, L48

Yang S., et al., 2021, A&A, 655, A90

Yao Y., et al., 2022, ApJ, 934, 104

Yaron O., et al., 2017, Nature Physics, 13, 510

Yoon S.-C., Cantiello M., 2010, ApJ, 717, L62

Yoon S.-C., Dessart L., Clocchiatti A., 2017, ApJ, 840, 10

York D. G., et al., 2000, AJ, 120, 1579

Yoshida T., Umeda H., Maeda K., Ishii T., 2016, MNRAS, 457, 351

Young T. R., 2004, ApJ, 617, 1233

Yuan F., et al., 2016, MNRAS, 461, 2003

Zackay B., Ofek E. O., Gal-Yam A., 2016a, ApJ, 830, 27

Zackay B., Ofek E. O., Gal-Yam A., 2016b, ApJ, 830, 27

Zapartas E., et al., 2019, A&A, 631, A5

Zapartas E., de Mink S. E., Justham S., Smith N., Renzo M., de Koter A., 2021, A&A, 645, A6

Zimmerman E., Schulze S., Johansson J., Yang Y., Perley D., Bruch R., Gal-Yam A., 2021, Transient Name Server AstroNote, 91, 1

Zimmerman E. A., et al., 2024, Nature, 627, 759

Zwicky F., 1938a, PASP, 50, 215

Zwicky F., 1938b, ApJ, 88, 529

Zwicky F., 1942, ApJ, 96, 28

Zwicky F., 1964, Annales d'Astrophysique, 27, 300

de Jaeger T., et al., 2018, MNRAS, 476, 4592

de Jaeger T., et al., 2019, MNRAS, 490, 2799

de Jager C., Nieuwenhuijzen H., van der Hucht K. A., 1988, A&AS, 72, 259

van Loon J. T., Cioni M. R. L., Zijlstra A. A., Loup C., 2005, A&A, 438, 273

van der Walt S. J., Crellin-Quick A., Bloom J. S., 2019, Journal of Open Source Software, 4

van der Wilk M., Dutordoir V., John S., Artemev A., Adam V., Hensman J., 2020, arXiv e-prints, p. arXiv:2003.01115